STUDIES ON TITANIUM CARBIDE REINFORCED FERROUS COMPOSITES PREPARED BY PLASMA SMELTING OF ILMENITE ORE

A Thesis Submitted to the
Indian Institute of Technology, Kharagpur
for the Award of the Degree
of

Doctor of Philosophy

BY

RAMCHANDRA KRISHNARAO GALGALI

Department of Metallurgical and Materials Engineering
INDIAN INSTITUTE OF TECHNOLOGY
KHARAGPUR - 721 302 INDIA
1995

DEDICATED
TO
*My father Shri Krishna Ramachandra Galgali
and to the memory of my Late mother Syamalabai*

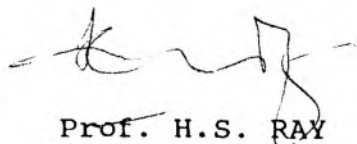"There is a great difference between knowing a thing and understanding it.

- Charles Kettering

METALLURGICAL AND MATERIALS ENGINEERING DEPARTMENT
INDIAN INSTITUTE OF TECHNOLOGY
KHARAGPUR - 721 302, INDIA
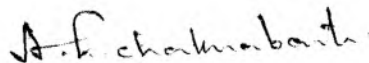
Kharagpur
Date: May 12, 1995

CERTIFICATE

This is to certify that the thesis entitled **"STUDIES ON TITANIUM CARBIDE REINFORCED FERROUS COMPOSITES PREPARED BY PLASMA SMELTING OF ILMENITE ORE"** submitted by Shri Ramchandra Krishnarao Galgali for the Ph.D. degree is a record of bonafide research work carried out by him in the Metallurgical and Materials Engineering Department at the Indian Institute of Technology, Kharagpur, under our guidance and supervision. In our opinion the work fulfills the requirement for which it is being submitted.

The work incorporated in this thesis has not been submitted to any other University or Institute for the award of any degree or diploma.

Prof. H.S. RAY
Director,
Regional Research Laboratory
Bhubaneswar

Dr. A.K. CHAKRABORTI
Professor,
Metallurgical and Materials
Engineering Department
I.I.T., Kharagpur

Acknowledgement

I express my sincere thanks to Prof. A.K. Chakraborti, Department of Metallurgical and Materials Engineering, Indian Institute of Technology, Kharagpur and Prof. H.S. Ray, Director, Regional Research Laboratory, Bhubaneswar for their constant encouragement and valuable guidance throughout the course of this work. I am also thankful to Prof. P.K. Jena, Former Director, Regional Research Laboratory, Bhubaneswar who was instrumental in starting the R&D activities on thermal plasma and rendering guidance during the initial part of this work.

Thanks are also due to Shri B.C. Mohanty, Head, Special Materials Division, RRL, Bhubaneswar and Prof. U.K. Chatterjee, Head, Department of Metallurgical Engineering, Indian Institute of Technology, Kharagpur for their encouragement and advice. I wish to thank Prof. B.K. Dhindaw, Prof. S.B. Sarkar, Prof. M.M. Godkhindi, Prof. P.G. Mukunda and Dr. B.S.Murthy for the suggestions, advice and support they have so generously given from time to time.

Many of my colleagues have extended their whole hearted co-operation in carrying out this work. It is not possible to thank them individually and I can make special mention of only some of them. I acknowledge gratefully the help rendered by Dr. U. Syamaprasad, Dr(Mrs.) S. Bhattacharjee, Dr. J. Muralidhar, Dr. P. Dutta, Dr. B. Das, Shri K.K. Rao, Shri S. Prakash, Dr. B.S. Acharya and Shri K.C. Das. They have helped whenever I have approached them.
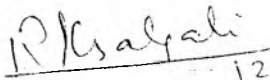
Dated : May 12, 1995   [RAMCHANDRA KRISHNARAO GALGALI]

BIO-DATA

The author was born in April 1948 at Bijapur, Karnatak. He completed graduation in Metallurgical Engineering from Visweswaryya Regional College of Engineering, Nagpur and then obtained post graduate degree in Metallurgical Engineering from the Indian Institute of Science, Bangalore. In between he worked as a temporary lecturer for a year and half at REC Warangal. He first joined the Central Electro Chemical Research Institute, Karaikudi in 1975 as Scientist. Since 1979 he has been with the Regional Research Laboratory, Bhubaneswar. Presently he holds the post of Scientist EII.

His research and developmental interests have been in the area of Ferrous Metallurgy, Plasma Technology as well as Special Materials. He has published over 35 papers in national and international journals and has seven patents to his credit.

Dated   May 1995

[RAMCHANDRA KRISHNARAO GALGALI]

iii

ABSTRACT

The present investigation is aimed at preparation of TiC reinforced ferrous composites by smelting of ilmenite ore in a plasma reactor and at characterising the products. The main objectives of the investigation were as follows.

a)   Design and fabrication of a 35 kW dc extended transferred arc plasma reactor for composite preparation.

b   Preparation of TiC rich Fe-TiC master alloys and TiC reinforced cast iron composites by carbothermic reduction of ilmenite in a bed of steel scrap using a plasma reactor.

c)   Preparation of TiC reinforced steel composites through incorporation of TiC rich Fe-TiC master alloy in a liquid steel.

d)   Study of the metallurgical characteristics of TiC rich Fe-TiC master alloys and TiC reinforced cast iron as well as steel composites.

e)   Evaluation of the wear characteristics of TiC reinforced cast iron and steel composites.

The master alloys and cast iron composites were prepared by carbothermic reduction of ilmenite ore in a graphite crucible. Steel composites were prepared by dissolving TiC rich Fe-TiC master alloy in plain carbon or alloy steel melts in an induction furnace. While Fe-TiC master alloys were obtained as semifused masses, TiC reinforced cast iron and steel composites were fluid and could be cast in metal or sand moulds. The effect of slag basicity, percent excess of reductant, gas composition, crucible material etc., on recovery, carbon pick up etc., has been studied.

The master alloys and composites were characterised by various standard techniques. The mechanical and wear properties of the products were also determined.

It has been shown that TiC rich Fe-TiC master alloy and TiC reinforced cast iron composites can be produced by carbothermic reduction of ilmenite ore. Composites containing 8-10 wt pct Ti and 3-4 wt pct carbon can be readily cast. TiC reinforced cast iron composites possess attractive wear resistance properties. TiC reinforced steel composites also possess attractive wear resistance and mechanical properties.

---

iv

CONTENTS

LIST OF TABLE TITLES

LIST OF FIGURE CAPTIONS

CHAPTER - ONE

INTRODUCTION

1.0 GENERAL

In recent years, research on composite materials has gained considerable momentum and cast aluminium metal matrix composites have already been commercialised [1]. The literature on TiC reinforced ferrous composites [2-5] indicate that generally TiC is introduced in ferrous matrix either through powder metallurgy route or through direct precipitation from the melt of the appropriate alloy [2,6,7]. One research group, however, has tried direct carbothermic reduction of ilmenite in a levitation melting furnace to produce small quantities of composite [8]. The liquid base route for producing composites provides an opportunity for casting the components into different shapes and, therefore, offers advantages over the powder metallurgy route. In the present investigation an attempt has been made to produce TiC reinforced composites by carbothermic reduction of ilmenite ore in a plasma furnace. A 35 kW dc transferred arc plasma reactor was specially designed and fabricated for this purpose.

The feasibility of various reactions and temperatures required for smelting of ilmenite by carbon can be readily ascertained by the knowledge of thermodynamics. Some of the important reactions considered are as follows.
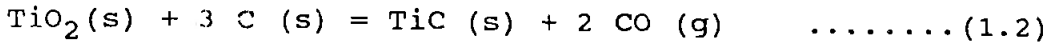
TiO_2 (s) + 2 C (s) = Ti (s) + 2 CO (g) ....(1.1)

ΔG^O_T = 165,058.73 - 83.675 T Cal

Hence, ΔG^O_T = 0 at T = 1973 K

TiO_2 (s) + 3 C (s) = TiC (s) + 2 CO (g) ....(1.2)

ΔG^O_T = 120, 458.3 - 81.515 T Cal

Hence, ΔG^O_T = 0 at T = 1496 K

TiO_2 (s) + 2 TiC (s) = 3 Ti (s) + 2 CO (g) ....(1.3)

ΔG^O_T = 254,258.3 - 89.995 T Cal

Hence, ΔG^O_T = 0 at T = 2825 K

3 TiC(s) + Fe_2O_3(s) = 2 Fe(s) + 3 Ti(s) + 3 CO(g).(1.4)

ΔG^O_T = 234,560 - 125.13 T Cal

Hence, ΔG^O_T = 0 at T = 1874.5 K

2 TiC (s) + Fe_2O_3(s) + C (s) = 2 FeTi (s) + 3 CO (g)

.....(1.5)

ΔG^O_T = 189,960 - 121.96 T Cal

Hence, ΔG^O_T = 0 at T = 1558 K

TiC (s) + Fe_2O_3(s) = 2 Fe (s) + TiO_2(s) + CO (g)..(1.6)
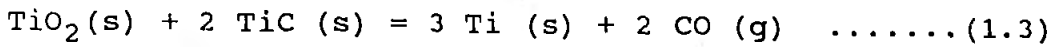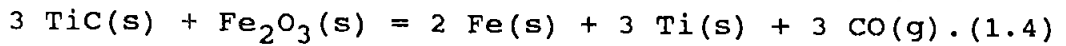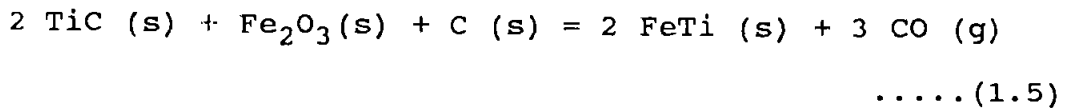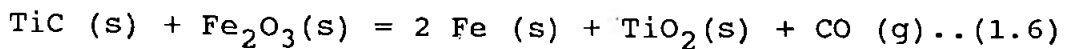
ΔG^O_T = - 19,698.33 - 35.135 T Cal

Hence, ΔG^O_T = 0 at well below room temperature

The thermodynamic data used are from the litera-
ture [Metallurgical Thermochemistry by O. Kubaschewski and
E. LL. Evans, Pergamon press, Oxford, 1965] [9]. The thermo-
dynamic calculations for ilmenite reduction are similar to
those of TiO_2 reduction and are presented in Appendix I.

It may be noted that TiC formation [Eq. 1.2] requires a lower temperature compared to that for the formation of metallic titanium [Eq. 1.1]. Hence, the reaction product of carbothermic reduction of ilmenite would contain TiC. To prepare a composite by direct smelting of ilmenite, it becomes essential to control the carbon content of the reaction product. One of the options available is to carry out carbide – oxide reaction [Eq. 1.3] which requires a temperature in excess of 2825 K. The other possibility is to oxidise away the carbon from the reaction product of Eq. 1.2 by iron ore. These reactions [Eq. 1.4 and Eq. 1.5] appear to be feasible at temperatures above 1875 and 1558 K, respectively. However, another reaction possible, which would convert TiC back to TiO_2 during TiC – iron ore reaction [Eq. 1.6]. This reaction is thermodynamically feasible well below the room temperature. Therefore, the method of controlling carbon by reacting TiC with iron ore would result in loss of titanium. Another option available is to prepare composites by carrying out smelting of ilmenite in a bed of steel scrap or reduce ilmenite along with iron ore. To carry out this reaction one can use either a resistance heated electrical furnace or an arc furnace or a plasma reactor. A resistance heated furnace does not allow quick response to heating of charge. Hence, it was decided to use either an arc furnace or a plasma reactor. A plasma reactor offers several advantages for the preparation of such composites. The plasma arc covers almost the entire surface of the bath in the crucible furnace and as a result the bath can be easily superheated.

This is a positive advantage because TiC particles remaining suspended in molten iron reduce its fluidity. This problem can be eliminated to some extent by raising the melt temperature. The carbothermic reduction of ilmenite to TiC is also likely to proceed easily within the arc crater. Moreover a transferred arc plasma reactor can be conveniently designed and fabricated utilising the principle of gas injection through an axial hole of an electrode. An ordinary welding transformer can be used as a power source. Hence, it was decided to design and develop indigenously an extended transferred arc plasma reactor for smelting of ilmenite.

Amongst all the thermodynamically feasible routes, there are several options regarding preparation of Fe-TiC composites. The objectives of the present investigation were defined after a careful consideration of all the available options.

OBJECTIVES

The specific objectives of the present investigation were as follows:

i) To design and fabricate a 35 kW dc transferred arc plasma reactor for composite preparation.

ii) To prepare TiC rich Fe-TiC master alloys as well as TiC reinforced cast iron composites by carbothermic reduction of ilmenite in a bed of steel scrap contained in a plasma reactor.

iii) To prepare TiC reinforced steel composites by incorporation of TiC rich Fe-TiC master alloy in liquid steel.

iv) To study the metallurgical characteristics of TiC rich Fe-TiC master alloys and TiC reinforced cast iron as well as steel composites.

v) To evaluate the wear characteristics of TiC reinforced cast iron and steel composites.

The thesis consists of five Chapters. The first Chapter introduces the subject and defines the problem. Literature review is presented in Chapter II. Design of the extended transferred arc plasma reactor and experimental aspects for preparation and characterisation of composites are described in Chapter III. The results, discussions and conclusions of various investigations are presented section wise in the next Chapter while a general discussion and major conclusions are summarised in Chapter V. List of references, figure captions, Table titles, biodata of the author etc., are included in appropriate places.

CHAPTER - TWO

LITERATURE REVIEW

2.0 INTRODUCTION

The present investigation envisages preparation of TiC reinforced ferrous composites by smelting of ilmenite ore in a plasma reactor. A brief review is presented here first on the application of thermal plasma technology in metallurgy. Some data pertaining to thermodynamics and phase equilibria of iron-titanium-carbon system are presented next in different sections. A detailed literature review on preparation and characterisation of Fe-TiC composites is then presented followed by a brief summary of the literature review.

2.1 METALLURGICAL APPLICATIONS OF THERMAL PLASMA

The present day thermal plasma arc systems have evolved over the past two to three decades as a modern processing technology. The arc heaters were developed at power levels of 500 kW to 35 MW during 1960s [10] for aerospace testing of materials in USA. These systems were developed for generating extremely high temperatures to simulate the conditions for reentry of space vehicles into earth's atmosphere. Reentry requires only a few minutes of testing time. Thus, the design criteria for thermal arc systems require high enthalpy content of gas at high temperatures instead of long service life of the torches at a given power level. With the evolution of plasma technology over the years,

various industrial applications were envisaged which led to the development of reliable, high powered thermal arc plasma systems.

In metallurgical applications of thermal plasma arc technology for a specific process development several unique advantages can be considered. Some of them are as follows [11-13]:

a) Gas environment control : Energy can be provided to a system with any desired oxygen potential (ie., oxidising, reducing or inert gas conditions) independent of the temperature.

b) Fine particle feed capability : Plasma arc reactors can operate with a wide range of gas flow rates. Hence pneumatic transport can be used to introduce fine particles into the plasma flowing stream. Thus, the process of agglomeration of the fine particle feed can be avoided.

c) High temperature : The average gas temperature in a plasma reactor can range from 3000 to $6000^{\circ}C$, which is far above that attainable in conventional reactors.

d) High energy fluxes : A maximum heat flux attainable in an argon plasma jet is 4.5 kW/cm^2 as against 0.3 kW/cm^2 for oxygen-fuel flame. The energy flux for a dc transferred arc, around 16 kW/cm^2, and is due to

additional heat flux coming from electron transfer in the area of anode arc root attachment.

e) High throughput : There is considerable scope for achievement of high throughput in open bath processes because of attainment of high reaction rates.

f) Plasma state conditions : Activated species, ions electrons etc., are present in the plasma depending on the degree of ionisation of gases. Conditions exist to exploit the activated species, ions etc., for a possible `Plasma effect' to occur, however, these have not been done commercially as yet.

g) Rapid quenching : High temperature gradients in localised plasma and surrounding gas permit ultra rapid quenching of both gases and particles.

h) Control of refractory consumption : The directionality of plasma jet prevents the flaring of arcs to side walls. Refractory erosion of roof can be controlled by proper control of the charge and slag layer.

i) Rapid response : The reactors can respond to temperature changes within a relatively short time.

j) Low noise level : Acoustical and electrical noise levels are decreased considerably.

Thus, the application of plasma technology to metallurgical systems offer greater degree of freedom as regards charge composition, particle size distribution, operation etc.. Like any other process, plasma processes too suffer from a few limitations and some of them are as follows [14-16]:

a)   Plasma system necessarily requires electrical power as a source of energy.

b)   Input of gas is essential to generate and sustain plasma. The use of gas adds to the cost of production.

c)   The potential advantages namely, the rapid response time and greater flexibility in process control may also prove to be disadvantageous, since operational difficulties can be experienced if appropriate control measures are not available and enforced rapidly. Therefore, for an effective operation of a plasma reactor levels of control required are stricter than that for conventional submerged arc furnaces.

d)   There is high loss of energy via radiation from the exposed surface of the bath and plasma arc column in particular in open bath configuration.

e)   Sensible energy of high temperature off gases is lost if no heat recovery system is envisaged.

f)   There is need for continuous balancing of the feed and

power inputs, particularly in the arc attachment zone, to minimise unwanted side reactions. The unwanted reactions demand additional energy and result in production of undesirable reaction products.

g)   Plasma arc heat does not penetrate deep in a molten metal pool, hence, innovations are required to improve heat transfer in the system.

In spite of the limitations listed above there are overall advantages due to the availability of high temperature with high enthalpy content enhancing the reaction kinetics and improving productivity. Therefore, considerable interest lies in the development of plasma systems suitable for a given process and interfacing it in a reactor to obtain maximum advantages.

2.1.1 Plasma State

A plasma, some times referred to as fourth state of matter, is a gas containing neutral atoms and molecules in their fundamental or excited states, photons, ions and free electrons being on the whole electrically neutral. The term `plasma' was introduced by Langmuir [17] in 1923 while investigating electrical charges. He defined plasma `as a gas composed of equal number of positive ions and electrons'.

Neutral at room temperature, a gas becomes an electrical conductor at sufficiently high temperatures. When a gas is heated, the molecules are dissociated at about 2300 K [18]. At still higher temperatures of about 3300 K, the thermal agitation of atoms causes them to collide, and disintegrate into free electrons and positively charged ions. At sufficiently high density of charges, an ionised gas becomes a plasma. A basic property of plasma is its quasineutrality i.e., the number of negative charges and positive ions per unit volume of plasma are approximately equal. The percentage or degree of ionisation of a plasma, which is a function of its energy content, results from a dynamic equilibrium between the rate of formation of positive ions and free electrons from parent atoms or molecules. This is counterbalanced by a recombination process, where a free electron coming too close to a positive ion is captured and the initial atom or molecule is reconstituted.

Plasma is classified into two types depending on its thermodynamic state [19, 20]. First is the thermal plasma, also referred to as equilibrium, hot or atmospheric plasma, which occurs when heavy particle (ion) temperature (T_h) and electron temperature (T_e) are approximately equal. In this case thermodynamic state of plasma reaches equilibrium. The thermal plasma is generated when the pressure in a reacting system is greater than 10^4 Pa. Such type of plasma

may be produced by high intensity arcs or high power RF
discharges. The other type of plasma, referred to as non-
equilibrium or cold plasma, occurs at pressures less than
10^4 Pa. This type of plasma is identified by low, heavy
particle temperature (T_h) and high electron temperature
(T_e). Glow discharges are the examples of such plasma. The
difference between thermal and nonequilibrium plasma is
shown in Fig. 2.1.

2.1.2 Plasma Devices

The thermal plasma device essentially consists of
electrodes, power supply unit and control input of chosen
gas composition to obtain a stable arc with a provision to
increase voltages to a maximum that can be used. Three basic
type plasma devices [21] are used in various plasma process-
es. These include ac, dc plasma devices and the electrode-
less high frequency induction plasma heating devices. The
ac, dc plasma devices are classified according to the mode
of arc attachment namely, transferred and nontransferred
devices as illustrated in Fig. 2.2.

In a transferred arc system the energy dissipation
is by the gas phase and also by heating of condensed phase
(solid/liquid), while in a non-transferred arc system the
energy dissipation is due to gas phase alone [10]. Hence the
transferred arc device efficiency is greater. These devices
can operate at extremely high currents upto 100,000 amperes
and have low rate of gas flow. The non-transferred arc
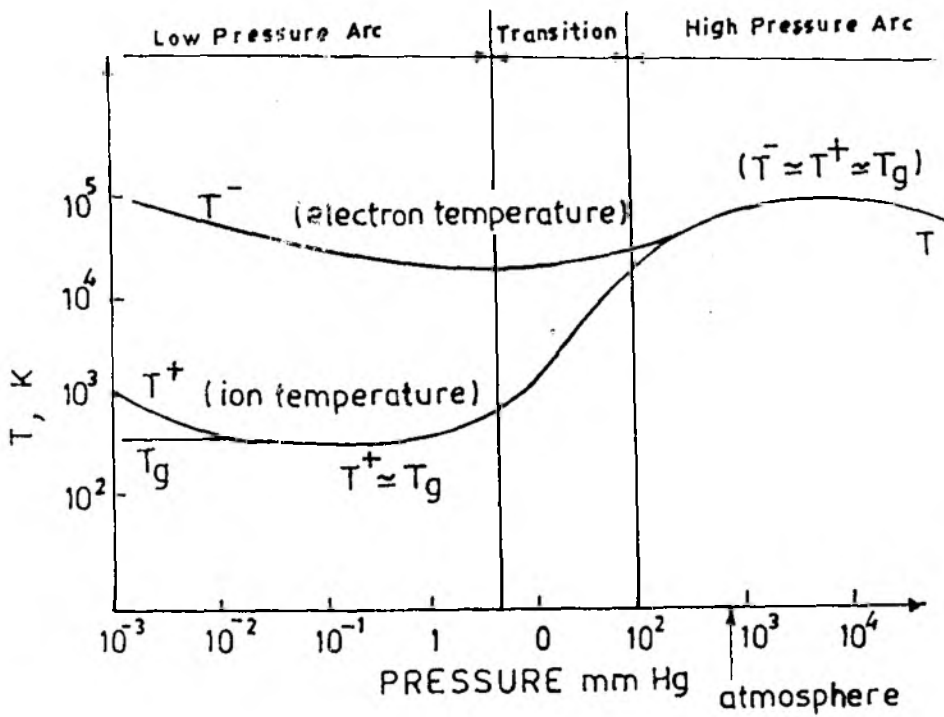
Fig. 2.1 Low-pressure versus high-pressure arc and approximate definition of local thermodynamic equilibrium. (Ref.19)
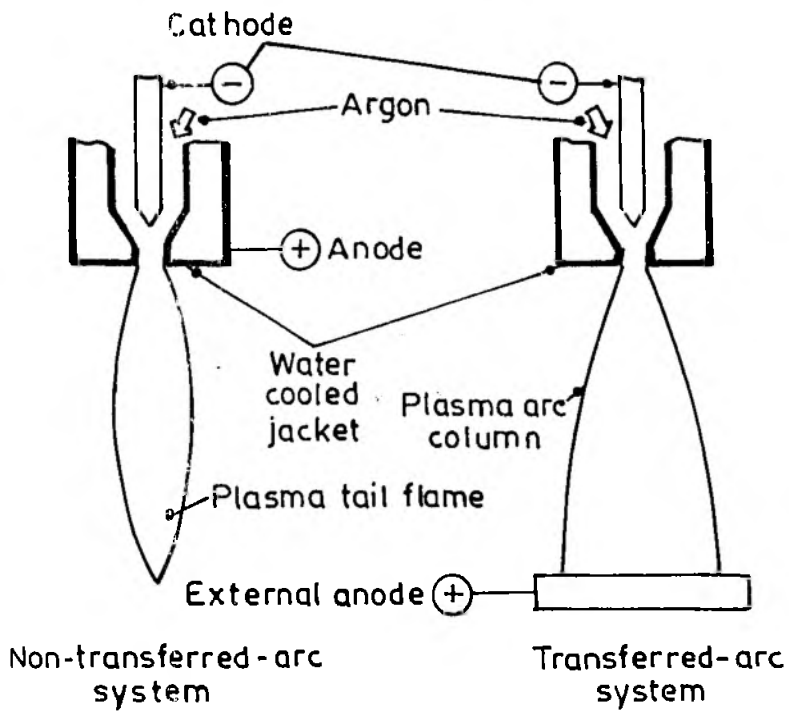
Fig. 2.2 Non-transferred-arc and transferred-arc systems (Ref. 10)

devices operate at high voltages upto 6000 V and require high rates of gas flow. The operating characteristics of the transferred and non-transferred devices are indicated in Table 2.1.

2.1.3 Electrodes

The plasma arc devices of industrial significance operate with currents ranging from 10^2 to 10^5 amperes. A solid electrode requires good electrical conductivity to carry current in this range without prohibitive heat loss and/or erosion rates. The electrodes must not only carry the arc currents, but also be in contact with the arc itself. Most materials are vapours at the temperature needed to get the current density typical of plasma arc torch operation namely, 10^3 to 10^4 A/cm^2. In practice graphite and `doped' tungsten are two materials used for cathode since these two substances can deliver sufficiently high current densities below their sublimation or melting points. Usually tungsten electrodes are water cooled while massive graphite electrodes can be used without water cooling. About 2 wt pct thoria is added to tungsten to reduce the work function from 4.5 to 2.6 eV. A 10 mm diameter water cooled thoriated tungsten can carry a current upto 10 kA. The current density for thermionic emission is about 12 kA/cm^2. The life time of such electrodes is 300 hour.

Graphite electrodes are used in a plasma reactor both for ac and dc operating conditions. The work function

Table 2.1

Operating characteristics of nontransferred and

transferred plasma reactors [10]

	Non transferred	Transferred
Gas flow rate	High	Low
Gas type	Reactive	Inert (reactive)
Torch efficiency	80 pct	High(95 pct)
Power level	<30 MW	<40 MW
Current voltage	<2000 amp <6000 V	<100,000 amp <1000 V
Reactor design	Shaft tube	Crucible bath
Energy recovery	Desirable	Not required

of graphite is 4.6 eV. Typical current carrying capacity of graphite is 20 to 30 A/cm^2 depending on the quality. Fig. 2.3 shows relationship between electrode diameter and the current carrying capacity for two grades of graphite for ac and dc operation [22]. At a current density of 20 A/cm^2, a 435 mm diameter graphite electrode is required to carry 30 kA, but an electrode of the same diameter can carry 50 kA under dc operating conditions. This is because of the absence of skin effect in dc operating conditions. Usually graphite electrodes are not water cooled. The electrodes can be replenished while the reactor is in operation.

The current densities at anode attachment are usually somewhat lower than that at the cathode, the choice of anode material can include a number of metals with fairly good thermal conductivity. Copper is frequently used as anodes in plasma torches.

In plasma torches cathode may have rod, button or tube shape. The rod can have either flat or pointed end. Both anode and cathode are water cooled. The rate of electrode erosion is largely a function of current and hence, lower current rates are used wherever higher voltages are allowed. To minimise the electrode erosion, the arc attachment points are rotated by adopting thermal pinch effect and/or applying magnetic fields whenever torches are designed to operate with moderately high current.
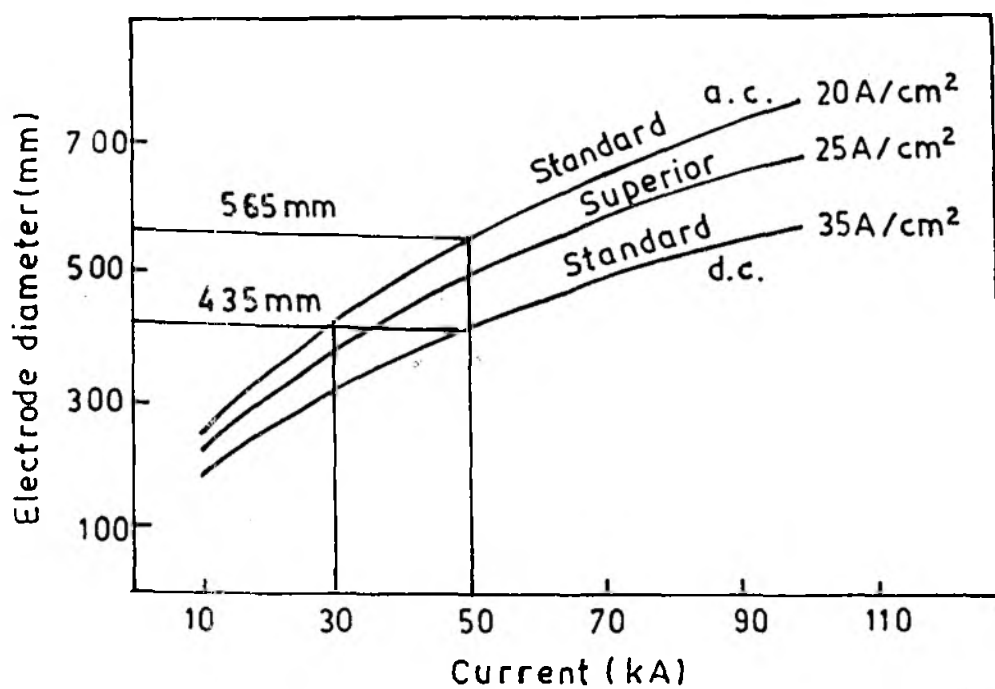
Fig. 2.3 The relationship between electrode diameter and current for graphite electrodes (Ref.22)

2.1.4 Gas Injection Through an Axial Hole of Graphite Electrode

The important development of transferred arc reactors is the use of graphite as electrode and passing plasma forming gas through the axial hole of the electrode. Maddever and Segsworth [23] have studied the influence of gas injection on arc stabilisation and electrode consumption in electric arc furnaces while investigating some of the problems inherent in electric arc steel making. These are the instability of arc during meltdown period resulting in extinguishing and reigniting of arc many times. This causes disturbance in arc voltage, arc current and power levels and produce high level of acoustical noise. The transformers are subjected to greater stresses. Another problem inherent in electric arc melting is the amount and rate at which energy is supplied by the arc. A short arc having low resistivity supplies less heat than a long arc. However, long arc is inefficient as its radiation accelerates refractory wear.

Injecting a gas through an axial hole of an electrode drastically improves the arc stability, reduces acoustical noise, smoothen the oscillograms of voltage curve which is otherwise a square wave form indicating higher noise level. With the injection of a gas it is possible to increase the arc length considerably eg., from say 3/4 inch to at least 3 to 4 inches at a given power level [24]. Ex-

tended arc is less prone to extinguishing and arc is softer and more diffuse.

The Metallurgy and Materials Science Department of the University of Toronto has developed extended arc flash reactor [25-27] in both transfer and nontransfer mode using the principle of gas injection through an axial hole of electrode. A major breakthrough in the use of transferred arc heaters for processing of solid fine particulate was the development of hollow graphite electrodes by Mintek/ASEA [28]. This development eventually resulted in the 30 MW ferro-chromium plant installation at Middleburg Steel and Alloy (MS&A) in Krugersdrop, South Africa. The relative advantages of use of graphite as an electrode in a transferred arc plasma reactor are as follows [29]:

a) lower consumption of gas

b) absence of source of water in the furnace reactor

c) variability of the current carrying capability

d) possible use of nitrogen to replace argon

e) capital savings on deionised water circuit and on instrumentation

f) tolerance of foaming slags during operation

g) little energy loss through cooling of electrodes

h) little need of skilled repair

The stated disadvantage is consumption of graphite electrode. Insulation of graphite electrode and roof seal is critical.

2.1.5 Trends in Design of Plasma Reactors

Plasma reactor systems are built around the plasma arc device which may be referred to as a heater, torch, generator or gun. The reactor may be a simple melter or complex smelter. It includes a reactor chamber such as a crucible or hearth or may be a space such as the reaction zone cavity formed in front of plasma tuyers in a shaft furnace. The mode of arc attachment as transferred or non-transferred is only the first of several design options for plasma device or heater. In addition to mode of arc attachment other design options include the following [28]:

a) The electrode material ; eg. copper, tungsten, graphite

b) Water cooled and non water cooled cathodes

c) Ac or dc operations

d) Electrode polarity for dc arc

e) Single or multiphase ac arcs

f) Composition and feed rate of plasmagen gas

g) Powder feeding up stream, within or down stream of the fully developed arc and/or through the electrode body, and

h) Arc stabilisation by magnetic, mechanical and/or aero-dynamic means.

A variety of plasma devices have been designed based on various array of options and have been patented and promoted for high temperature processing applications. Thus

it is important to note that the selection of plasma device strongly determines the reactor configuration and design of plasma process systems.

A major feature that distinguishes a plasma arc reactor from the conventional electric arc furnace is the influence of gas phase on the reactor design. The following factors are considered as more relevant:—

a)   Type of gas; inert or reactive

b)   The flow rate of gas; high or low

c)   The interaction of gas with reactants; chemical or physical

d)   The importance of gas as a heat transfer medium, and

e)   The effect of gas on the arc stability

Initially plasma reactors were designed with the concept of "Plasma enhanced reactions" i.e by excited gas species and emphasis was laid on direct contact of particles passing through the plasma. Non-transferred gas heaters are used for bulk processing of materials while transferred arc system would have low gas flow rate as a distinct advantage. Thus, subsequent developments concentrated on use of transferred arc attachment mode to augment various advantages built in the reactor system. The major breakthrough was the development of transferred arc process for processing solid fine particles through hollow graphite electrode, a Mintek development.

Thus, recent developments in plasma reactors have been towards simplicity.

2.1.6 Development of 35 kW DC Extended Arc Plasma Reactor

A 35 kW d.c extended arc plasma reactor has been designed and developed indigenously at Regional Research Laboratory, Bhubaneswar [30] following the principle of gas injection through an axial hole of a graphite electrode. It is a pot type reactor, with two graphite electrodes arranged in vertical configuration in the reactor. The top electrode (cathode) is having an axial hole to pass plasmagen gas. The bottom electrode (anode) is connected to crucible hearth. The top electrode has a provision to move up and down for stabilisation of arc. The reactor has a facility to tap both metal and slag. A 35 kW DC arc welding power source has been connected for supplying power to the reactor. The detailed design parameters and operation of the reactor are explained subsequently in the Experimental Chapter.

2.2 THERMODYNAMICS AND PHASE EQUILIBRIA OF IRON - TITANIUM - CARBON SYSTEM

The iron-titanium carbide composite under investigation is a three component system consisting of iron, titanium and carbon. An understanding of Fe-Ti, Fe-C and Ti-C binary phase diagrams and Fe-Ti-C ternary phase diagram is essential to develop Fe-Ti-C composites. A literature review

on the phase equilibria and transformations in the Fe-Ti-C system is presented below.

2.2.1 Iron - Titanium Phase Diagram

Iron-titanium phase diagram [31] is shown in Fig. 2.4 it may be seen from the diagram that there is a τ iron loop with its vertex located at 0.6 wt pct (0.7 at pct) Ti. The solubility of Ti in α iron decreases from 6.3 wt pct (7.2 at pct) Ti at 1350° C to about 2.5 wt pct (2.9 at pct) Ti at 600° C. An eutectic reaction occurs at 14 wt pct (16 at pct) Ti resulting in primary solid solution of iron (about 6 wt pct (6.9 at pct) Ti) and $TiFe_2$ phases. The eutectic temperature is located at 1340°C. The $TiFe_2$ phase contains 30.0 wt pct Ti and has a maximum melting point of 1530° C. $TiFe_2$ is isotypic with $MgZn_2$ (C14 type) crystal structure and has the following lattice parameters:
a = 4.64°A, C = 7.80°A and c/a = 1.633.

FeTi phase has been identified by X-ray analysis of alloys containing 46-75 wt pct (49.8 to 77.8 at pct) Ti after prolonged annealing between 560 to 650° C. The phase is reported to be b.c.c. with a lattice constant of 2.975°A. There is a peritectoid reaction in titanium rich side i.e., at 85 wt pct (87 at pct) Ti, 590° C, where ß-Ti transforms to α-Ti and FeTi phases. The solubility of iron in α-Ti is less than 0.2 at. pct. There is an eutectic reaction at 68 wt pct (71 at pct) Ti and 1085°C where liquid Fe-Ti alloy solidifies into ß-Ti and FeTi phases. There has
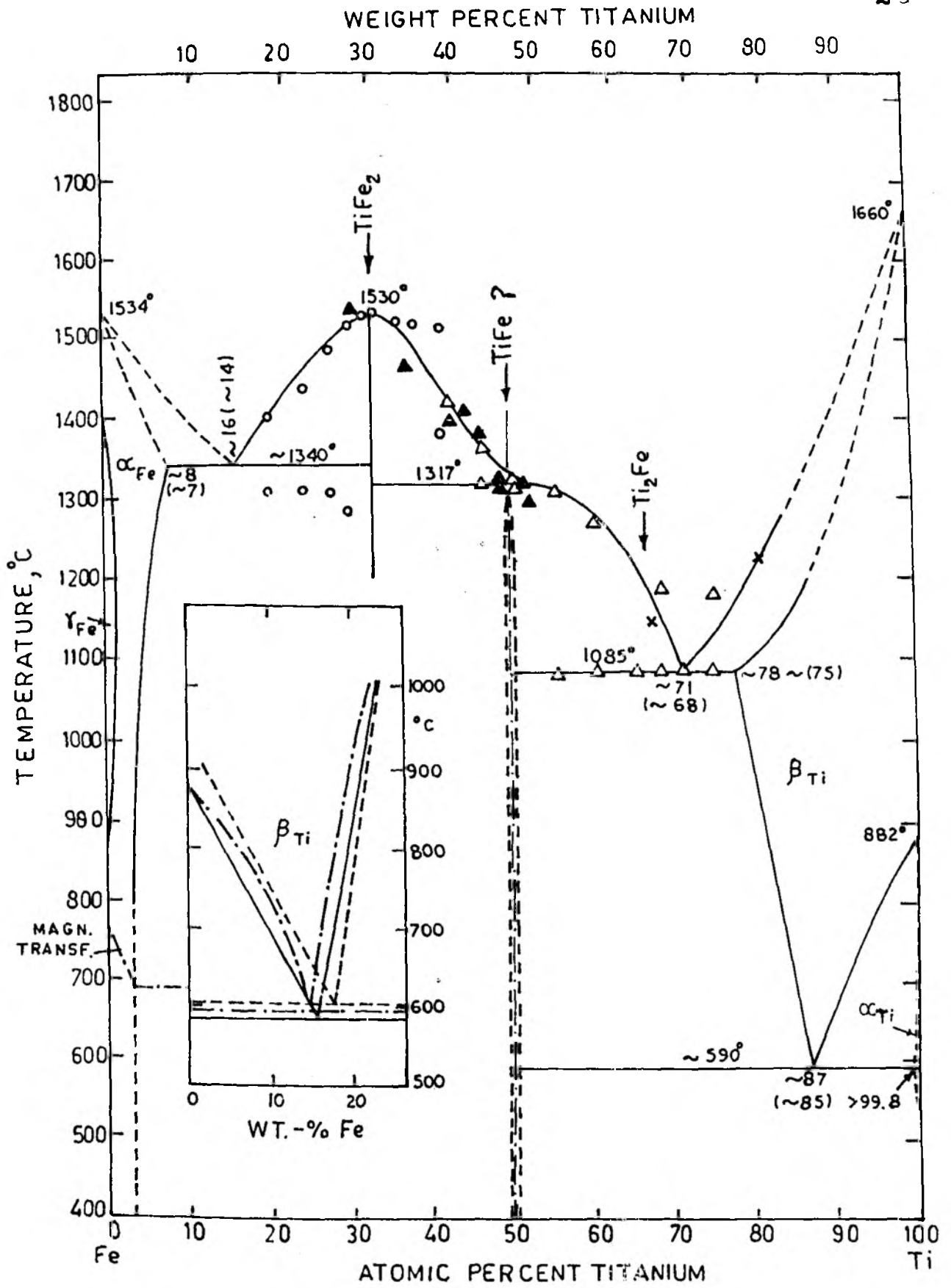
Fig. 2.4 Fe-Ti phase diagram. (Ref.31)

been many conflicting reports about the presence of Ti_2Fe phase [32-35].

2.2.2 Iron - Carbon Phase Diagram

Iron-carbon phase diagram [31] is shown in Fig. 2.5. The phase diagram is well known. Therefore, it is not being discussed here.

2.2.3 Titanium - Carbon Phase Diagram

Figure 2.6 shows titanium-carbon phase diagram [36]. Ti-C system has been worked out upto 70 at pct C. In addition to ß-Ti (bcc) and α-Ti(cph) solid solutions, there is an equilibrium carbide phase TiC with 32 to 48.8 at pct C. It may be noted from the phase diagram that there is yet another carbide phase, Ti_2C, in which vacancies are ordered in the carbon sublattice. Ti_2C carbide phase which contains 33.3 at pct carbon, is the product of congruent reaction of TiC at 1900°C. The phase diagram shows the following two eutectic reactions:-

L = ß-Ti + Ti_2C ; at 1.8 at pct C at 1648 ± 5°C .... (2.1)

L = TiC + C ; at 63 at pct C at 2776 ± 6°C ....(2.2)
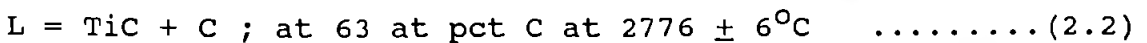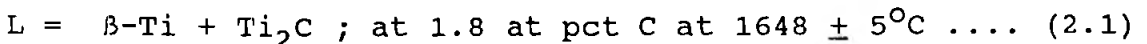
There is a peritectoid reaction written as follows:-

ß-Ti + TiC = α-Ti ; at 0.6 at pct C at 920°C ...(2.3)
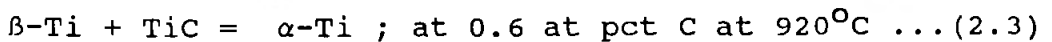
TiC containing 44 at pct C is formed by the following congruent reaction.

L = TiC ; at 44 at pct C at 3067 ± 15°C ....(2.4)
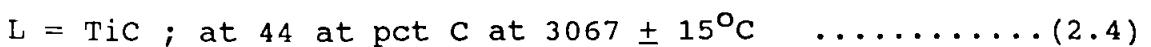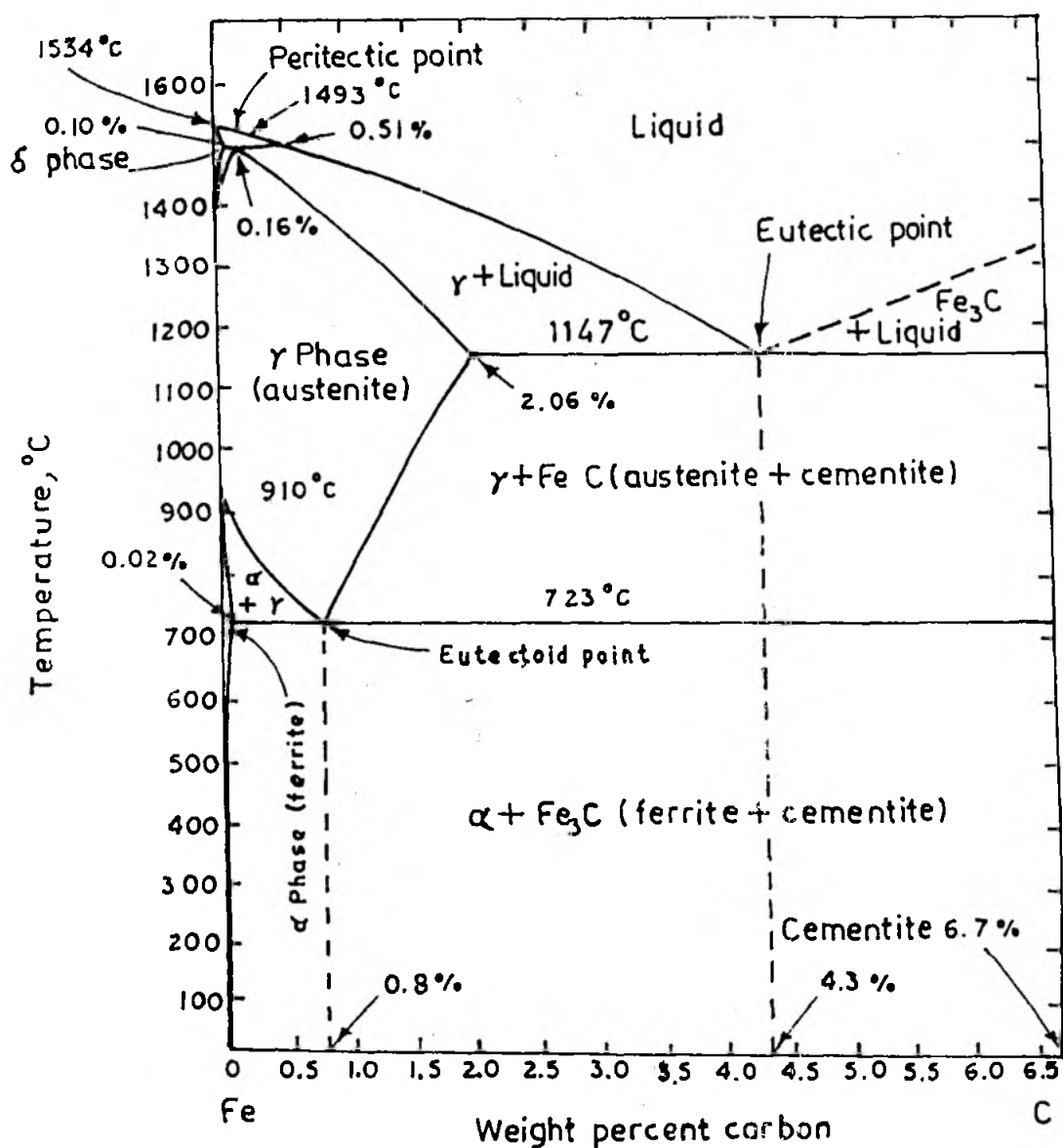
Fig. 2.5 The metastable system Fe-Fe$_3$C. (Ref. 31)
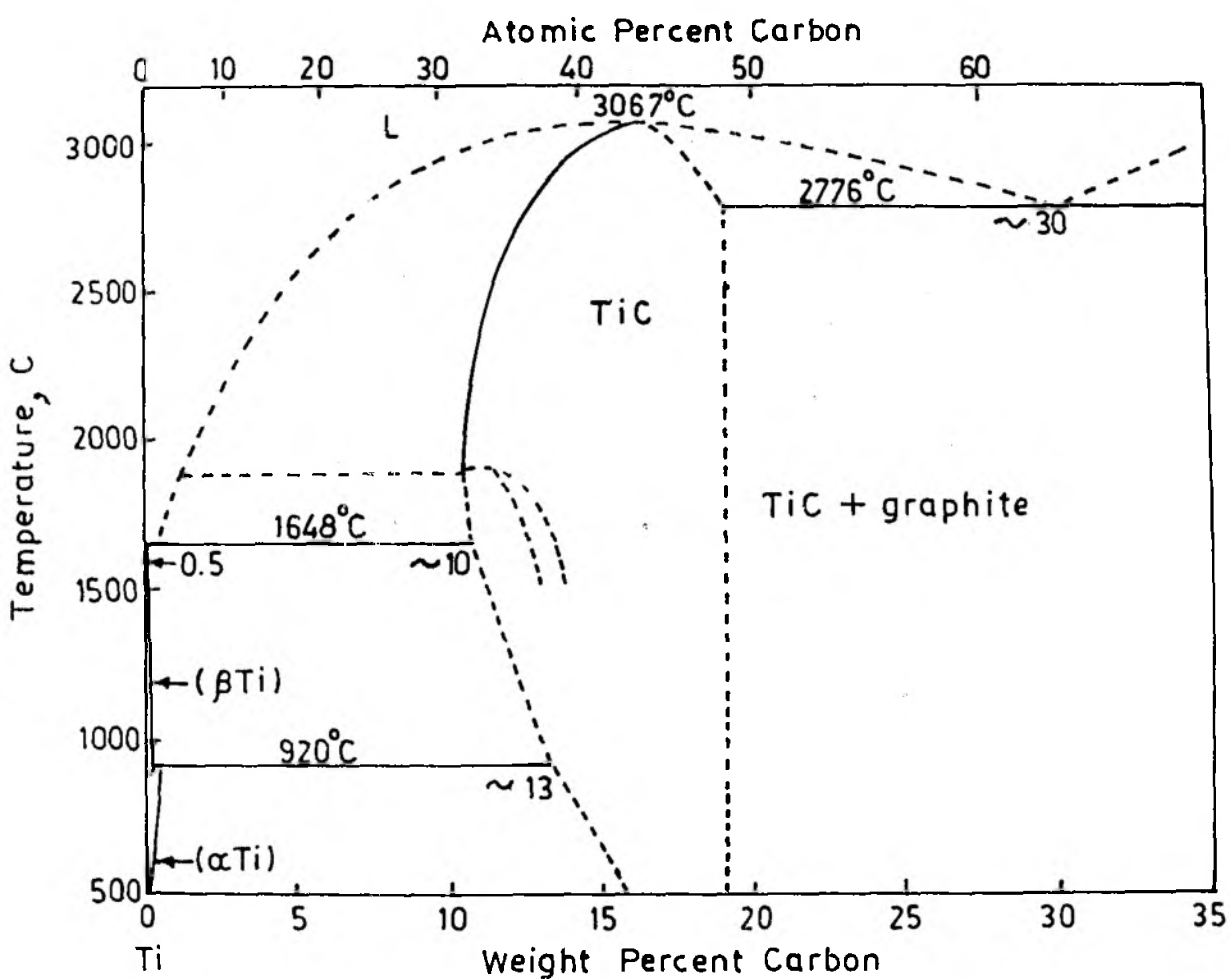
Fig. 2.6 Ti - C Phase diagram (Ref. 36)

The various stable phases present in Ti-C system are shown in the phase diagram.

2.2.4 Iron - Titanium - Carbon Phase Diagram

Iron rich corner of Fe-Ti-C [3, 37] phase diagram with basal projects of liquid surfaces is shown in Fig. 2.7. The phase diagram shows the boundaries where $TiFe_2$, TiC, α-Ti, τ-Fe, Fe_3C and graphite phases exist.

Amongst various phases present in Fe-Ti-C system, TiC phase is of greater interest because of its refractory properties. The following section presents thermodynamic properties of TiC, its solubility in τ-iron and its properties.

2.2.5 Thermodynamic Properties of TiC

The heat of formation of TiC has been measured by various researchers [38-40] and Humphrey's corrected value [41] of -184.51 ± 1.63 kJ mol^{-1} is taken as a standard. The standard entropy of formation i.e., S^o_{298} of TiC is reported to be [42] 24.23 ± 0.2 J mol^{-1} K^{-1}. The free energy of formation of TiC from α-Ti, β-Ti and Ti (liquid) have been derived by various investigators and the following values have been taken as standards [41, 43, 44].

Ti (α) + C(s) = TiC (s) .... (2.5)
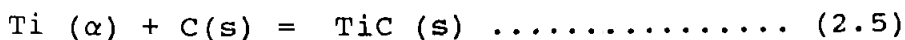
$G^o(\pm 12,600) = -183,050 + 10.08$ T Jmol^{-1}K^{-1} (298 - 1150 K)

Ti (β) + C(s) = TiC (s) .... (2.6)
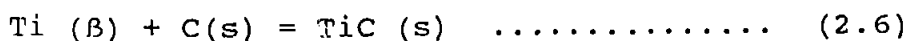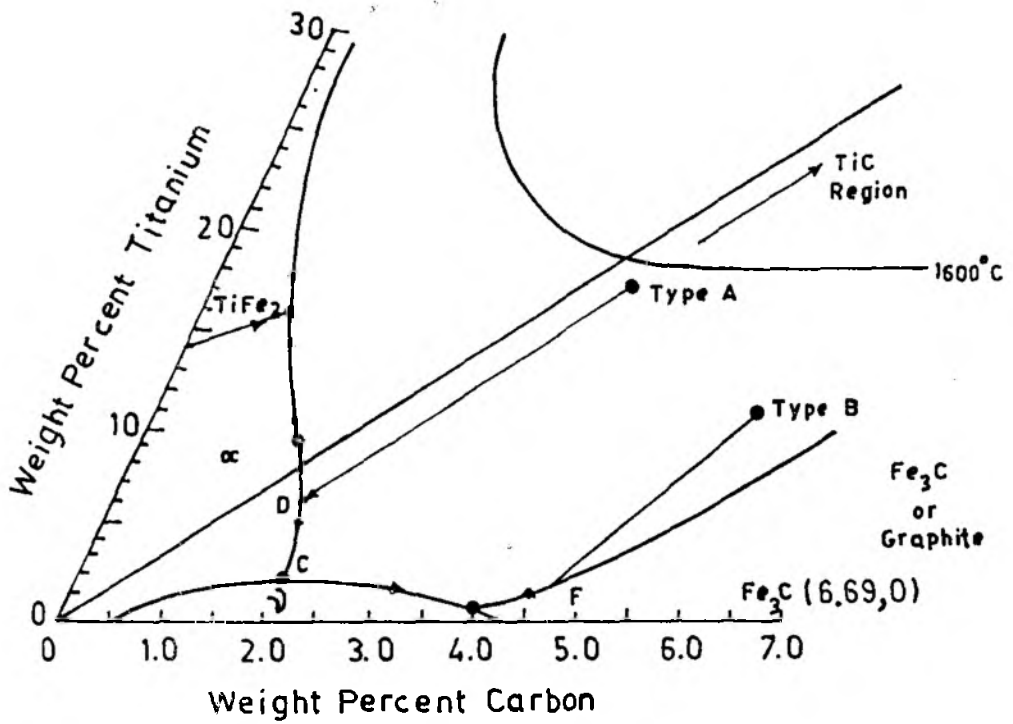
Fig.2.7   Iron-rich corner of the Fe-Ti-C phase diagram showing the basal projection of liquidus surface. (Ref.3)

$$G^O(\pm 12,600) = -186,606 + 13.22 \; T \; Jmol^{-1}K^{-1} \; (1150 - 2000 \; K)$$

and

$$Ti(liquid) + C(s) = TiC \; (s) \; \ldots\ldots\ldots\ldots \; (2.7)$$
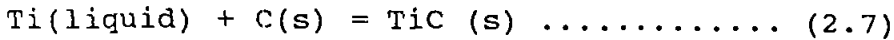
$$G^O_T(\pm \; 8,400) = -590,211.8 + 146.4 \; T \; Jmol^{-1}K^{-1} \; (2383-2593 \; K)$$

2.2.6 Role of Titanium in Microalloyed Steels

Titanium can behave as both a precipitation strengthener and a grain refiner depending on its concentration in the steel [45, 46]. Precipitation strengthening increases with decreasing particle size and increasing volume fraction. Titanium carbide begins to exert a strengthening effect over 0.05 wt pct Ti in a steel. Addition of titanium in the range of 0.01 to 0.02 wt pct retards austenite grain growth and improve toughness. Irvine et al., [47] have studied the effect of titanium addition (upto 0.3 wt pct) on grain refining and precipitation strengthening in steels. There is no increase in strength properties with increasing titanium content above 0.03 wt pct in 0.5 and 1.0 wt pct Mn steels. The average grain size decreases as the titanium content in the steel is increased. Addition of higher amounts of Ti to steel seems to oppose the beneficial effect of grain refinement by precipitation of TiC and depletion of Ti in solution. El-Fawakhry et al., [48] have shown that as quenched hardness of V- and Ti-microalloyed steels depend solely on carbon content. Tempering of quenched microalloyed steels produces secondary hardening at 550-600°C (1 hour). Titanium microalloyed steels have shown higher overaging

resistance compared to vanadium microalloyed steels. El-Fawakhry et al., [49] have also observed coarse titanium nitride particles (> 5 μm) together with carbosulphide particles in Ti microalloyed steels. Mekkawy et al., [50] have studied the effect of rolling schedule on mechanical properties of V and Ti microalloyed steels. Increase in finish rolling reduction is effective in producing fine grains in microalloyed steels. However, there was a decrease in precipitation strengthening effect. Robertson [51] has studied the temper resistance of pressure hull steels microalloyed with Nb, V and Ti. Most of the Ti added to the steel precipitated as TiN cuboids at high temperatures and acted as nuclei centres for precipitation of Nb(C, N).

From the preceding discussion it may be deduced that titanium added to microalloyed steels acts as a precipitation hardener and grain refiner. The effect varies depending on titanium content and carbon content in the steel and to bring about precipitation hardening it is essential to bring titanium in solution. Presence of nitrogen in steel leads to TiN formation whereas presence of non metallic inclusions like sulphides brings down the dissolution of titanium in steel. The particle size and volume fraction of titanium carbide play very important role in improving strength properties and influencing the grain size.

2.2.7 Solubility of TiC in Austenite

Improvements in properties of steel are achieved by addition of various alloying elements. Factors that control the properties of a steel include grain size, solid solution hardening, dispersion hardening by carbides and nitrides and the amount of pearlite in the microstructure. For example, addition of niobium results in grain refining because of the formation of carbide particles and these particles may also produce dispersion strenthening. These effects are influenced by controlling the heating cycle to bring an alloying element in solution, while the cooling cycle controls the precipitation. Therefore, it is important to study the solubility relationships of elements in steel.

Irvine et al., [52] have studied the solubility of titanium in a silicon killed steel containing 0.1 wt pct C, 1 wt pct Mn and 0.007 wt pct N. The titanium content was varied from 0.058 to 0.35 wt pct. The chemical analysis technique was used to evaluate the solubility product relationship. The results indicate that the solubility of TiC is described by the following equation:

$$\text{Log } [Ti] [C] = \frac{-7000}{T} + 2.75 \quad \ldots\ldots\ldots\ldots \quad (2.8)$$

Their study on the effect of austenitising temperature and cooling rate on tensile properties and grain size of 0.105 wt pct Ti steel with 0.1 wt pct C did not show any significant variation in properties. This indicates that there

is little solubility of TiC in austenite and, hence, little precipitation. However, the study on a steel with 0.375 wt pct Ti plus 0.15 wt pct C, 1.5 wt pct Mn, 0.35 wt pct S and 0.0055 wt pct N steel showed that it was possible to improve the strength properties through austenitising at 1250°C followed by air cooling. The electron micrograph of this steel showed precipitation of TiC particles indicating that the alloy with Ti and C contents nearer to the stoichiometric Ti : C ratio has greater solubility.

Balasubramanian et al., [53] have carried out experimental investigations on thermodynamics of Fe-Ti-C austenite and solubility of TiC. They have derived thermodynamic relationships for alloys containing higher amount of carbon taking into account the solute interaction parameter. The solubility of carbides at high carbon levels is expressed by the following equation.

$$Log[(wt \ pct \ Ti)(wt \ pct \ C)] = -\frac{9070}{T} + 4.10 + [\frac{1205}{T} + 0.24] \ wt \ pct \ C \ ...(2.9)$$

This equation has been experimentally verified in steels containing carbon upto 1.903 wt pct and titanium upto 0.95 wt pct. A linear relationship has been obtained for the plot of solubility product of TiC vs carbon content. As the carbon content in steel increases the solubility product increases. Further, as the temperature of austenitising

increases the solubility product increases for a given carbon content in the alloy.

2.2.8 Properties of TiC

The elements of group IV and V transition metals namely Zr, Ti, Hf, V, Ta and Nb form refractory carbides. These carbides exist over a wide range of composition [54, 55] without a change in crystal structure [56]. The carbon to metal ratio may change from 0.5 to 0.97. These compounds are isomorphic and crystallise in NaCl structure. They all share properties of exceptional hardness, high melting point, low thermal conductivity and semimetallic electrical conductivity. The physical properties of TiC [57] are given in Table 2.2.

TiC crystals become sufficiently soft for plastic deformation at temperatures above 800°C in uniaxial compression [58]. The slip systems for this is {111}, <110> [59]. The hardness drops by two orders of magnitude from room temperature following an exponential temperature dependence.

It may be noted that TiC is a refractory carbide. The high temperature softening properties of TiC brings in a serious limitation on application of TiC as a structural material. Boron doping of TiC significantly changes the hardness properties.

Table 2.2

Physical properties of TiC [57]

Structure type	B1
Lattice parameter	4.330 A
Melting point	3250°C
Density g/cc	4.95
Electrical conductivity (ohm-cm)	60-250
Thermal conductivity Cal sec. cm^{2}c^O/cm	0.041
Young's modulus (Units 10^6 psi)	60.0
Co-eff. linear thermal expansion (Units 10^{-6} / ^{O}C)	5.5
Poisson's ratio	0.20
Hardness kg/mm^2	3200
Modulus of rupture (Units 10^3 psi)	124
Surface energy, erg/cm^2	1200

2.3 PRODUCTION AND CHARACTERISATION OF Fe-TiC COMPOSITES

In recent years considerable attention has been paid to the development of metal matrix composites which offer significant improvements in structural efficiency, reliability and mechanical performance over monolithic alloys [60]. Composites based on lighter structural metals like aluminium, titanium and magnesium are being developed world wide to improve strength and wear resistance [61]. The development of iron based metal matrix composites is aimed at improving wear resistance, and/or cutting performance with sufficient toughness while reducing the cost of production over existing materials eg., Co-WC cemented carbide. One such composites developed is iron - titanium - carbide composite.

Iron based TiC metal matrix composites are produced commercially by the powder metallurgy route and are sold under various trade names like Ferro-TiC, TiC alloy and Ferro titanate [4, 5, 62]. In recent years, investigations have been carried out to produce these composites by following routes:

a)   In situ production of Fe-TiC composites by reactions in liquid iron alloys

b)   Carbothermic reduction of ilmenite and rutile

c)   Dispersion of TiC in liquid iron alloys

Various aspects of these processes have been discussed in detail later in this Chapter. A brief review on the principles of preparing cast metal matrix composites is presented at first.

2.3.1 Principles of Preparation of Cast Metal Matrix Composites

The development of aluminium graphite cast composites by injecting nickel coated graphite particles with argon gas into a molten bath of aluminium marked the beginning of cast metal matrix particulate composites [63]. In 1968, Ray [64] developed cast aluminium-alumina composites by incorporating alumina particles by stirring the molten alloy with an impeller as the particles were added and thus, the process of stir-casting emerged. Today, a number of processes have been developed and commercialised. A recent review on 'Synthesis of cast metal matrix particulate composites' by Ray [1] has discussed comprehensively various techniques developed for preparation of cast composites and Fig. 2.8 shows different cast routes for synthesis of such composites. Table 2.3 shows a list of cast metal matrix composites developed over the last three decades [65]. Excepting the XD process, where dispersoids are produced by a chemical reaction in situ in an alloy matrix, other processes involve introduction of dispersoid phase externally.
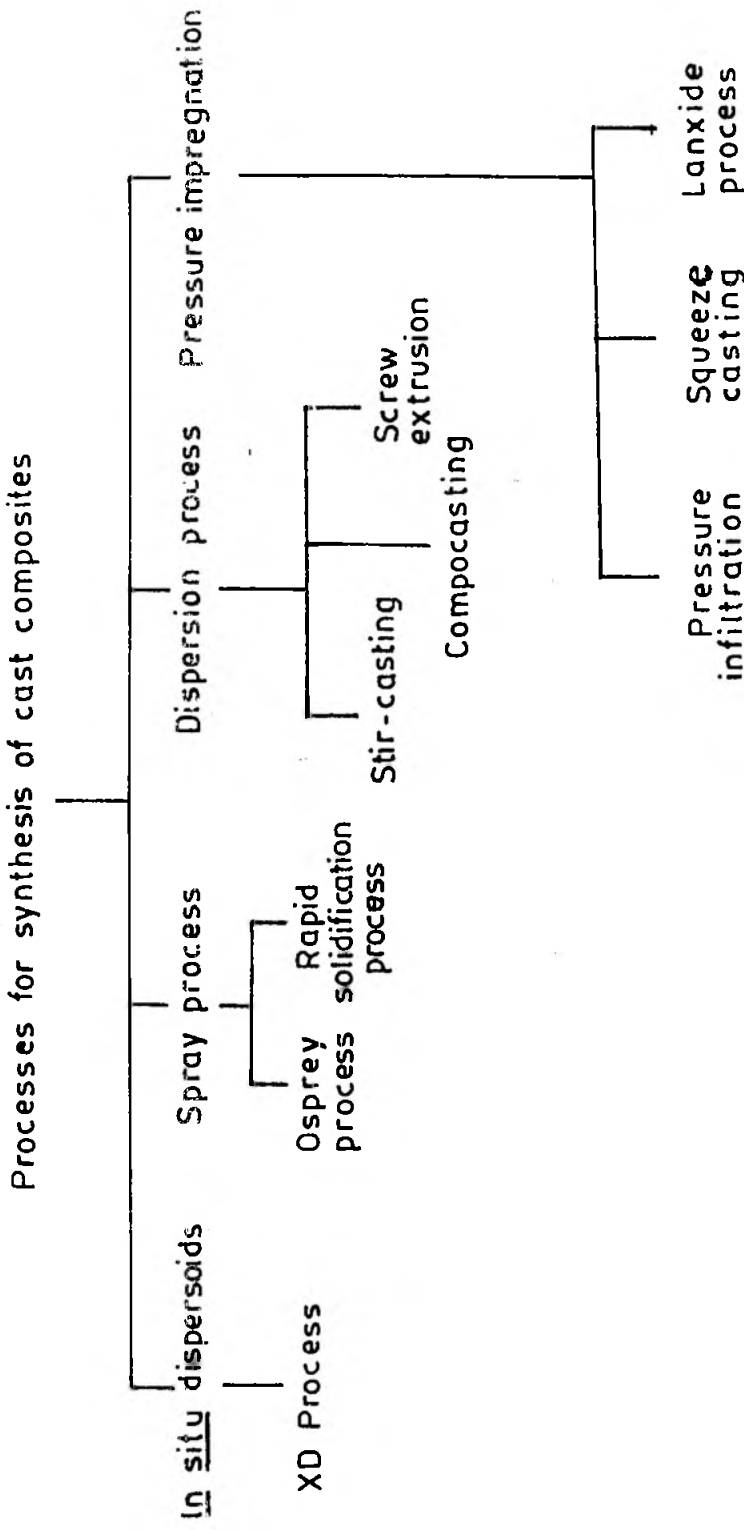
Fig.2.8 Different casting routes for synthesis of cast metal-matrix composites. (Ref.1)

Table 2.3

List of composites developed [65]

Matrix	Dispersoids	Amount
Aluminum based	Graphite flake	0.9-0.815 pct
	Graphite granular	1-8 pct
	Carbon microballoons	
	Shell char	15 pct
	Al_2O_3 particles	3-30 pct
	Al_2O_3 discontinuous	0-23 vol pct
	SiC particles	3-20 pct
	SiC whiskers	10%, 0-0.5 vol
	Mica	3-10 pct
	SiO_2	5 pct
	Zircon	0-30 pct
	Glass particles	8 pct
	Glass beads (spherical)	30 pct
	MgO (spherical)	10 pct
	Sand	36 vol pct
	TiC particles	15 pct
	Boron nitride particle	8 pct
	Si_2N_4 particle	10 pct
	Chilled iron	36 vol pct
	ZrO_2	4 pct
	TiO_2	4 pct
	Lead	10 pct
Copper based	Graphite	
	Al_2O_3	vol fra. 0.74
	ZrO_2	2.12 vol pct
Steel	TiO_2	
	CeO_2	
	Illite clay	3 pct
	Graphite microballoons	
Tin-based babbitt metal	Graphite particle	
	Al_2O_3	
Tin based	Zn	
Mg based	Graphite fibres	40 vol pct
Zn based	Ni-coated graphite	
	Pb	7 pct

Early attempts to introduce ceramic particles into a molten bath either by manually plunging or by injection below the bath surface through an inert gas had limited success due to rejection of particles from the melt [63, 66]. The fundamental requirement for transfer is the wetting between ceramic particle and the melt [65]. Generally, ceramics are poorly wetted by molten metals and they can be introduced by inducing wettability or by use of mechanical agitation like stirring [65].

In recent years a number of techniques to improve wetting have been developed based on the principle that the contact angle θ can be decreased by increasing surface energy of the solid, τ_{sv}, decreasing the solid/liquid interfacial energy, τ_{sl}, or by decreasing the surface tension of liquid metal, τ_{lv} [67]. The techniques to promote wetting between ceramics and molten metals are listed below.

i)   Metallic coating of refractory particles such as Ni or Cu

ii) Additions of reactive elements like Mg, Ca, Ti, Zr and P to the melt

iii) Heat treatment of dispersoids

iv) Ultrasonic irradiation of the melt

Metallic coating of ceramic particles improve the wetting by changing the contacting interface to metal/metal instead of metal/ceramic. Heat treatment of dispersoid particles before their dispersion in the melt aids their

transfer by causing desorption of adsorbed gases from the ceramic surfaces. Ultrasonic irradiation of melt promote wetting as a result of partial desorption of adsorbed gases from the surface of particles and supply energy for melt cavitation which facilitate particle dispersion in the melt.

The addition of reactive elements to the melt promote wetting by reducing the surface tension of the melt and decreasing the solid/liquid interfacial energy of the melt or by inducing wettability by chemical reaction. Reactive elements segregate either to the melt surfaces or at the metal/ceramic interfaces improving the wettability. Thus, wetting of ceramic particles by metallic melt is an important criteria for preparation of metal matrix particulate composites.

Some of the techniques developed to disperse dispersoids in a liquid melt [68-74] are listed in Table 2.4.

2.3.2 Wetting of TiC by Iron

To disperse the particles in a melt, the fundamental requirement is the wetting between ceramic particles and the melt. The wettability of TiC in liquid iron has been determined by measuring the contact angle by sessile drop method. Table 2.5 shows various values of contact angle obtained by Naidich [75].

Table 2.4

Techniques developed to disperse dispersoids in the melt

Technique (1)	Reference (2)	Remarks (3)
Dispersions chemically produced within melt	68	Dispersoids are produced through chemical reactions. It is the oldest method.
Gas injection in melt or stream	69,70	Powder is introduced through a pneumatic injection gun. Some times dispersoids are added in the mould while filling the melt.
Pellet method	71	Pellets or briquettes are formed by co-pressing dispersoid and base alloy powder. The pellets are plunged in liquid melt while stirring it either manually or mechanically.
Vortex method	72	A vortex is created by stirring the liquid melt by an impeller and simultaneously dispersoids are added. It is an extensively used method.
Ultrasonic dispersion	73	Dispersoids are injected through a shot gun while irradiating liquid melt by ultrasonic sound.
Centrifugal dispersion	74	The particles are dispersed using centrifugal acceleration.

Table 2.5

Values of contact angle [75]

$T^O C$	Atmosphere	Contact angle θ deg
1550	Hydrogen	49
1550	Helium	35
1490	Vacuum	28

From the Table it may be noted that the measurement of contact angle depends on the gas atmosphere. The wettability is highest under vacuum followed by helium and hydrogen atmosphere.

2.3.3 Dispersion Test

The degree of dispersion that can be achieved in liquid matrices is known to depend on various process parameters namely temperature, liquid matrix composition, composition and surface properties of dispersoid and ambient atmospheric composition [76]. Though wettability is an important criteria, one cannot infer the degree of dispersion by knowing the wettability. Terry et al., [76] have developed a dispersion test for development of TiC dispersed iron composite. The test relies on electromagnetic levitation of molten metal drop with the dispersoid phase where effects of parameters like melt composition, gas atmosphere, surface properties of dispersoid and temperature, on degree of dispersion can be studied easily. The dispersion test provides qualitative assessment of dispersion as the levitated metal-dispersoid phase droplet is quenched and examined by optical/electron microscope and phases identified by X-ray diffraction. There are several advantages of such a levitation test. Some are as follows:—

a)   Use of crucible is eliminated and therefore, crucible material contamination is avoided.

b) Well mixed heterogeneous melts are obtained which can
    indicate the wetting of solid component achieved as a
    result of vigorous stirring.

c) Gas surrounding the melt can be changed and its effects
    can be studied, and,

d) Quick heating and attainment of equilibrium provide
    the basis for a rapid test procedure.

The limitation of the test lies in its inability
to assess the segregation behaviour of the dispersoid as the
quantity of charge is very small.

2.3.4 Conventional Method of Production of Fe-TiC Composites

Fe-TiC composites are produced and marketed by
M/s. Alloy Technology Inc. (USA) under a trade name of Ferro
- TiC [2]. The composites are produced by distributing TiC
in a hardenable steel, stainless, tool or alloy steel ma-
trices. The composites are produced by powder metallurgical
route involving a vacuum sintering at 1500^0C to attain
full density. The reinforcing TiC particles are of typically
5 μm in diameter. The composites are fully heat-treatable to
impart various physical and mechanical properties. Table 2.6
indicates the range of composites produced by M/s.Alloy
Technology Inc., USA. Principal uses of such a composite are
in cutting, machining and wear resistant applications.

Table 2.6

Fe-TiC composites developed by

M/s. Alloy Technology Inc. USA [2]

Grade	Carbide (Vol pct)	Matrix alloy type	Remarks
CM	45	High chrome tool steel	Good temper resistance, wear parts or general purpose tooling and heavy forming upto 600°C.
C	45	Medium alloy tool steel	Tools, dies and wear parts. Excellent dampening in annealed condition.
SK	40	Hot work tool steel	Good thermal shock and impact resistance, hot work appli-cations, cold heading dies and hammers.
CS-40	45	Martensitic stainless	High hardness with corrosion resistance of 400 series stainless steels.
HT2	45	Age harden-able nickel	Very good oxidation and corrosion resistance Excellent size stability. Resistant to stress corrosion and thermal shock.
CN-5	45	Age hardnable copper-nickel	Excellent resistance to sea water environment.
J	40	High speed steel	Good temperature resistance for elevated temperature tooling upto 730°C.
S-45	45	Austenite stainless steel	Excellent corrosion resistance of 300 series stainless steels.

TiC alloy (trade name) is developed by M/s.Seil-strofer, Germany. The composite typically contains 40 volume percent of TiC in a heat treatable alloy steel matrix. These are produced by hot isostatic pressing.

Composites containing 40-45 volume percent TiC embedded in alloy steel matrix are available from M/s. Thyssen, Germany under trade name Ferro-titanit.

The following are the limitations when a component is produced by a powder metallurgical technique:-

a)   Mixing of carbide and matrix powder must be thorough in order to achieve uniform dispersion of reinforcing phase.

b)   Mould design must be simple in order to avoid segregation of reinforcing phase during compaction and sintering.

c)   Sinter parts must be trimmed or machined into final shape and such operations become difficult because of extreme hardness of the materials, and,

d)   Sintering cycle and environment are very critical to obtain dense components with near theoretical density.

Therefore, attempts are being made to develop alternate, cost effective processes.

2.3.5 In situ Production of Fe-TiC Composites by Reactions in Liquid Iron Alloys

Beeley and co-workers [77, 78] have developed a method of producing primary dispersion of hard carbide particles by addition of carbide forming elements to molten steel bath. They have modified tungsten-bearing high speed tool steel structure and properties by introducing additional alloying elements designed to form primary carbide dispersions. The dispersions provide enhanced hardening of the steel and also refine the otherwise coarse dendrite pattern in the cast structure.

Generally, component of complicated shape such as milling cutters are produced by machining mechanically wrought blanks. The process involves heavy stock removal, high machining costs and low metal yields in terms of useful products. Therefore casting processes, by virtue of their capacity to fill the moulds to obtain finished net shape, offer considerable advantages over the conventional process. Cast to shape products have inferior properties due to their relatively coarse structure characterised by massive carbide net work. The addition of carbide forming elements just before casting was first developed for hot die steel application using maraging steel as a base alloy [77]. Stoichiometric addition of Nb or V and carbon to high speed tool steel produced highly modified as cast structure. The

volume of carbide fraction created was about 14 pct with 3 to 10 μm carbide particle size.

A similar technique was adopted by Terry et al., [6] while developing in situ Fe-TiC composite by reactions in liquid iron alloys. To develop such a composite two approaches have been made namely a) addition of carbon to iron-titanium alloy and b) addition of titanium to iron-carbon alloy. The findings of these experiments are described.

Addition of carbon to iron-titanium alloy :

Iron 5.2 wt pct Ti alloy was prepared in an induction furnace by melting appropriate quantities of carbonyl iron and titanium. The iron-titanium alloy was remelted in an alumina crucible by induction heating and stoichiometric amount of carbon was added in the form of coal to convert alloy titanium to titanium carbide. The melt was maintained at 1550 $^{\circ}$C for 20 minutes to complete the reaction. The microstructure of the alloy showed uniform distribution of discrete TiC particles. Based on the results of the above study, an iron - 24 wt pct Ti alloy was prepared by melting requisite quantities of elements at 1700 $^{\circ}$C for 20 minutes. The 24 wt pct Ti alloy showed the presence of Fe_2Ti intermetallic phase and the alloy was brittle. About 33 g of Fe - 24 wt pct Ti alloy was remelted and 4 g graphite powder was added to the melt. The resultant

mixture was held at 1600 °C for 15 minutes in a graphite crucible by induction heating. The microstructure of the alloy showed an excellent dispersion of well-rounded TiC particles in ferrite matrix. The volume fraction of TiC generated was in excess of 40 pct. The material was ductile as significant deformation could be given when samples were crushed for analysis. The carbide dispersion appears to be uniform and the metallographic examination showed dendritic net work of carbide phase in an iron matrix.

Addition of titanium to iron-carbon alloy :

The composite was developed by addition of titanium filings to a levitated drop of 3 wt pct carbon cast iron. The reaction time was as short as 80 seconds at 1600°C and the conversion of titanium to titanium carbide was virtually complete. The metallographic examination showed even distribution of TiC particles of 10 μm size dispersed in pearlite matrix. This is so because the addition of titanium was such that 0.75 wt pct carbon remained in the matrix thus confirming the pearlite observed during the metallographic examination.

The various advantages claimed by the investigators for in situ production of Fe-TiC composites are as follows:

i) The need for preparation of filler reinforcing carbide is avoided.

ii) In situ reaction results in stronger bonding between matrix metal and reinforcing phases.

iii) Gas absorption, oxidation and other detrimental surface reactions at metal filler phase interface are avoided.

iv) Liquid base route provides an opportunity to cast composites of required final shape, and

v) The conditions for good dispersion of filler reinforcing materials could be established to achieve a minimum porosity.

Thus technical feasibility on preparation of in situ TiC reinforced composite by reaction in liquid iron was established by Terry et al, [6].

2.3.6 Carbothermic Reduction of Ilmenite and Rutile

Terry et al., [8] have investigated the carbothermic reduction of rutile and ilmenite to produce Ti(O,C) metal matrix composite. The reactions that were considered by the investigators are as follows.

For ilmenite
$$xFe + Fe_2TiO_3 + 4 C = (x+1) Fe + TiC + CO \quad ....(2.10)$$
and for rutile
$$xFe + TiO_2 + 3c = xFe + TiC + 2 CO \quad ....(2.11)$$
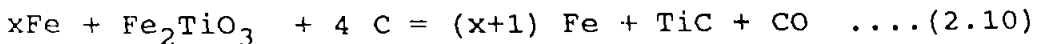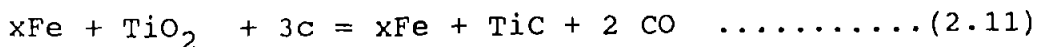
To obtain a required Fe/TiC ratio in the composite an excess amount `x' iron powder was added. The experiments were carried out with 1 g of premixed iron powder

(carbon saturated), ilmenite or rutile and collie coal in various proportions. The premixed powder was compacted and reduced in a tube furnace under argon atmosphere. Reduction temperature was varied between 1300 to 1600°C. A few experiments were carried out with 60 g charge in an induction furnace. Investigations were also carried out with addition of fluxes like $CaCl_2$, CaF_2, $MgCl_2$ or $BaSO_4$. The important results of the investigations may be summarised as follows:-

a)   The reaction product contained Ti(O,C) rather than TiC, and has been attributed to lower reduction temperature.

b)   At lower reduction temperatures (1300 to 1430°C) very often conversion to TiC or Ti(O,C) was incomplete and some oxide phase M_2O_3 remained. The energy dispersive x-ray analysis in SEM of M_2O_3 showed that bulk of metal M was titanium and bulk of manganese impurity in ilmenite was also associated with it.

c)   As the temperature of reduction was increased, Ti(O,C) phase became richer in carbon.

d)   Excellent dispersion of Ti(O,C) was obtained when carbon saturated iron in premixed powder was replaced by iron-titanium-carbon alloy powder.

e)   In general, addition of flux improved the kinetics of Ti(O,C) formation and promoted separation of Ti(O,C) product from iron phase.

f)   Formation of Ti(O,C) was rapid when rutile was reduced instead of ilmenite.

g)   The oxycarbide product was often found to be agglomerated in clusters of roughly the same size as original rutile particles, similar to those obtained in experiments with ilmenite without flux.

h)   The optimum conditions for composite formation appear to be achieved by reducing ilmenite or rutile with carbon at temperatures of the order of 1500°C in presence of excess carbon.

i)   The scaling up experiments required maintenance of reducing atmosphere and removal of carbon monoxide gas from the reaction site.

It is seen that the technical feasibility on preparation of Fe-Ti(O,C) composites by carbothermic reduction of ilmenite or rutile has been established.

2.3.7 Dispersion of TiC in Liquid Iron Alloys

Terry et al., [76] have also investigated the dispersion of TiC and Ti(O,C) in iron, iron-carbon, iron-titanium and iron-titanium-carbon alloys by electromagnetic levitation technique. Ti(O,C) was prepared by carbothermic reduction of rutile and coal at 1500°C. Experiments were also conducted on the _in situ_ preparation of Ti(O,C) by levitating a mixture of carbon saturated iron, rutile and

collie coal and a mixture of ilmenite, carbon saturated iron and collie coal at 1500°C. Large scale experiments were carried out in an induction furnace by melting metal and TiC pellets weighing 20 g in an alumina crucible. The important findings of the investigation are as follows:

1. In the temperature range studied i.e., 1500 - 1600°C, temperature had little effect on the degree of dispersion.

2. Dissolution of TiC is favoured in low carbon iron alloy. Dispersion of TiC is improved by prolonging the levitation with higher quantities of TiC in low carbon iron alloy.

3. Dispersion of TiC was minimal in pure iron or low carbon iron alloy. Semiquantitative electron probe analysis showed 0.5 to 1 wt pct Ti dissolution in the matrix.

4. Dispersion of TiC is favoured as the carbon content in the alloy is increased. Generally, 0.2 to 0.8 wt pct Ti is dissolved in the matrix of such alloys.

5. TiC dispersion was better in Fe-3.7 wt pct C alloy compared to that of Fe-5.2 wt pct Ti alloy. The presence of titanium and carbon in solution in iron alloy promotes dispersion of TiC.

6. The dispersion of Ti(O,C) prepared _in situ_ was

better compared to that of Ti(O,C) prepared separately and levitated in iron-carbon alloy. This may be due to surface oxidation or contamination of Ti(O,C) prepared separately thus reducing the wettability.

7. The ternary phase diagram of Fe-Ti-C system shows that the carbon content of iron has negligible effect on solubility of TiC. However, the micro structures of levitated samples do not show complete dissolution of TiC. This observation has been attributed to a kinetic barrier for the dissolution of TiC especially in the high carbon iron melts.

8. The precipitation of TiC from Fe-Ti-C matrix would be expected to occur on cooling both in the liquid and solid state as the TiC solubility decreases with temperature. The precipitation of TiC could occur on pre-existing TiC or as separate precipitates.

9. TiC is more easily wetted than Ti(O,C). The degree of wetting improves as the temperature of reduction in case of _in situ_ composite preparation is increased as the reaction product changes from Ti(O,C) to TiC.

The technical feasibility of TiC dispersion in liquid iron is now well established and the dispersion test developed gives a fairly good indication on the degree of dispersion.

2.3.8 Tribological Properties of Fe-TiC Composites

There is a substantial improvement in abrasive resistance of alloys when particulate carbides are dispersed in it [79]. In the past it has been observed in cobalt, iron and nickel base alloys that a larger volume fraction of carbide improves abrasive wear resistance [80]. Gradually SiC-Al composites are being adopted in automotive internal combustion engines due to their enhanced wear resistance and desirable frictional properties [81]. Thus, volume fraction, particle size of dispersoid and their uniform distribution in the matrix are found to effect the mechanical properties very significantly [82-84]. Wear resistance properties of some of the aluminium metal matrix composites [85-89] are presented in Table 2.7. Iron with 40 to 45 volume percent TiC reinforced particulate composites, fabricated by conventional powder metallurgical route, and sold under various trade names are being successfully adopted in tools, dies, heavy forming or warm working upto 600°C and wear parts [2]. In the following section tribological properties of some iron-TiC reinforced cast composites are presented.

There have been some studies on evaluation of wear resistant properties of iron-TiC reinforced cast composites [79, 90, 91]. The effect of volume fraction of TiC and their particle size on wear resistant properties have been stud-

Table 2.7

Wear resistant properties of metal matrix composites.

Authors Ref.	Composite	Testing procedure	Remarks
85	Al 2024-Al$_2$O$_3$ 20 wt pct	Sphere on disc	Best result obtained with 142 μm dispersoid particle size, wear rate decreased 50% that of unreinforced alloy.
86	Al-10 wt Zn -5 wt pct Al$_2$O$_3$ -15 wt pct Al$_2$O$_3$ -25-30 wt pct Al$_2$O$_3$	Pin on disc	Wear rate decreased with increasing wt pct of dispersoid. Composite with 25.30 wt pct Al$_2$O$_3$ showed less than 1 pct wear rate to that of unreinforced alloy.
87	Al-6061 SiC 20 vol. pct	Reciprocating dry sliding	A decrease in wear rate over 300 times to that of unreinforced alloy.
88	Al-72 Si-Ni + Graphite	Rotating steel with disc lubrication	Wear resistance properties are better than those of alloys without dispersoids. Composite containing 2 vol. pct could be run for longer duration once the lubricant was stopped. Composites containing 0.5 and 1 vol. pct graphite seized immediately after stopping lubricant.
89	Al-10 to 40vol pct Al$_2$O$_3$	Sliding wear against WC-Co surface	Increase is wear rate by a factor of 2 to 2.5 compared to unreinforced metal.

ied. Co-efficient of friction has been measured and effect of heat treatment and volume fraction of carbides in composites have been determined. Table 2.8 gives briefly the details of various investigations. From the above studies it may be seen that tribological studies on cast Fe-TiC composites have not been very extensive.

2.4 SUMMARY

A wide range of Fe-TiC composites have been developed by powder metallurgical techniques and are commercialised under various trade names. Alternate methods of preparing Fe-TiC composites have been in the initial stages of development and the technical feasibility of these processes have been established. The scale of investigation in these developments have been so low (i.e. g scale), it is difficult to assess the degree of dispersion visa-a-vis the segregation of TiC particles in iron matrix. The composites have been characterised mostly by metallographic techniques, XRD analysis, electron microscopy and electron probe analysis. A few micro hardness data are available.

Thus, there is a need to develop iron - TiC reinforced cast composites in large scale and evaluate their properties.

Table 2.8

Wear properties of Fe-TiC composites

Ref. (1)	Composition Wt pct (2)	Vol. fraction TiC (3)	Test procedure (4)	Remarks (5)
79	Fe-16.85 Ti-4.22C Fe-11.1i Ti-3.5C Fe-10.88 Ti-5.8C Fe-8.1 Ti-3.1C Fe-0.4C Fe-3.8C	0.3 0.22 0.20 0.18 0.20 0.72	Abrasive wear against 600 grit SiC paper weight loss method 2.709 N load	(1) Specific wear rate decreases as vol. fraction of carbide increases. (2) Wear rates increased as carbide spacing increased. (3) Specific wear rates are 105 to 1000 times less compared to i020 steel in as rolled and heat treated condition as well as white cast iron.
			Friction test by automatic scratch testing apparatus	(1) Co-efficient of friction is lower for martensitic matrix compared to pearlitic matrix. (2) Lower friction correspond to lower specific wear rate.
90	Fe-TiC	25 vol pct	Pin-on-drum weight loss method 67 N load	(1) Distribution of TiC is important. (2) Wearing occurred primarily by ploughing mechanism.

(1)	(2)	(3)	(4)	(5)
91	304 stainless steel IN 1000	0.082 to 0.32	Pin on disc 600 grit SiC paper 3.11 N load	(1) Decrease in specific wear rate as vol fraction of carbide increases.
				(2) As average carbide particle size increases, specific wear rates of composites increases.
				(3) Wear rate depends on carbide particle spacing.
			Friction measurement 10 and 20 N load particle size	(1) Co-efficient of friction decreases with decreasingTiC.
				(2) There is a decrease in coefficient of friction as micro hardness of composite increases.

CHAPTER - THREE

EXPERIMENTAL

3.0 INTRODUCTION

The investigations on preparation of iron-titanium carbide composites were carried out in the following four phases:

1. Design and fabrication of transferred arc plasma reactor

2. Preparation of TiC rich Fe-TiC master alloys and TiC reinforced cast iron and steel composites

3. Metallurgical characterisation of TiC rich Fe-TiC master alloys, TiC reinforced cast iron and steel composites

4. Determination of wear characteristics of the composites

The composites prepared and cast in either metal mould or sand moulds were subsequently characterised by chemical analysis, metallography, image analysis, scanning and transmission electron microscopy, x-ray diffraction studies and energy dispersive x-ray analysis. Mechanical properties like tensile strength, toughness and hardness of the composites were evaluated. Tribological tests like adhesive wear and abrasive wear were carried out to evaluate wear resistant properties of composites. The experimental details are described in subsequent sections.

3.1 Phase I

DESIGN AND FABRICATION OF TRANSFERRED ARC PLASMA REACTOR FOR COMPOSITE PREPARATION

The smelting of ilmenite was carried out in an indigenously developed 35 kW DC extended arc plasma reactor [30]. The description of the reactor is presented below.

35 kW DC extended arc plasma reactor

A schematic sketch of the extended arc plasma reactor is shown in Fig.3.1.

It is a pot reactor where a magnesia lined graphite crucible serves as the reactor hearth. The crucible is thermally insulated by bubble alumina in a mild steel casing. The hearth is provided with a tap hole and a graphite spout is connected to it for tapping both metal and slag. Two graphite electrodes are arranged in a vertical configuration in the reactor. The bottom electrode, anode, is kept fixed and the arc plasma stabilisation is done by movement of top electrode, cathode, which is actuated by a rack and pinion mechanism. The ends of both the electrodes are water cooled. The cathode has an axial hole to pass plasma forming gas. A graphite sleeve is provided in the lid with ceramic insulation to promote free travel of the electrode without electrically shorting the body. The lid is thermally insulated by magnesia ramming mass and is furnished with an
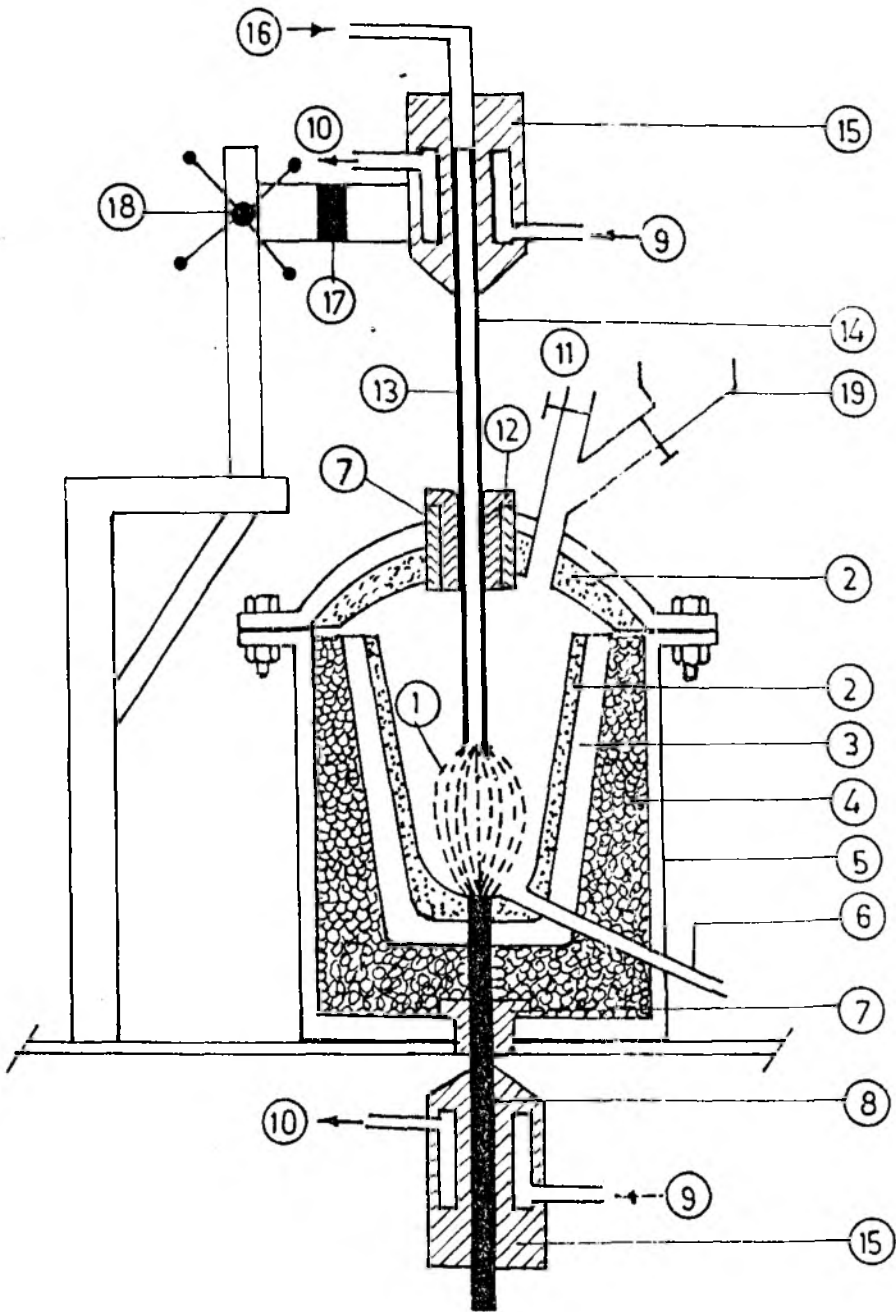
1. Plasma 2. Magnesia Coating 3. Graphite Crucible 4. Bubble Alumina
5. M.S. Casing 6. Tap hole 7. Alumina Bush 8. Bottom Graphite Electrode
9. Water Inlet 10. Water Outlet 11. Outlet for Exhaust Gases 12. Graphite
Sleeve 13. Top Graphite Electrode 14. Axial Hole 15. Copper Block
16. Plasma Forming Gas 17. Electrical Insulation 18. Rack & Pinion
Mechanism 19. Hopper

Fig.3.1 Schematic diagram of an Indigenously developed extended arc
plasma reactor. (Ref.30)

opening for the exhaust gases. The anode is introduced into the hearth through a ceramic insulating bush to avoid the shorting of the reactor body. The power to the reactor is supplied by a dc arc welding power source.

Design data of the reactor

The most important design data are summarised.

Diameter of graphite electrode	25 mm
Diameter of the axial hole	3 to 6 mm
Electrode travel	300 mm
Diameter of the graphite crucible	175 mm
Height of the crucible	215 mm
Diameter of the steel casing	210 mm
Height of the casing	320 mm
Rate of flow of plasma forming gas	0.5 to 3 liters /min
Rate of flow of water for cooling electrodes	3 liters/min
DC Power Supply	35 kW (100V, 350 A)
Maximum arc length	200 mm

Operation of the reactor

Both the electrodes are kept in contact with each other. The smelting charge consisting of ore, reductant and flux are thoroughly mixed and charged into the reactor hearth through the opening provided in the reactor. Water for cooling of electrodes and regulated flow of plasma forming gas like argon or argon and hydrogen mixture are

ensured. As soon as the power to the reactor is switched on, the cathode is moved away slowly after striking the arc to stabilise the arc plasma. Metal and slag are tapped by opening the tap hole after completing the smelting operation. The power supply to the reactor is then switched off and flow of plasma forming gas stopped. The water circulation to the electrode is stopped when the reactor hearth temperature is below 600°C. Generally, smelting a charge of 1 to 2 kilogram takes 30-45 minutes.

3.2 Phase II

PREPARATION OF TiC RICH Fe-TiC MASTER ALLOYS AND TiC REINFORCED CAST IRON AND STEEL COMPOSITES

The experimental procedure for preparation of various master alloys and TiC reinforced ferrous composites are described in this section.

3.2.1 Experimental Parameters for Preparation of TiC Rich Fe-TiC Master Alloys

The influence of following experimental variables were studied to improve titanium content of the master alloy while smelting ilmenite by carbothermic reduction.

a) Carbon requirement - Stoichiometric to 200 wt pct excess carbon

b) Addition of flux - Silica, calcia, magnesia and calcium fluoride

c)   Coating of reactor hearth - Magnesia and zircon

d)   Addition of hydrogen to the plasma forming gas namely,
     argon - 20 to 40 pct by volume H_2 in argon and hydro-
     gen gas mixture

Charge preparation

All the investigations were carried out utilising
ilmenite ore concentrates obtained from Kerala beach sand
supplied by M/s. Indian Rare Earth's Ltd.. The elemental
analysis of the ilmenite and its particle size distribution
is shown in Table 3.1 and Table 3.2 respectively. Graphite
powder with 98.5 wt pct fixed carbon was used as a reduct-
ant. Chemical reagent grade oxides and fluorides were used
as fluxes. Ilmenite was dried at $110^{\circ}C$ to remove the mois-
ture in an oven. The smelting charge calculations were based
on 400 g ilmenite in a batch. A typical charge composition
for smelting is shown in Table 3.3. The smelting of ilmenite
was carried out following the procedure described in section
under the operation of reactor. Flow of argon gas was regu-
lated at 1.6 litres/minute throughout the period of experi-
ment unless otherwise mentioned. An arc voltage of 45-50 dc
and 300 amperes current were maintained during the experi-
ment. The temperature of the molten bath was estimated by
measuring temperature by optical pyrometer at short inter-
vals as soon as switching off the power to the reactor. The
temperature-time plot was extrapolated to zero time to
estimate the batch temperature just before power switch off.

Table 3.1

Chemical analysis of ilmenite

	Wt pct
TiO_2	54.63
FeO	34.31
SiO_2	2.60
Al_2O_3	1.13
ZrO_2	0.43
MnO	0.36
MgO	0.57

Table 3.2

Particle size analysis of ilmenite

μm	Wt pct
+ 250	20.04
- 250 + 210	25.63
- 210 + 180	22.72
- 180 + 150	19.56
- 150 + 125	2.02
- 125 + 90	8.45
- 90	0.09

Table 3.3

A typical smelting charge mix for
preparation of Fe-TiC master alloy

	Wt (g)
Ilmenite	400.00
Graphite	94.28
Steel scrap	220.00
Flux (CaO+CaF)	16.00

3.2.2 Preparation of TiC Reinforced Cast Iron Composites by Smelting of Ilmenite

Iron-TiC composites were prepared by smelting 200 to 250 g ilmenite with 100 wt pct excess carbon over stoichiometric requirement and a kilogram of mild steel (0.1 wt pct C) scrap. The experimental parameters that were investigated are as follows.

a) Duration of smelting - 25 to 35 minutes

b) Crucible coating - Magnesia and zircon.

No fluxes were added to the charge. The smelting was carried out under argon plasma. The composite were cast into sand and metal moulds.

3.2.3 Preparation of TiC Reinforced Steel Composites

These composites were developed by melting mild steel scrap (0.1 and 0.03 wt pct C) in an induction furnace of 5 kg capacity with a magnesia lined crucible. The TiC rich Fe-TiC master alloy was added to a liquid steel so that the titanium content in the composite ranged between 0.05 to 1.0 wt pct. Prior to addition of weighed quantity of the master alloy, the molten steel was deoxidised by the addition of Fe-Si (80 wt pct Si) and Fe-Mn (65 wt pct Mn) each amounting to 0.1 wt pct and the slag was removed. After complete dissolution of the master alloy the melts were poured into sand and permanent moulds. An experiment was carried out on dissolution of chemically pure TiC powder in a molten steel bath. Another experiment was carried out on

oxidising away of excess carbon of Fe-TiC master alloy by reacting it with iron ore (blue dust - 97.8 wt pct Fe_2O_3 a variety of iron ore).

The cast test pieces were in the form of cylinders of 50 mm diameter x 200 mm length and rods of 25 mm diameter x 150 mm length. The chill cast test pieces were of rectangular cross section of 15x15 mm square section and 240 mm long.

3.3 Phase III

METALLURGICAL CHARACTERISATION OF TiC RICH Fe-TiC MASTER ALLOYS AND TiC REINFORCED CAST IRON / STEEL COMPOSITES

This section describes the procedure for characterisation of products of the present investigation.

3.3.1 Chemical Analysis

The titanium rich master alloy and TiC reinforced cast iron samples were analysed for titanium, iron and silicon following wet chemical analytical procedures. The trace elements like Mg, Ca, Al, Zr, S, P etc. were estimated by energy dispersive x-ray method by scanning the samples over a large number of spots. The values of these elements have been expressed in terms of ranges rather than as average values. The carbon content of master alloy and TiC-rein-

forced cast iron composites were determined by using Stroh-lein's apparatus. Lead peroxide was used as a catalyst while combusting the samples for carbon analysis.

TiC-reinforced steel base composites were analysed by means of spectroscopes.

3.3.2 X-ray Diffraction Analysis

Various phases present in the master alloy, TiC reinforced cast iron and steel base composites were deter-mined by x-ray diffraction analysis. The analysis was car-ried out on Phillips x-ray Diffractometer PW 1710 model. X-ray diffraction was carried out on powder samples of master alloy, while solid specimens were used for analysis of com-posites. Cu $K\alpha$ or Mo $K\alpha$ targets were used in this investiga-tion. X-ray diffraction patterns were taken for 2θ varying from 6 to 70° when Cu $K\alpha$ target was used and 10 to 40° when Mo $K\alpha$ target was used. Scan speed was $1.2^{\circ}/\text{min}$. The peak positions were identified and compared with the microproces-sor output to obtain the corresponding 'd' values. The 'd' values were matched with standard ASM x-ray diffraction tables and the phases were identified and (hkl) planes were noted. The phases were classified based on relative intensi-ty as strong (80-100 pct), medium (40-79 pct) and weak (10-39 pct).

3.3.3 Metallography and Image Analysis

The microstructures of the master alloy and the TiC reinforced cast iron and steel base composites were examined after usual metallographic polishing and etching. Metallographic samples were always drawn from the bottom sections of the cast rods and corresponding portions of the forged rods. Photomicrographs of the representative samples were taken.

Leica Cambridge Quantimet Q 570 image analyser with microprocessor was used to determine carbide volume fraction, carbide particle size distribution and grain size in TiC reinforced steel base composites. A number of scans were taken to estimate correct volume fraction and carbide particle size distribution. The grain size measurement and pearlite fraction in the composites were estimated after scanning whole sample area. In case of TiC-reinforced cast iron base composites volume fractions of carbide and graphite were estimated.

3.3.4 Mechanical Properties of TiC Reinforced Steel Composites

Mechanical properties like tensile strength, ductility and hardness of TiC reinforced steel composites were evaluated.

Tensile strength

Tensile testing of TiC reinforced steel composites were carried out on as forged samples. 50 mm diameter cast rods were hot forged down to 15 mm diameter. The forged rods were homogenised at 1150°C for 2 hours and forced air cooled. The normalised composite rods were machined to prepare tensile test specimens of dimensions shown in Fig. 3.2. The specimens were subjected to tensile testing in either 4 Ton universal testing machine UP M4 model from M/s. Trebel Werk, Dusseldorf, Germany or in a tensometer.

Tensile strength and ultimate breaking strength were calculated. The percentage reduction of cross sectional area and elongation of specimen were also determined. The fractured surface of tensile test specimens were studied in SEM to know the nature of failure.

Hardness

Bulk hardness of composites were determined using a Rockwell hardness tester with diamond indenter under 150 kg load. The hardness values have been expressed in Rc scale. Indentations were made at a number of sites and variation in hardness values have been reported. Hardness of both TiC reinforced steel as well as cast iron based samples have been reported.

Hardness of the various phases was determined by means of a microhardness hardness tester (Leco-m-400) under

(a)

(b)
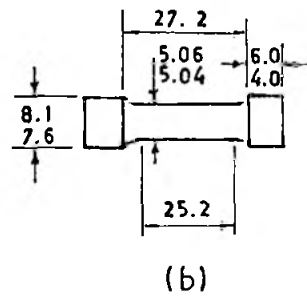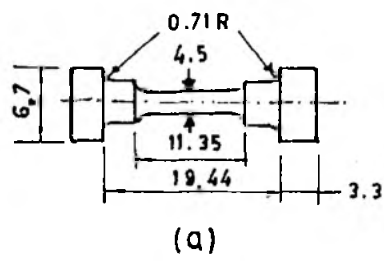
Fig.3.2 Tensile test specimen (a) UTM
(b) Tensometer . (Dimensions in mm)

10, 25 or 100 g load depending on the particle/phase and its hardness. A large number of readings were taken and the range in which they are varying are reported.

Impact strength

Impact test specimens were prepared from the forged and normalised TiC reinforced steel base composites. Charpy impact tests were carried out at room temperature $(15^{o}C)$. The energy absorbed while breaking the sample was noted.

3.4 Phase IV

WEAR TESTING OF TiC REINFORCED COMPOSITES

Adhesive wear and abrasive wear testing of TiC reinforced composites were carried out. The equipments used and procedure adopted are described below.

3.4.1 Adhesive Wear Testing

Adhesive wear of TiC reinforced composites were carried on a 'Horizontal pin-on-disc friction and wear test rig' manufactured by Ducom, Bangalore Model TR-20. The schematic sketch of the rig is shown in Fig.3.3. The machine has a facility to vary normal load to the pin, rotational speed and wear track diameter. The tangential frictional force and wear were monitored with electronic sensors available in the machine. Both these parameters were recorded against time at a given speed of the disc and normal load.
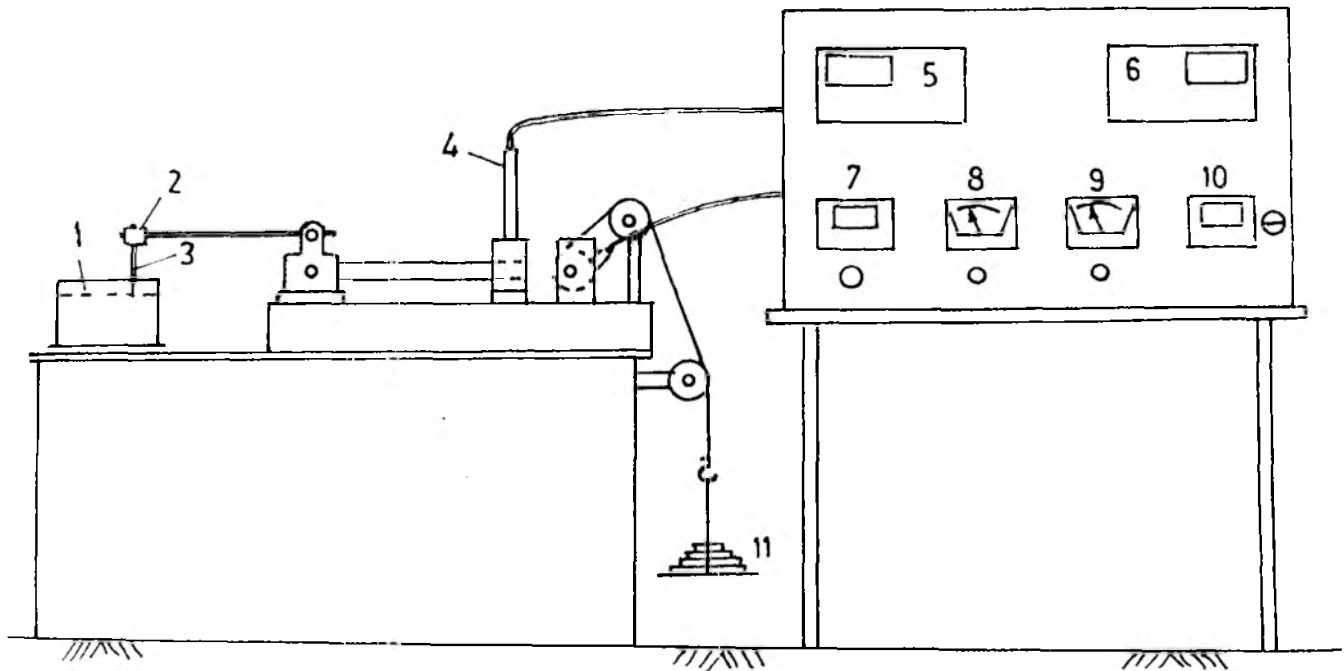
1. Rotating disc
2. Pin holder
3. Pin
4. Load cell
5. Load indicator (kg)
6. Displacement indicator (μm)
7. RPM indicator
8. Voltmeter
9. Ammeter
10. Set time meter
11. Weight

Fig. 3.3   Schematic diagram of horizontal pin on disc frictional wear test rig.

The specification of the machine and parameters varied are mentioned below:

Specifications of the machine

The important specifications are as follows.

Pin diameter : 4, 6, 8, 10 and 12 mm

Disc size : 215 mm and 8 mm thick

Disc material : 103 Cri-Ens-31 HRS 60 W 62

Disc rotation : 100-1100 rpm continuously
variable with digital tachometer

Wear track : 180 mm θ max, 50 mm θ min

Normal load : 20 kg max

Frictional force : 0-20 kg, digital readout with
measurement recorder out put.

Wear measurement range : ± 2 mm range

Drive : 1.1 kW DC motor constant torque
230 V ± 5 pct, 15 amps 3 phase 50
Hz AC

Motor control : Thyristor converter with full
motor protection

Parameters varied

Pin diameter : 6 mm θ and 8 mm θ

Wear track diameter : 17 cm and 12.5 cm θ

Disc speed : 600 rpm

Sliding speed : 5.5 m/sec and 3.92 m/sec

Normal load : 2, 6, 8 and 10 kg

TiC – reinforced cast iron and steel base composites were normalised after soaking at 950°C for 4 h and pins of 6 mm and 8 mm diameter were machined with 20 mm length. Wearing surface of pin was polished metallographically up to 600 grit SiC paper. The wear characteristics of the experimental cast iron composite specimens were compared with a standard spheroidal graphitic iron sample under identical experimental conditions. Similarly the wear behaviour of the steel based composites were compared with that of a standard low alloy steel. Wear track diameter, normal load and disc speed were kept constant during each test. Variation in frictional force and wear were measured from sensor outputs as a function of time. The testing of specimens were carried out till constant wear was obtained or till a specified amount of wear of 6 mm took place. Worn out surface of composites and standard specimens were examined in the scanning electron microscope to ascertain the probable mechanism of wear. In some cases debris of samples were also collected.

3.4.2 Abrasive Wear Testing

Abrasive wear tests were carried out using a modified pin-on-disc machine [92]. A laboratory metallographic polishing machine was modified by fixing a 20 cm diameter alumina grinding wheel (Grade A.60 QV) in place of polishing wheel. A specimen clamp holder was mounted as shown in the schematic sketch of the modified Pin-on-disc machine

(Fig. 3.4). The TiC reinforced cast iron and steel based composites of 15 mm x 15 mm x 50 mm was clamped in a holder and was held against the rotating wheel under load rigidly. Three different loads were applied for the test namely, 0.5, 1.0 and 1.5 kg corresponding to 4.9 N, 9.8 N and 14.7 N respectively. The spindle speed was 250 rpm, which at an average distance of 8.5 cm from the centre gave a linear speed of 2.2 m/sec. The loss in weight of specimens were measured at an interval of 10 minutes. The tests were conducted till a constant loss in weight over two consecutive readings were obtained.

The abraded surfaces of the samples were examined in SEM to ascertain the probable mechanism of wear.

3.5 Scanning Electron Microscopy and Energy Dispersive x-ray Analysis

A Camscan Series 2 DV, model scanning electron microscope was used for examination of the master alloy, TiC - reinforced cast iron and steel base composite samples. Metallographically polished samples were deep etched in concentrated HCl acid for 5 to 15 minutes and washed. The etched surfaces were then gold coated before examination in SEM. The carbide morphology in the master alloy and in the cast iron composites were examined. The graphite morphology in case of TiC-reinforced cast iron composite samples were also examined. The worn out surfaces of the wear test samples were examined to study the wear tracks and nature of
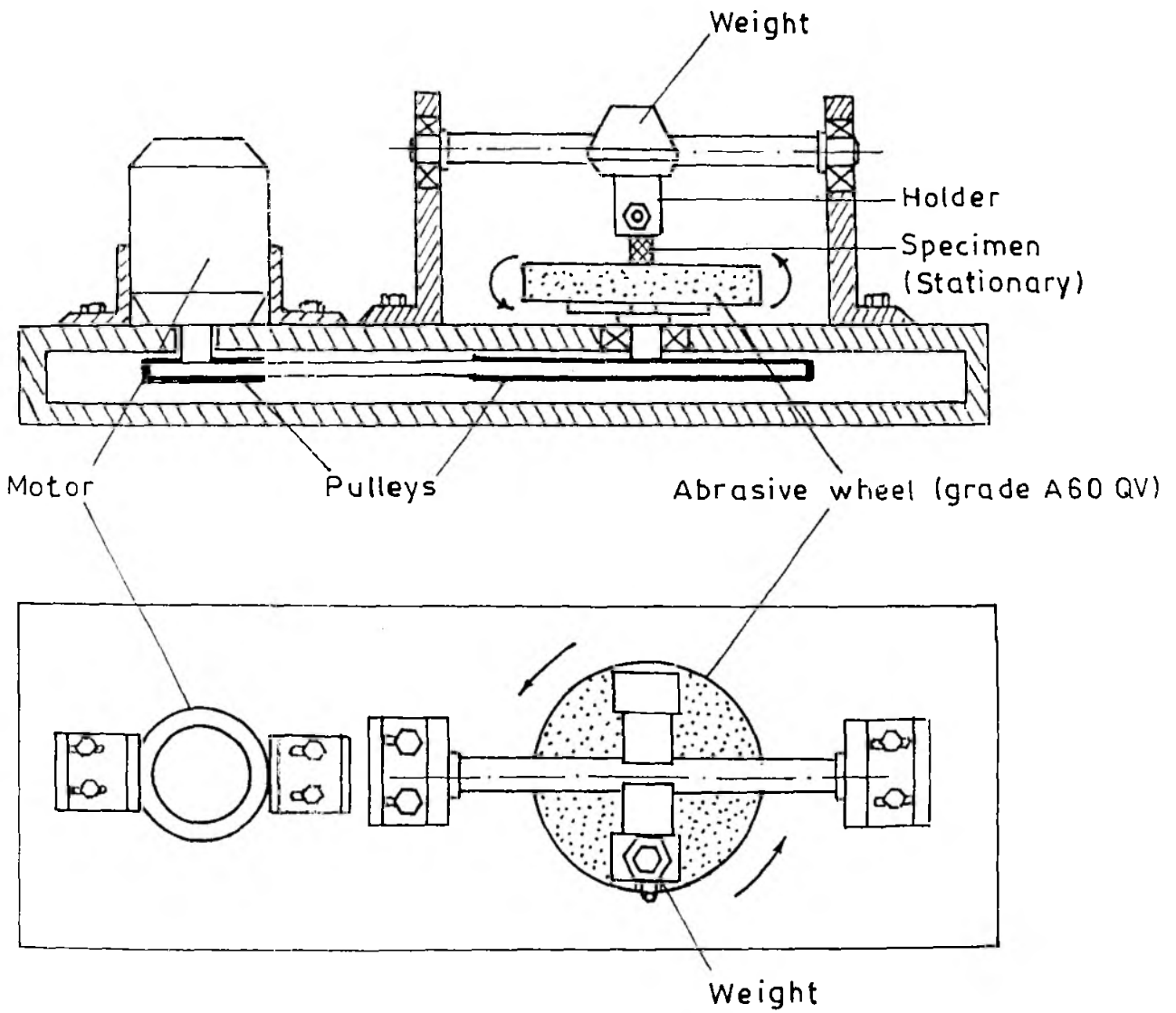
Fig. 3.4   Schematic diagram of modified pin-on-disc machine,
used in the present study.

wear. Fractographs of broken tensile test specimens were also taken.

Energy dispersive x-ray analysis of samples was carried out using analysers attached to SEM. Some of the samples were analysed in a JOEL 35 - EDX analyser. Other samples were analysed using analysing system attached to a Camscan scanning electron microscope. Number of spots were analysed to arrive at the data. Elemental analysis has been reported as a variation over a range rather than average values. EDX analysis of carbide/matrix interface and inclusions were also carried out. Bulk analysis of various composites were carried out to arrive at concentration of trace elements. Here again scanning was done over a large area and elemental variation in a range is reported.

3.6 Transmission Electron Microscopic Investigation (TEM)

A few forged and normalised steel base composite samples were also examined in TEM by two stage replication technique. At first a plastic replica was prepared. This was then coated with carbon by sputtering. The plastic base was then dissolved in acetone. The carbon replica was next repeatedly washed and dried for examination in a Phillips CM3 transmission electron microscope. Examination was carried out at 100 kV.

CHAPTER - FOUR

RESULTS, DISCUSSION AND CONCLUSIONS

4.0 INTRODUCTION

Results and discussion of various investigations carried out are presented here in four sections namely, a) smelting of ilmenite in the plasma reactor, b) TiC reinforced cast iron composites, c) TiC reinforced steel composites, and d) wear testing of composites. Relevant conclusions drawn are presented at the end of each section.

4.1 SMELTING OF ILMENITE IN THE PLASMA REACTOR

In this section the results on smelting of ilmenite are described followed by a discussion and conclusions.

4.1.1 Results

The effect of basicity on the titanium content of alloys is shown in Table 4.1.1. The titanium content increased from 0.72 to 3.05 wt pct as the slag basicity $[(CaO + MgO)/(SiO_2 + Al_2O_3)]$ increased from 0.61 to 1.76. The XRD data (Table 4.1.2) for the alloy A3 shows the presence of Fe_3C, FeTi and TiO phases while in the alloy A5 the phases identified are Fe_3C, α-Fe and TiC.

The effects of excess carbon over the stoichiometric requirement for reduction of ilmenite, addition of flux $(CaO/CaF_2 = 60/40)$ by weight percent of ilmenite in the charge and hydrogen content in argon-hydrogen plasmagen gas

Table 4.1.1

Effect of basicity on titanium content of alloy

Alloy	Basicity	Alloy composition Wt Pct			
No.		Ti	Fe	Si	C
A1	0.61	0.72	93.89	1.11	3.31
A2	0.99	1.83	92.84	1.27	3.09 ⌄
A3	1.19	1.77	92.98	1.18	3.14
A4	1.38	2.52	93.03	1.10	2.37
A5	1.76	3.05	91.30	0.14	4.57

Trace element analysis of alloys by SEM-EDAX (Wt Pct)

Mn 0.28 to 0.46,   Al 0.13 to 0.35,   S 0.038 to 0.047
P 0.002 to 0.007, Ca 0.033 to 0.066, Mg 0.000 to 0.034
and Zr 0.12 to 0.15

Table 4.1.2

XRD analysis of alloys

Alloy No.	Phases identified	Intensity	(hkl) planes
A3	Fe_3C	S	(031), (102), (241), (200), (321)
	FeTi	W	(110), (200)
	TiO	W	hkl plane data not available
A5	Fe_3C	S	(031), (220), (102), (210), (002)
	α- Fe	S	(110)
	TiC	W	(200), (111)
A9	TiC	S	(200), (111), (220)
	Fe_3C	M	(031), (211)
A11	TiC	S	(200), (220)
	α-Fe	M	(110), (200)
	Fe_3C	M	(031), (121), (200), (132)
A16	Fe_3C	S	(031), (211), (201), (121)
	TiC	M	(200), (111), (220)
	Ti_2O_5	M	(110), (134)
A21	TiC	S	(200), (111), (220)
	α-Fe	M	(110), (200)
A23	TiC	S	(200), (111), (220)
	α-Fe	M	(110), (200)

Relative intensity

S = 80 to 100 pct, M = 40 to 79 pct, W = 10 - 39 pct

mixture on the metallisation of titanium are summarised in Table - 4.1.3. ⌐Pct degree of metallisation of Ti = (Wt Pct Ti in alloy) x (Wt of alloy)/(Wt of Ti in the charge)⌐

It may be seen from the Table that there is an improvement in the recovery of titanium in general as the reductant is increased from stoichiometric composition to 50 wt pct excess carbon. The metallisation of titanium increases as the flux content in the charge increases from 2 wt pct (alloys A6 and A7) to 4 wt pct (alloys A8 and A9). The effect of variation in hydrogen content of plasmagen gas mixture can be seen on the basis of the values of the degree of metallisation of Ti in alloys A8 and A9 as compared to those in alloys A10 and A11. There is some decrease in metallisation of titanium as the hydrogen content in the plasmagen gas is increased from 20 to 40 volume percent. From the data presented in Table 4.1.3, it is seen that a maximum of nearly 80 pct titanium metallisation is obtained in alloy A9. It was, however, not possible to tap any of these alloys even after smelting the charge completely. The chemical composition of alloys prepared as per the experimental conditions mentioned in Table 4.1.3 are shown in Table 4.1.4. The titanium content of alloys varies from 13.47 to 30.79 wt pct. It may be noted from the results reported in Table 4.1.4 that the carbon content of alloys prepared with stoichiometric carbon requirement for reduction of ilmenite (alloys A6, A8 and A10) varies between 6.13 to 6.60 wt pct whereas that for alloys prepared with 50 wt pct excess

Table 4.1.3

Effect of excess carbon, flux and hydrogen on the
metallisation of titanium

Alloy No.	Experimental parameters			Melt temp- erature ^{o}C	Pct degree of metallisation	
	Excess carbon	Wt Pct flux	Vol. Pct H_2 in gas mix- ture		Ti	Fe
A6	0	2	20	1660	16.29	30.95
A7	50	2	20	1730	37.20	55.28
A8	0	4	20	1640	23.61	55.21
A9	50	4	20	1770	79.90	60.64
A10	0	4	40	1580	17.59	39.67
A11	50	4	40	1760	65.12	79.18

Table   4.1.4

Chemical composition of alloys indicated in Table 4.1.3

| Alloy | Wt pct | | | |
No.	Ti	Fe	Si	C
A6	15.82	75.37	1.42	6.60
A7	19.32	71.26	0.37	8.24
A8	13.47	78.42	1.04	6.24
A9	30.79	58.27	0.14	9.95
A10	13.97	78.55	0.42	6.13
A11	22.45	68.07	0.29	8.32

Trace element analysis of alloys by SEM-EDAX (Wt Pct)

Mn 0.28 to 0.46,   Al 0.13 to 0.35,   S 0.038 to 0.047
P 0.002 to 0.007,   Ca 0.033 to 0.066, Mg 0.000 to 0.034
and Zr 0.12 to 0.15.

carbon (alloys A7, A9 and A11) varies from 8.24 to 9.95 wt pct. Trace element analysis of these alloys was carried out by energy dispersive X-ray analysis (EDAX) attached to a scanning electron microscope. Some results are presented in Table 4.1.4. After analysing all the alloys over a number of spots the lowest and the highest amounts of individual trace elements are reported as a range. Both TiC and Fe_3C phases are present in alloys A9 and A11 (Table 4.1.2). Alloy A11 contains α-Fe phase.

The data presented in Table 4.1.5 show the effect of excess carbon on titanium content of alloys obtained from experiments carried out in magnesia coated graphite cruci- bles. There is an improvement in the titanium content of alloys as the quantity of carbon is increased to levels which are 100 to 200 wt pct in excess of the stoichiometric requirements. The titanium content of alloys increases from 0.83 to 3.27 wt pct (alloys A12, A14). It is evident from the data presented in the Table that the carbon content of alloys are in the cast iron composition range. This clearly indicates that, it is possible to prepare titanium rich cast irons by plasma smelting of ilmenite.

The data presented in Table 4.1.6 indicate the effect of addition of iron ore or steel scrap to the charge mix on the titanium content of alloys. It is seen that the degree of metallisation of titanium increases with the addition of more steel scrap. A metallisation value as high as 47.32 pct has been obtained in the case of alloy A19.

Table 4.1.5

Effect of excess carbon on titanium content of alloys
produced in magnesia coated graphite crucible

Alloy No.	Wt pct excess carbon	Alloy composition Wt pct				Degree of metallisation of Ti (pct)
		Ti	Fe	Si	C	
A12	100	0.83	94.26	0.76	3.24	0.50
A13	200	2.74	92.67	0.87	2.79	12.69
A14	200	3.27	91.51	0.82	3.48	12.23

Trace element analysis of alloys by SEM-EDAX (Wt Pct)

Mn 0.32 to 0.49,   Al 0.23 to 0.42,   S 0.037 to 0.061
P 0.001 to 0.003, Ca 0.016 to 0.043, Mg 0.087 to 0.109
and Zr 0.12 to 0.17

Table 4.1.6

Effect of iron ore or steel scrap addition on titanium content of alloys produced in magnesia coated graphite crucible

| Alloy No. | Experimental charge | | | Alloy composition Wt pct | | | | Degree of metallisation of Ti (pct) |
	Ilmenite (g)	Wt Pct carbon	Iron ore/BD (g)	Ti	Fe	Si	C	
A15	100	100	200(BD)	0.35	94.65	0.67	3.37	1.01
A16	200	200	100(BD)	8.98	86.18	0.73	3.13	13.71
A17	200	200	160(Fe)	3.37	92.67	0.47	2.55	8.74
A18	200	200	120(Fe)	5.32	91.00	0.43	2.30	6.09
A19	200	200	1000(Fe)	2.87	92.6	0.93	2.62	47.32
A20	200	200	1000(Fe)	3.11	92.18	0.82	2.92	44.09

Trace element analysis of alloys by SEM-EDAX (Wt Pct)

Mn 0.32 to 0.49, Al 0.23 to 0.42, S 0.037 to 0.061, P 0.001 to 0.003,
Ca 0.016 to 0.043, Mg 0.087 to 0.109 and Zr 0.12 to 0.17

BD - Blue dust (Fe_2O_3) or Fe - Steel scrap

Comparing the data for alloys A15 and A16 it is again seen that there is considerable improvement in the degree of metallisation as the percentage of excess carbon is increased from 100 to 200 wt pct. Table 4.1.7 presents some data obtained during preparation of titanium carbide rich Fe-TiC master alloys. The data show the effect of increase in the weight of charge mix on the degree of metallisation of titanium. There is some improvement in metallisation as the weight of ilmenite is doubled. For example, in the case of alloy A21 the degree of metallisation of titanium is 62 pct, whereas it is 73 pct in the alloy A22 where the weight of ilmenite is double the amount used in the preparation of alloy A21. The titanium content of the alloy, however, does not change significantly as it varies only in the range 20.32 to 23.97 wt pct. Addition of MgO as a flux improved the degree of metallisation of titanium in alloy A23 compared to that of alloy A22 which was prepared without any flux. The degree of metallisation of titanium with and without flux are 81.31 pct (alloy A23) and 73.19 pct (alloy A22), respectively.

Table 4.1.7

Effect of change in charge weight on recovery of titanium

Alloy No.	Charge composition			Alloy composition Wt Pct				Pct degree of metallisation	
	Ilmenite (g)	Excess carbon pct	Steel scrap (g)	Ti	Fe	Si	C	Ti	Fe
A21	200	100	120	20.32	69.92	0.45	8.43	62.04	80.17
A22	400	100	240	23.97	66.41	0.43	8.30	73.19	76.62
A23*	400	100	240	24.77	64.73	0.37	9.26	81.31	80.28

Trace element analysis of alloys by SEM-EDAX (Wt Pct)

Mn 0.32 to 0.49, Al 0.23 to 0.42, S 0.037 to 0.061, P 0.001 to 0.003,
Ca 0.016 to 0.043, Mg 0.087 to 0.109 and Zr 0.12 to 0.17.

* The charge contained 20g MgO (Chemical reagent grade)

4.1.2 Discussion

The results of carbothermic reduction of ilmenite carried out in an extended arc plasma reactor have been presented in the preceding section. The experimental data summarised describe the effects of various parameters like slag basicity, amount of reductant, flux and hydrogen content in argon hydrogen plasmagen gas mixture on titanium content of alloys produced and the degree of metallisation of titanium. It should be noted that experiments have been carried out in both coated and uncoated graphite crucibles. Before discussing those experimental results some thermodynamic calculations are presented for a theoretical understanding of the reactions.

Thermodynamic analysis

Carbothermic reduction at high temperature generally involves reaction of metal oxides with carbon to produce carbon monoxide gas, intermediate oxides, metal carbides and metals. The basic reactions are as follows.

$$MO(s) + 2\ C(s) = MC(s)\ +\ CO\ (g) \ldots\ldots(4.1)$$

$$MO(s) +\quad C(s) = M\ (s)\ +\ CO\ (g) \ldots\ldots(4.2)$$

$$MO(s) +\ MC(s) = 2M(s)\ +\ CO\ (g) \ldots\ldots(4.3)$$
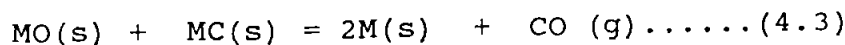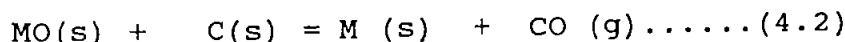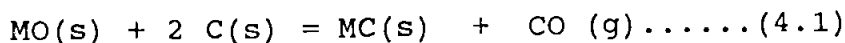
The minimum temperature for operation of the reactor can be determined from the free energy of formation, which is a measure of the tendency for a reaction to occur. In the case

of carbothermic reduction of ilmenite, the standard free energy change for various reactions have been computed and the temperature at which ΔG^{O}_{T} becomes zero has been calculated. Further values of ΔG^{O}_{2000} at 2000 K have also been calculated. The thermodynamic data used are from the literature [Metallurgical thermochemistry by O. Kubaschewski and E. LL. Evans, Pergamon press Oxford, 1965] [9]. The data presented are in calories and the conversion to kJ is obtained by multiplying calories by 4.186×10^{-3}.

The values of the standard free energy change for formation of titanium suboxides are as follows:

$TiO(s) = Ti(s) + 1/2\ O_2(g)$ ..... (4.4)
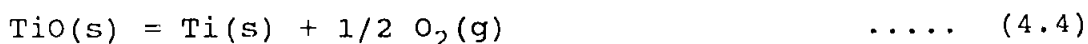
$\Delta G^{O}_{T} = 122,300 - 21.3\ T\ Cal, \quad 600 - 2000\ K$

$Ti_2O_3(s) = 2\ TiO(s) + 1/2\ O_2(g)$ ..... (4.5)
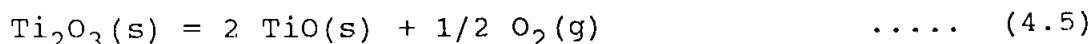
$\Delta G^{O}_{T} = 114,500 - 19.05\ T\ Cal, \quad 298 - 2000\ K$

$2Ti_3O_5(s) = 3Ti_2O_3(s) + 1/2O_2(g)$ ..... (4.6)
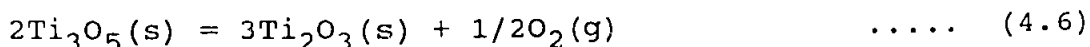
$\Delta G^{O}_{T} = 88,500 - 19.7\ T\ Cal, \quad 700 - 2000\ K$

$3TiO_2(s) = Ti_3O_5(s) + 1/2\ O_2(g)$ ..... (4.7)
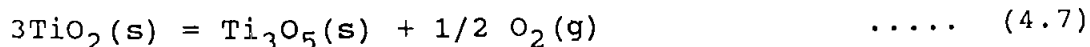
$\Delta G^{O}_{T} = 73,000 - 23.0\ T\ Cal, \quad 298 - 2123\ K$

By utilising these data the standard free energy change for formation of TiO_2 can be calculated. The reaction is

$TiO_2(s) = Ti(s) + O_2(g)$ ..... (4.8)

Combining Eq.[4.4 - 4.7] one obtains;

$\Delta G^{O}_{T} = 218,458.31 - 41.775\ T\ Cal.$

The standard free energy change for formation of carbides is obtained thus;

$$TiO_2(s) + 3C(s) = TiC(s) + 2CO(g) \qquad \ldots\ldots \quad (4.9)$$
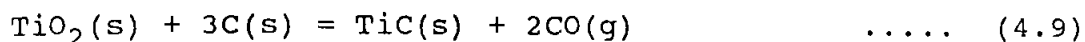
$$\Delta G^O_T = 120,458.3 - 81.515 \ T \ Cal$$

Hence, $\Delta G^O_T = 0$ at $T = 1496 \ K$

$$\Delta G^O_{2000} = - 42.57 \ k \ Cal$$

The standard free energy change for formation of titanium carbide becomes zero at 1496 K which is an equilibrium temperature for the reaction. Thus the formation of TiC is feasible over 1496 K only. At 2000 K there is appreciable driving force.

The standard free energy change values for reduction of titanium oxides to metallic titanium are obtained as follows:

$$TiO_2(s) + 2C(s) = Ti(s) + 2CO(g) \qquad \ldots\ldots \quad (4.10)$$

$$\Delta G^O_T = 165,058.73 - 83.675 \ T \ Cal$$

Hence, $\Delta G^O_T = 0$ at $T = 1973 \ K$

$$\Delta G^O_{2000} = - 2.29 \ k \ Cal$$

$$Ti_3O_5(s) + 5C(s) = 3Ti(s) + 5CO(g) \qquad \ldots\ldots \quad (4.11)$$
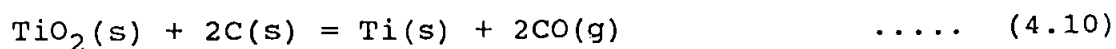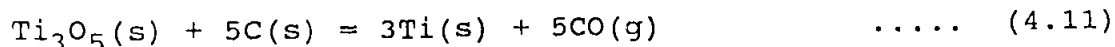
$$\Delta G^O_T = 448,875 - 207.075 \ T \ Cal$$

Hence, $\Delta G^O_T = 0$ at $T = 2168 \ K$

$$\Delta G^O_{2000} = 34.72 \ k \ Cal$$

$$Ti_2O_3(s) + 3C(s) = 2 \ Ti(s) + 3CO(g) \qquad \ldots\ldots \quad (4.12)$$
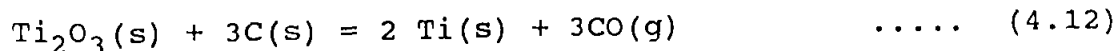
$$\Delta G^O_T = 278,650 - 124.5 \ T \ Cal$$

Hence, $\Delta G^O_T = 0$ at T = 2238 K

$\Delta G^O_{2000} = 29.65$ k Cal

$$TiO(s) + C(s) = Ti(s) + CO(g) \qquad \cdots \cdots \quad (4.13)$$
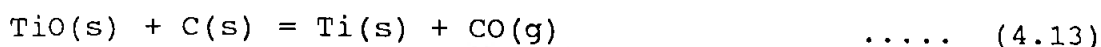
$\Delta G^O_T = 95,600 - 42.25$ T Cal

Hence, $\Delta G^O_T = 0$ at T = 2263 K

$\Delta G^O_{2000} = 11.1$ k Cal

Eq.[4.10] indicates that the standard free energy change for reduction of titanium dioxide to metallic titanium requires temperatures above 1973 K. The titanium suboxides can be reduced to metallic titanium (Eq.[4.11] to Eq.[4.13]) above a temperature of 2263 K. Further, it may be seen from Eq.[4.4] to Eq.[4.7] that the thermal decomposition of titanium oxides takes place only well above 4000 K, a temperature which is rarely encountered in any metallurgical reactor. Even at temperatures where the thermodynamic feasibility for reduction of titanium dioxide to metallic titanium is favourable, the free energy change for carbide formation Eq.[4.9], becomes more negative.

Thus, $\Delta G^O_{2000} = -2.29$ k Cal for Eq.[4.10] compared to $\Delta G^O_{2000} = -42.57$ k Cal for Eq.[4.9], indicates that the formation of titanium carbide is favoured over metallic titanium when TiO_2 is reduced by carbon.

The standard free energy change for carbide-oxide reaction is as follows:

$$TiO_2(s) + 2TiC(s) = 3Ti(s) + 2CO(g) \qquad \cdots \cdots \quad (4.14)$$
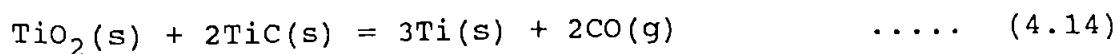
$\Delta G^o{}_T = 254,258.3 - 89.995 \text{ T Cal}$

Hence, $\Delta G^o{}_T = 0$ at T = 2825 K

The titanium carbide-oxide reaction is feasible above 2825 K which is more than the temperature required for titanium carbide formation as well as that for reduction of titanium oxides to metallic titanium. One may examine the question, if it is possible to lower the carbon content of iron-TiC composite and control the titanium carbide content, using the reaction between titanium carbide and iron oxide. The thermodynamic data for this reaction are as follows:
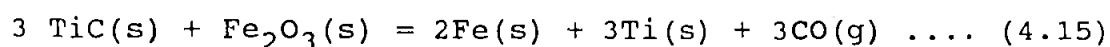
$3 \text{ TiC(s)} + \text{Fe}_2\text{O}_3(s) = 2\text{Fe(s)} + 3\text{Ti(s)} + 3\text{CO(g)} \dots (4.15)$

$\Delta G^o{}_T = 234,560 - 125.13 \text{ T Cal}$

Hence, $\Delta G^o{}_T = 0$ at T = 1874.5 K

$\quad\quad \Delta G^o{}_{2000} = - 15.7 \text{ k Cal}$

$2 \text{ TiC(s)} + \text{Fe}_2\text{O}_3(s) + \text{C(s)} = 2 \text{ FeTi(s)} + 3\text{CO(g)} \dots (4.16)$

$\Delta G^o{}_T = 189,960 - 121.96 \text{ T Cal}$

Hence, $\Delta G^o{}_T = 0$ at T = 1558 K

$\quad\quad \Delta G^o{}_{2000} = - 53.96 \text{ k Cal}$

$\text{TiC(s)} + \text{Fe}_2\text{O}_3(s) = 2\text{Fe(s)} + \text{TiO}_2(s) + \text{CO(g)} \dots (4.17)$
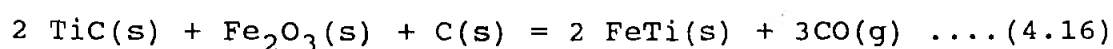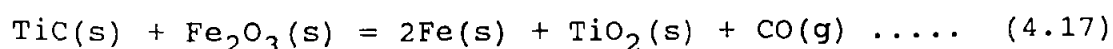
$\Delta G^o{}_T = -19,698.33 - 35.135 \text{ T Cal}$

Hence, $\Delta G^o{}_T = 0$ at well below room temperature

$\quad\quad \Delta G^o{}_{2000} = - 89.97 \text{ k Cal}$

Thus, it may be seen from reactions represented by Eq.[4.15] to Eq.[4.17] that it is not possible to convert titanium carbide to metallic titanium through reactions with iron

oxide as the free energy change for the formation of titanium dioxide is much more negative. For example at 2000 K, free energy change for the formation of titanium dioxide is - 89.97 k Cal (Eq.[4.17]) while for reactions expressed by Eq.[4.15] and Eq.[4.16] it is -15.7 and -53.96 k Cal respectively. This indicates that formation of titanium dioxide is thermodynamically feasible.

The preceding discussion leads to the conclusion that carbothermic reduction of ilmenite results in the formation of titanium carbide. The titanium carbide content in the composite cannot be controlled by carrying out oxide-carbide reactions. The carbon content of Fe-Ti-C alloys, however, can be controlled by the addition of silicon [93]. The addition of 20 to 25 wt pct silicon in the alloy brings down carbon content to about 1 wt pct through formation of titanium silicide.

The other possible methods for reducing carbon content would include dilution of the carbothermic reduction product by addition of steel scraps and reduction of ilmenite along with iron ore.

Some thermodynamic calculations based on ilmenite reduction are given in Appendix-I and the trends of results are same as just discussed. The conclusions therefore, are similar.

Effect of basicity on reduction of ilmenite

The experiments to study the effect of slag basicity on the titanium content of alloys show that as the basicity $[(CaO + MgO)/(SiO_2 + Al_2O_3)]$ increases the titanium content of the alloy also increases (Table 4.1.1). The reduction of titanium dioxide proceeds in stages and lower oxides of titanium are formed first [93]. Two stable suboxides of titanium are Ti_2O_3 and TiO. These are basic in nature while titanium dioxide is amphoteric. Therefore, at lower basicity values there is a tendency for the lower oxides to form compounds with silica and alumina thus reducing the activity of titanium oxides in the bath. By increasing the basicity with the addition of a strong base such as CaO it is possible to replace titanium oxide in the compound by CaO and in turn increase the activity of titanium oxides. In the present investigation on smelting of ilmenite in the plasma reactor, it is found that alloy A3 prepared with a slag basicity of 1.19 shows presence of TiO phase (Table 4.1.2). This result corroborates the fact that reduction of titanium dioxide proceeds in stages forming lower oxides at first. Results of thermodynamic calculations on the formation of lower oxides of titanium through reduction of titanium dioxide by carbon are as follows.
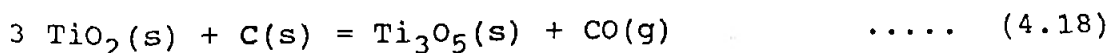
$$3\ TiO_2(s) + C(s) = Ti_3O_5(s) + CO(g) \qquad \cdots\cdots \quad (4.18)$$

$$\Delta G^o_T = 46,300 - 43.95\ T\ Cal$$

Hence, $\Delta G^O_T = 0$ at $T = 1053$ K

$\Delta G^O_{2000} = -41.6$ k Cal

$2Ti_3O_5(s) + C(s) = 3Ti_2O_3(s) + CO(g)$ ..... (4.19)

$\Delta G^O_T = 61,800 - 40.65\ T$ Cal

Hence, $\Delta G^O_T = 0$ at $T = 2185$ K

$\Delta G^O_{2000} = -19.5$ k Cal

$Ti_2O_3(s) + C(s) = 2TiO(s) + CO(g)$ ..... (4.20)
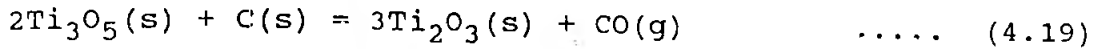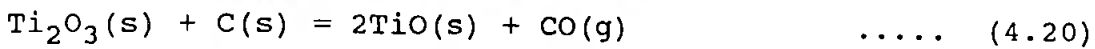
$\Delta G^O_T = 87,400 - 40\ T$ Cal

Hence, $\Delta G^O_T = 0$ at $T = 2185$ K

$\Delta G^O_{2000} = 7.4$ k Cal

From these calculations it is seen that free energy change for formation of titanium suboxide (Eq.[4.18]) which is -41.6 k Cal at 2000 K, is very close to that for titanium carbide formation (Eq.[4.19]) which is - 42.57 k Cal at 2000 K. This indicates that titanium suboxides can form a mixture containing titanium carbide. Further, the formation of a lower suboxide like TiO requires higher bath temperature and such temperatures are available below the plasma arc impingement zone.

The XRD of alloy prepared under a slag cover of basicity 1.76 (alloy A5) indicates absence of titanium suboxide phases (Table 4.1.2). This indicates the formation of compounds with silica and/or alumina by calcia replacing titanium suboxides. Thus the activity of titanium oxide is improved.

It should be noted that there is an increase in titanium content of alloy from 0.72 wt pct Ti at 0.61 basicity to 3.05 wt pct Ti at 1.76 basicity. This can be explained on the basis of increase in activity of titanium oxide due to increase in slag basicity. In this respect, the process of carbothermic reduction of ilmenite is analogous to alumino-thermic reduction of ilmenite where addition of 20 pct CaO by weight of aluminium improves the recovery of titanium in the alloy.

Effect of excess carbon and flux in the charge mix and hydrogen in plasmagen gas mixture on metallisation of titanium

The effects of excess carbon (over the stoichiometric requirement), addition of flux (CaO : CaF_2 = 60/40) in the charge mix and hydrogen content in argon-hydrogen plasmagen gas mixture on the degree of metallisation of titanium are summarised by the data presented in Table 4.1.3. It is readily seen that the degree of metallisation of titanium increases two to three folds when the amount of reductant in the charge mix is increased by 50 wt pct. The thermodynamic analysis presented in the preceding section has shown that while titanium carbide forms at about 1500 K, the formation of metallic titanium requires temperatures over 1993 K. Further, it has also been shown that the experimental conditions are more favourable for the formation of

titanium carbide than for the formation of metallic titanium. The XRD data of alloys A9 and A11 (Table 4.1.2) indicate the presence of TiC. Thus the presence of excess carbon in the charge mix facilitates the formation of titanium carbide. Dissolution of TiC in metallic iron drives the reaction [Eq.4.9] in the forward direction. The results are from a set of experiments where 220 g of steel scrap were mixed with reduction charge.

Addition of more flux to the charge mix improves the degree of metallisation of titanium. For example, the extent of metallisation increased from 16.29 pct to 23.61 pct on increasing the quantity of flux addition to the charge mix from 2 wt pct. (alloy A6) to 4 wt pct (alloy A8). Stoichiometric amount of reductant was used in both the cases. A similar trend was observed when the alloys were prepared with 50 wt pct excess carbon. It has been shown earlier that increasing slag basicity improves the titanium recovery in alloys by enhancing the activity of titanium oxides. In this case also it is expected to follow the same trend as the flux is strongly basic.

Experiments on the effect of variation in hydrogen content of plasmagen gas mixture show a minor change in the degree of metallisation of titanium. The metallisation of titanium decreased from 23.61 pct (alloy A8) to 17.59 pct (alloy A10) as hydrogen content increased from 20 to 40 vol. pct. Similar trend is noticeable in the results obtained

with 50 wt pct excess carbon when hydrogen content in the plasmagen gas mixture is increased. The minor role of hydrogen in reduction of titanium dioxide is readily understood if one examines the thermodynamic data for the hydrogen reduction reaction.

$$TiO_2(s) + 2 H_2(g) = Ti(s) + 2H_2O(g) \quad \ldots\ldots \quad (4.21)$$
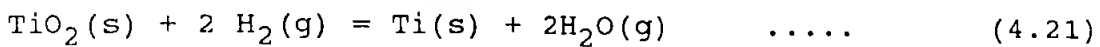
$$\Delta G^O_T = 119,250 - 224.5 \ T \ Cal$$

Hence, $\Delta G^O_T = 0$ at $T = 5315 \ K$

The reaction is feasible only above 5315 K, a temperature rarely attained in a metallurgical reactor. Therefore, one may conclude that hydrogen does not have a significant role in the reduction of titanium oxide.

Addition of hydrogen to a plasmagen gas (in this case argon) aims at increasing the enthalpy content of plasma. Fig. 4.1.1 shows the variation of enthalpy content of gases as a function of temperature [94]. It is seen that the heat content of diatomic gases like hydrogen and nitrogen are more compared to that of monoatomic gases like argon and helium. In the case of diatomic gases like hydrogen, dissociation of hydrogen molecule has to take place first. The dissociation energy of hydrogen molecule is 4.48 eV. [95]. The ionization energy of hydrogen atom is comparable to that of argon atom (15.7 eV). Thus, with the addition of hydrogen to argon gas the enthalpy content of the gas increases.
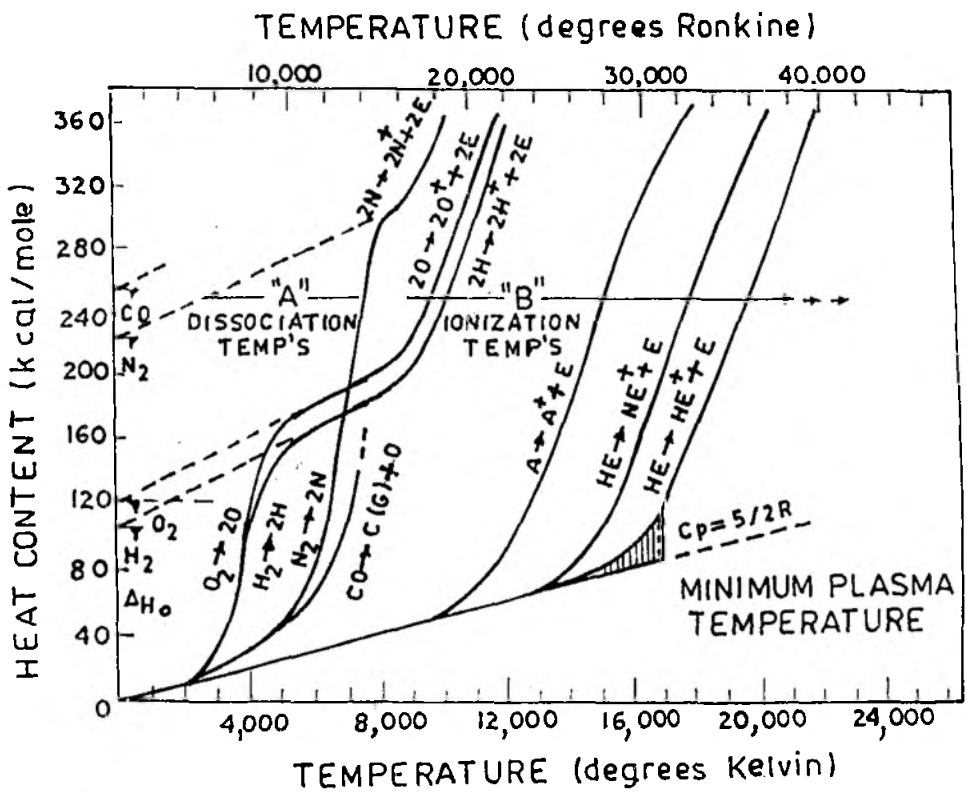
Fig.4.1.1 Heat content of monatomic and diatomic gases as a function of temperature at 1 atm. (Ref.94)

It may be noted from the data given in Table 4.1.3 that the bath temperature practically remains the same. It should be noted that the temperature of the bath is not a measure of the enthalpy content of plasma gas. Hydrogen increases the enthalpy of plasma gas but does not have much role in the reduction of titanium dioxide. It is, however, not clear why there is some decrease in the degree of metallisation of titanium in general when there is hydrogen.

One of the important aspects that needs clarification is the relative importance of the variation in the reductant used. All these experiments were carried out in uncoated graphite crucibles. It is expected that carbon from graphite crucible also participated in the chemical reaction (Eq.[4.9]). It has been already explained that reduction of ilmenite leads to the formation of TiC in ferrous matrix when carbon is used as a reductant. This has been confirmed by XRD analysis of a few samples (Table 4.1.2). Also from the data in Table 4.1.4, it may be noted that alloys prepared with stoichiometric carbon (alloys A6, A8 and A10) show a variation of carbon content in the range of 6.13 to 6.60 wt pct. On the otherhand, alloys prepared with 50 wt pct excess carbon (alloys A7, A9 and A11) show a variation of carbon content from 8.24 to 9.95 wt pct. This clearly indicates that even in case of the uncoated graphite crucible, the amount of excess carbon present in the initial charge has an influence on carbon pickup in the alloy. In general, there is an improvement in recovery of titanium as

the carbon content in the alloy increases. This clearly indicates that presence of excess carbon in the initial charge mix improves the reduction of TiO_2 and formation of TiC. The contribution of carbon from the crucible as a reductant becomes clearer when results of plasma smelting of ilmenite in a magnesia coated crucible are considered.

The high carbon alloys could not be tapped. This may be due to the presence of discrete TiC particles suspended in the melt making it very viscous.

Effect of excess carbon on reduction of ilmenite in a magnesia coated graphite crucible

It may be noted from the data presented in Table 4.1.5 that the overall recovery of titanium as well as the titanium content in the alloys are considerably lower in spite of having 200 wt pct excess carbon in the initial charge mix. The application of magnesia coating in graphite crucible eliminates reaction of the crucible wall and, accordingly, the recovery values are low. Thus, it is apparent that the contribution of the carbon from graphite crucible is very significant (see Table 4.1.4 and Table 4.1.5). It is likely that a significant amount of carbon is lost through reaction with the oxygen in the ambient atmosphere. The arc crater area does not cover the total surface area of the charge in the crucible. Thus, there is a possibility of oxygen circulation in the atmosphere above the bath which

presumably leads to loss of carbon from the charge mix through aerial oxidation.

The carbon content of alloys prepared in magnesia coated graphite crucible shows a variation in the range of 2.79 to 3.48 wt pct which is similar to that of cast irons. Thus, these experiments indicated a possibility of preparing titanium rich cast irons directly by smelting of ilmenite. In this case the titanium content of alloys has to be kept low so as to obtain a clear slag/metal separation and flowability. However, when a titanium carbide rich Fe-TiC master alloy is required then it is preferable to carry out smelting of ilmenite in an uncoated graphite crucible. The importance of such high carbon , high titanium alloys in preparation of titanium carbide reinforced steel composites is explained in the subsequent Chapters.

Preparation of titanium carbide reinforced cast irons

An attempt was made next to prepare cast irons with different titanium contents by smelting of ilmenite in the plasma reactor using magnesia coated graphite crucible. In order to produce such cast irons, iron ore (blue dust, 97.6 wt pct Fe_2O_3) or steel scrap was added to the initial charge mix. The titanium content of alloys were controlled by varying the amounts of excess carbon, blue dust and steel scrap addition.

It is obvious from the data presented in Table 4.1.6 that enhanced dilution with iron ore/steel scrap reduces the titanium content of the alloy. However, recovery of titanium increased from 6 to 47 pct as the addition of steel scrap varied from 120 g to 1000 g. This indicates that the presence of iron in the initial charge mix promotes titanium recovery by dissolving titanium carbide as soon as it is formed during smelting of ilmenite. The titanium content of alloys varied from 0.3 to 9 wt pct in these alloys. The carbon content of alloys varied within cast iron range and they could be cast into metal and sand moulds.

Effect of change in weight of initial charge mix on recovery of titanium

To prepare titanium carbide rich Fe-TiC master alloys for subsequent development of steel base titanium carbide composite, experiments were carried out to improve the recovery of titanium in alloys by changing the initial weight of the charge mix. Table 4.1.7 presents some data which shows that by doubling the ilmenite content in the charge mix it was possible to improve recovery from 62 pct (alloy A21) to 73 pct (alloy A22). Addition of flux to the charge further improved the degree of metallisation of titanium to 81 pct (alloy A23). The titanium content of these alloys did not vary significantly and was in the range of 20.32 to 24.77 wt pct.

Production of ferro-titanium by carbothermic reduction of ilmenite in a plasma reactor

The present investigations on reduction of ilmenite by carbon in an extended arc plasma reactor does not seek to produce ferro-titanium. However, the experimental data bring out the limitations in preparation of ferro-titanium by carbothermic reduction of ilmenite in a plasma reactor.

The requirement of low carbon ferro-titanium used in the manufacture of stainless steel and other low carbon alloy steels is presently met by aluminothermic reduction of ilmenite. The carbothermic reduction of ilmenite results in the formation of high titanium, high carbon nonflowable alloy. To make this alloy flowable, carbon content of the alloy has to be lowered. In theory this is possible through oxide-carbide reaction (Eq.[4.14]). The thermodynamic calculations show that the reaction is feasible at 2825 K. In a plasma reactor one can achieve such temperatures. As a matter of fact, the microstructure of quenched reaction product of ilmenite smelting (Fig. 4.1.2) does show dendritic network of TiC, indicating that melting point of TiC (3250°C) is attained at least below the plasma arc root. However, it is difficult to increase the overall bath temperature sufficiently (>2825 K) while preparing the ferro-alloy without considerable iron loss, as the vapour pressure of iron is one atmosphere at 3008 K [96]. Thermodynamic

Fig.4.1.2   SEM photograph of TiC rich Fe-TiC
            master alloy A21 showing dendritic
            TiC.

calculations for carrying out iron oxide/TiC reaction (according to Eq.[4.15] to Eq.[4.17]) show that free energy change for formation for TiO_2 is much more negative than that for the formation of metallic titanium.

Thus, it may be concluded that, it is not possible to carry out carbothermic reduction of ilmenite to produce low carbon ferro-titanium.

4.1.3 Conclusions

The following conclusions can be drawn based on the preceding results and discussions:

a)   It is possible to prepare titanium carbide rich Fe-TiC master alloys and titanium containing cast irons by carbothermic reduction of ilmenite in a plasma reactor.

b)   High titanium containing alloys can be prepared by carrying out smelting in uncoated graphite crucibles where carbon supply is abundant.

c)   Addition of lime to the charge mix and corresponding increase in the basicity improves the degree of metallisation of titanium.

d)   Carbon content in the master alloy increases simultaneously with the increase in titanium recovery.

e)   Addition of iron ore or steel scrap to initial charge mix improves degree of metallisation of titanium.

f) Carbon pick up in the alloy can be controlled by carrying out the smelting in a magnesia or zircon coated graphite crucible which eliminates carbon pick up from the crucible wall.

g) Cast iron melts containing 10 wt pct Ti or less possess adequate fluidity to permit casting in sand or chill mould.

4.2 TiC REINFORCED CAST IRON COMPOSITES

In this section the results on TiC reinforced cast iron composites are presented. The results are then analysed and relevant conclusions are drawn.

4.2.1 Results

Titanium carbide reinforced cast iron composites were produced in a single stage by smelting in a plasma reactor ilmenite ore with large quantity of steel scrap. Smelting was carried out in either magnesia and zircon coated graphite crucibles. Molten metal from the reactor was tapped to fill a metal or sand mould directly. Cast iron composites of 15 mm square x 160 mm long chill cast rods or 10 mm diameter x 250 mm long sand cast rods were prepared.

The molten metal lacked fluidity when smelting of ilmenite ore was carried out without sufficient quantity of steel scrap in the plasma reactor. In such cases, the molten metal was allowed to freeze in the reactor hearth itself. This happened particularly when titanium content and, consequently, titanium carbide content was high. Various investigations have been carried out to characterise the cast iron composites and they are as follows:

a)   Chemical analysis

b)   Microstructural features of as cast and heat treated

      composites

c)   SEM and EDAX analysis

d)   X-ray diffraction analysis

e)   Image analysis to determine the carbide particle size
     distribution and graphite volume percent in composites

The details of the characterisation studies are given below. The microstructural aspects and SEM-EDAX analysis of TiC rich Fe-TiC master alloys are also presented. The details of chemical analysis and x-ray diffraction studies on TiC rich Fe-TiC master alloys have been presented in the previous section(4.1.1).

Chemical analysis

The chemical analysis of TiC reinforced cast iron composites prepared in magnesia coated graphite crucible is presented in Table 4.2.1. The Table shows that it has been possible to prepare TiC reinforced cast iron composites with 1.48 to 4.17 wt pct Ti. The silicon content of the composites which varies between 0.35 to 0.63 wt pct is quite low compared to that in the usual grades of gray cast irons. The other important feature of these composites is the presence of magnesium from 0.067 to 0.109 wt pct.

The chemical analysis of TiC reinforced cast iron composites produced in zircon coated graphite crucible is presented in Table 4.2.2. It may be seen from the Table that composites containing 2.86 to 10.86 wt pct Ti have been prepared. Here, again silicon content of composites varies between 0.20 to 0.23 pct only. The zirconium content of the

Table 4.2.1

Chemical analysis of TiC reinforced cast iron composites

(Prepared in magnesia coated graphite crucible)

| Composite | Wt Pct | | | |
No.	Ti	Fe	Si	C
B1	1.48	94.42	0.37	2.78
B2	1.84	91.67	0.61	4.90
B3	1.98	93.25	0.35	3.52
B4	2.27	92.74	0.36	3.65
B5	3.11	92.41	0.39	3.12
B6	3.61	91.34	0.63	3.43
B7	4.17	90.59	0.46	3.86

Trace element analysis of composites by SEM-EDAX (wt pct)

Mn 0.32 to 0.49,   Al 0.23 to 0.42,   S 0.037 to 0.061
P 0.001 to 0.003,   Ca 0.016 to 0.043,   Mg 0.067 to 0.109
and Zr 0.12 to 0.17

Table 4.2.2

Chemical analysis of TiC reinforced cast iron composites
(Prepared in zircon coated graphite crucible)

Composite	Wt Pct			
No.	Ti	Fe	Si	C
B8	2.86	92.31	0.22	3.49
B9	3.49	91.38	0.23	3.80
B10	5.62	88.25	0.20	4.78
B11	6.80	88.26	0.21	2.60
B12	10.86	82.08	0.22	5.72

Trace element analysis of composites by SEM-EDAX (wt pct)

Ca 0.030 to 0.088,   Mg 0.00 to 0.002,   Al 0.20 to 1.98,
S 0.007 to 0.038,   P 0.001 to 0.028,   Mn 0.692 to 1.317
and Zr 0.178 to 0.521

composites varies between 0.178 to 0.521 wt pct while magnesium content was low.

Microstructural features of as cast and heat treated composite specimens.

The microstructural details of the as cast as well as heat treated TiC reinforced cast iron composites have been presented in Table 4.2.3.

Salient features in the microstructures of cast composites

It may be seen from the Table 4.2.3 that the chill cast composites prepared in magnesia coated graphite crucibles show a typical white cast iron structure with dendritic transformed austenite (pearlite) and eutectic carbide. Tiny TiC particles are seen in both transformed austenite and eutectic carbide, for example, in composites B1 and B5 (Fig. 4.2.1 and Fig. 4.2.3, respectively). As the Ti content in the composite increases (3.61 wt pct Ti), the chill cast composite B6 shows both TiC dendrites and discrete particles. On the contrary the sand cast composite B4 shows presence of graphite in transformed austenite (pearlite) (Fig. 4.2.2(a to d)) in spite of the low silicon content in the alloy. TiC particles are distributed throughout the matrix even in the sand cast samples. TiC dendrites are prominently visible only in the relatively high titanium composites irrespective of the type of crucible coating used.

Table 4.2.3

Microstructural details of TiC reinforced
cast iron composites.

Composite No. (1)	History of the specimen (2)	Microstructural details (3)
Composites prepared in MgO coated crucibles		
B1	Chill cast	Dendrites of transformed austenite (pearlite) and continuous mass of eutectic carbide. Micro hardness of pearlite varied between 468 to 503 VPN (Fig. 4.2.1).
	Soaked at 950°C for 4h and normalised	Uniformly distributed titanium carbide and compacted graph ite particles. Ferrite - pearlite matrix. Pearlitic carbide is fully granular.
B2		Dendrites of transformed austenite (pearlite) and continuous mass of eutectic carbide.
	Soaked at 950°C for 4h, normalised	Graphite rosettes in pearlite matrix. TiC particles are distributed in the matrix. Both coarse and fine TiC particles are seen.
B3	Chill cast	Dendrites of transformed austenite (pearlite) and continuous mass of eutectic carbide.
	Soaked at 950° for 4h, normalised	Matrix is pearlitic. Various types of graphite particles such as rosettes, exploded nodules and of compacted form are present in the matrix. TiC carbide particles distributed throughout the matrix. Some of them are cuboidal and others exhibit dendritic structure.

(1)	(2)	(3)
B4	Sand cast	Compacted and other degenerate forms of graphite present in transformed austenite (pearlite) matrix. Patches of ferrite is also visible around graphite. TiC particles are distributed throughout the matrix. The morphology of carbide and graphite particles are clearly revealed on SEM examination of the samples after deep etching (Fig. 4.2.2 (a-d)).
	Soaked at 950° for 4h, normalised	Rosettes and other forms of graphite in pearlite matrix. TiC particles are embedded in the matrix. Dendritic as well as cuboidal TiC are visible. The TiC particles are more or less uniformly distributed.
B5	Chill cast	White cast iron structure. Transformed austenite (pearlite) + interdendritic plate like eutectic carbide. Fine TiC particles are present within pearlite (Fig. 4.2.3).
	Soaked at 950°C 4h, normalised	Uniformly distributed TiC particles in pearlite matrix. Graphite is mostly in flake form.
B6	Chill cast	Dendritic network of transformed austenite (pearlite) and eutectic carbide. Dendrites of TiC are also seen along with discrete TiC particles. SEM examination of the sample after deep etching shows the distribution of the TiC particles in the chilled matrix (Fig. 4.2.4).

(1)	(2)	(3)
B6	Soaked at 950° for 4h, normalised	Pearlite matrix with numerous tempered carbon rosettes. TiC particles are distributed throughout the matrix. The microhardness of TiC, eutectic carbide and pearlite varies form 3256 to 3386, 1232 to 1258 and 546 to 562 VPN respectively.
B7	Sand cast	Dendritic TiC and discrete TiC particles present in transformed austenite (pearlite) matrix. Graphite colonies are also seen.
	Soaked at	Ferrite pearlite matrix. Rosettes and flake graphite are present. TiC particles are dispersed throughout the matrix. The carbide particles are smaller in size compared to those of composite B4.

Composites prepared in zircon coated graphite crucibles

B10	Chill cast	A fine eutectic structure showing transformed austenite (pearlite) and eutectic carbide. Graphite particles of various degenerate forms are also visible. TiC carbide particles can be distinguished only at 1000 x magnification.
	Soaked at 1000°C for 6h, normalised	Uniform distribution of TiC particles in a granular pearlite matrix. Streaks of graphite flakes are also seen (Fig. 4.2.5).
B12	Chill cast	Fine eutectic structure showing transformed austenite (pearlite) and eutectic carbide. Some degenerate graphite particles and coarse long streaks of proeutectic carbides are also seen.

(1)	(2)	(3)
B12	Soaked at 1000°C for 6h, normalised	Uniform distribution of TiC in pearlite matrix. Numerous graphite rosettes of various sizes are present. Interdendritic massive carbide particles are also seen (Fig. 4.2.6).
B13	Sand cast	Eutectic white cast iron structure (Fig. 4.2.7).
	Soaked at 950°C for 4h and normalised	Partial graphitisation occured
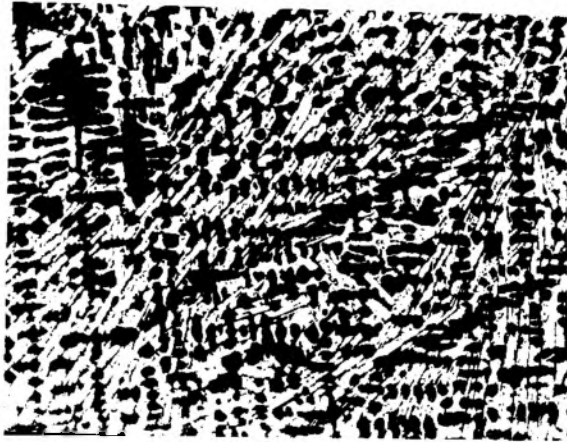
Fig.4.2.1   TiC reinforced cast iron composite
            B1 (chill cast). A typical white
            iron structure, 200 x

Fig. 4.2.2 (a)

Fig. 4.2.2 (b)

Fig. 4.2.2 (c)
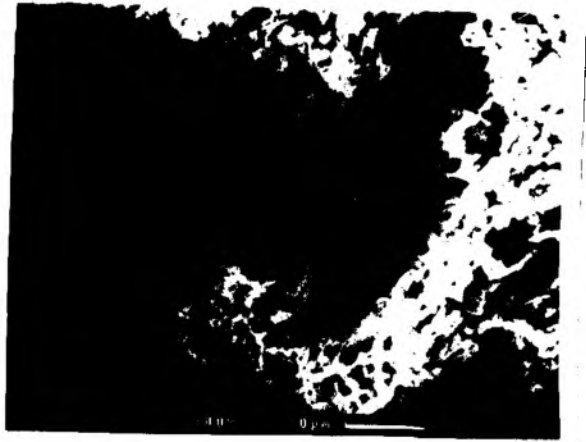
(d)

Fig.4.2.2   SEM photographs of the cast iron
  (a-d)   composite B4 (Sand cast) after
            deep etching.
            a) As cast,
            b-d) After α   ferritising
            anneal at 700°C showing graphite
            and carbide morphology.
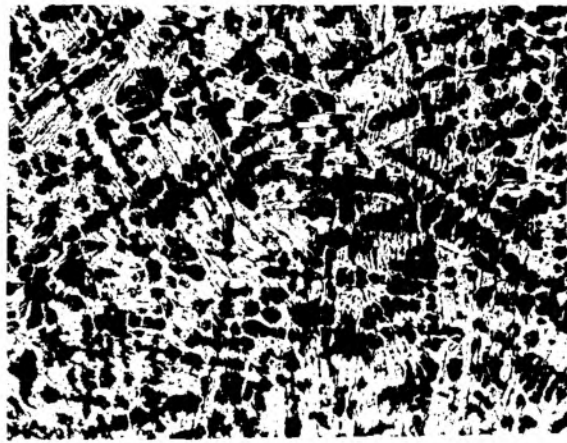
Fig.4.2.3   Cast iron composite B5 (As cast),
            200 X.
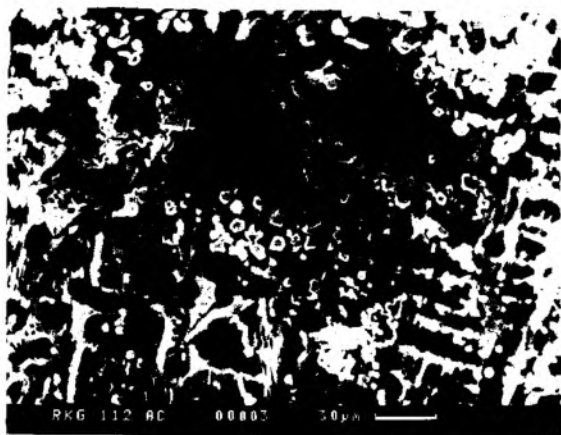
Fig.4.2.4   SEM photograph of the cast iron
             composite B6 (As cast) after deep
             etching showing distribution of
             TiC particles and dendritic net-
             work of transformed austenite
             (pearlite).
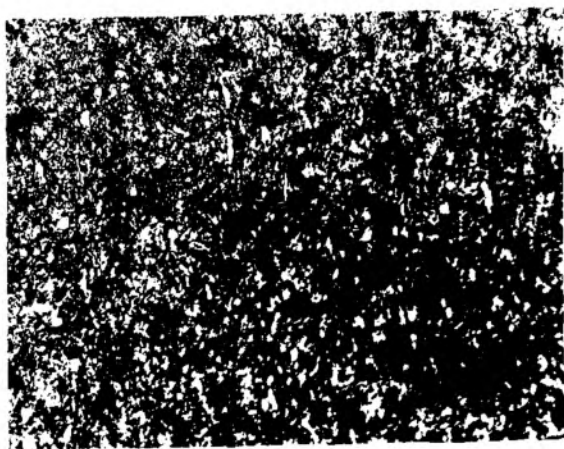
Fig.4.2.5 Cast iron composite B10 normalised
          at 1000°C after soaking for 6h.
          Uniform distribution of TiC and
          granular pearlite, 200 X.
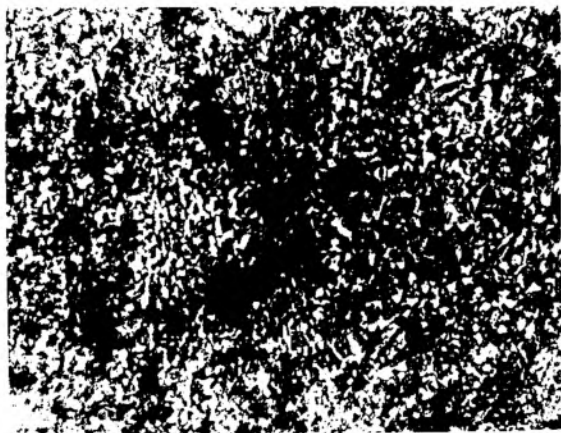
Fig.4.2.6 Cast iron composite B12 normalised
at 1000°C after soaking for 6h.
Uniform distribution of TiC and
graphite particles of various con-
figurations, 200 X

Fig.4.2.7 Cast iron composite B13 (As cast).
Eutectic white cast iron structure,
100 X.

Salient features in the microstructures of heat treated composites.

TiC reinforced cast iron composites prepared in magnesia coated graphite crucibles were normalised after homogenising at 950°C for 4 hours. The eutectic carbide in the chill cast composites suffered graphitisation during heat treatment, in spite of the low silicon content in the composites. Another conspicuous feature was the granular morphology of pearlitic carbide.

The composites prepared in zircon painted graphite crucibles required higher graphitisation temperature (1000°C) and a longer period of holding (6 hours) at this temperature compared to those prepared in magnesia coated crucibles. The photomicrograph of the heat treated composite, B12 is an evidence of graphitisation of the chill cast samples (Fig. 4.2.6). The distribution of fine TiC particles in the pearlite matrix is found to be nearly uniform.

SEM and EDAX analysis

The SEM photographs of a TiC rich Fe-TiC master alloy A24 which contained 35.49 wt pct Ti, 53.08 wt pct Fe, 0.25 wt pct Si, 0.36 wt pct Al, 1.2 wt pct Zr and 8.82 wt pct C are shown in Fig. 4.2.8(a&b). The photomicrographs reveal dendritic TiC growth. The titanium x-ray map of the same area as that in Fig. 4.2.8(b) is shown in Fig. 4.2.9 which confirms that the dendritic areas are rich in Ti.
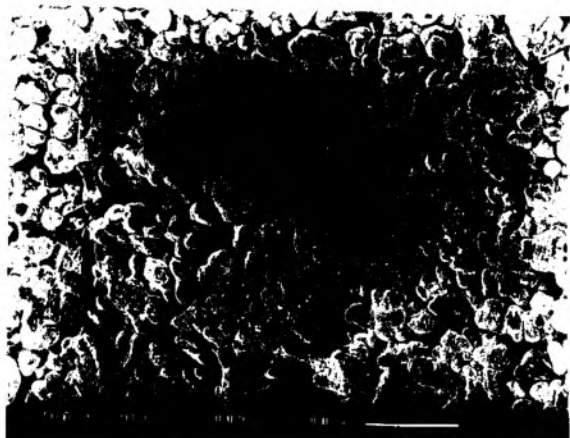
(a)

(b)

Fig.4.2.8   SEM photographs of a TiC rich Fe-
  (a,b)   master alloy showing
             (a) discrete, and
             (b) dendritic
             TiC particles.
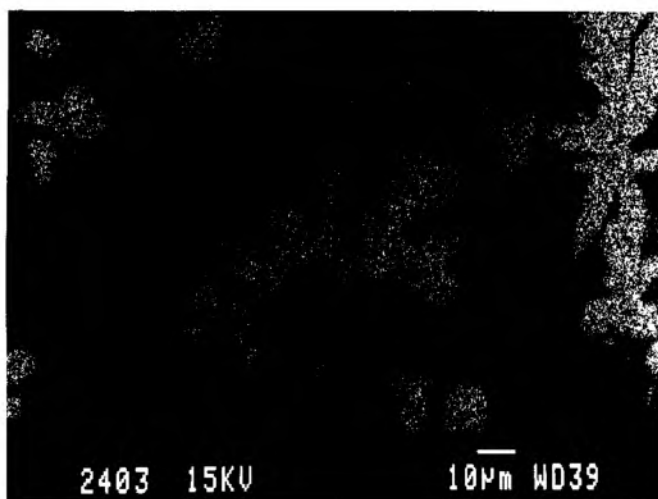
Fig.4.2.9 Titanium X-ray mapping of Fig.4.2.8(b)
        showing dendritic area rich in Ti.

Fig. 4.2.10, shows a SEM photograph of the TiC rich Fe-TiC master alloy (A24) where a star like carbide particle is surrounded by a gray area. The SEM-EDAX analysis of the particle showed presence of 96.59 wt pct Ti, 2.39 wt pct Fe and 1.02 wt pct Zr (Fig. 4.2.10). The gray area contained only 3.40 wt pct Ti and 96.6 wt pct Fe. The microhardness of the star like particle varied between 3386 to 3577 VPN confirming the formation of TiC [57]. The x-ray diffraction studies of such master alloys also confirm (Table 4.1.2) the presence of TiC. The gray area has hardness values varying between 2191 to 2692 VPN, while pearlite has hardness values between 460 and 472 VPN.

The SEM photographs of composites B6 and B7 show presence of dendritic TiC and cuboidal carbide particles in Fig. 4.2.11 and Fig. 4.2.12, respectively. Fig. 4.2.13 shows SEM photograph of composite B6 at yet another location. The x-ray mapping of same area for Ti, Fe and Mn are shown in Fig. 4.2.14 to Fig. 4.2.16. It may be seen from the figures that cuboids and dendrites are rich in titanium. Uniform distribution of Mn in the matrix may be seen.

The titanium carbide morphology of TiC reinforced cast iron composite B11 has been studied in detail. The SEM photographs (Fig. 4.2.17 to Fig. 4.2.20) show various morphological features like dendritic growth, star like particles, rod type particles and discrete well defined polyhedrons. The SEM - EDAX analysis of carbide particles show a variation of Ti content from 94.33 to 95.33 wt pct and that
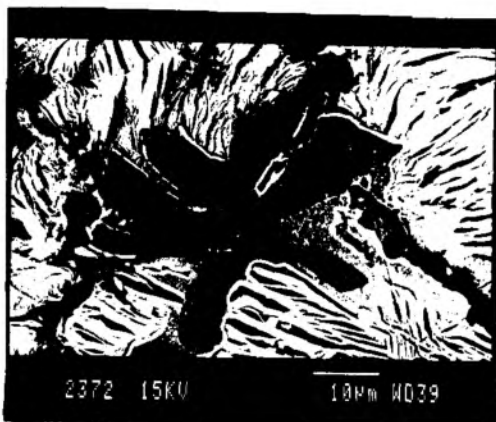
Fig.4.2.10   SEM photograph of a TiC rich
              master alloy A24 showing a star
              like TiC particle surrounded by
              gray area. Gray area contained
              3.40 wt pct Ti.

Fig.4.2.11   SEM photograph of a cast iron
              composite B6 showing dendritic
              TiC morphology.

Fig.4.2.12 SEM photograph of a cast iron
composite B7 showing TiC parti-
cles of various configurations.
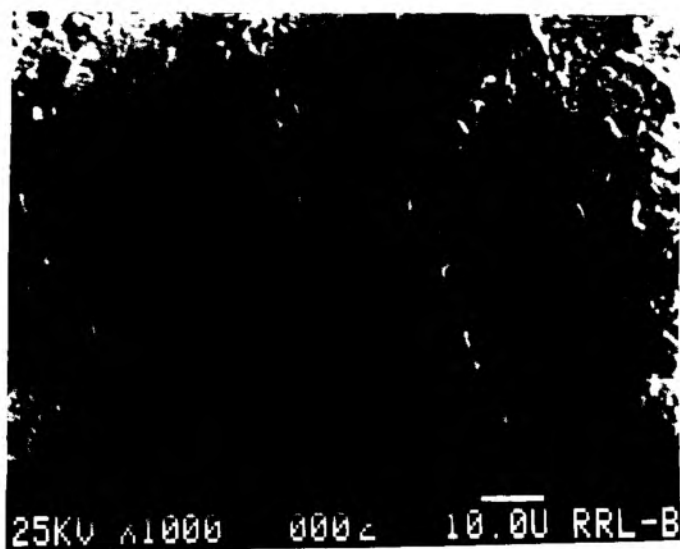
Fig.4.2.13 SEM photograph of cast iron com-
posite B6 showing TiC particles
in cuboidal form.
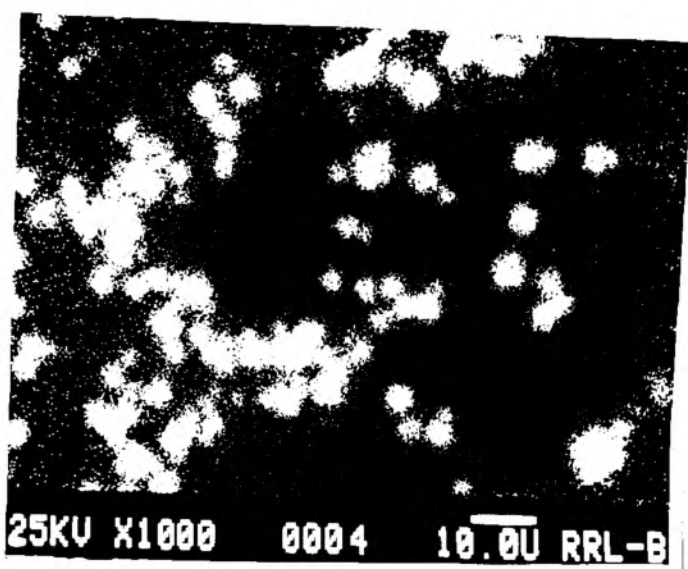
Fig.4.2.14 Ti, X-ray mapping of cast iron
composite B6.
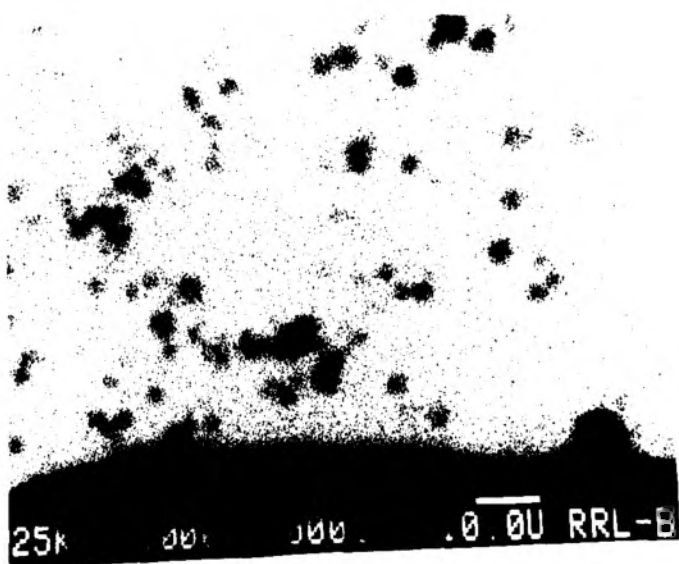
Fig.4.2.15 Fe, X-ray mapping of cast iron
composite B6.
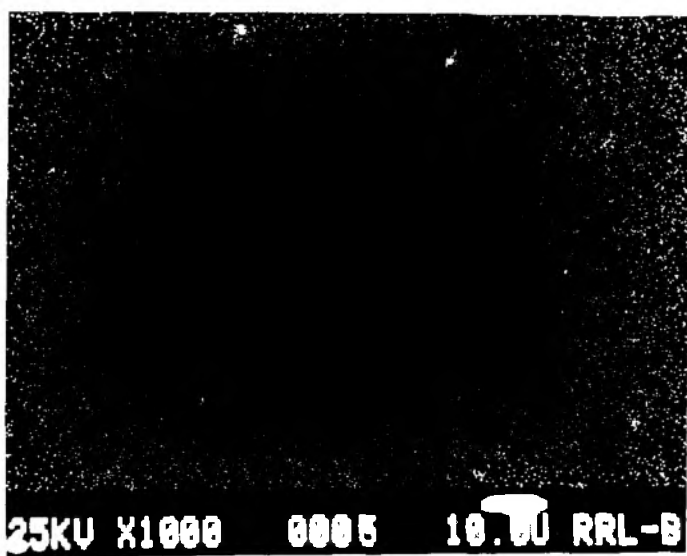
Fig.4.2.16   Mn, X-ray mapping of cast iron
              composite B6

3-Dec-1993 11:08:48
Execution time = 3 seconds
NML/RKG/126/HT/M
Vert= 500 counts   Disp= 1   Com

ELEMENT & LINE	WEIGHT PERCENT	ATOMIC PERCENT*	PREC 2 S
Si KA	0.24	0.47	0
Ti KA	6.03	6.95	0
Mn KA	1.31	1.32	0
Fe KA	92.41	91.26	1
TOTAL	99.99		

*NOTE: ATOMIC PERCENT is normalized to 100

**NOTE: K-RATIO = K-RATIO x R

Quantex> where R = reference(standard)/reference(sample)

0.000   Range= 10.230 keV   Integral 0 = 6947

10.110
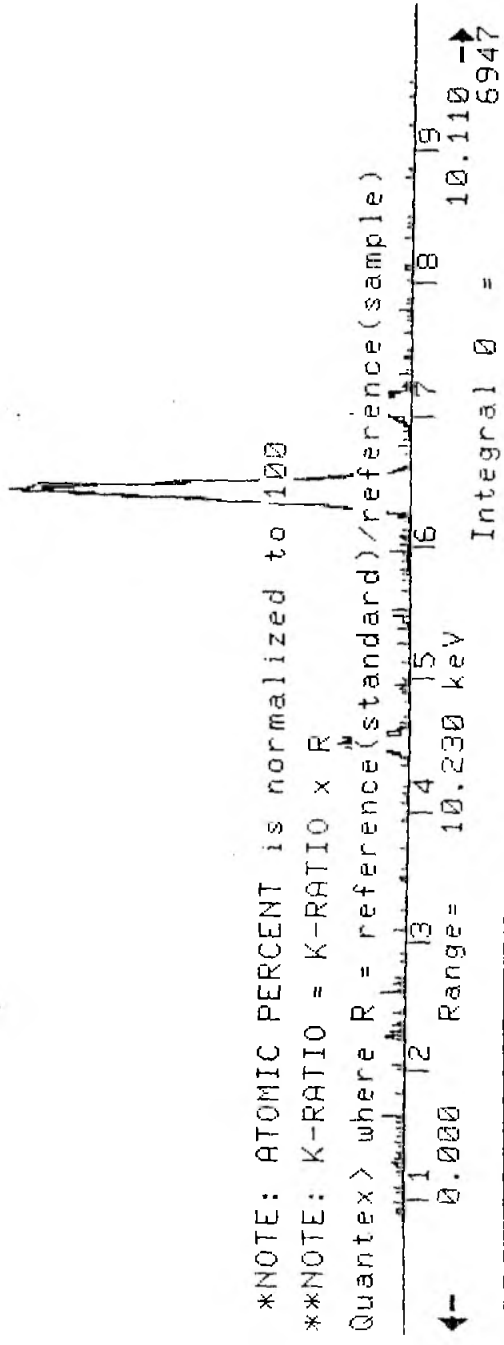
Fig. 4.2.17 SEM-EDAX, bulk analysis of composite B11

```
3-Dec-1993 10:53:43
Execution time = 2 seconds
NML/RKG/126/HT/D-CARBIDE/3198
Vert= 1000 counts  Disp=1    Com
ELEMENT  WEIGHT   ATOMIC    PREC
& LINE   PERCENT  PERCENT*  2 S

Ti KA    95.33    95.97     0
Fe KA     4.67     4.03     0
TOTAL   100.00
```

*NOTE: ATOMIC PERCENT is normalized to 100
**NOTE: K-RATIO = K-RATIO x [R|A]
Quantex> where R = reference(standard)/reference(sample)

0.000   Range= 10.230 keV   Integral 0 =   10.110
                                                  17134
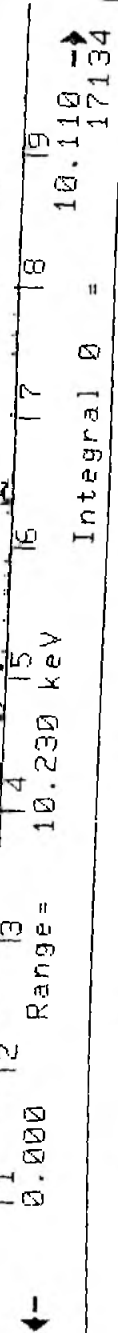
Fig. 4.2.18 SEM-EDAX analysis of maize like carbide in composite B11

Fig. 4.2.19 SEM-EDAX analysis of rod like carbide in composite B11

3-Dec-1993 10:36:15
Execution time = 3 seconds
NML/RKG/126/m
Vert= 1000 counts   Disp= 1

ELEMENT & LINE	WEIGHT PERCENT	ATOMIC PERCENT*
Si KA	0.00	0.00
Ti KA	3.91	4.53
Mn KA	1.22	1.23
Fe KA	94.87	94.24
TOTAL	100.00	

*NOTE: ATOMIC PERCENT is normalized to 100
**NOTE: K-RATIO = K-RATIO x R
Quantex> where R = reference(standard)/reference(sample)

0.000   Range= 10.230 keV   10.110
Integral 0 = 10263
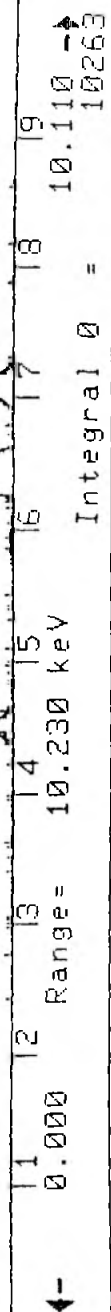
Fig. 4.2.20   SEM-EDAX analysis of composite B11 avoiding carbide particles.

in iron from 4.67 to 6.56 wt pct (Fig. 4.2.18 and Fig. 4.2.19). A typical matrix composition taken avoiding carbides show presence of 3.91 wt pct Ti, 1.22 wt pct Mn and 94.89 wt pct Fe (Fig. 4.2.20).

X-ray diffraction analysis

X-ray diffraction data for some of the cast iron composites are presented in Table 4.2.4. It may be seen from the Table that the presence of TiC phase has been identified in all the composites.

Carbide particle size distribution in TiC reinforced cast iron composites by image analysis.

The data on particle size distribution of carbides and the volume percent in various size fractions as evaluated by Quantimet Q570 for some of the composites are presented in Table 4.2.5 to Table 4.2.7. It may be seen from the Tables that significant quantities of carbide particles of size less than 8μm (referred to as under size in the Tables) are present in the TiC cast iron composites. Chill cast composites B1 and B5 (titanium content varying from 1.48 to 3.11 wt pct) show that nearly 95 pct of particles are having a size below 16μm. As the titanium content of the cast iron composite is increased to 5.62 wt pct in composite B10 the coarser particles become more numerous. After a normalising treatment, the volume percent of coarser particles increase and the count for under size particles decrease. A similar

Table 4.2.4

X-ray diffraction analysis of TiC reinforced
cast iron composites

Composite No.	Phases	Relative intensities	(hkl) Planes
B1	α-Fe	S	(110), (200)
	Fe_3C	S	(031), (121), (221), (022), (231)
	TiC	W	(200), (311)
B5	α-Fe	S	(110), (200), (211)
	Fe_3C	S	(031), (102), (221), (201), (311)
	TiC	W	(200)
B10	α-Fe	S	(110), (200)
	Fe_3C	S	(031), (102), (210), (221), (131)
	TiC	W	(200)

Relative intensity

S = 80 to 100 pct, M = 40 to 79 pct, W = 5 to 39 pct

Table 4.2.5

Titanium carbide particle size distribution in TiC reinforced cast iron composites (chill cast).

| Composite No.---> | B1 | | B5 | | B10 | |
| Crucible lining | MgO | | MgO | | Zircon | |
Diameter μm	Count	Vol pct	Count	Vol pct	Count	Vol pct
Under size*	749	-	2013	-	1335	-
8 - 11.31	17	19.61	60	52.97	100	5.73
11.31 - 16	2	6.52	16	39.95	48	7.79
16 - 22.62	-	-	1	7.06	24	11.09
22.62 - 32	-	-	-	-	11	14.28
32 - 45.25	1	73.85	-	-	3	11.01
45.25 - 64	-	-	-	-	2	20.77
64 - 90.5	-	-	-	-	1	29.37
90.5 - 128	-	-	-	-	-	-
Total count--->	769		2090		1524	

* Particle size below 8 μm are not considered for estimation of volume

Table 4.2.6

Titanium carbide particle size distribution in TiC reinforced cast iron composite

(Normalised specimens at 950°C, 4h soaking)

Composite No.→	B2		B3		B6	
Diameter μm	Count	Vol pct	Count	Vol pct	Count	Vol pct
Under size*	443	-	740	-	553	-
8 - 11.31	93	31.36	227	46.19	99	15.61
11.31 - 16	38	36.25	25	48.92	62	27.65
16 - 22.62	12	32.27	3	4.88	28	35.32
22.62 - 32	-	-	-	-	6	21.4
32 - 45.25	-	-	-	-	-	-
45.25 - 64	-	-	-	-	-	-
64 - 90.5	-	-	-	-	-	-
90.5 - 128	-	-	-	-	-	-
Total count→	586		1055		748	

* Particles below 8μm size are not considered for estimation of volume pct.

Table 4.2.7

Titanium carbide particle size distribution in TiC reinforced cast iron composites

(Normalised specimens)

Composite No. →	B4		B7		B12	
Temperature (°C) →	950		950		1000	
Soaking period (h) →	4		4		6	
Diameter μm	Count	Vol pct	Count	Vol pct	Count	Vol pct
Under size*	850	-	282	-	191	-
8 - 11.31	217	8.21	91	1.76	171	4.54
11.31 - 16	132	14.13	72	3.94	110	8.27
16 - 22.62	82	24.84	41	6.35	70	14.89
22.62 - 32	39	33.41	31	13.59	23	13.84
32 - 45.25	8	19.38	10	12.40	15	25.54
45.25 - 64	-	-	i2	42.09	4	19.26
64 - 90.5	-	-	2	19.84	1	13.62
90.5 - 128	-	-	-	-	-	-
Total count →	1328		541		585	

* Particles below 8μm size are not considered for estimation of volume pct.

increase in the volume fraction of the coarser particles is noticeable in case of sand cast samples. The data for samples B7 (4.17 wt pct Ti) is a typical example. An increase in the titanium percentage in the composite as in the normalised cast iron composite B12 (10.86 wt pct Ti) results in further increase in the volume percent of carbide particles in the coarser range i.e, over particle size of 22.62 μm.

4.2.2 Discussion

The results of the experiments on the preparation of TiC reinforced cast iron composites may be analysed to highlight the following:

i) Characteristics of the as cast and heat treated micro-structures of cast iron composites, and

2) Morphology and distribution of titanium carbide particles in the composites

The titanium content in the cast irons prepared by plasma smelting of ilmenite varied considerably (Table 4.2.1 and Table 4.2.2), eventhough the charge mix and other smelting parameters were kept constant. Because of the small size of the reactor, it was difficult to achieve clear slag/metal separation. Lower oxides of titanium such as TiO and Ti_2O_3 are produced as intermediate products of ilmenite reduction when no flux is added. These lower oxides of titanium react with the magnesia lining of the crucible forming compounds like $Fe_2MgTi_3O_{11}$, Mg_2TiO_4 etc. It is likely that the titanium lost in the slag as complex compounds is not recovered in the metal phase during smelting. The titanium metal recovery, therefore, varies with the amount of titanium lost in the slag.

It is interesting to note that the cast iron melt picked up considerable amount of magnesium or zirconium

depending upon the type of lining used. Thermodynamic calculations for carbothermic reduction of MgO and ZrO_2 are as follows:

$MgO(s) + C(s) = Mg(g) + CO(g)$ ....(4.22)
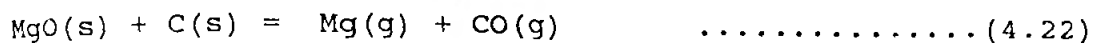
$\Delta G^o_T = 154,900 + 7.37 \, TlogT - 96.65 \, T \, Cal; \quad 298 - 2500 \, K$

Hence, at T = 2073 K; $\Delta G^o_{2073} = + 5215 \, Cal$

at T = 2173 K; $\Delta G^o_{2173} = - 1677.4 \, Cal$

$ZrO_2(s) + 2C(s) = Zr(s) + 2CO(g)$ ....(4.23)
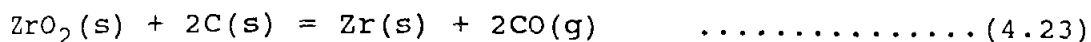
$\Delta G^o_T = 206,800 + 6.44 \, TlogT - 107.89 \, T \, Cal; \quad 298 - 2138 \, K$

Hence, at T = 2073 K; $\Delta G^o_{2073} = 27,421 \, Cal$

at T = 2473 K; $\Delta G^o_{2473} = - 5971 \, Cal$

$ZrO_2(s) + 3C(s) = ZrC(s) + 2CO(g)$ ....(4.24)
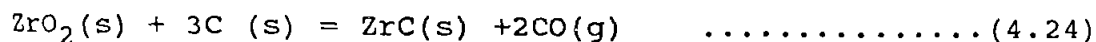
$\Delta G^o_T = 162,700 + 6.44 \, TlogT - 105.69 \, T \, Cal; \quad 298 - 2000 \, K$

Hence, at T = 1873 K; $\Delta G^o_{1873} = 4216 \, Cal$

at T = 1973 K; $\Delta G^o_{1973} = - 3938 \, Cal$

The calculations show that the carbothermic reduction of MgO requires a temperature of about 2173 K [Eq. 4.22] while ZrO_2 reduction requires a temperature of about 2473 K [Eq.4.23]. The formation of ZrC requires a temperature around 1973 K [Eq.4.24]. The temperature in the plasma reactor, particularly in the arc crater, is usually quite high. Hence, reduction of MgO to Mg and ZrO_2 to ZrC is thermodynamically feasible in the plasma reactor.

Introduction of magnesium or zirconium from the lining into the cast iron melt exerted some effect on both the chill cast and sand cast microstructures. The magnesium alloyed sand cast composites were almost free from any eutectic carbide (Fig. 4.2.2a), whereas those alloyed with zirconium were heavily mottled. The silicon content in all these composites was quite low. In cast iron silicon is the main graphitiser. The graphitising effect of aluminium is much less than that of silicon [97], while the chilling tendency of the magnesium free samples was the consequence of very low silicon content in the alloys. It is interesting to note that incorporation of magnesium from the lining reduced this chilling tendency significantly. The mechanism is not clear at this stage. Zircon is a likely impurity in ilmenite, since the original beach sand from which ilmenite is separated also contains zircon. In addition to the reduction of zircon in the ilmenite, the reduction of zircon paint applied to graphite crucible accounts for the presence of higher amount of zirconium in the composites B8 to B12 (0.178 to 0.521 wt pct). Although zirconium is known to be a graphitiser[98], it did not exert any significant graphitising effect in these samples. It is likely that the zirconium is tied up entirely as carbide and hence is unable to exert its intrinsic effect.

The pick up of magnesium influenced the graphitisation kinetics greatly. In spite of the low silicon level, all the chill cast magnesium containing cast iron composites

could be graphitised within a rather short period of 4 hours at 950°C. The resulting microstructures consisted of a unique combination of graphite rosettes and well dispersed TiC particles in a pearlite matrix. The graphitising influence of magnesium in the white iron has been thoroughly studied [99-101]. However, the present result is unique in two respects. First, the magnesium was picked up in the present series of composites by in situ reduction of magnesia. Secondly, all the cast iron samples had an extremely low silicon.

A comparison of the TiC particle size distribution in the as cast and normalised composites (Table 4.2.5 to Table 4.2.7) reveal that the size of TiC particles in the magnesium free composites were finer than those in the magnesium containing composites. This difference can be further appreciated by examining the microstructures of the normalised magnesium bearing and magnesium free composites (B6 and B11 shown in Fig. 4.2.4 and Fig. 4.2.17, respectively). It is likely that the greater chilling tendency of the magnesium free samples ensured better distribution of TiC particles and prevented their coarsening.

When the charge mix was adjusted to have a high titanium containing master alloy, the product became semi-fluid and did not flow. On examination of the microstructures of TiC rich Fe-TiC master alloys, two distinct morphologies of TiC could be observed. These are dendritic and

discrete idiomorphic crystal type (Fig. 4.2.8(a&b)). Such type of microstructures were also observed in TiC reinforced cast iron composites (Fig. 4.2.18 to Fig. 4.2.20). TiC has a melting point of 3250°C and has extremely low solubility in molten iron. But the presence of dendritic TiC particles suggest that these particles had grown in a different fashion. It can be noted from Ti-C phase diagram (Fig. 2.6) that TiC and graphite forms an eutectic at 2760°C. Just below the plasma arc roots temperatures of such order is quite likely. Hence, the formation of TiC-graphite binary solutions is also possible. The as cast microstructure in Fig. 4.2.2b shows dendritic TiC and graphite growing together in the matrix. The dendritic morphology is, therefore, believed to be the product of solidification of a binary TiC-graphite solution through a distinct solidification temperature range according the Ti-C phase diagram.

4.2.3 Conclusions

Following conclusions are deduced from the above discussion. As regards cast iron composites the main conclusions are as follows.

a) It is possible to prepare TiC reinforced cast iron composites by carbothermic reduction of ilmenite in a bed of steel scrap in the plasma reactor.

b) The coating of magnesia or zircon on the graphite crucible surface is partially reduced during smelting

operation. The magnesium or zirconium released is picked up by the melt.

c)   Low silicon cast iron melts prepared in the plasma reactor have adequate fluidity to permit casting in a sand or metal mould.

d)   During solidification the magnesium bearing melts suffer less chilling than the melts free from magnesium.

e)   Magnesium bearing chill cast samples can be graphitised at $950^{\circ}C$ within 4 hour. Magnesium free composites require heat treatment for longer durations for graphitisation.

f)   Titanium carbide particles are finer in magnesium free samples.

Regarding master alloys the main conclusions are as follows.

a)   Two types of TiC morphology - dendritic and discrete particle type are observed in the frozen samples.

b)   The dendrite morphology is the result of TiC - graphite alloy formation.

4.3 TiC REINFORCED STEEL COMPOSITES

In this section the results on TiC reinforced steel composites are presented. The results are then analysed and relevant conclusions are drawn.

4.3.1 Results

TiC reinforced steel composites were prepared by dissolving predetermined quantity of TiC rich Fe-TiC master alloy in a liquid plain carbon steel or an alloy steel bath. In one such instance, such a composite was prepared by melting the TiC rich iron - TiC master alloy and addition of iron ore (blue dust variety containing 97.6 wt pct Fe_2O_3) to oxidise away excess carbon present in the master alloy. An experiment was also carried out on dissolution of chemically pure TiC in a plain carbon steel bath. All these experiments were carried out in an induction furnace.

Various investigations have been carried out to characterise the TiC reinforced steel composites and they are as follows :

1. Chemical analysis
2. Microstructural characteristics
    a) Optical microstructure
    b) Image analysis studies for carbide particle size distribution and grain size measurements.

c) Microstructural   features by transmission   electron microscopy.

3. SEM-EDAX analysis

a) Microstructural features

b) Inclusion analysis

c) Carbide matrix interface analysis.

4. Mechanical properties.

a) Tensile test

b) Impact test

The details of various characterisation studies are presented below :

Chemical analysis

TiC reinforced steel composites were prepared by dissolving TiC rich iron - TiC master alloy (containing 30.92 wt pct Ti, 0.549 wt pct Al, 0.60 wt pct Si, 0.067 wt pct Mg, 0.178 wt pct Zr and 11.8 wt pct C) in a plain carbon steel (containing 0.1 or 0.03 wt pct C) melt. The addition of master alloy was in a proportion of 0.5, 1, 5 and 10 wt pct of the weight of steel scrap. Low carbon steel scrap (0.03 wt pct C) was used when the addition of master alloy was in a proportion of 0.5 and 1 wt pct. The chemical analy-sis of a few   composites as evaluated by spectroscopic analysis are presented in Table 4.3.1. It may be noted from the data presented in the Table that titanium content of composites varied from 0.0028 to 0.71 wt pct. The carbon

Table 4.3.1

Chemical analysis of TiC reinforced steel composites

Composite No.	Ti	C	Si	Mn	S	P	Cu	V	Al
					Wt pct				
C1	0.0028	0.0538	0.2430	0.1546	0.0447	0.0940	0.1051	0.0018	0.0001
C2	0.0053	0.03	0.009	0.03	0.075	0.05	NA	NA	NA
C3	0.082	0.27	0.095	0.26	0.05	0.039	NA	NA	NA
C4	0.1362	0.3236	0.1035	0.3487	0.0426	0.0603	0.1055	0.0068	0.0075
C5	0.2974	0.5877	0.3127	0.5468	0.0510	0.0621	0.1121	0.0122	0.0074
C6	0.71	0.486	0.481	0.50	0.035	0.07	NA	NA	NA
C7*	0.141	0.612	0.577	0.55	0.016	0.034	NA	NA	NA
C8	7.481	1.485	3.639	0.217	0.040	0.050	NA	NA	NA
C9	0.033	0.17	0.011	0.24	0.011	0.016	NA	NA	NA

NA - Not analysed

* Contains 0.798 Cr, 0.189 Ni, 0.391 wt pct Mo

content of TiC reinforced steel composites increased as the addition of master alloy is increased. Composite C8 was prepared by reacting 360 g master alloy with 225 g blue dust in an induction furnace. Composite C9 was prepared by addition of 100 g pure TiC to 2 kg steel melt. The percent recovery of titanium in the composites is reported in Table 4.3.2. It may be seen from the Table that titanium recovery varied from 2 to 23 pct when master alloy was dissolved in the liquid steel. A recovery of 27 pct Ti has been obtained in the case of composite C8 prepared by reacting master alloy with iron ore. Composite C9 has shown the lowest Ti recovery of 0.82 pct, which was prepared by dissolution of pure TiC in steel melt.

Microstructural characteristics

Optical microstructures

TiC reinforced steel composite castings were forged as mentioned in `experimental' (section 3.3.4) and were normalised by holding the specimens at different homogenisation temperature and duration.

As cast microstructure of steel composite C6 is shown in Fig.4.3.1. The microstructure shows presence of pearlite grains with grain boundary ferrite. The presence of TiC particles in the pearlite matrix may be seen. The micro-structures of composites C4 and C5 in as forged condition is shown in Fig. 4.3.2 and Fig. 4.3.3, respectively. Angular ferrite grains with TiC particles in it are seen. The micro-

Table 4.3.2

Recovery of titanium in TiC reinforced composites.

Composite No.	Wt pct Fe-TiC master alloy addition	Pct Ti recovery
C1	0.5	2.03
C2	1.0	1.75
C3	1.0	13.53
C4	5.0	8.99
C5	10.0	9.82
C6	10.0	23.40
C7	10.0	4.60
C8*		26.89
C9**		0.82

* Composite prepared by reacting master alloy and iron ore.

** Prepared by addition of pure TiC to steel melt.

Fig.4.3.1 Steel composite C6 (As cast), 100 X
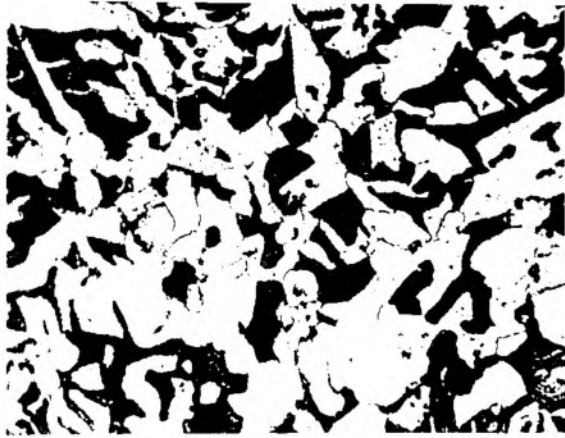
Fig.4.3.2 Steel composite C4 (As forged) show
apolygonisation of grains, 200 X
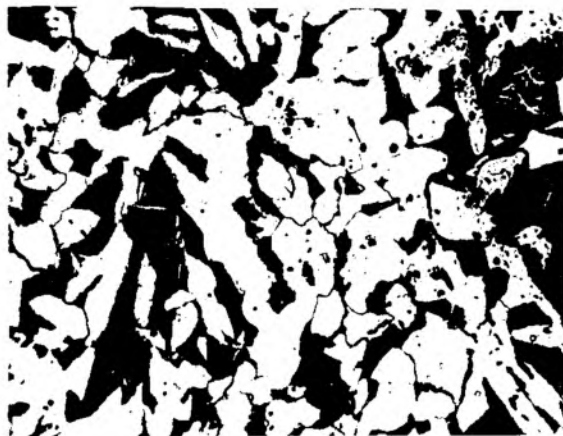
Fig.4.3.3 Steel composite C5 (As forged) shows
apolygonisation of grains, 200 X.

structures of composites C4 and C6 after normalising the forged specimen by soaking at 950°C for 2 hours are presented in Fig. 4.3.4 and Fig. 4.3.5, respectively. Rounded equiaxial grains of ferrite are observed in Fig. 4.3.4 with uniform distribution of carbide particles. Fine pearlite grains with uniform distribution of TiC particles are seen in Fig. 4.3.5. TiC particles are seen even within pearlite colonies at high magnification (Fig. 4.3.6) in composite C4, which was normalised after homogenising at 1150°C for 2 hours. The composite C7 prepared with alloy steel as a matrix showed uniform distribution of TiC particles in ferrite and pearlite after normalising (homogenising at 950°C, 2 hours). The microstructure of TiC reinforced steel composite C8 prepared by reacting master alloy and iron ore is shown in Fig. 4.3.7. TiC particles in cuboidal forms are seen in the pearlite matrix.

Carbide particle size distribution and grain size measurements in composites

The TiC particle size distribution and grain size measurements of steel composites were carried out on Quanti-met Q 570 image analyser. The carbide particle size and its distribution in some of the TiC reinforced composites are presented in Table 4.3.3 and Table 4.3.4. Many carbide particles present in the composites have sizes below 8 μm (Table 4.3.3 and Table 4.3.4). The effect of homogenisation temperature on carbide particle size distribution is shown

Fig.4.3.4 Steel composite C4 normalised at
950°C after soaking for 2 h show-
ing distribution of TiC particles
200 X
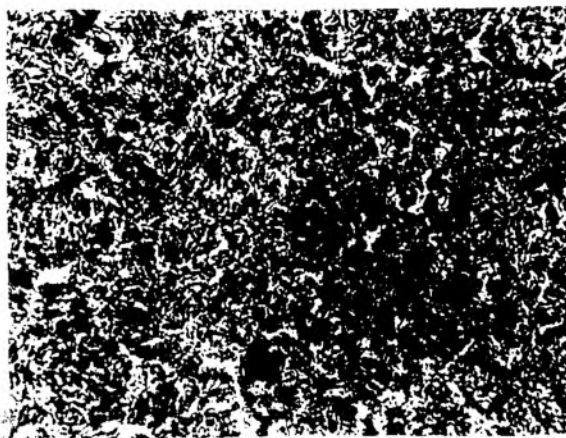
Fig.4.3.5 Steel composite C6 normalised at
950°C after soaking for 2h uniform
distribution of TiC particles, 200 X

Fig.4.3.6   Steel composite C4 normalised at
            1150°C after soaking for 2h show-
            ing   uniform distribution   of   TiC
            particles, 1000 X.
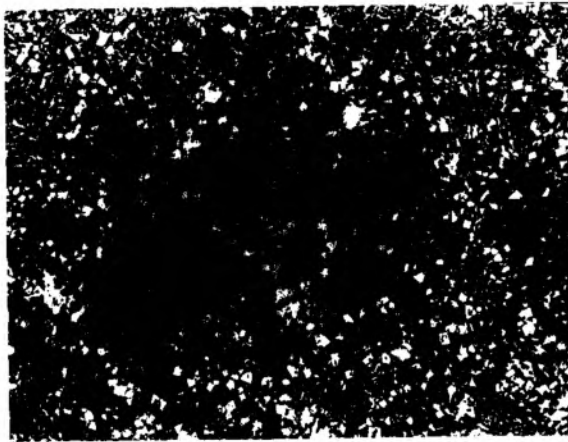
Fig.4.3.7 Steel composite C8 (As cast) shows
          cuboidal TiC particles, 200 X.

Table 4.3.3

Titanium carbide particle size distribution in TiC reinforced composites

| Composite No. ⟶ | C1 950°C 1h | | C2 1150°C 2h | | C3 950°C 1h | | C8 950°C 1h | |
Normalising conditions ⟶ Diameter μm	Count	Vol. pct	Count	Vol. pct	Count	Vol. pct	Count	Vol. pct
Under size*	461	-	578	-	382	-	51	-
8 - 11.31	475	4.84	503	4.19	258	22.02	65	0.67
11.31 - 16	269	7.76	366	8.63	111	26.79	58	1.69
16 - 22.62	176	14.36	244	16.28	25	17.07	57	4.71
22.62 - 32	70	16.16	105	19.82	12	23.17	63	14.72
32 - 45.25	31	20.24	40	21.36	2	10.92	34	22.47
45.25 - 64	9	16.62	14	21.14	0	0	10	18.69
64 - 90.5	1	5.22	2	8.54	0	0	7	37.02
90.5 - 128	1	14.77	0	0	0	0	0	0
Total count ⟶	1493		1852		790		345	

* For calculation of volume percent below 8μm size particle are not considered.

Table 4.3.4

Titanium carbide particle size distribution in TiC reinforced steel composites

Composite No. →	C4		C4		C5		C5	
Normalising conditions →	950°C 1 h		1150°C 2 h		950°C 1 h		1150°C 2 h	
Diameter μm	Count	Vol. pct	Count	Vol. pct	Count	Vol. pct	Count	Vol. pct
Under size*	1204	-	1092	-	3004	-	1386	-
8 - 11.31	1331	5.92	1144	2.64	2293	15.51	1476	1.49
11.31 - 16	1063	13.38	869	5.67	1146	21.92	1179	3.37
16 - 22.62	718	25.57	565	10.43	428	23.16	870	7.04
22.62 - 32	265	26.69	283	14.77	123	18.82	559	12.80
32 - 45.25	63	17.94	132	19.49	23	9.95	254	16.45
45.25 - 64	13	10.47	55	22.97	3	3.67	93	17.04
64 - 90.5	-	-	9	10.63	2	6.92	41	21.25
90.5 - 128	-	-	4	13.36	-	-	14	20.52
Total count →	4657		4153		7022		5872	

in Table 4.3.4 . There is a decrease in the count of parti-
cle size below 8 μm as well as increase in volume percent of
coarse particles when homogenisation temperature is in-
creased from 950° to 1150°C.

The results of grain size measurements for some of
the TiC reinforced steel composites along with aspect ratio
of grains and pearlite area fraction are presented in Table
4.3.5. There is hardly any change in grain size measurement
of composites C4 and C5 as the homogenisation temperature
during heat treatment is increased from 950° to 1150°C .
Lowest average grain size of 4.44 μm was obtained in compos-
ite C1 while, composite C7 showed highest average grain size
of 20.91 μm. The aspect ratio of grains vary mostly between
0.8 and 0.9 indicating the presence of nearly equiaxial
grains in the composites. The area fraction of pearlite has
varied from 0.27 to 0.9 depending on the carbon content of
the composites.

Microstructural features by transmission electron microscopy

The transmission electron photomicrograph of
composite C4 shows presence of fine carbide precipitates in
ferrite matrix (Fig. 4.3.8). Sharp grain boundary is seen in
TEM photomicrograph of composite C4 in Fig. 4.3.9. The grain
boundary precipitation (Fig. 4.3.10) is observed in TEM
photomicrograph of composite C5.

Table 4.3.5

Grain size measurements of TiC reinforced steel composites

Composite No.	Normalising conditions Soak Temp. °C	Duration h	Minimum grain μm	Maximum grain μm	Mean grain μm	H/W ratio	Pearlite Area
C1	950	1	4.11	4.61	4.44	0.8	0.35
C2	1150	2	10.83	10.96	10.89	0.9	0.27
C3	950	1	5.72	5.94	5.85	0.9	0.48
C4	950	1	10.60	10.65	10.62	0.9	0.38
C4	1150	2	10.71	10.77	10.75	0.8	0.44
C5	As forged		11.7i	11.24	11.15	0.8	0.90
C5	950	1	10.74	10.86	10.74	0.7	0.70
C5	1150	2	10.80	10.92	10.85	0.8	0.87
C7	950	2	20.832	0.97	20.91	0.9	0.70
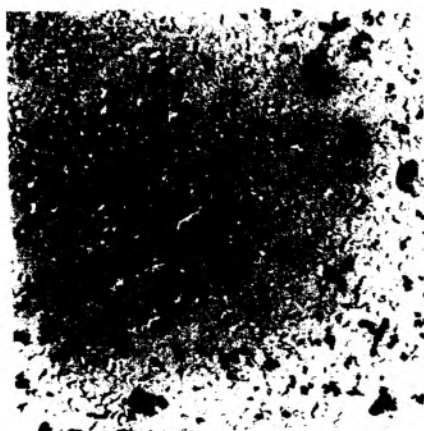
Fig.4.3.8 TEM photograph of the steel
        composite C4 showing fine
        precipitate of TiC, 5000 X.

Fig.4.3.9 TEM photograph of the steel composite
        C4 showing sharp grain boundary, 3400
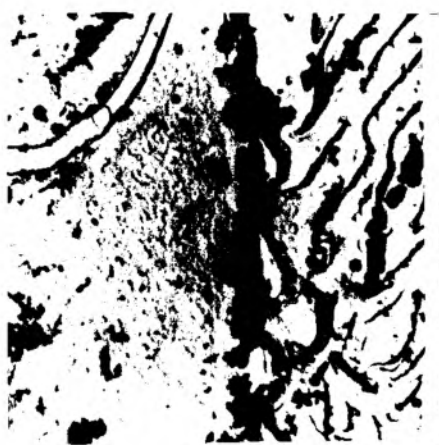
Fig.4.3.10 TEM photograph of the composite C5
showing grain boundary
precipitate, 8300 X.

SEM - EDAX analysis

Microstructural features

Scanning electron photograph of as cast TiC rein-forced steel composite C7 is shown in Fig. 4.3.11. Cuboidal TiC particles are seen in the matrix. The normalised (950°C, 2 hours) specimen of composite C7 shows presence of a cluster of TiC particles in Fig. 4.3.12. EDAX analysis of cuboids of composite C7 showed presence of 95.4 wt pct Ti and 4.6 wt pct Fe. The analysis of a cuboid in composite C6 in as cast condition showed the presence of 94.2 wt pct Ti and 5.80 wt pct Fe. The carbide analysis of composite C8 has shown the presence of 98.89 wt pct Ti and 0.45 wt pct Si, 0.28 wt pct Al and 0.22 wt pct Mn.

Inclusion analysis

SEM-EDAX analysis of inclusions present in some of the composites have been carried out and their elemental analysis data are presented in Table 4.3.6. The inclusions are found to be rich in Ca, Mg, Ti, Al, Si, Mn etc. and these are inclusion morphology modifiers.

Carbide - matrix interface analysis

Carbide - matrix interface area has been studied for a few of TiC reinforced steel composites. The spot analysis data are presented in Table 4.3.7. It is known in aluminium metal - matrix composites, at interface between
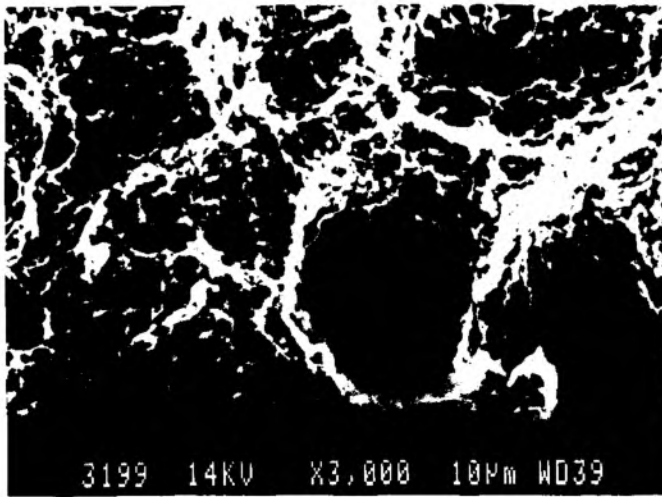
Fig.4.3.11 SEM photograph of the steel
composite C7 (As cast) showing a
cuboidal TiC particle in a deep
etched section.
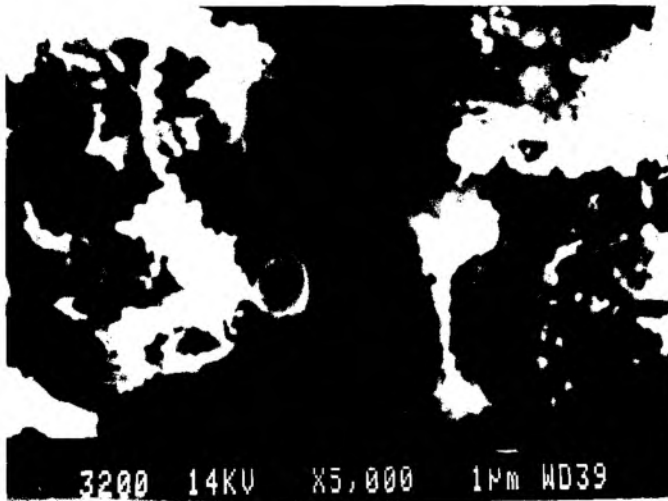
Fig.4.3.12 SEM photograph of the steel
composite C7 normalised from
950°C after soaking for 2h
showing a cluster of TiC
particles.

Table 4.3.6

Inclusion analysis of TiC reinforced steel composites by SEM-EDAX

Composite No.	Al	Si	S	P	Ca	Fe	Mn	Ti				
					Wt pct							
C1	0.728	0.349	0.256	0.000	0.561	95.174	0.000	0.033				
	95.184	0.000	0.024	0.000	0.218	3.251	0.000	1.182				
	0.547	0.000	0.036	0.000	0.074	99.114	0.102	0.000				
	0.455	0.041	0.060	0.000	0.000	99.336	0.107	0.000				
	0.670	0.243	0.061	0.000	0.095	98.586	0.146	0.024				
	2.666	4.119	9.331	0.342	3.701	69.989	0.348	1.521				
	0.209	0.567	1.487	0.147	0.388	96.351	0.000	0.081				
	8.349	18.233	0.595	0.123	1.927	67.192	0.602	0.425				
C2	3.880	21.875	4.024	0.156	0.111	11.041	54.372	4.107	0.216 Cr	0.205 Mg		
	3.525	19.850	4.335	0.283	0.288	10.356	55.834	4.797	0.367 Cr	0.158 Mg		
C5	2.593	4.540	2.539	0.000	3.167	84.014	0.48	0.421	1.069 Zr	1.174 Mg		
	0.063	0.278	0.051	0.054	0.050	98.736	0.457	0.067	0.102 Zr	0.143 Mg		
	0.059	0.287	0.104	0.140	0.152	98.512	0.413	0.161	0.166 Zr	0.006 Mg		
C4	0.221	0.170	0.167	0.395	0.336	97.941	0.558	0.173	0.000 Zr	0.039 Mg		

Table 4.3.7

Carbide matrix interface analysis by SEM-EDAX

Composite No.	Ca	Mg	Al	Si	S	P	Mn	Ti	Zr	Fe
					wt pct					
C5	0.047	0.039	0.205	0.283	0.015	0.048	0.664	0.044	0.008	98.646
	0.070	0.043	0.128	0.250	0.045	0.044	0.614	0.117	0.048	98.642
C7*	0.014	0.044	0.007	0.562	0.020	0.001	0.481	0.049	0.095	97.490
	0.004	0.036	0.054	0.464	0.001	0.001	0.520	0.000	0.318	97.280
C8	0.000	0.067	0.268	2.754	0.066	0.002	0.323	0.470	0.129	95.924
	0.072	0.077	0.229	2.630	0.089	0.002	0.330	0.445	0.151	95.975
	0.047	0.000	0.242	2.245	0.038	0.021	0.522	0.620	0.000	75.765

* Composite contains 0.759-0.802 Cr, 0.210-0.212 Ni, and 0.228-0.353 wt pct Mo

ceramic particle and matrix, reactive elements like Mg, Zr, p etc., are said to be present.

Mechanical properties

Tensile test

The tensile test results of a few of TiC rein-forced steel composites are presented in Table 4.3.8. The data presented are the average values of a minimum of three readings close to each other. A typical load vs elongation plot for composite is shown in Fig. 4.3.13. It may be seen from the Table that ultimate tensile strength increased from 37 kg/mm^2 (composite C1) to 79 kg/mm^2 (composite C5) indi-cating an increase in tensile properties as titanium content is increased from 0.0028 to 0.2974 wt pct. There is no significant improvement in strength properties of composites containing titanium over 0.3 wt pct. The percent elongation varied between 20 to 55 pct. The tensile strength property of composite C8 prepared by reacting master alloy and car-bide varied between 80-85 kg/mm^2. The percent elongation and reduction in area are not reported as the failure took place out side the gauge length.

SEM photographs of a few fractured surfaces of tensile test specimens are presented in Fig. 4.3.14 to Fig. 4.3.16 for composites C2, C6 and C8. The nature of failure appears to be ductile and intergranualr. Dimples around carbide particles may be noted at some places.

Table 4.3.8

Tensile strength properties of TiC reinforced
steel composites

(Normalised from 950°C after soaking for 1 hour)

Composite No.	Wt Pct Ti	C	UTS kg/mm^2	Pct Elongation	Pct reduction in area
C1	0.0028	0.0538	37.78	34.5	56.50
C2	0.0053	0.03	49.05	23.75	37.70
C4*	0.1362	0.3236	54.83	25.30	55.00
C5*	0.2974	0.5877	79.07	18.60	36.60
C6	0.71	0.486	84.27	19.25	35.90
C7**	0.141	0.612	88.05	20.00	20.99
C8	7.481	1.485	85.00	NA	NA

NA - not analysed as specimen failed
beyond gauge length.

* - Normalised from 1150°C after soaking for 2 h

** - The composite contains Cr, Ni and Mo
as alloying elements

Fig.4.4.13 A typical load vs elongation plot for steel composites.
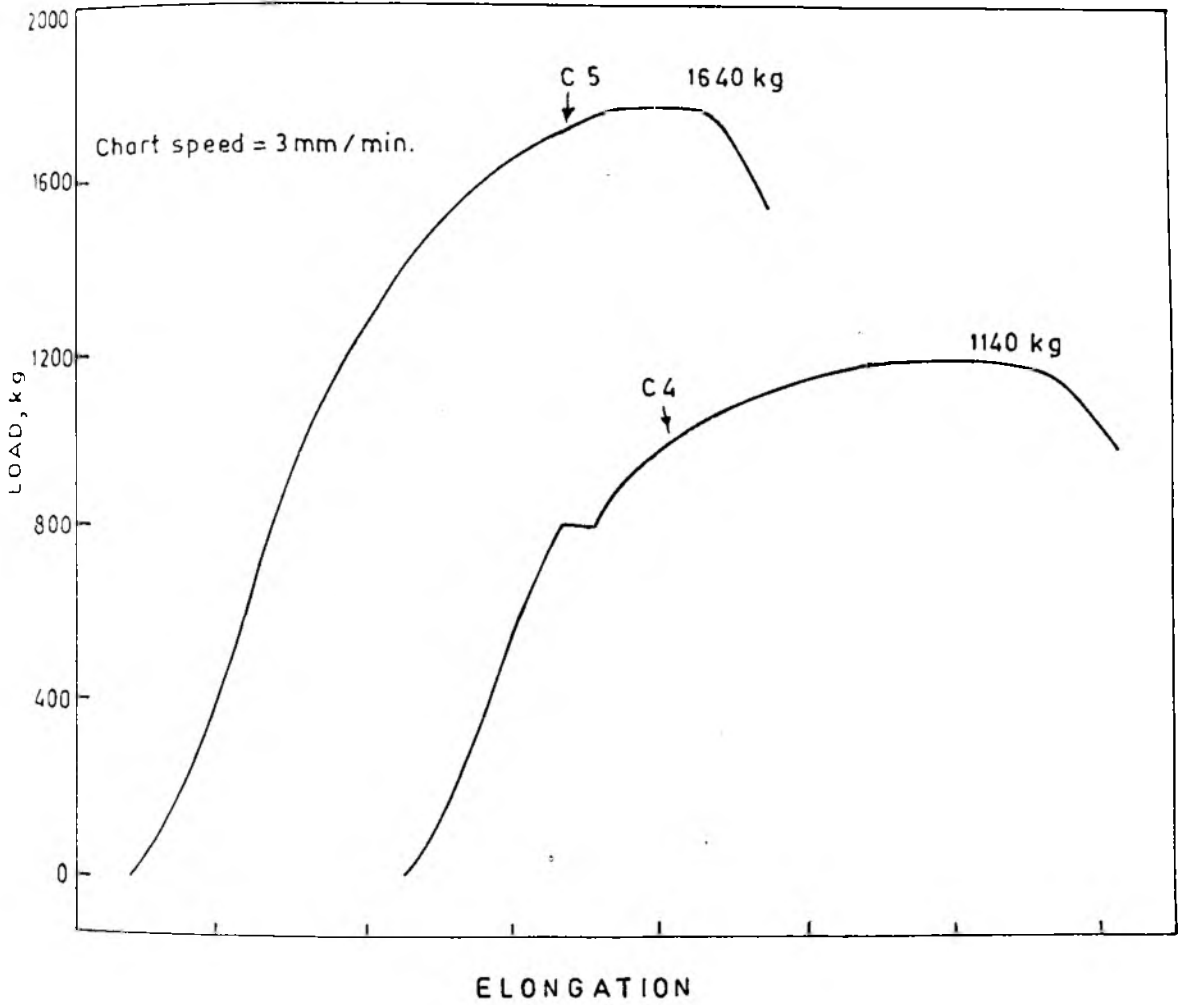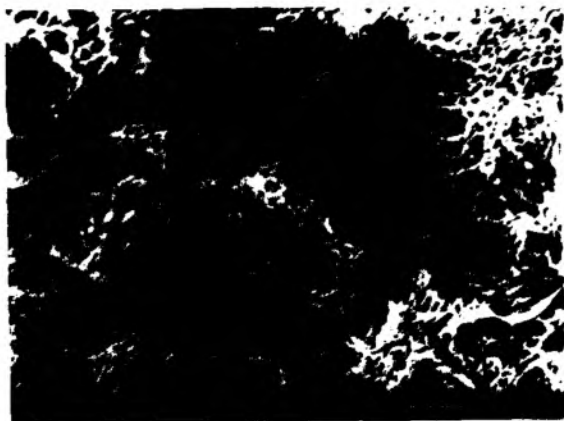
Fig.4.3.14   SEM   photograph   of   the   tensile
fracture   surface   of   the   steel
composite C2. A ductile fracture.
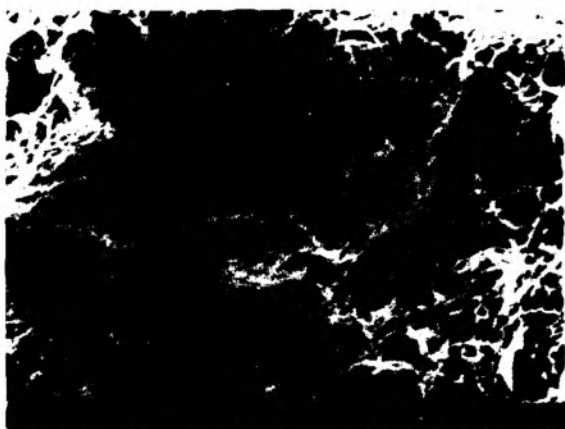
Fig.4.3.15   SEM photograph of the tensile
fracture surface of the steel
composite C6. A ductile fracture.

Fig.4.3.16   SEM photograph of the tensile
             fracture surface of the steel
             composite C8. A ductile fracture.

Impact test

TiC reinforced steel composites were evaluated for toughness property by Charpy impact test. The results of impact tests are presented in Table 4.3.9. The data presented are the average values of a minimum of two readings close to each other. Highest impact test values of 90 joules were obtained in composite C1 while the lowest value of 15 Joules was obtained in composite C5 (Table 4.3.9). The impact test values decreased as the titanium content in the composites was increased. The fractured surfaces of impact test specimens were examined under scanning electron microscope. Fig. 4.3.17 to Fig. 4.3.19 show impact fracture surface as observed under SEM for composites C1, C4 and C5. The composite C1 has shown ductile fracture which is having 0.0028 wt pct Ti. As the titanium content in the composite increases the fracture changes from ductile to partly ductile and partly brittle (Fig. 4.3.19). The dimples in ductile fracture have formed around some inclusions and EDAX analysis of such inclusions are presented in Table 4.3.10.

Table 4.3.9

Impact test results of TiC reinforced steel composites

(Normalised from 950°C after soaking for 1 hour)

Composite No.	Wt Pct Ti	C	Impact test values Joules
C1	0.0028	0.0538	91
C4	0.1362	0.3236	27
C5	0.2974	0.5877	15

Table 4.3.10

Analysis of inclusions on the fracture surface
of the impact test specimens

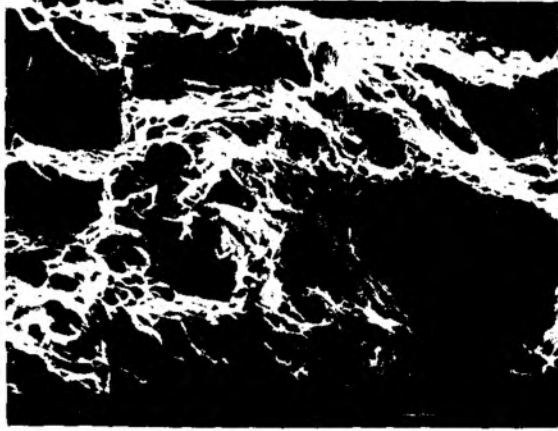| Composite No.	Wt pct					
	Si	Mn	Fe	S	Ti	Cr
C1	16.397	58.08	25.546	–	–	–	–
	19.171	45.432	32.914	1.905	0.023	0.555
C4	0.069	29.036	28.495	20.724	21.665	–

Fig.4.3.17   Fractograph of composite C1
              (Impact fracture).
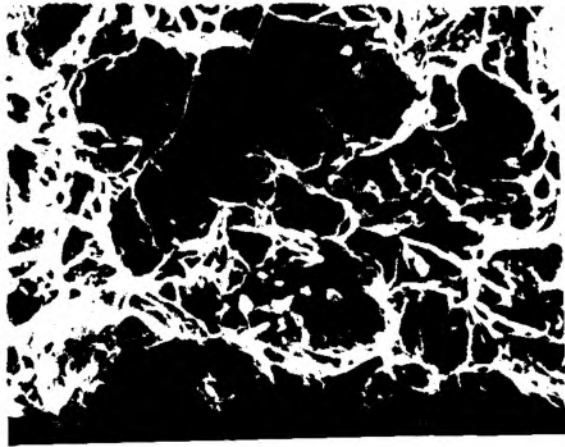

Fig.4.3.18   Fractograph of composite C4
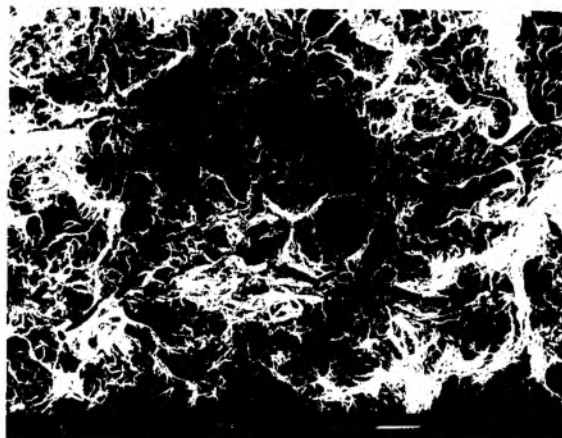   (Impact fracture)

Fig.4.3.19   Fractograph of composite C5
             (Impact fracture). A brittle
             fracture.

4.3.2 Discussion

TiC reinforced steel composites were produced by dissolving TiC rich Fe-TiC master alloy (prepared by carbothermic reduction of ilmenite ore in the plasma reactor) in a molten steel bath in an induction furnace. Results of various characterisation studies like chemical analysis, light metallography, scanning electron micrography, transmission electron micrography, energy dispersive x-ray analysis and mechanical testing have been reported in the preceding section. These results are discussed in the following sections.

Chemical analysis and recovery of titanium in the composites

The chemical analysis data presented in Table 4.3.1 show that as the titanium content of the composites is increased the carbon content also increases. This is expected. As the quantity of master alloy addition to the steel melt is increased the carbon input to the steel bath is also increased mainly by dissolution of the carbon present in the master alloy as iron carbide. The recovery of titanium in the composites show a considerable scatter (Table 4.3.2). It has been as low as 2 pct and as high as 23 pct. The likely reasons for such a variation are, a) loss of titanium by the process of deoxidation of steel and b) loss of titanium by direct oxidation. Though the deoxidation of steel bath by addition of Fe-Si, Fe-Mn and Al was carried out and the oxide slag was removed prior to addition of the master

alloy, the open bath conditions and continuous induction stirring allowed pick up of oxygen in the bath. It is well known that titanium is a deoxidiser [102] and it has already been shown by the reaction [Eq.4.17 in section 4.1.2] that reduction of Fe_2O_3 by TiC is thermodynamically feasible and the reaction product is titanium oxide. Hence, there is a scatter in recovery of titanium while preparing the composites. The recovery is likely to improve if the master alloy addition is made under a cover of inert gas or in vacuum. However, the titanium recovery by addition of the master alloy to molten steel bath is significantly higher as compared to the addition of pure TiC. The likely reasons for poor recovery of Ti by addition of pure TiC are, a) the high melting point of TiC ($3250^{\circ}C$), b) fine particle size of such carbide, and c) low specific gravity.

The recovery of Ti in the composite prepared by reacting TiC rich Fe-TiC master alloy with iron ore is over 26 pct. The process is one of oxidising away excess carbon present in the master alloy by addition of iron ore. As observed during cast iron smelting, it is necessary to keep the titanium content below 10 wt pct to maintain sufficient fluidity of the melt. Both titanium and carbon content in composite C8 was higher compared to those prepared by dissolution technique still its fluidity was adequate for sample casting. Thus, the process of oxidising away excess carbon from the master alloy to produce steel composites appears

to be attractive for the production of composites with high titanium and carbon contents.

Microstructures

The light micrographs of composite specimens in as cast, as forged and in heat treated conditions have been presented in Fig. 4.3.1 to Fig. 4.3.6. A typical as cast structure of composite C6 is shown in Fig. 4.3.1. As in the microalloyed steels, some of the grains in the as forged TiC reinforced steel composites (Fig. 4.3.2) were apolygonal. It is likely that complete recrystallisation was prevented by fine TiC particles at the low forge finish temperature (850°C). After normalising, however, complete recrystallisation occurred. The TiC particles also became more prominently visible due to the particle coarsening (Fig. 4.3.4). The morphology of TiC particles is revealed more clearly in Fig. 4.3.7. Particle size in this composite is higher due to its relatively high titanium (7.481 wt pct) and carbon (1.485 wt pct) contents.

Titanium carbide particle size distribution and grain size measurements

The distribution of TiC in steel composites were determined by Quantimet Q570. The data presented in Table 4.3.3 and Table 4.3.4 show that there are a large number of particles below 8 μm. There is an increase in volume fraction of coarse particles as the titanium content increases in the steel composites. The precipitation of TiC in steel compos-

ites can be ascertained by knowing thermodynamic values for the solubility product and solubility of TiC in austenite. The solubility product for TiC is given by

$$k = \frac{[a_{Ti}] \, [a_C]}{[a_{TiC}]} \quad \ldots\ldots\ldots\ldots(4.25)$$

Where,   k = solubility product

a_{Ti} = activity of Ti

a_C = activity of C

a_{TiC} = activity of TiC

Considering the formation of pure TiC i.e., a_{TiC} = 1 and a dilute solution of Ti in steel matrix, then the Eq. 4.25 reduces to :

k = [wt pct Ti] x [wt pct C] $\ldots\ldots\ldots\ldots\ldots$(4.26)

Number of investigations have been carried out to arrive at the equilibrium solubility of TiC in austenite as a function of temperature [52, 103]. The relationship developed usually expresses the solubility of phase $A_m B_n$ as the solubility product [51] and it takes a form.

Log $[A]^{m/n}$ [B] = y - x/T $\quad\ldots\ldots\ldots\ldots\ldots$(4.27)

Where x and y are determined experimentally, T is the temperature in Kelvin, square brackets represent percent by wt of element A or B is solution in austenite. Many of the relationships developed by various investigators were for low carbon alloys and interaction parameters for solute

were not considered. Recently, Balsubramanian et al.,[53] have developed a relation for solubility of TiC in austenite considering the interaction parameters for solute and the equation is as follows :

$$\text{Log } [(\text{wt pct Ti}) \ (\text{wt pct C})] = \frac{9070}{T} + 4.10$$

$$+ \left[\frac{1205}{T} + 0.24 \right] \times \text{wt pct C} \quad ..(4.28)$$

The values of solubility product and solubility of TiC in austenite at two different temperatures namely, 1223 and 1423 K are presented in Table 4.3.11 for some of the steel composites. The equilibrium solubility product values for composites C1 and C2 are lower than the solubility of TiC in austenite indicating that all the TiC particles present in the composites go into solution in the austenite and reprecipitate as the composites are cooled from the normalising temperature. This is because the solubility of TiC in austenite decreases as the temperature decreases. The equilibrium solubility products for composites C3 to C8 are more than that for TiC solubility in austenite at both 1223 and 1423 K. This indicates that all the TiC present in the composites does not go into solution at the austenitising temperature under consideration. Presumably the coarse TiC particles are the ones which remain undissolved in the

Table 4.3.11

Solubility product and solubility of TiC in austenite

Composite No.	Solubility product	Solubility of TiC in austenite	
		1223 K	1423 K
C1	1.5064×10^{-4}	5.6198×10^{-4}	6.0893×10^{-3}
C2	1.59×10^{-4}	5.2548×10^{-4}	5.7372×10^{-3}
C3	0.02214	1.0343×10^{-3}	1.0460×10^{-2}
C4	0.0441	1.2031×10^{-3}	1.1962×10^{-2}
C5	0.1748	2.5345×10^{-3}	2.3164×10^{-2}
C6	0.3451	1.9023×10^{-3}	1.7959×10^{-2}
C7	0.0863	2.7144×10^{-3}	2.4616×10^{-2}
C8	11.1093	3.1867×10^{-2}	0.2189

austenite. Such observations have been made by K.A.El-Fawak-hry et al.,[49] while characterising vanadium and titanium micro alloyed steels.

The coarsening of TiC particles in steel composites can be seen (Table 4.3.4) when austenitising temperature is increased from 1223 to 1423 K. For example, in composites C4 and C5 the counts for particles below 8μm decreases as the austenitising temperature increases. Further, there is an increase in volume percent of coarse carbide particles.

SEM - EDAX analysis

SEM-EDAX analysis of carbide particles, carbide/matrix interface and inclusions has been carried out. The analysis of some of the inclusions present in the composites as given in Table 4.3.6 shows that Ti is associated with sulphide inclusions. This indicates that TiC participates in chemical reaction with the inclusions. In literature association of Ti with sulphide inclusions has been reported [49]. The carbide analysis has shown that upto 4 wt pct Fe is present in some of the carbides. The interface between carbide and matrix was analysed with a view to find any segregation of elements at the interface. In case of aluminium metal matrix composites presence of Mg, Zr or P etc., has been known to segregate at carbide/matrix interface [1, 104]. The data presented in Table 4.3.7 do not show any

clear indication for such segregations in TiC reinforced steel composites.

Mechanical properties

Tensile properties of a few TiC reinforced steel composites have been presented in Table 4.3.8. There is significant increase in UTS of composites from 37 kg/mm^2 (composite C1) to 79 kg/mm^2 (composite C5). The titanium content of composites varied from 0.0028 wt pct (composite C1) to 0.2974 wt pct (composite C5). The carbon content also increased simultaneously from 0.0538 wt pct (C1) to 0.5877 wt pct (C5). The improvements in UTS beyond 0.3 wt pct Ti has not been very significant. This type of trend in steels containing titanium have been reported by Irvine et al., [47]. TEM photographs of composites C4 and C5 (Fig. 4.3.8 and Fig. 4.3.10) show presence of submicron size precipitates of TiC. Therefore, the improvement in strength properties in low Ti containing composites may be due to precipitation strengthening of the matrix by TiC precipitates. The precipitation hardening of Ti microalloyed steels are well known and have been studied extensively [45, 105, 106]. Composites containing beyond 0.3 wt pct Ti have coarser TiC particles (Fig. 4.3.7) of composite C8). The coarser particles are cuboidal in morphology. Therefore, there is no significant increase in UTS beyond 0.3 wt pct Ti. The values of percent elongation and reduction in area have decreased in composites containing Ti beyond 0.3 wt pct. The SEM

photographs of tensile fracture (Fig.4.3.14 to Fig. 4.3.16) have shown ductile fracture. The dimples formed are deep in case of low Ti composite while, they are shallow for high titanium composite. This indicates a deterioration of ductility as the titanium content increases, which is corroborated by the results of the tensile tests.

The impact test results also show that the toughness deteriorates as the titanium content is increased (Table 4.3.9). The TEM photographs of composite C5 (Fig. 4.3.10) which had shown low impact test values (15 joules) show the presence of continuous films of grain boundary precipitates. Simultaneously coarse cuboidal TiC particles can also be seen in the sample under light microscope. The high tensile strength of this composite is derived from the combined effects of grain boundary precipitation, TiC dispersion and a relatively high carbon content. The fractured surfaces of impact test specimens of C1 and C4 have shown the formation of dimples around inclusions (Fig. 4.3.17 and Fig. 4.3.18, respectively). The scale of melting operation being small the inclusions do not get adequate chance to float up. Since Ti is also a deoxidiser and sulphide modifier new inclusions are also formed during dissolution of the master alloy. Effective removal from the liquid composite alloy prior to filling the mould may considerably reduce its inclusion content and improve the toughness.

4.3.3. Conclusions

Following major conclusions have been drawn from the investigations on TiC reinforced steel composites.

a)   It has been possible to prepare TiC reinforced steel composites by dissolution of TiC rich Fe-TiC master alloy in a plain carbon and alloy steel melts in an induction furnace. The titanium content of the composites could be varied from 0.0028 to 0.7 wt pct by increasing the dose of master alloy addition. The recovery of titanium from the master alloy into the melt is of the order of 25 percent.

b)   It is also possible to prepare a high titanium and high carbon steel composite with titanium recovery over 26 pct by reacting a Fe-TiC master alloy with iron ore in an induction melting furnace.

c)   TiC particles in the composites undergo coarsening as the normalising temperature is increased from 950 to 1150°C. But austenite grain growth is restricted.

d)   Ultimate tensile strength increases from 37 to 79 kg/mm^2 as the Ti content increases from 0.0028 to 0.3 wt pct. Of course, the carbon content also increases simultaneously from 0.0538 to 0.5877 wt pct due to incorporation of carbon from the master alloy. The low carbon, low titanium composites possess satisfactory toughness.

4.4 WEAR CHARACTERISTICS OF TiC REINFORCED COMPOSITES

In this section the results of the abrasive and adhesive wear tests are presented followed by a discussion and conclusions.

4.4.1 Results

Abrasive and adhesive wear tests have been carried out by adopting pin on disc method. The abrasive wear tests were conducted by using the composites as a pin and allowing it to abrade against a rotating grinding (alumina) wheel under a specified load. In the case of adhesive wear the composite specimen pin was made to slide against a rotating hardened steel disc (hardness Rc 62) under a predetermined load.

The results of wear tests have been presented under separate heads as follows:

i)   Metallurgical characteristics of TiC reinforced cast iron composites

ii) Metallurgical characteristics of TiC reinforced steel composites

iii) Abrasive wear characteristics of cast iron composites

iv) Adhesive wear characteristics of cast iron composites

v)   Adhesive wear characteristics of steel composites, and

vi) Abrasive wear characteristics of steel composites

The details of the investigations are as follows:

Metallurgical characteristics of TiC reinforced cast iron composites.

TiC reinforced cast iron composites B1, B5 and B10 were tested for abrasive wear. Chill cast specimens were used for the tests. Two standard chromium cast irons S1 and S2 were also tested to compare the wear data. The chemical composition of chromium cast irons are presented in Table 4.4.1.

The chemical composition of TiC reinforced cast iron composites have been presented in Table 4.2.1 and Table 4.2.2. The photomicrographs of TiC reinforced cast iron composites B1 and B5 are presented in Fig. 4.2.1, and Fig. 4.2.3, respectively. It may be noted from the microstructures that the composites contain mostly transformed austenite (pearlite), eutectic carbide and dispersed TiC particles. The size distribution of TiC particles in the composites are presented in Table 4.2.5 to Table 4.2.8. The histograms (Fig. 4.4.1 to Fig. 4.4.3) present carbide particle size distribution for composites B1, B5 and B10. It may be noted from the histograms that as the titanium content in the composites increases, the volume fraction of the coarser carbide particles also increases. A considerable number of particles are below 8 μm (noted as undersize count).

Table 4.4.1

Chemical analysis of the standards used in wear tests

Standard No.		Wt pct						
	C	Cr	Mn	Si	Al	Ti	Cu	Remarks
S1	3.43	12.50	0.93	1.00	0.01	0.03		
S2	3.30	12.00	2.45	0.98	0.01	0.03		300 ppm N
S3	3.36	−	0.25	2.24	−	−	0.945	P&S <0.02
S4	0.32	0.66	0.70	0.39	<0.01	<0.01	0.02	0.27 Mo,
								0.04 Ni, P&S 0.023 each.

Under size count=749
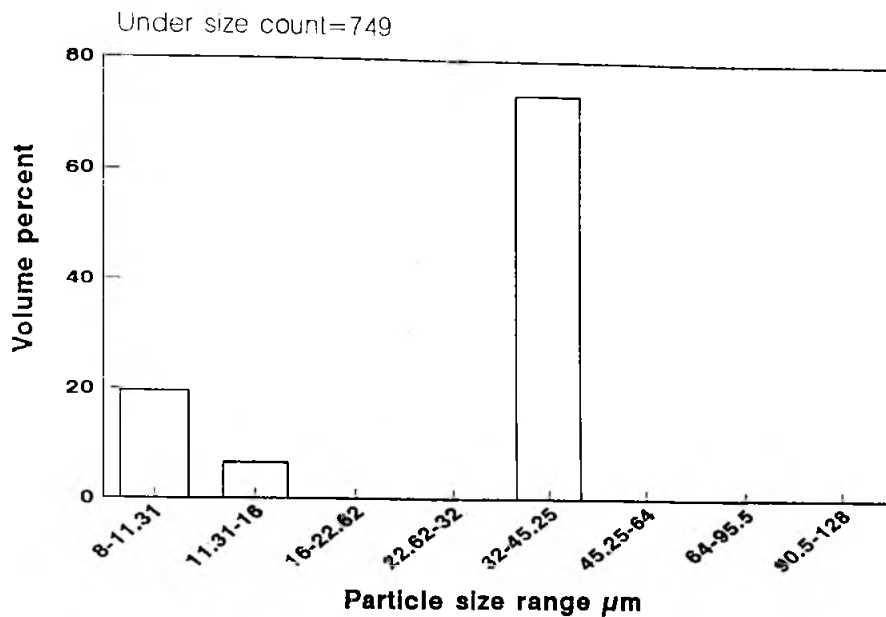
Fig.4.4.1 Titanium carbide particle size distribution
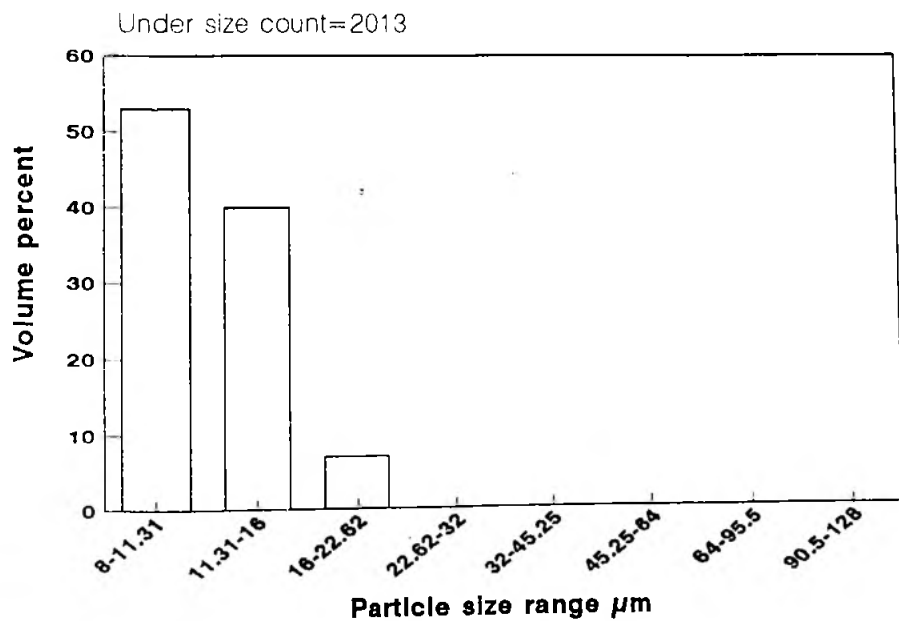
(Specimen B1),320X

Under size count=2013

Fig.4.4.2 Titanium carbide particle size distribution

(Specimen B5),320X
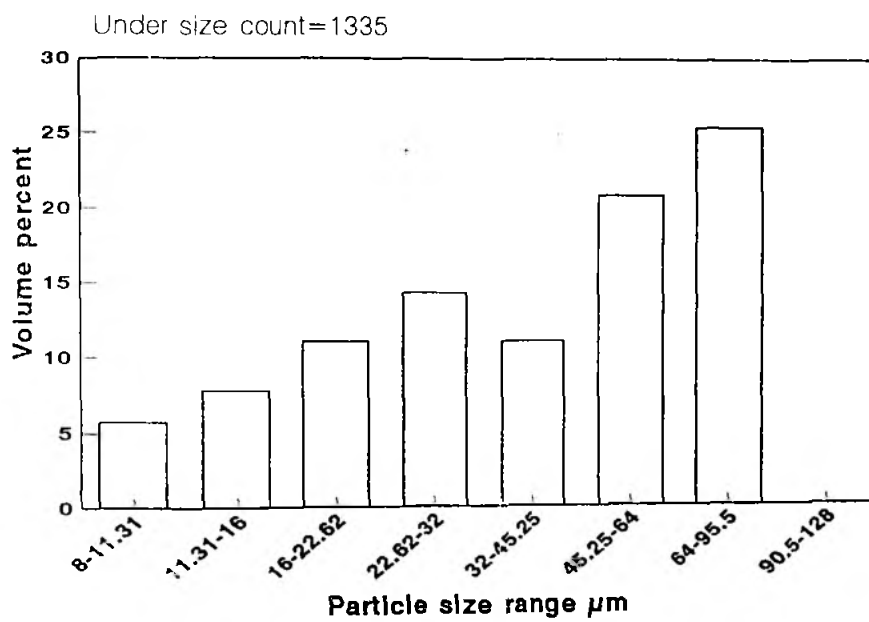
Under size count=1335

Fig.4.4.3 Titanium carbide particle size distribution

(Specimen B10),320X

Adhesive wear test of TiC reinforced cast iron composites have been carried out for six specimens of different titanium contents, Five of them namely, B2, B3, B4, B6 and B7 were normalised after soaking the composite specimen at 950°C for 4 hours. The composite specimen B12 was normalised after soaking at 1000°C for 6 hours. The chemical composition of these composites have been presented in Table 4.2.1 and Table 4.2.2. A spheroidal graphitic cast iron (S3) sample was also tested for adhesive wear for the purpose of comparison. The chemical analysis of the SG iron (S3) is given in Table 4.4.1.

The photomicrographs of the composites B2, B3 and B7 are presented in Fig. 4.4.4 to Fig. 4.4.6. The microstructure of composites B4, B6 and B12 are presented in Fig. 4.2.2, Fig. 4.2.4 and Fig. 4.2.6, respectively. The microstructures show the presence of pearlite, eutectic carbide and graphite. The TiC is distributed in the pearlite matrix. It also remains entrapped in the eutectic carbide. The details of the microstructures of these composites are presented in Table 4.2.3. The histograms presenting carbide particle size distribution for composites B2, B3, B4, B6, B7 and B12 are shown in Fig. 4.4.7 to Fig. 4.4.12. It may be seen from the figures that the counts for carbide particles below 8 μm are quite high.
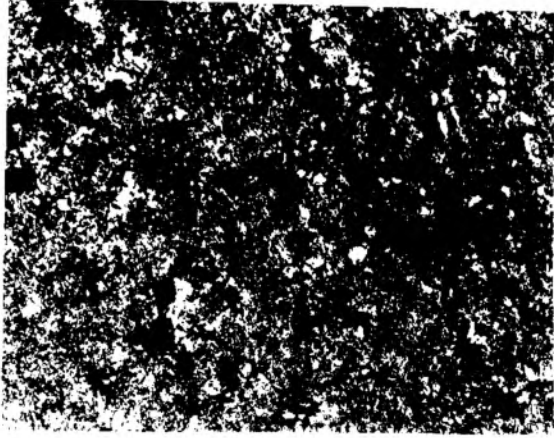
Fig.4.4.4 Cast iron composite B2, normalised
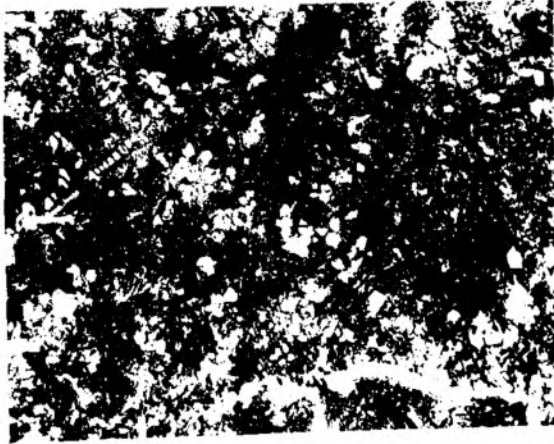from 950°C after 4 h soaking,
200 X.

Fig.4.4.5 Cast iron composite B3, normalised
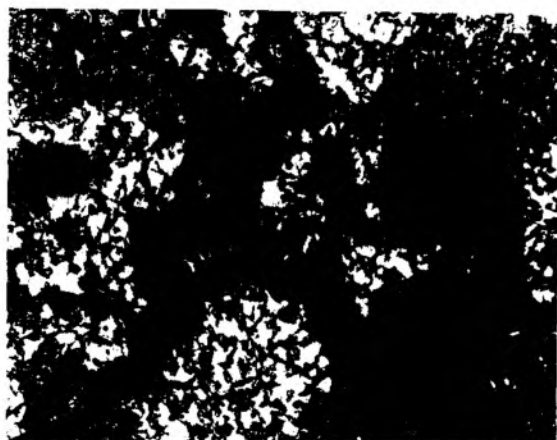from 950°C after 4 h soaking,
100 X.

Fig.4.4.6 Cast iron composite B7, normalised
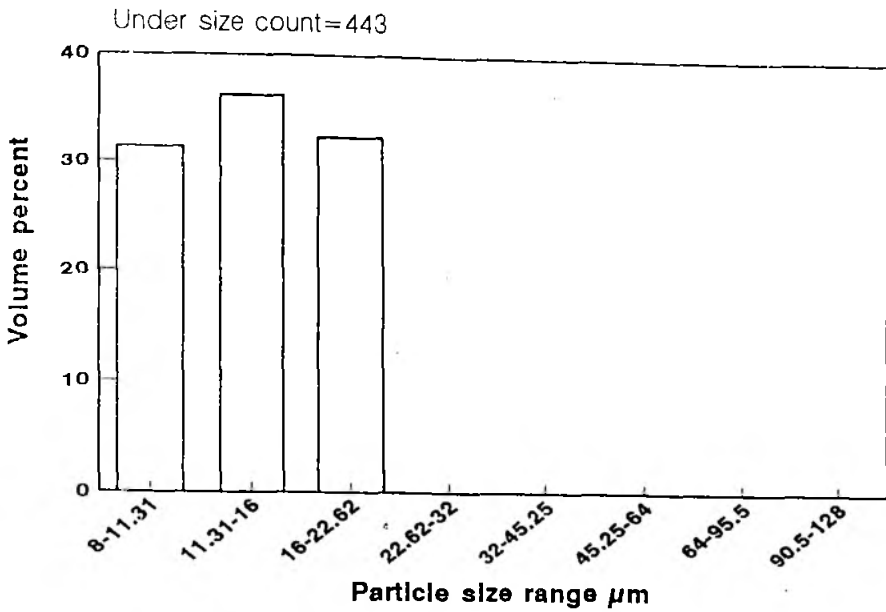   from 950°C after 4 h soaking,
        200 X

Under size count=443

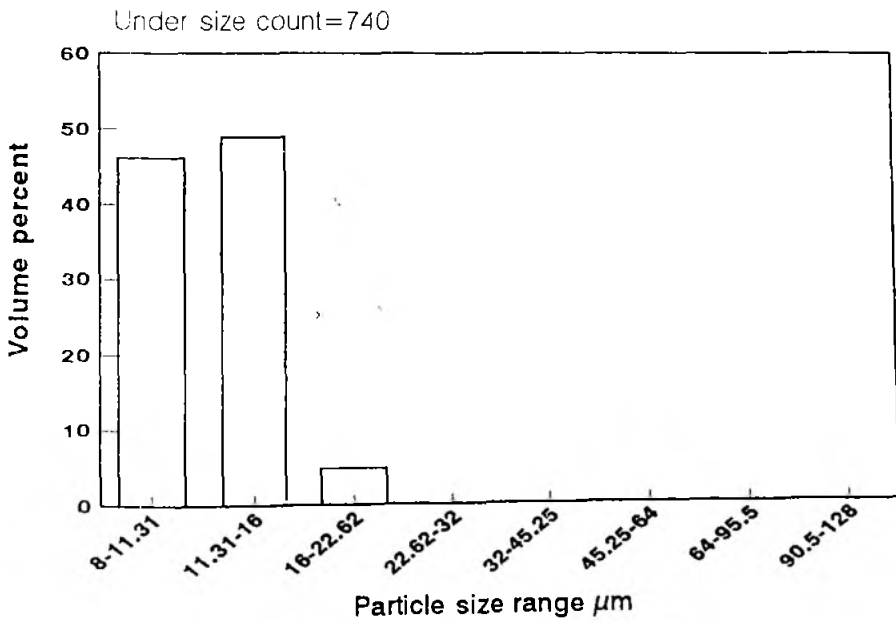Fig.4.4.7 Titanium carbide particle size distribution
(Specimen B2),160X

Under size count=740

Fig.4.4.8 Titanium carbide particle size distribution
(Specimen B3),160X

Under size count=850
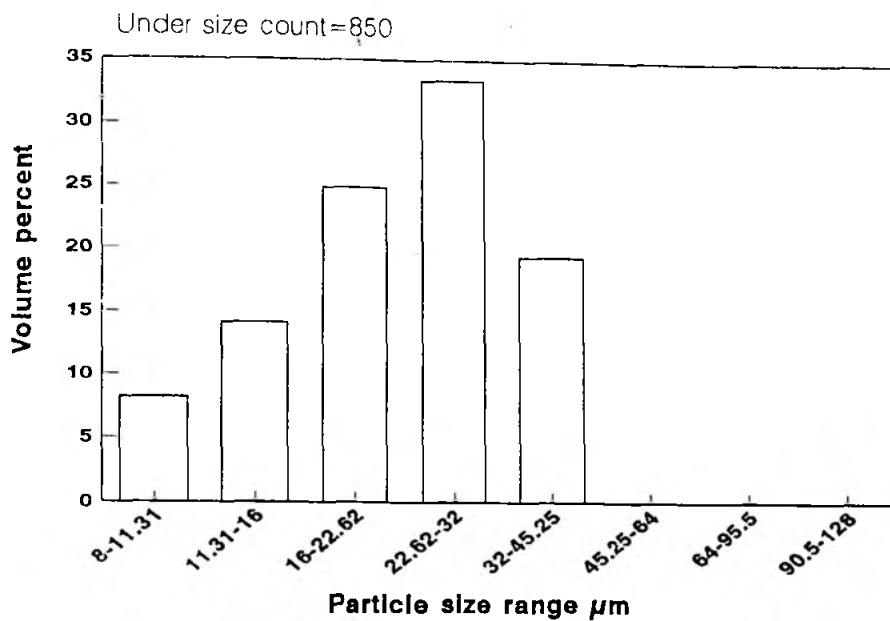
Fig.4.4.9 Titanium carbide particle size distribution
(Specimen B4),160X

Under size count=553

Fig.4.4.10 Titanium carbide particle size distribution
(Specimen B6),160X
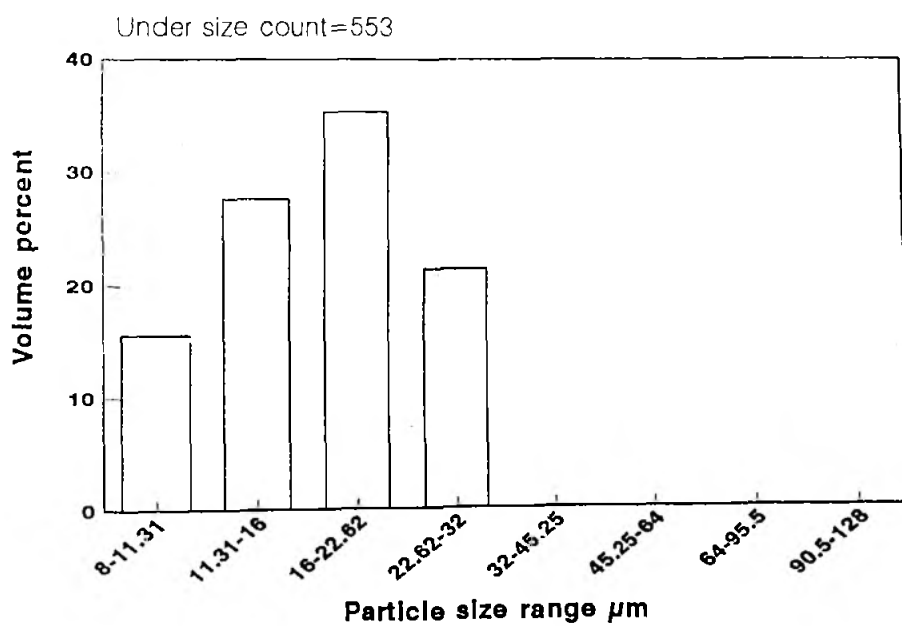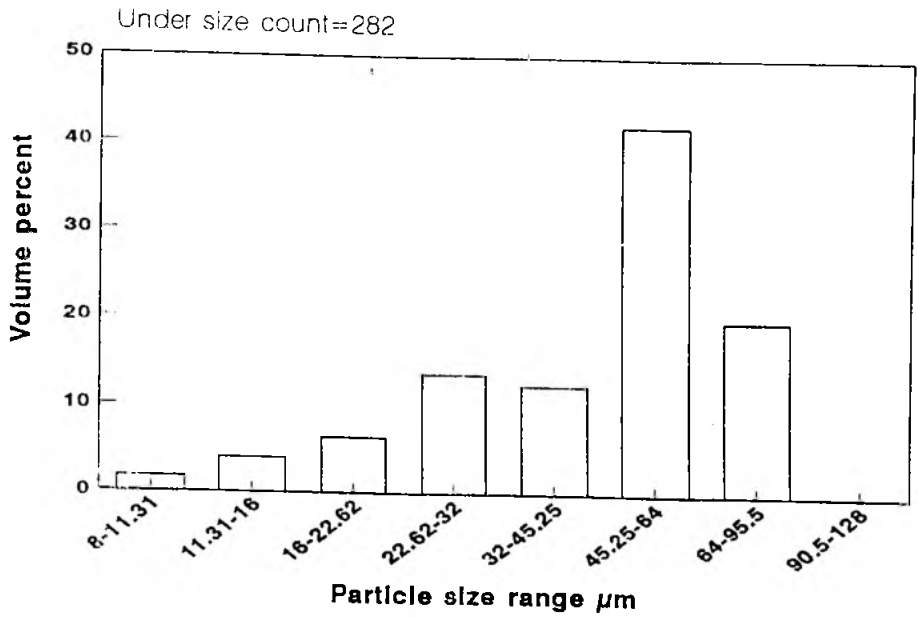
Under size count=282

Fig.4.4.11 Titanium carbide particle size distribution
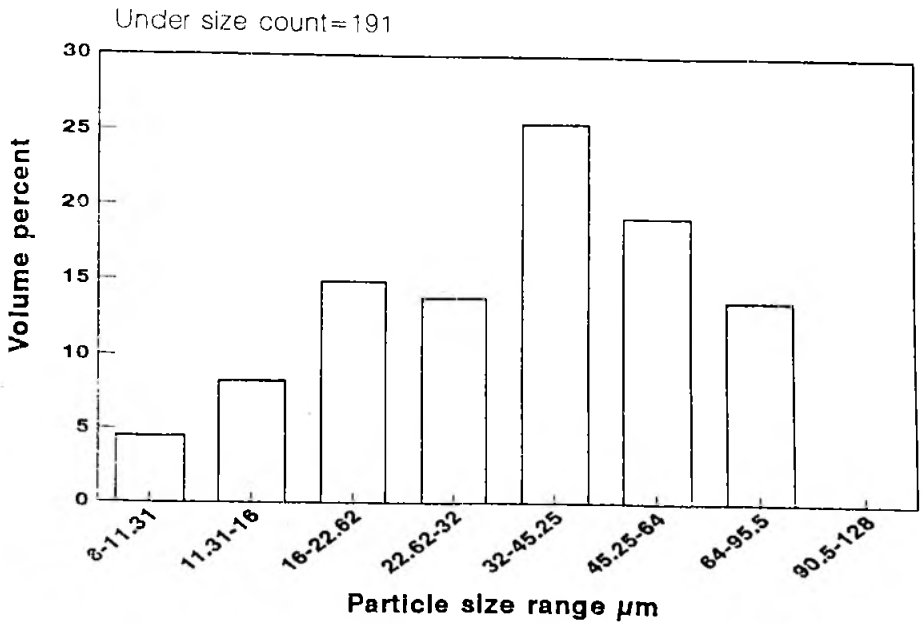(Specimen B7),160X

Under size count=191

Fig.4.4.12 Titanium carbide particle size distribution
(Specimen B12),80X

Metallurgical characteristics of TiC reinforced steel composites

TiC reinforced steel composites C6 and C7 were tested for adhesive wear. The specimens were oil quenched after soaking at 950°C for 30 minutes and then tempered at 150 °C for 1 hour. The chemical analysis of the steel composites are presented in Table 4.3.1. The microstructures of the composites C6 and C7 show the distribution of carbide particles in the pearlite matrix. A standard low alloy steel (S4) was tested for adhesive wear for comparison. The chemical analysis of the standard steel S4 is presented in Table 4.4.1. Prior to carrying out the wear test, the steel specimen S4 was also oil quenched after soaking at 950°C for 30 minutes and tempered at 150°C for 1 hour.

The abrasive wear tests were carried out on TiC reinforced steel composites C6 and C7. These were normalised after soaking at 950°C for 2 hours. The composite C7 was tested in two heat treated conditions, namely, a) normalised condition (as mentioned above) and b) oil quenched and tempered condition (oil quenched after soaking at 950°C for 30 minutes and tempered at 150°C for 1 hour).

Abrasive wear characteristics of TiC reinforced cast iron composites :

The abrasive wear tests of composites B1, B5 and B10, and those of two standard chromium cast irons were

Fig.4.4.13 Wear rate Vs sliding distance (4.9N load)
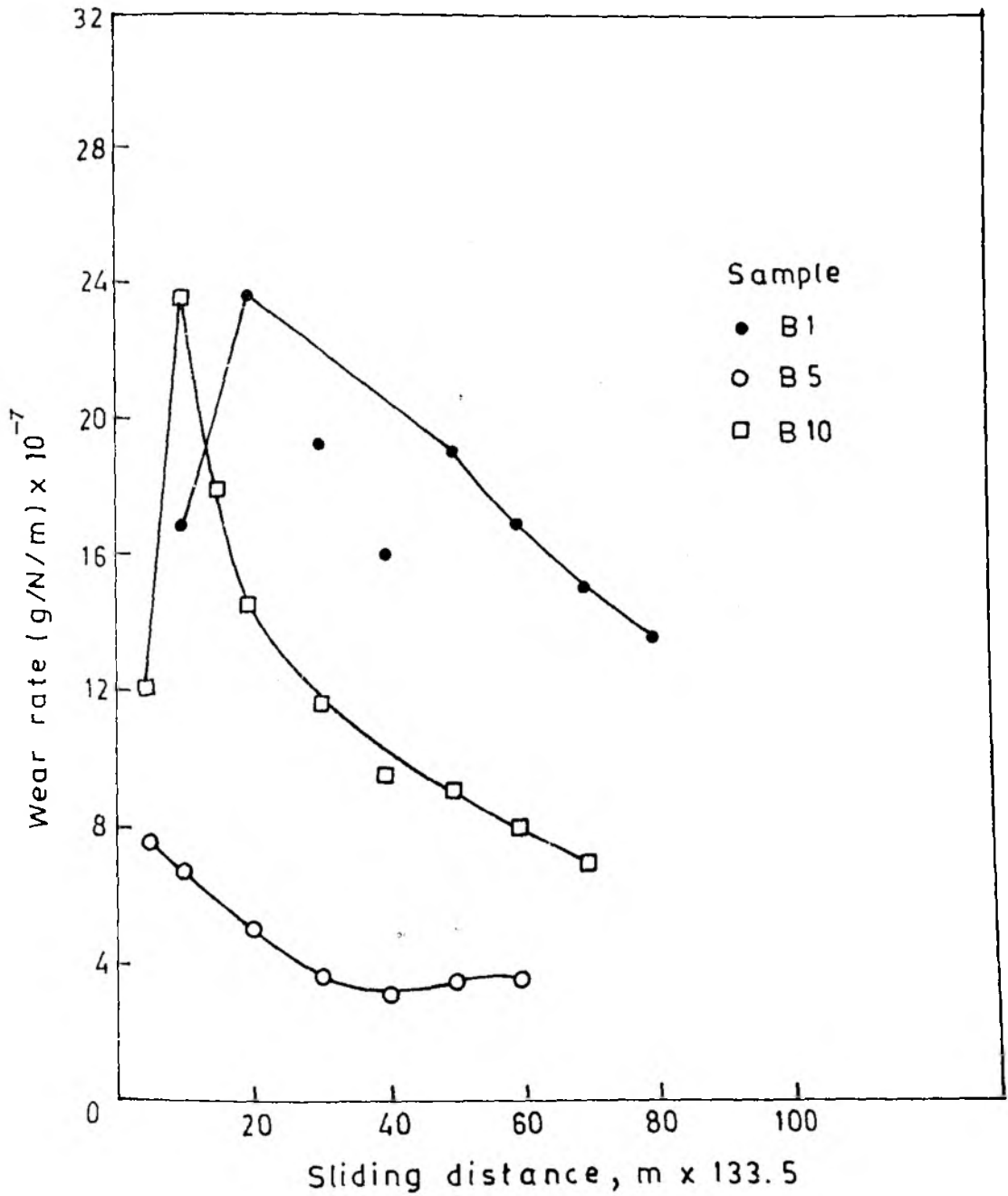
Fig.4.4.14 Wear rate Vs Sliding distance (9.8 N load)

Fig.4.4.15 Wear rate Vs sliding distance (14.7N load)

Fig.4.4.16 Cumulative wear Vs sliding distance (4.9 N load)

Fig.4.4.17 Cumulative wear Vs sliding distance (9.8 N load)

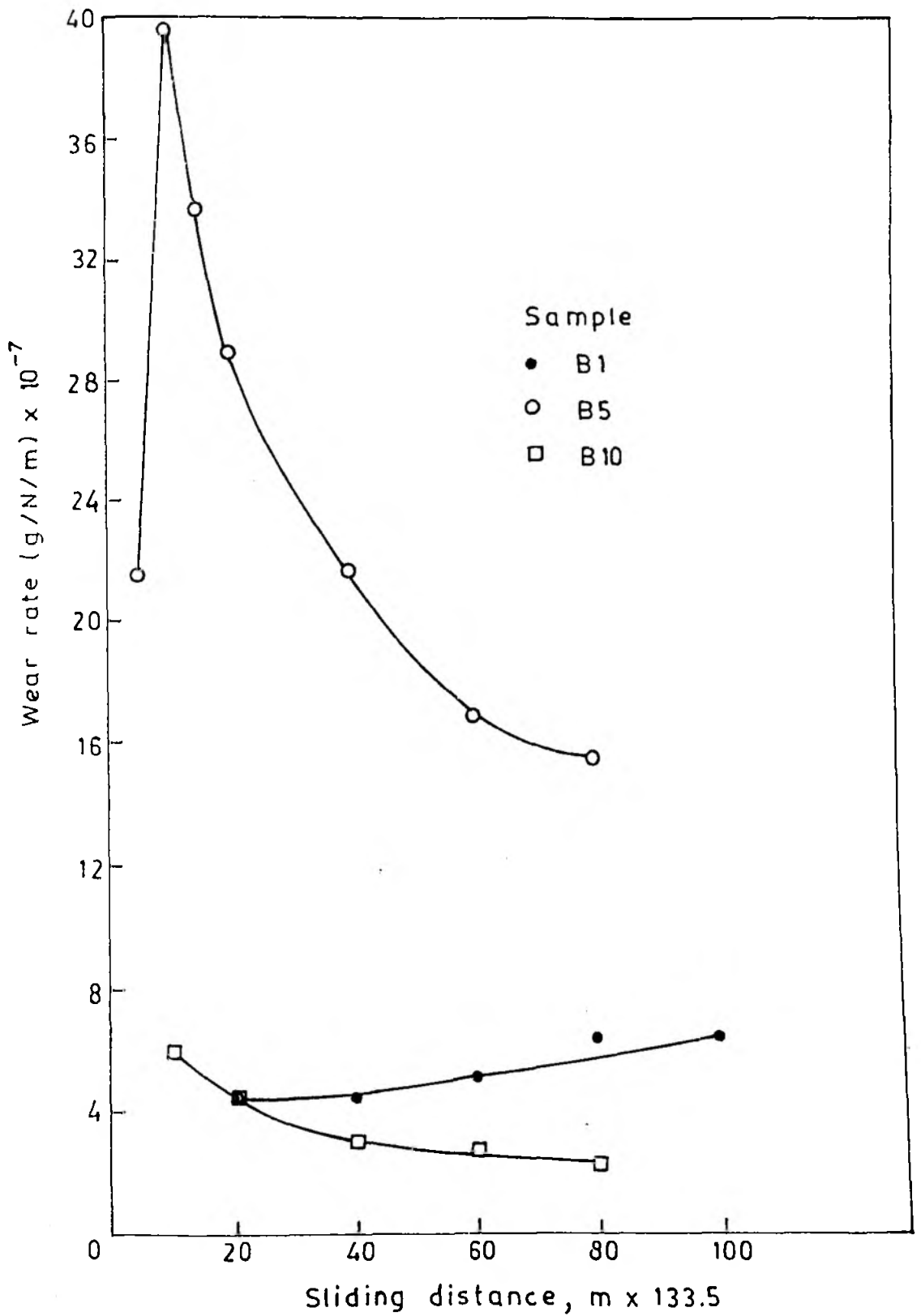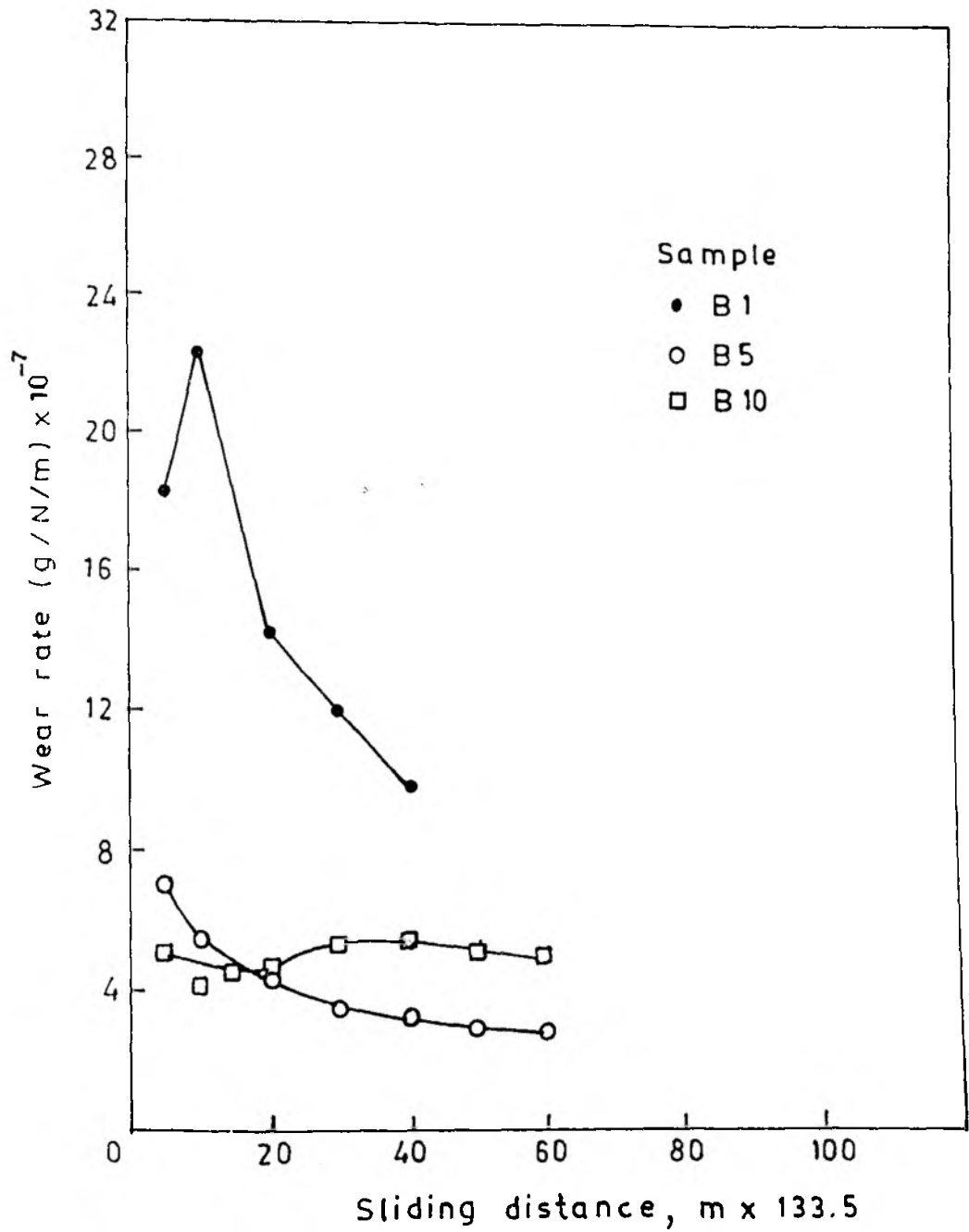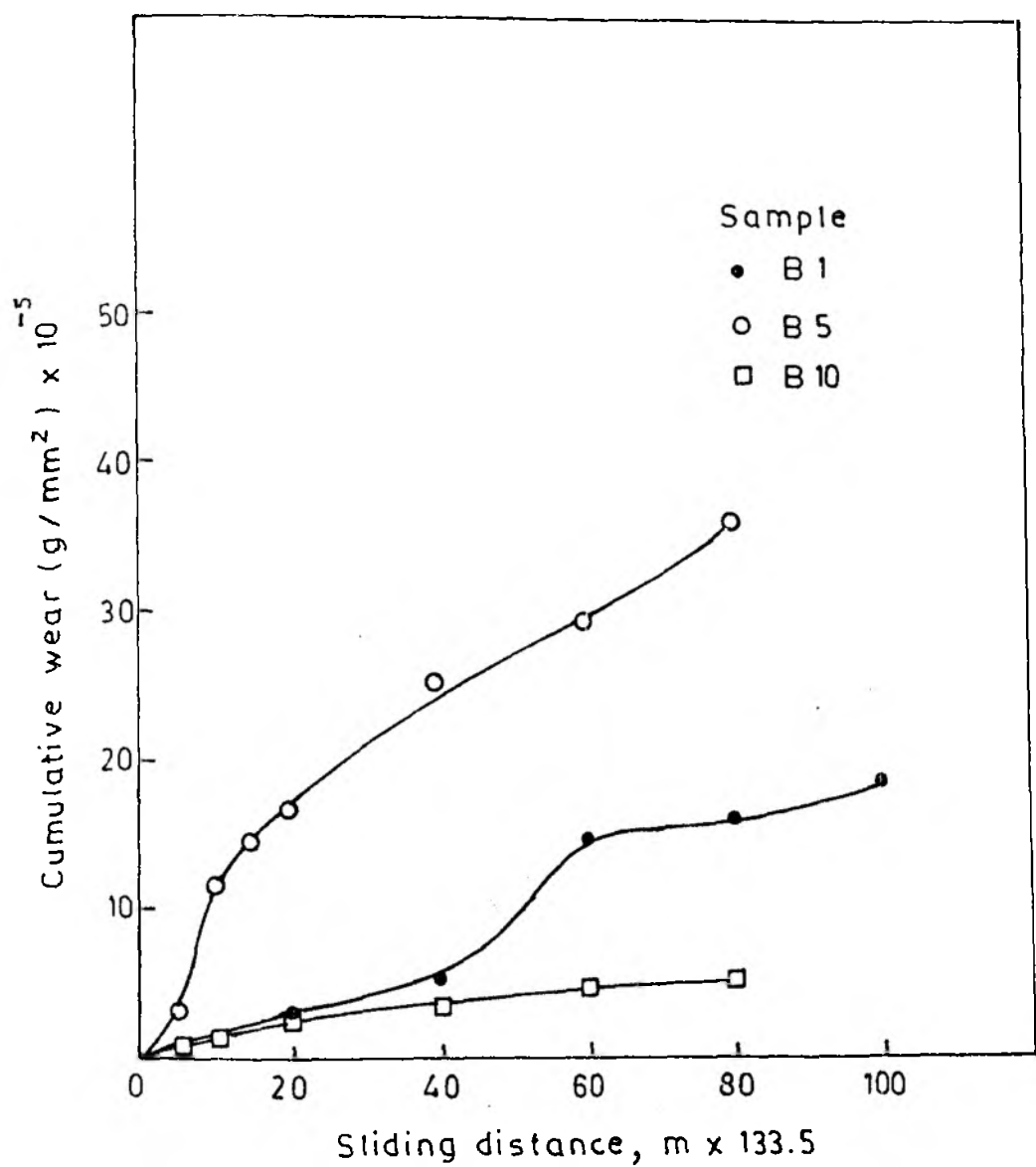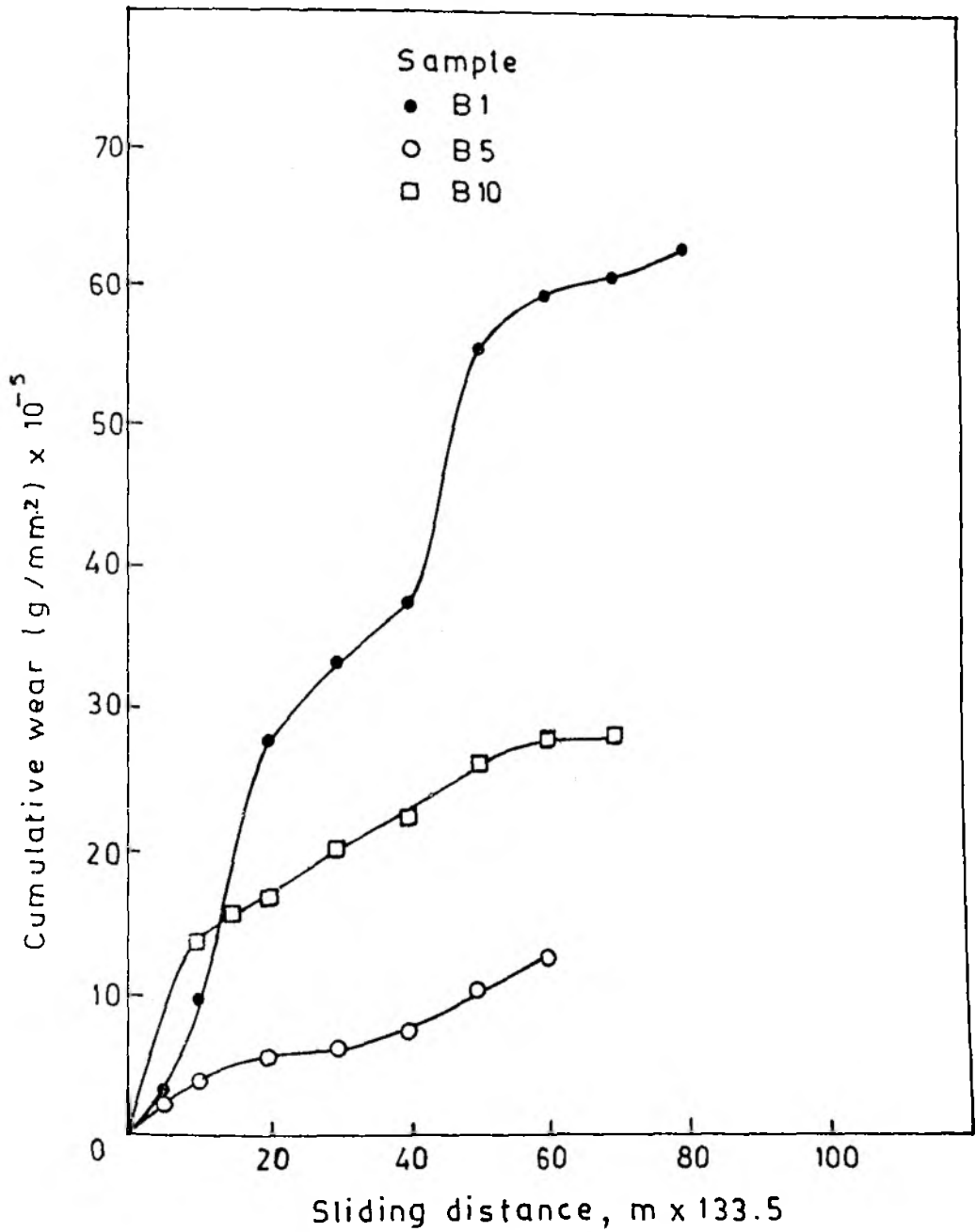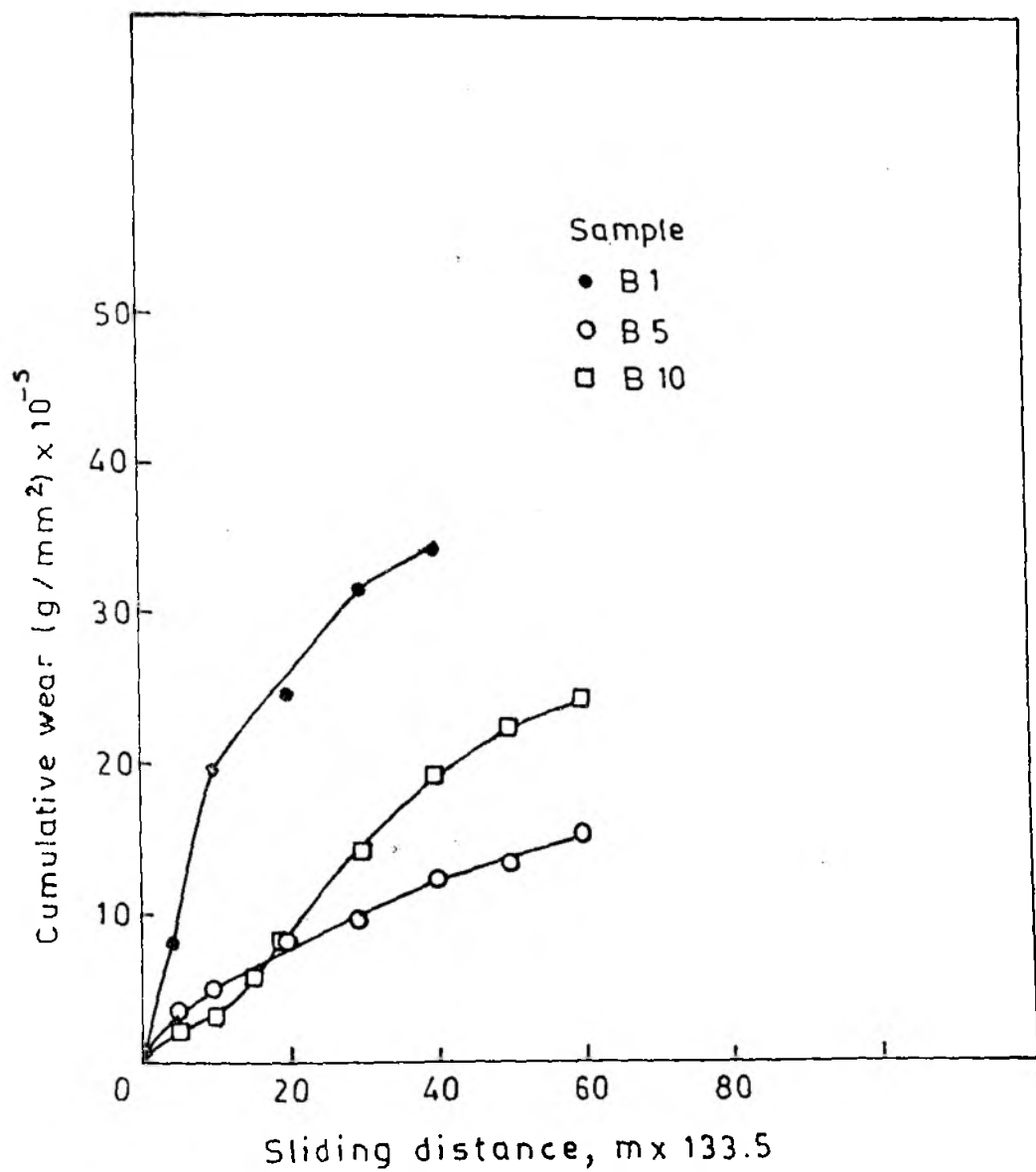Fig.4.4.18   Cumulative wear Vs sliding distance (14.7N load)
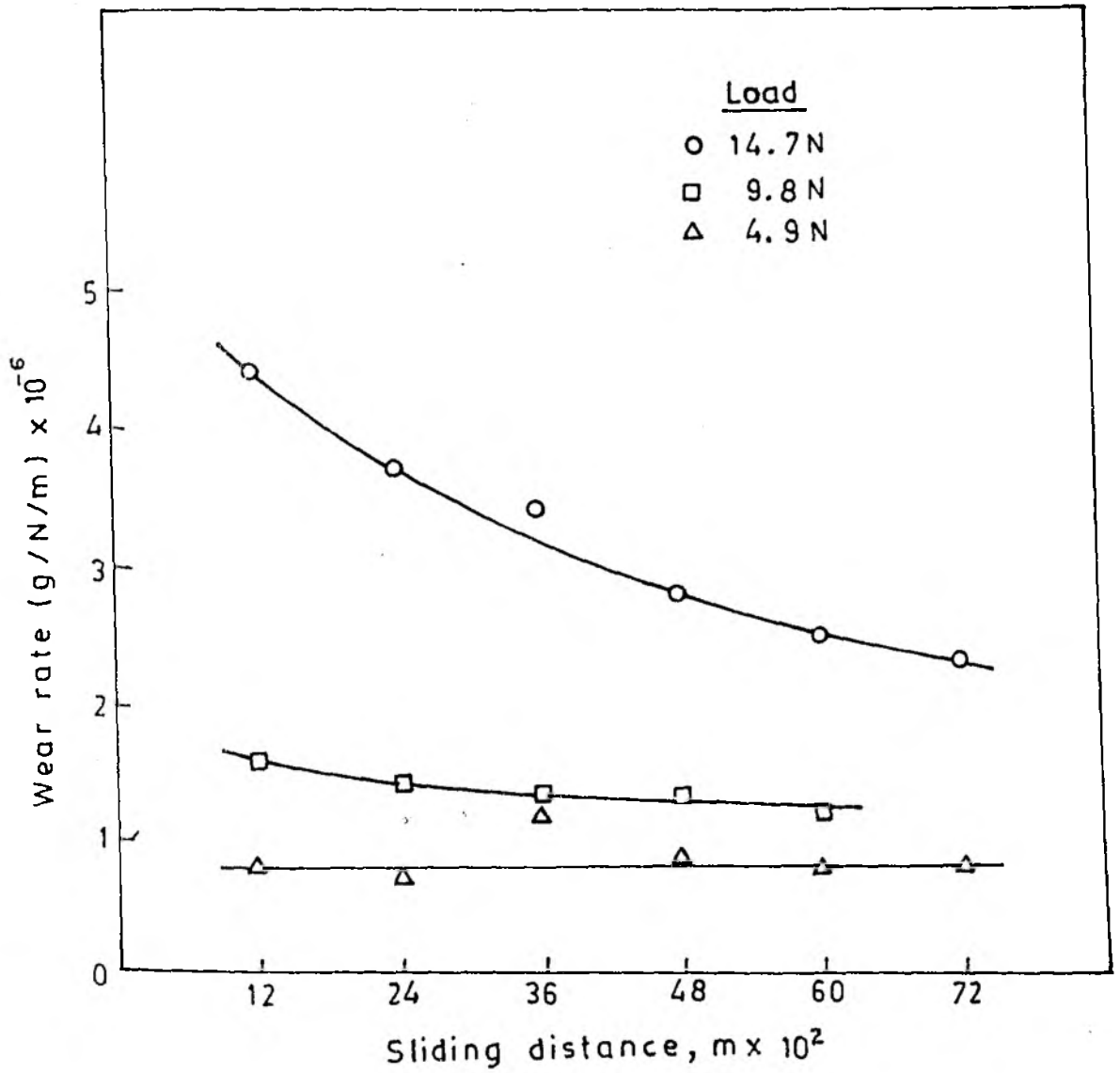
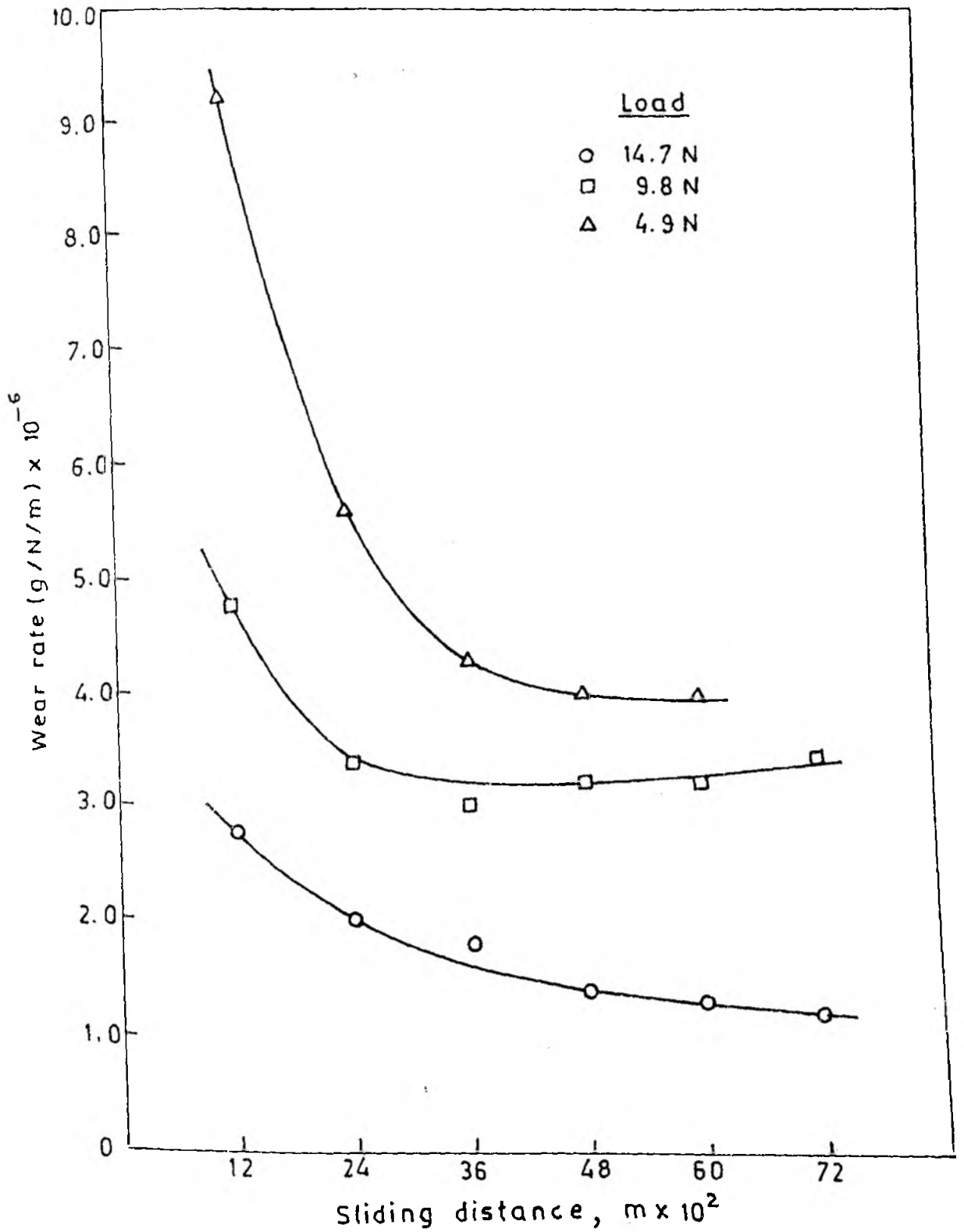Fig.4.4.19 Wear rate Vs sliding distance (Standard S1)

Fig.4.4.20 Wear rate Vs sliding distance (Standard S_2)
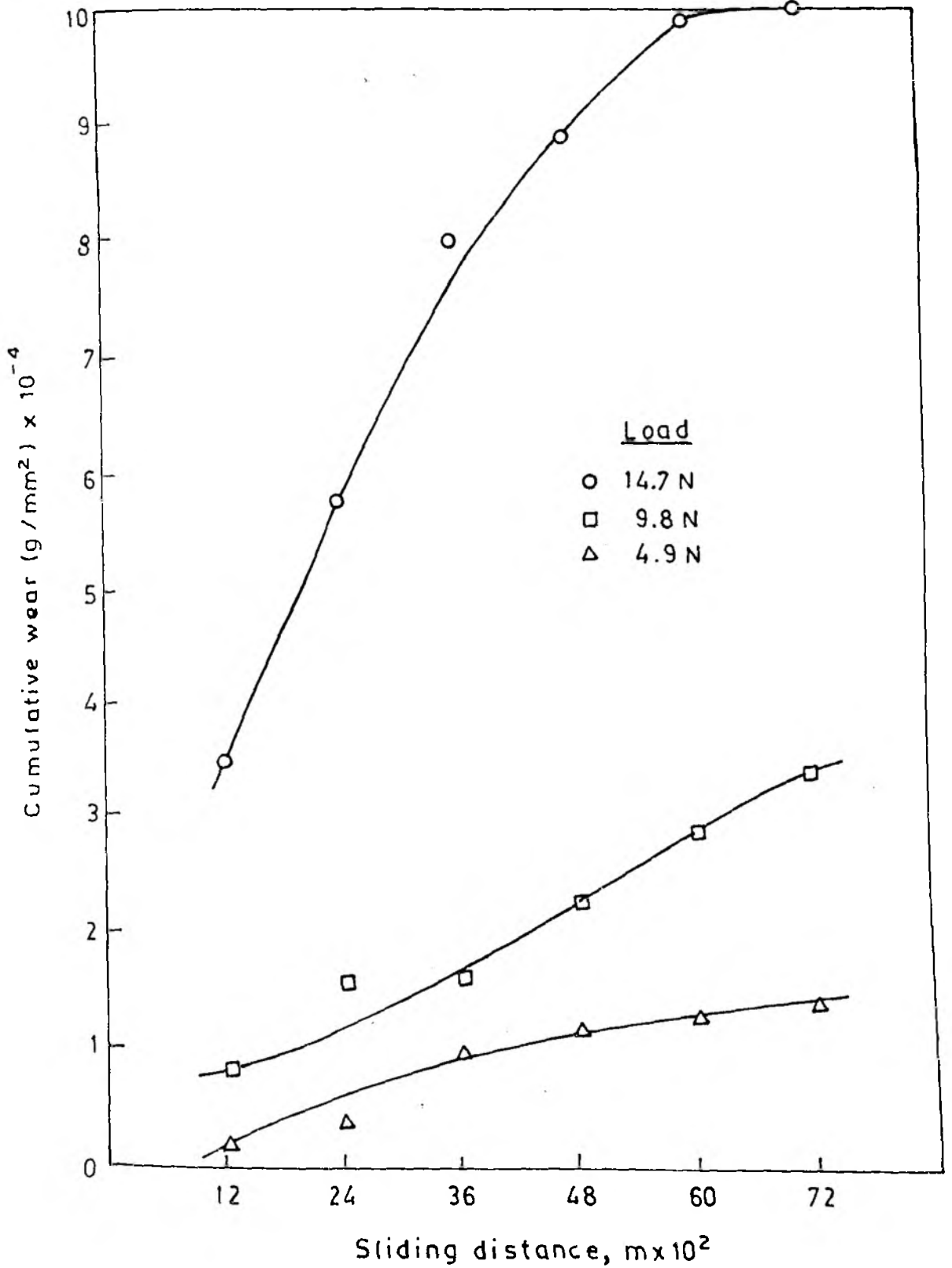
Fig.4.4.21 Cumulative wear Vs sliding distance (Standard S1)
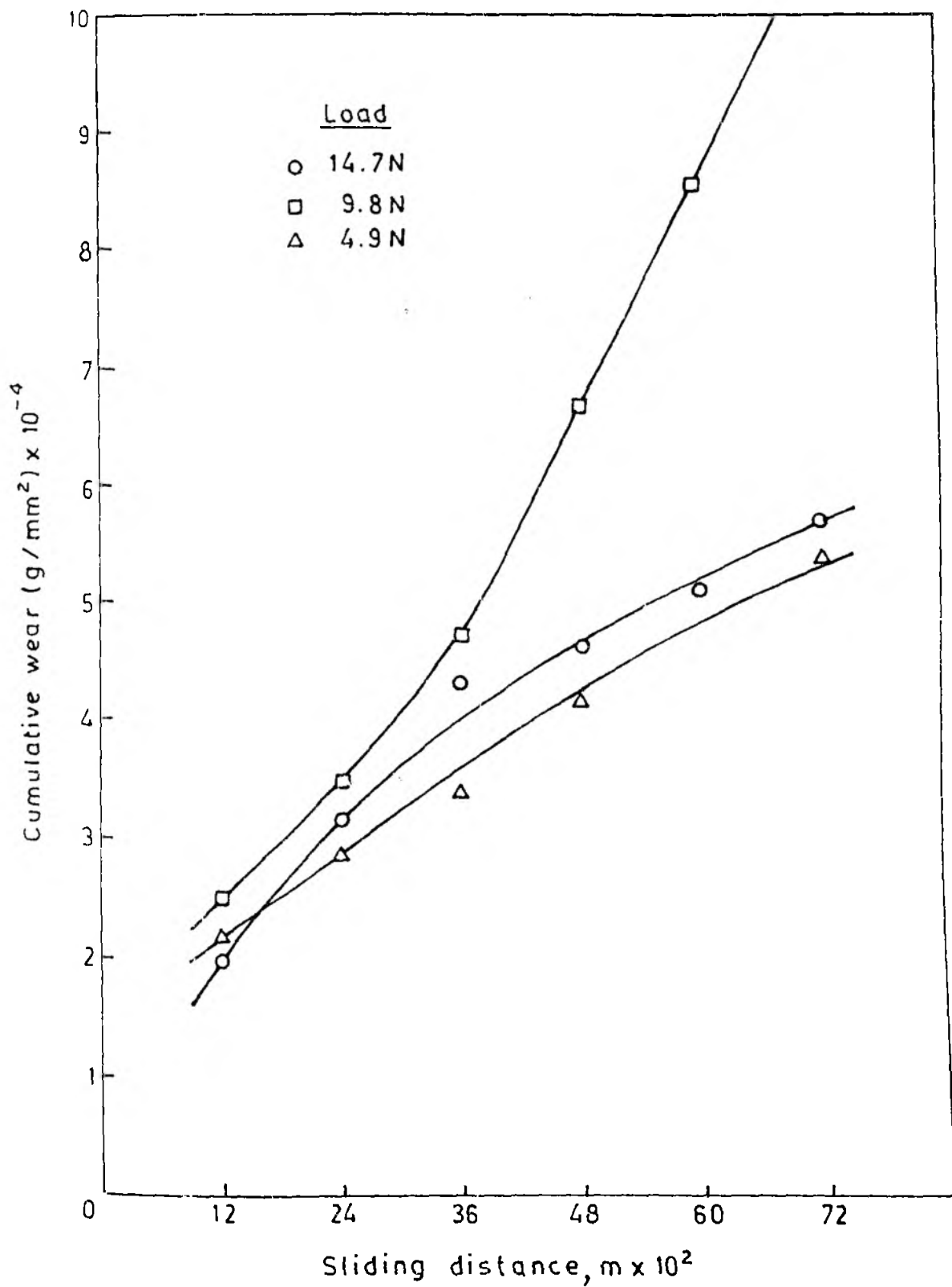
Fig.4.4.22 Cumulative wear Vs sliding distance (Standard S2)

evaluated under identical condition. The tests were carried out under 0.5, 1.0 and 1.5 kg load corresponding to 4.9, 9.8 and 14.7 N load on the composite pin. The sliding speed of each specimen was 133.5 m/min (2.2 m/sec). The test condition was one of high abrasion. The plots of wear rate vs sliding distance for composites B1, B5 and B10 for applied loads of 4.9, 9.8 and 14.7 N are presented in Fig. 4.4.13 to Fig. 4.4.15. It may be seen from the plots that wear rate is low for composite B5 at loads of 9.8 and 14.7 N, while it is high for composite B1. On the other hand wear rate is low for composite B10 at 4.9 N load, while it is high for composite B5. The plots of cumulative wear vs sliding distance are presented at 4.9, 9.8 and 14.7 N load for composite specimens in Fig. 4.4.16 to Fig. 4.4.18. The plots have trends similar to those of wear rate vs sliding distance. Wear rate vs sliding distance plots for standard chromium cast irons S1 and S2 are presented in Fig. 4.4.19 and Fig. 4.4.20 for all the three loads. The plots of cumulative wear vs sliding distance for standard chromium cast irons S1 and S2 are presented in Fig. 4.4.21 and Fig. 4.4.22, respectively. Comparing the wear data of TiC reinforced cast iron composites with those of standard chromium cast irons, it may be noted that wear rates are one order less for TiC reinforced cast iron composites. Table 4.4.2 indicates the hardness of the composite samples before and after the abrasive wear test. Composites B1 and B10 have shown an increase in hardness at the end of wear test whereas, composite B5 has shown a slight decrease. The SEM photograph of

Table 4.4.2

Hardness of composites tested for abrasive wear

Composite No.	Initial hardness (VPN)	Hardness after abrasive test (VPN)	
		4.9 N Load	14.7 N Load
B1	544	684	826
B5	679		620
B10	578	802	

the abraded surface of composite B5 tested at an applied load of 14.7 N is presented in Fig. 4.4.23. It may be noted from the figure that the wear tracks are fairly uniform and are light. At some places pits are observed which may be due to the removal of coarse carbide particles. SEM photographs of the abraded surfaces of the composite B1 and B10 are presented in Fig. 4.4.24 and Fig. 4.4.25, respectively. The wear tracks are deep and at some places pits are observed. The abraded surface of composite B1 appear to be oxidised at some places (Fig. 4.4.24).

Adhesive wear characteristics of TiC reinforced cast iron composites

The adhesive wear tests of the six TiC reinforced cast iron composites namely, B2, B3, B4, B6, B7 and B12, and the SG iron S3 (taken as a standard for comparing data) were carried out on a pin-on-disc machine. The composite specimen pins were held against a rotating hard steel disc of Rc 62 under loads of 6,8 and 10 kg corresponding to 58.8, 78.4 and 98 N load, respectively. The rotation of the disc was kept constant at 600 rpm. The sliding speed of each specimen was 5.5 m/sec. The plots of wear rate vs sliding distance are presented in Fig. 4.4.26 to Fig. 4.4.28 for loads of 58.8, 78.4 and 98 N for TiC reinforced cast iron composites. It may be seen from the figures that composites B4 and B12 have shown lower wear rates at all the loads. In case of composite B12 initial wear rate decreases as the load increases.

Fig.4.4.23 SEM photograph of the worn out
surface of cast iron composite B5
(abrasive wear, 14.7 N applied
load)

Fig.4.4.24 SEM photograph of the of the worn
out surface of cast iron composite
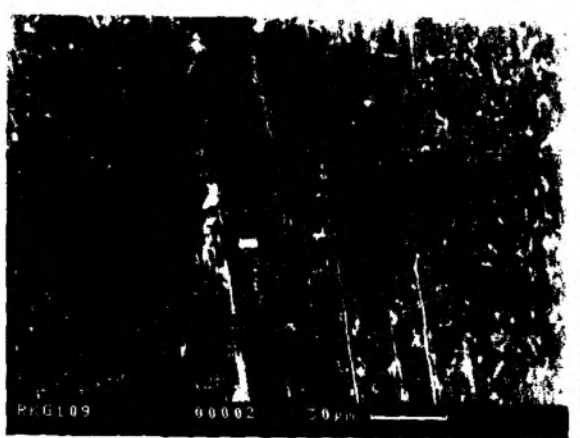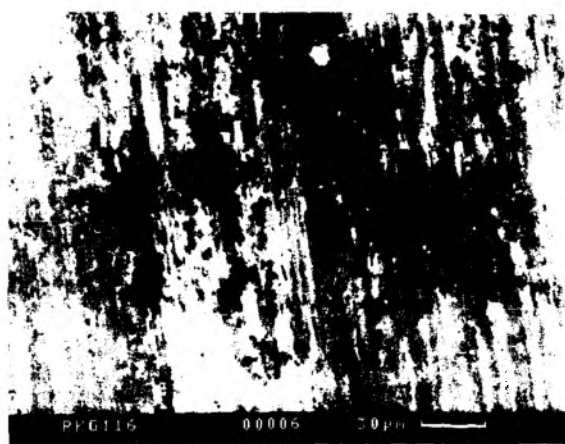B1 (abrasive wear, 14.7 N applied
load)
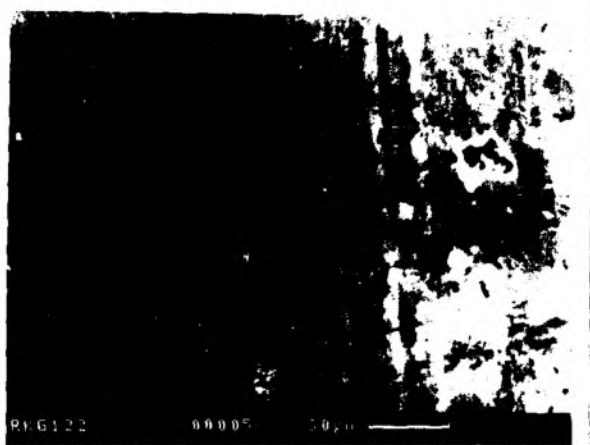
Fig.4.4.25   SEM photograph of the worn out
            surface of cast iron composite
            B10 (abrasive wear, 14.7 N
            applied load)
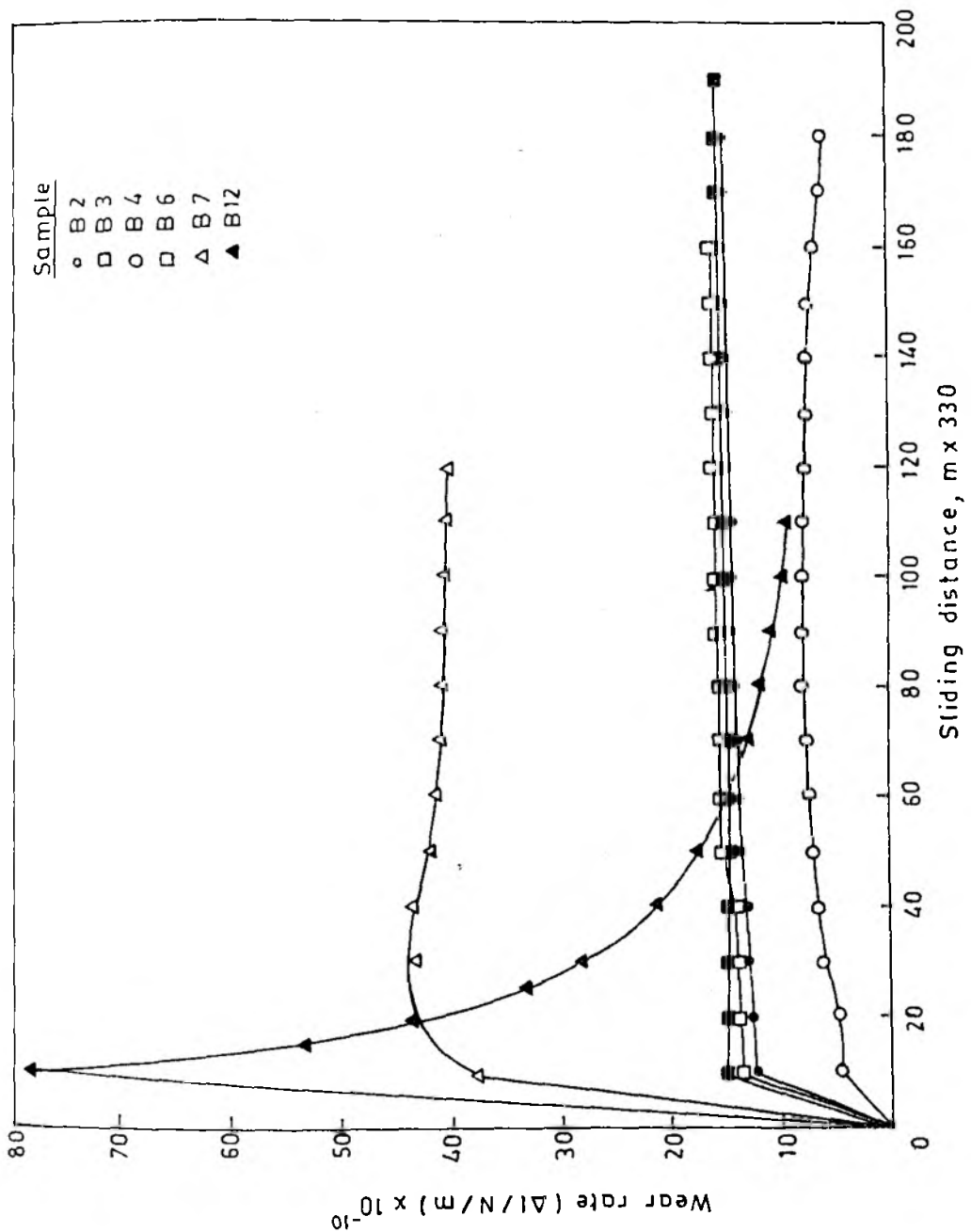
Fig.4.4.26 Wear rate Vs sliding distance (58.8 N load)
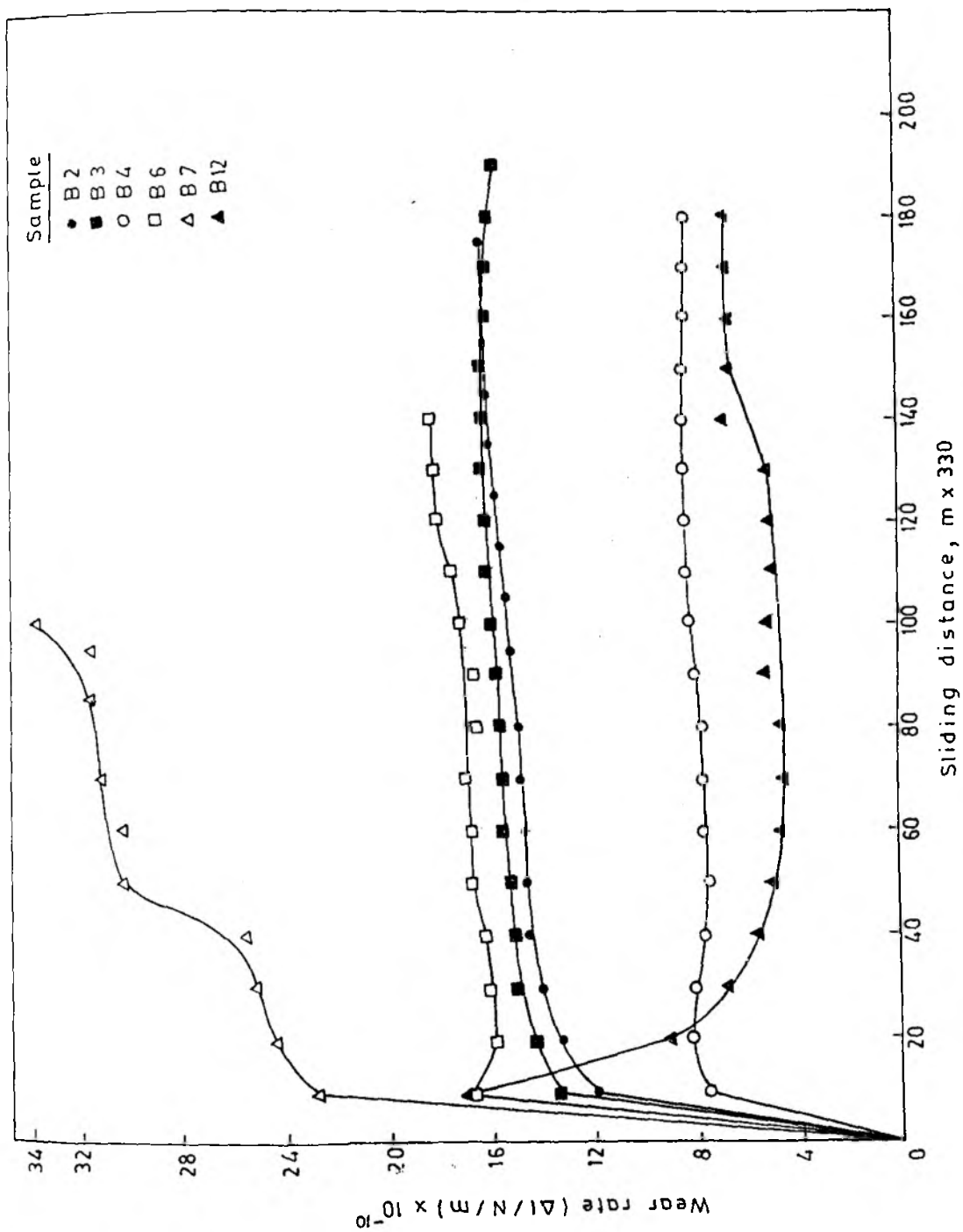
Fig. 4.4.27 Wear rate Vs sliding distance (78.4 N load)
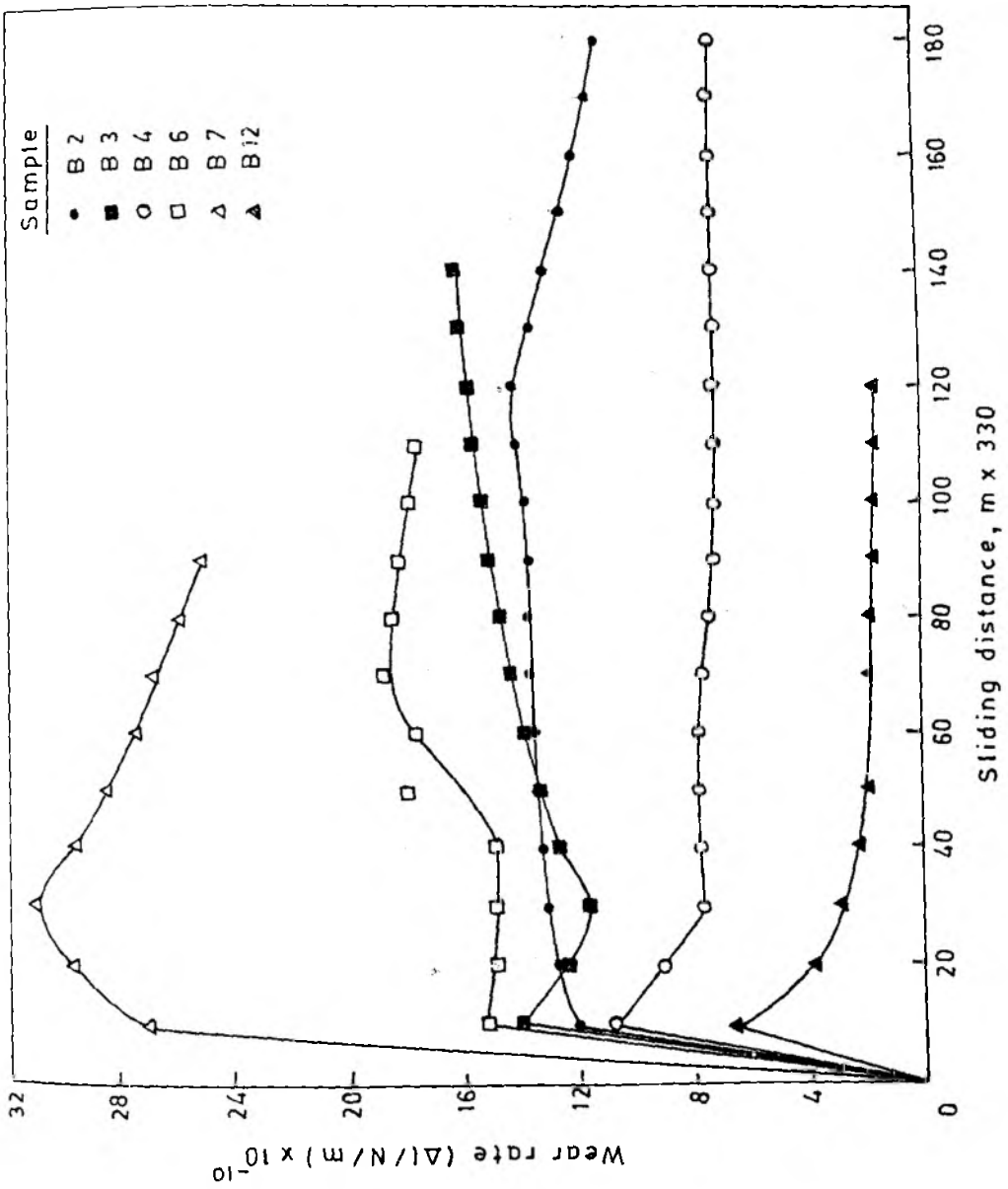
Fig. 4.4.28 Wear rate Vs sliding distance (98 N load)

At higher sliding distance the wear rate is considerably lower for composite B12 for higher loads namely, 78.4 and 98 N. The composites B2, B3 and B6 have shown intermediate wear rates while composite B7 has shown higher wear rates at all the three loads. Wear rate of SG iron (standard S3) at different loads is shown in Fig. 4.4.29. The wear rates of standard specimen S3 is in general more than that of composites. The plots of cumulative wear vs sliding distance are presented in Fig. 4.4.30 to Fig. 4.4.32 for 58.8, 78.4 and 98 N loads. The plots show similar trends as those of wear rates. It may be noted that cumulative wear is highest for standard S3 and has occurred over a short sliding distance compared to those of composites. The variation in co-efficient of friction vs sliding distance has been plotted for composite specimens in Fig. 4.4.33 to Fig. 4.4.35 for 58.8, 78.4 and 98 N load. Figure 4.4.36 shows the plots of co-efficient of friction vs sliding distance for standard specimen S3 at different loads. It may be noted from the figures that co-efficient of friction varies from 0.32 to 0.375 for composites B2, B3, B4 and B6 for all the loads while it varies from 0.4 to 0.45 for B7 and B12 at 58.8 and 78.4 N load. At a load of 98 N, the co-efficient of friction for B7 and B12 varies between 0.45 and 0.52. The standard specimen S3 has shown a variation in co-efficient of friction between 0.275 to 0.35. The plots of co-efficient of friction vs sliding distance are not smooth. Fluctuations in co-efficient of friction values can be noted in case of all specimens at all loads. Table 4.4.3 shows the hardness of
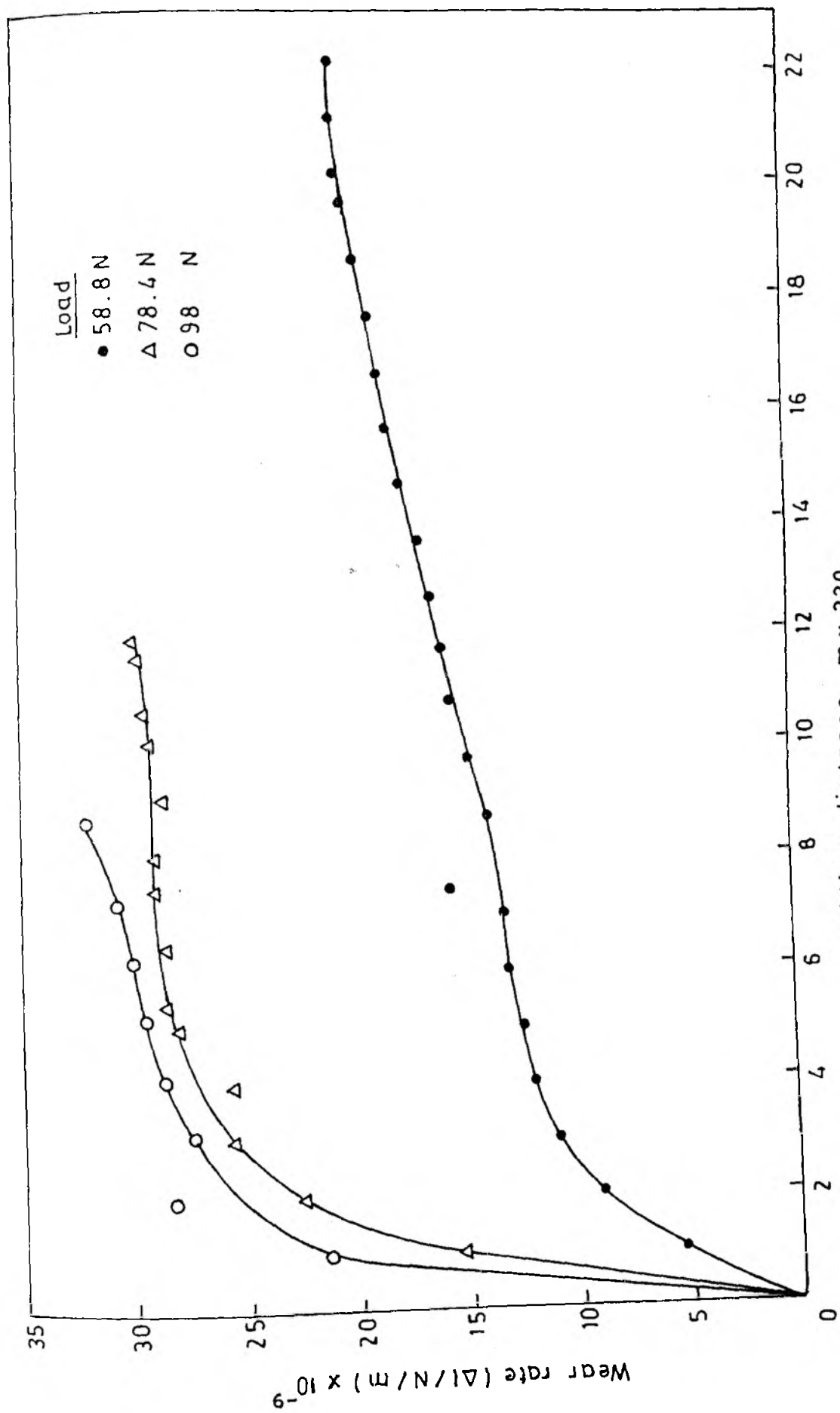
Fig.4.4.29 Wear rate Vs sliding distance (Standard S3)
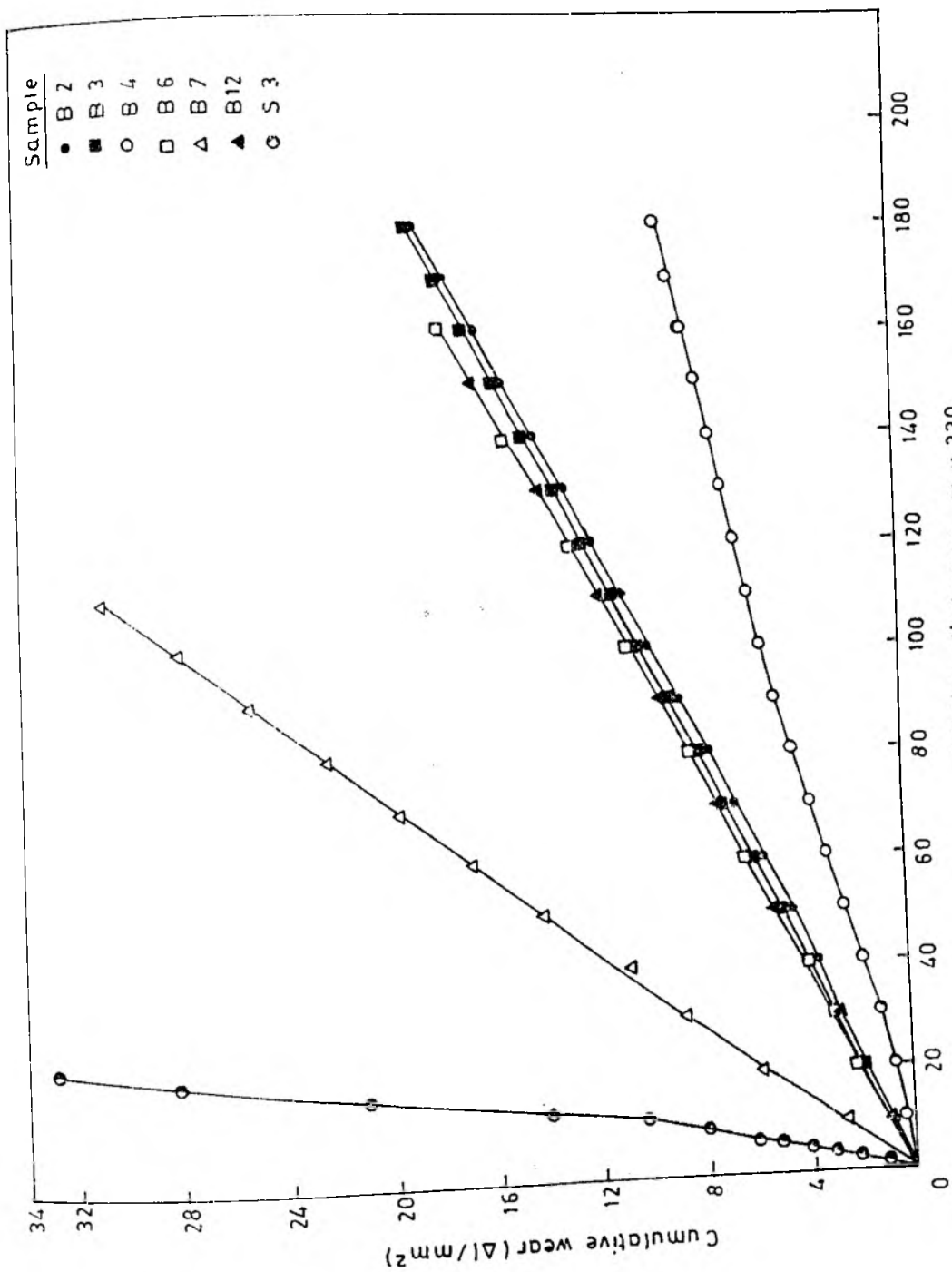
Fig.4.4.30 Cumulative wear Vs sliding distance (58.8 N load)
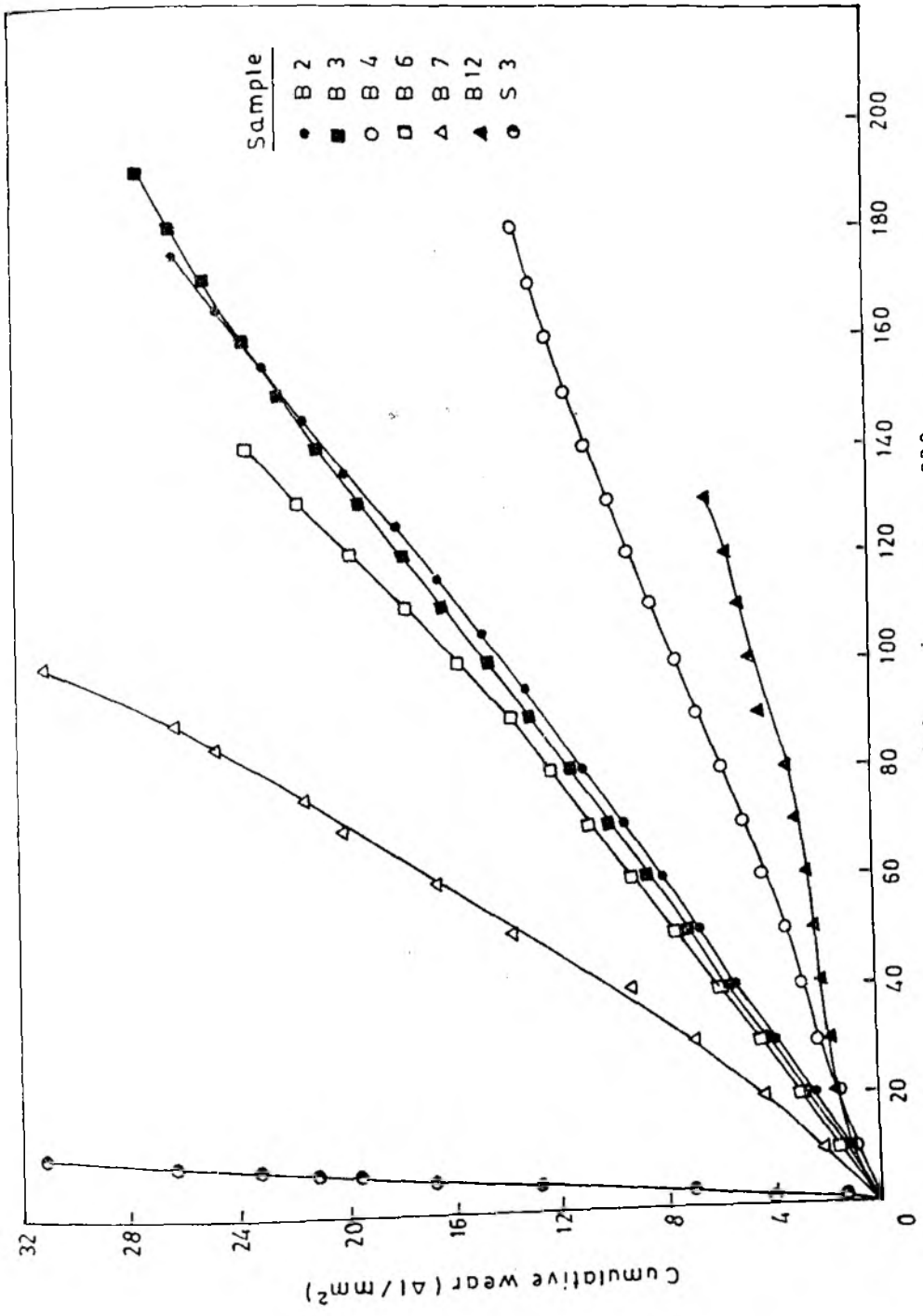
Fig.4.4.31 Cumulative wear Vs sliding distance (78.4 N load)
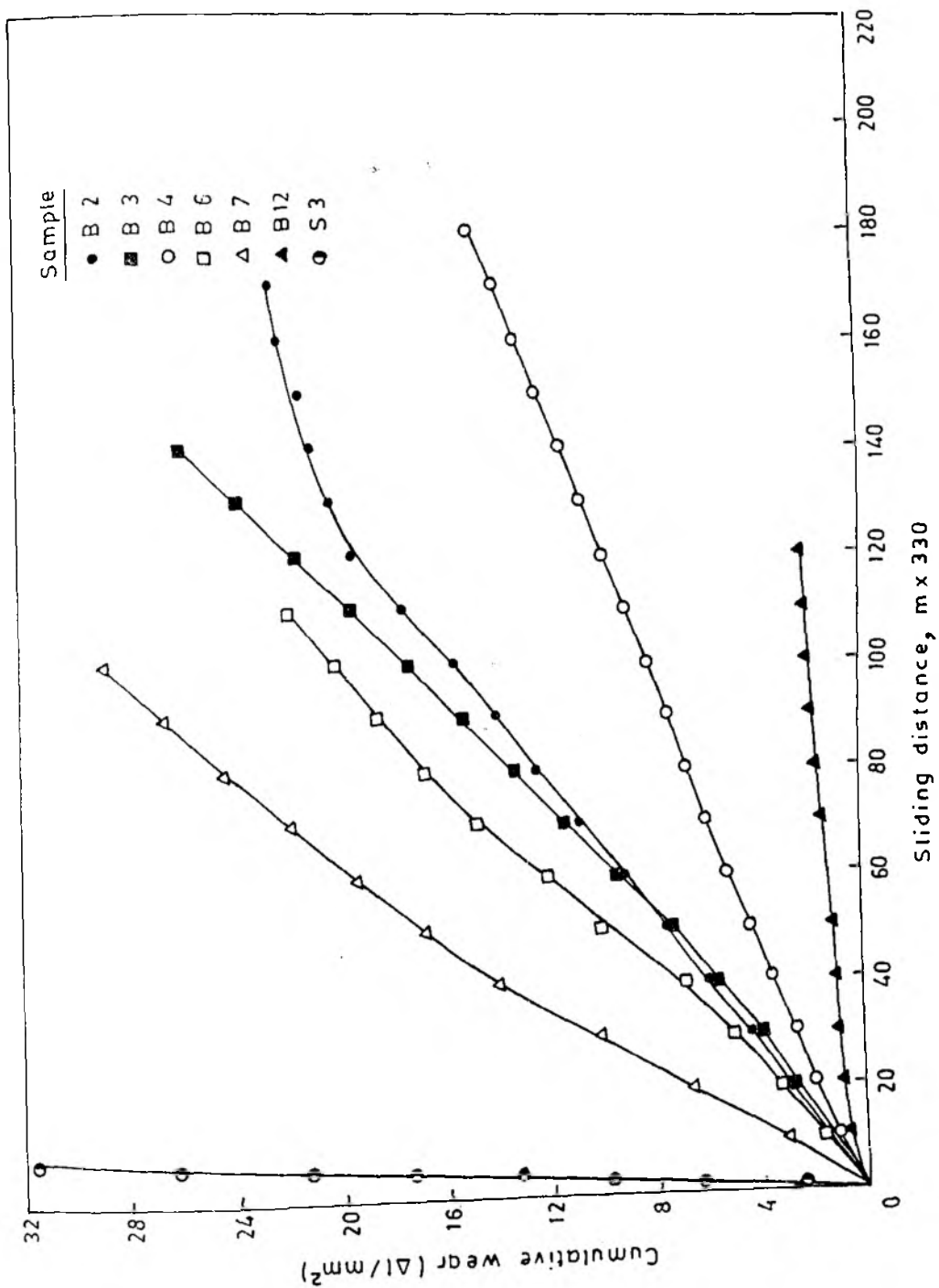
Fig.4.4.32 Cumulative wear Vs sliding distance (98 N load)
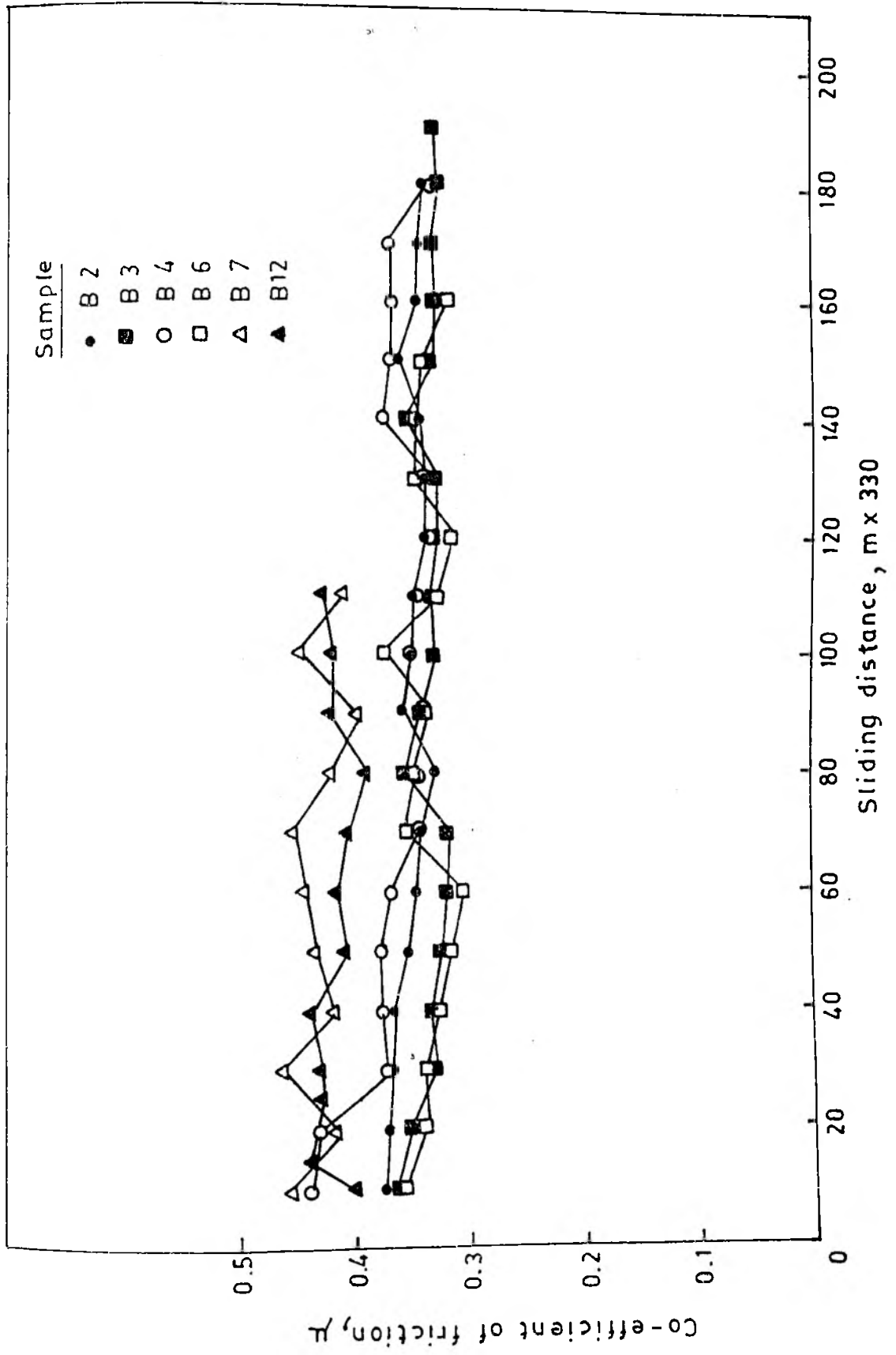
Fig.4.4.33 Co-efficient of friction Vs sliding distance (58.8 N load)
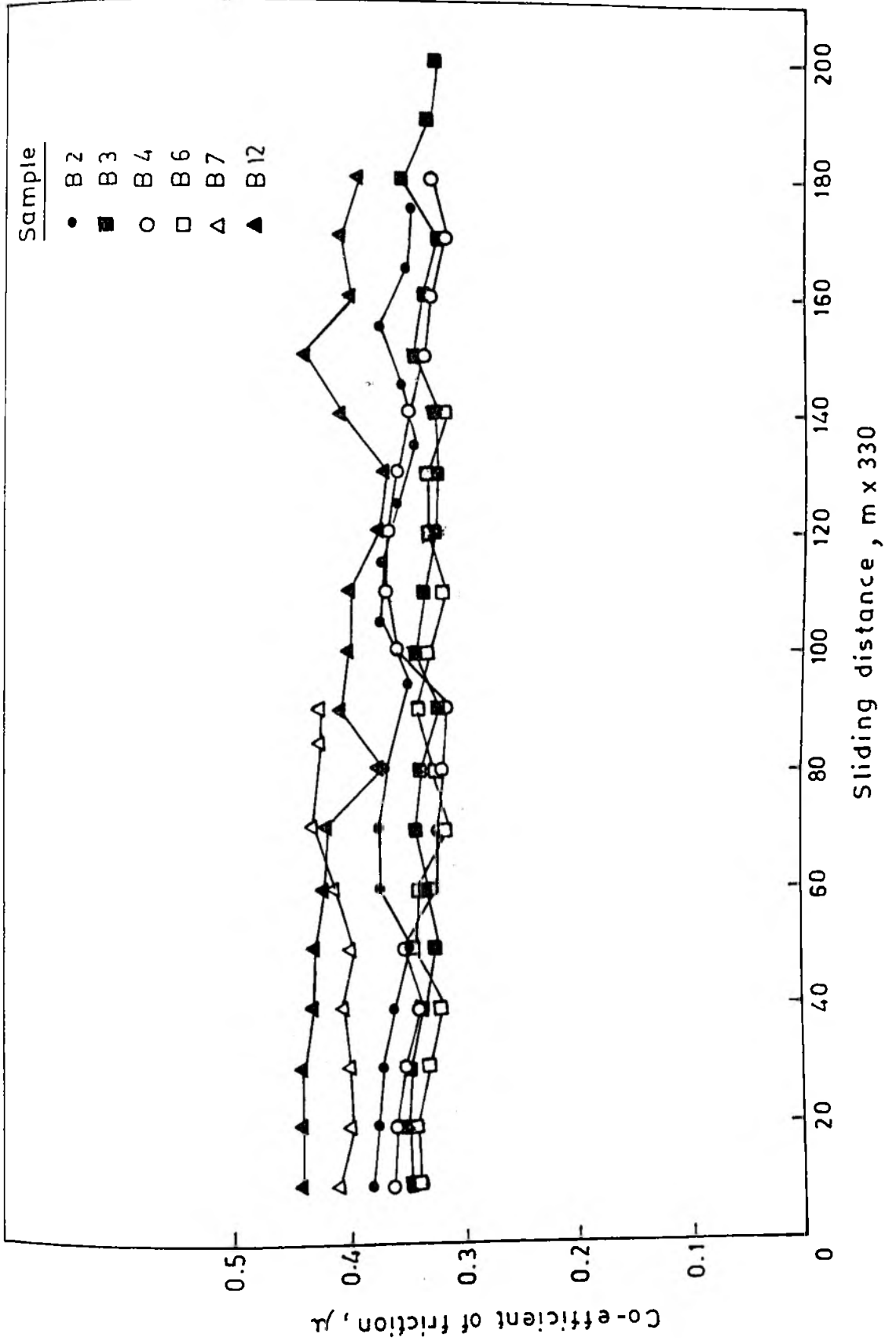
Fig.4.4.34 Co-efficient of friction Vs sliding distance (78.4 N load)
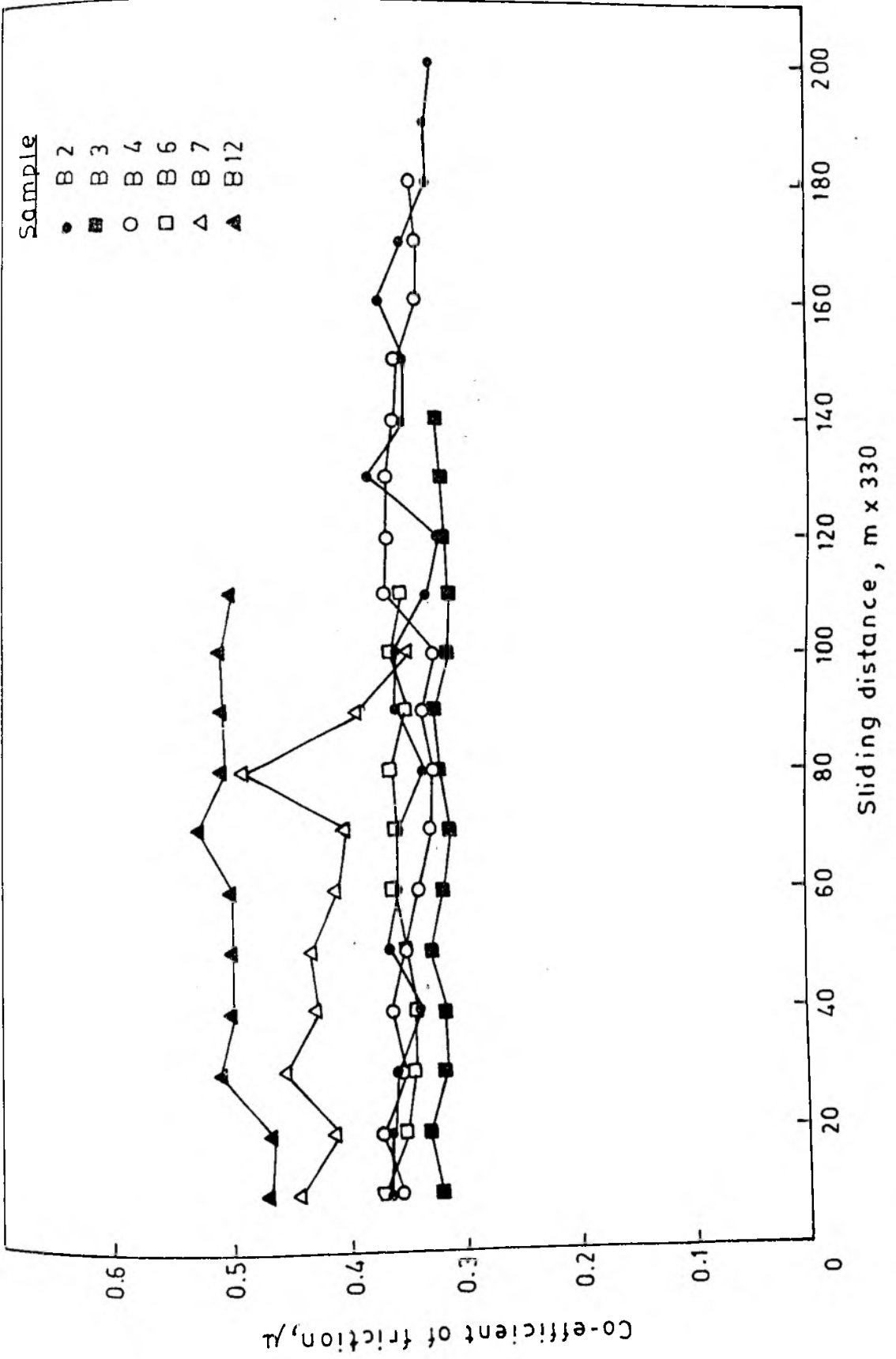
Fig.4.4.35 Co-efficient of friction Vs sliding distance (9.8 N load)
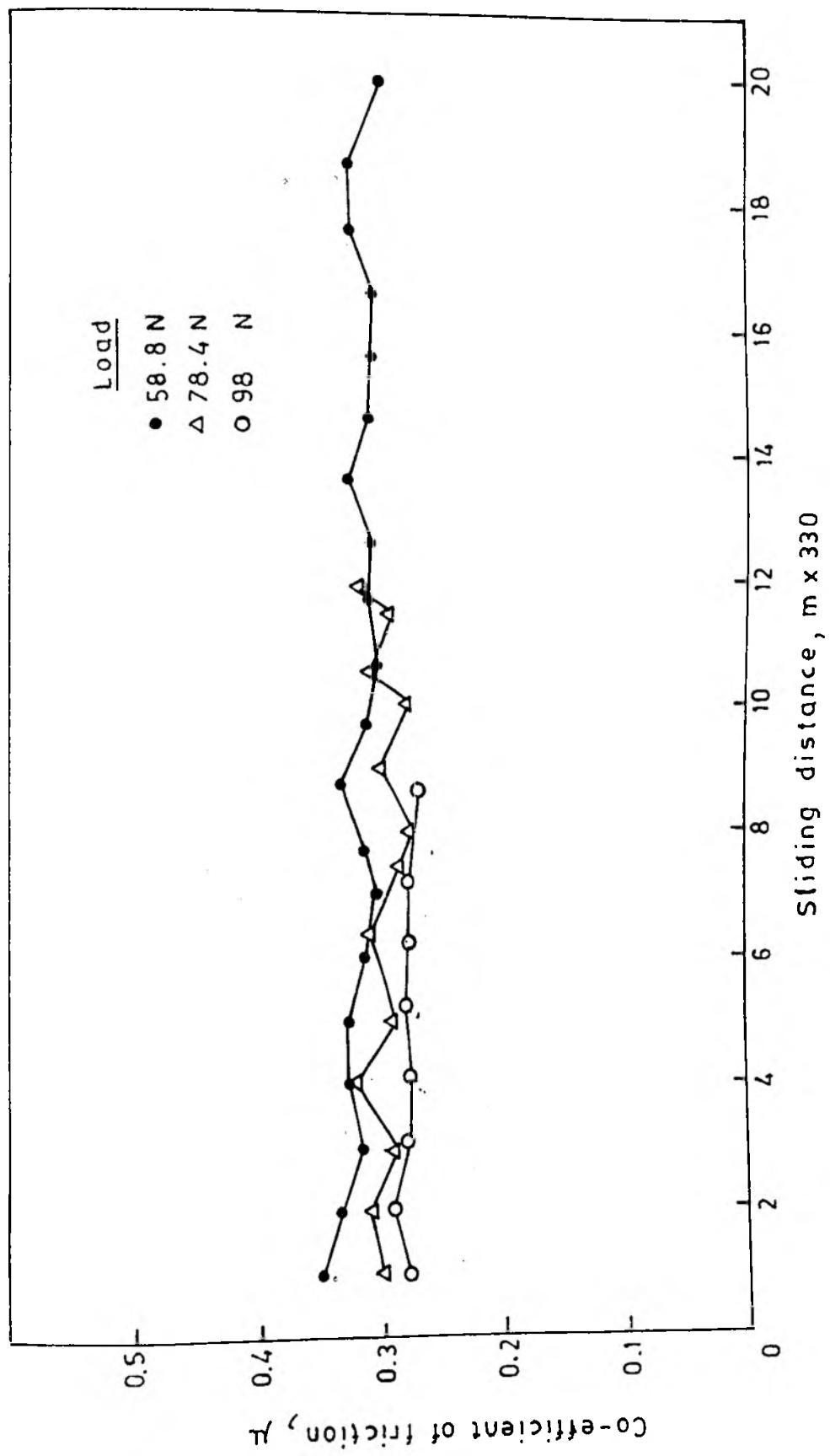
Fig. 4.4.36 Co-efficient of friction Vs sliding distance (Standard S 3)

Table 4.4.3

Hardness of composites tested for adhesive wear
(VPN)

Composite No.	Initial Hardness	Hardness after adhesive wear test		
		58.8 N Load	78.4 N Load	98 N Load
B2	286	333	326	292
B3	261	348	430	349
B4	205	404	436	577
B6	238	303	368	372
B7		304	341	
B12	378		370	477

composite samples before and after adhesive wear tests. Excepting composite samples B2 and B3, all other samples registered an increase in hardness after wear test at all the loads. Composite samples B2 and B3 have shown an increase in hardness when wear tested at 58.8 and 78.4 N load and on the other hand they have shown a decrease in hardness when tested at 98 N load.

The abraded surfaces on some of the adhesive wear test specimens were examined under SEM. The SEM photographs of abraded surfaces of composites B2, B3, B4 and S3 are presented in Fig.(4.4.37) to Fig. (4.4.40). From the figures it may be seen that patches (may be due to oxidation) formed on the abraded surface. Microcracks are observed on the surfaces of specimen B3 (Fig. 4.4.38) and S3 (Fig. 4.4.40). SEM view of the debris formed during the adhesive wear of specimen B12 is shown in Fig. 4.4.41. SEM-EDAX analysis spectra (Fig. 4.4.42) of the debris show prominent peaks for Ti and Fe.

Adhesive wear characteristics of TiC reinforced steel composites

The adhesive wear test of TiC reinforced steel composite C6 and C7 were carried out under 2 kg load (19.6 N) only. A standard Ni-Cr-Mo low alloy steel S4 was also tested for adhesive wear under identical condition for the purpose of comparison. The speed of rotating hard steel disc was kept constant at 600 rpm. The sliding speed of each

Fig.4.4.37   SEM photograph of the worn out
             surface of cast iron composite B2
             (adhesive wear, 98 N applied
             load)

Fig.4.4.38   SEM photograph of the worn out
             surface of cast iron composite B3
             (adhesive wear, 98 N applied
             load)
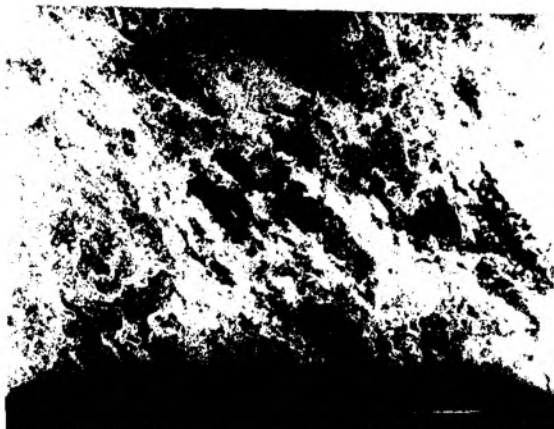
Fig.4.4.39   SEM photograph of the worn out
surface of cast iron composite B4
(adhesive wear, 98 N applied
load)
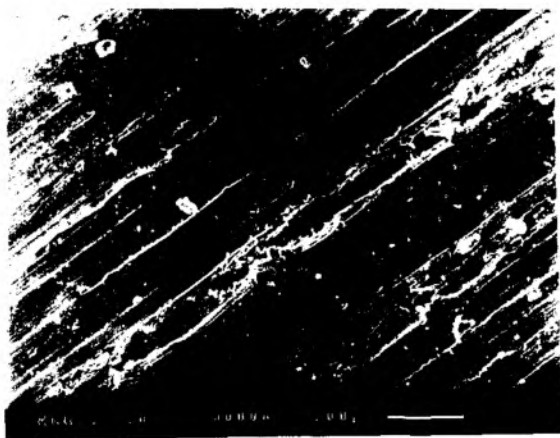
Fig.4.4.40   SEM photograph of the worn out
surface of SG iron S3 (adhesive
wear, 98 N applied load)
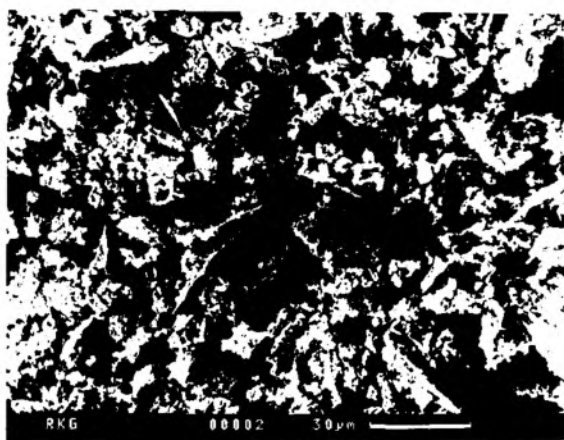
Fig.4.4.41   SEM photograph of the debris of
              cast iron composite B12
              (adhesive wear)
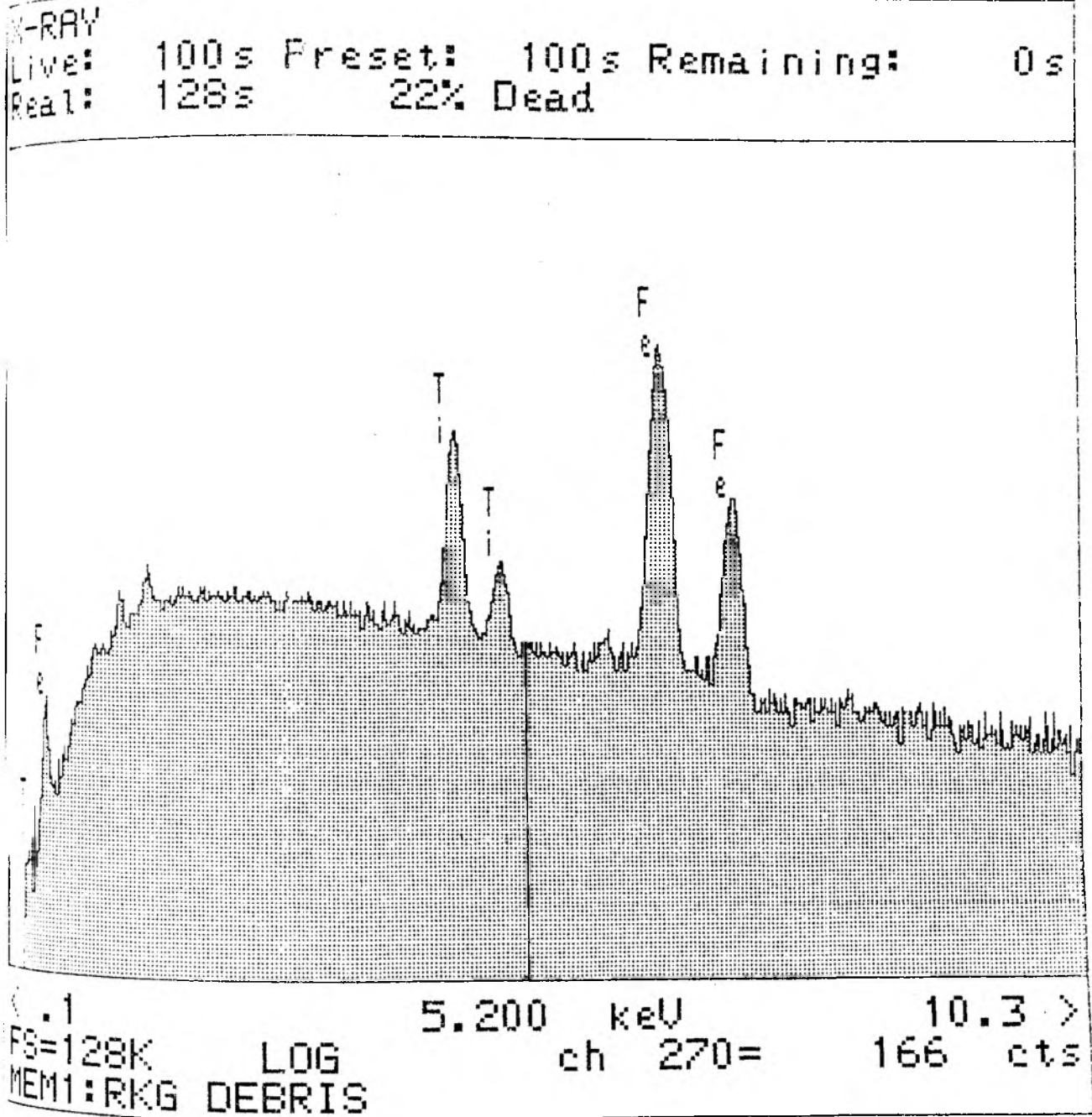
Fig. 4.4.42   SEM-EDAX analysis specctra for debris of
              adhesive wear sample.

specimen was 235.6 m/min (3.92 m/sec). Wear rate vs sliding distance plots for the composites and the standard are presented in Fig. 4.4.43. The plots suggest that the wear rate generally decreased as the sliding distance increased. The composite C6 showed low wear rates compared to those of composite C7 and the standard sample S4. A similar trend could be noticed in the plot of cumulative wear vs sliding distance in Fig. 4.4.44. The values of co-efficient of friction of the standard sample S4 and composites C6 and C7 were comparable. A comparison of the SEM photographs of the worn out surfaces of specimen C6 (Fig. 4.4.45), C7 (Fig. 4.4.46) and S4 (Fig. 4.4.47) show that the wear tracks are uniform and light in case of composite C6 while they are deep in case of composite C7. Pits and patches (may be due to oxidation) are observed on the wear surfaces of both the composite specimens and the standard. Cracks are observed on the surfaces of composite C7 and the standard S4.

Abrasive wear characteristics of TiC reinforced steel composites

The TiC reinforced steel composite specimens C6 and C7 were heat treated before the abrasive tests. The sliding speed of the test specimen was 133.5 m/min (2.22 m/sec). Wear rate vs sliding distance plots are presented in Fig. 4.4.48 for 14.7 N load. It may be noted from the figure that the normalised sample of composite C7 recorded a lower wear rate than that of C6 (normalised) as well as C7 (oil
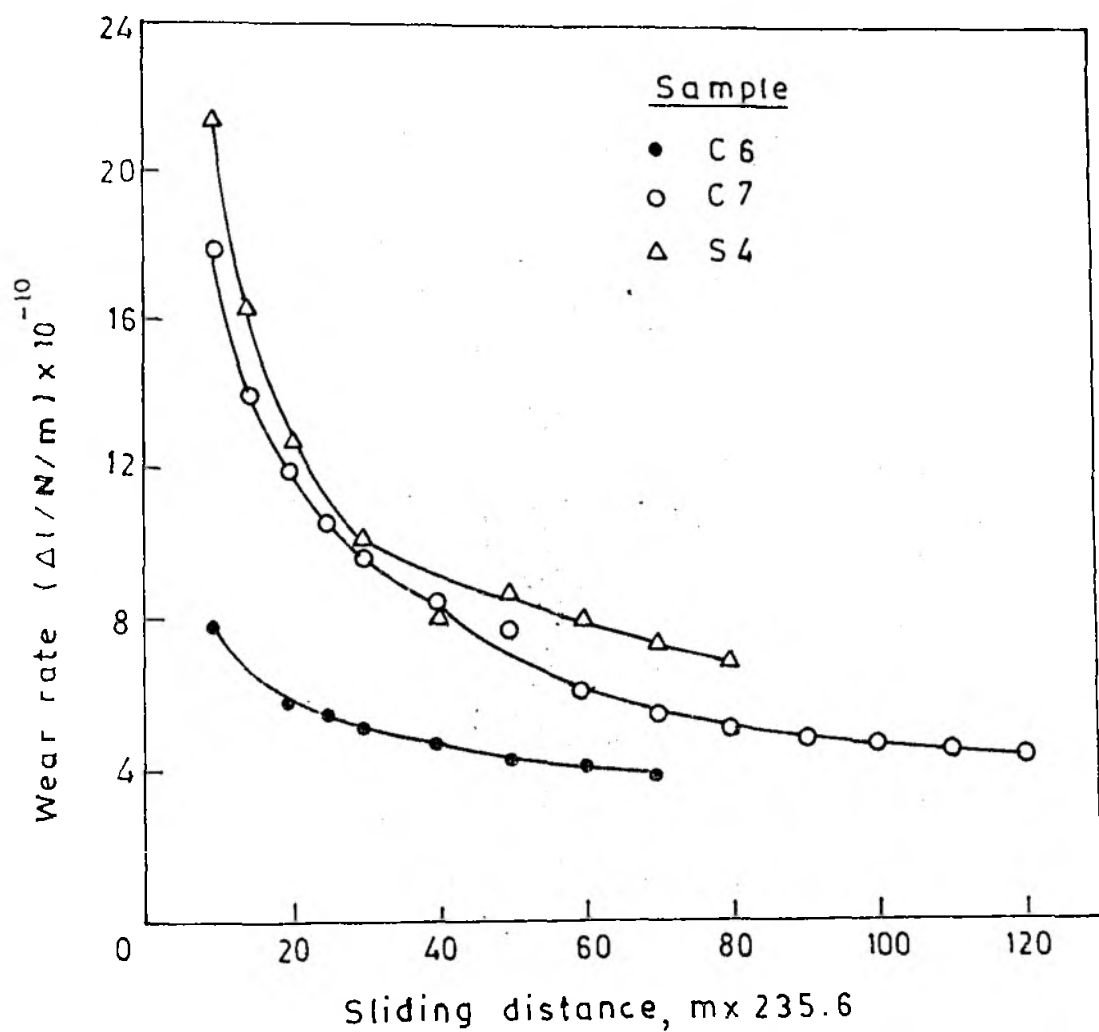
Fig.4.4.43 Wear rate Vs sliding distance (19.6 N load)
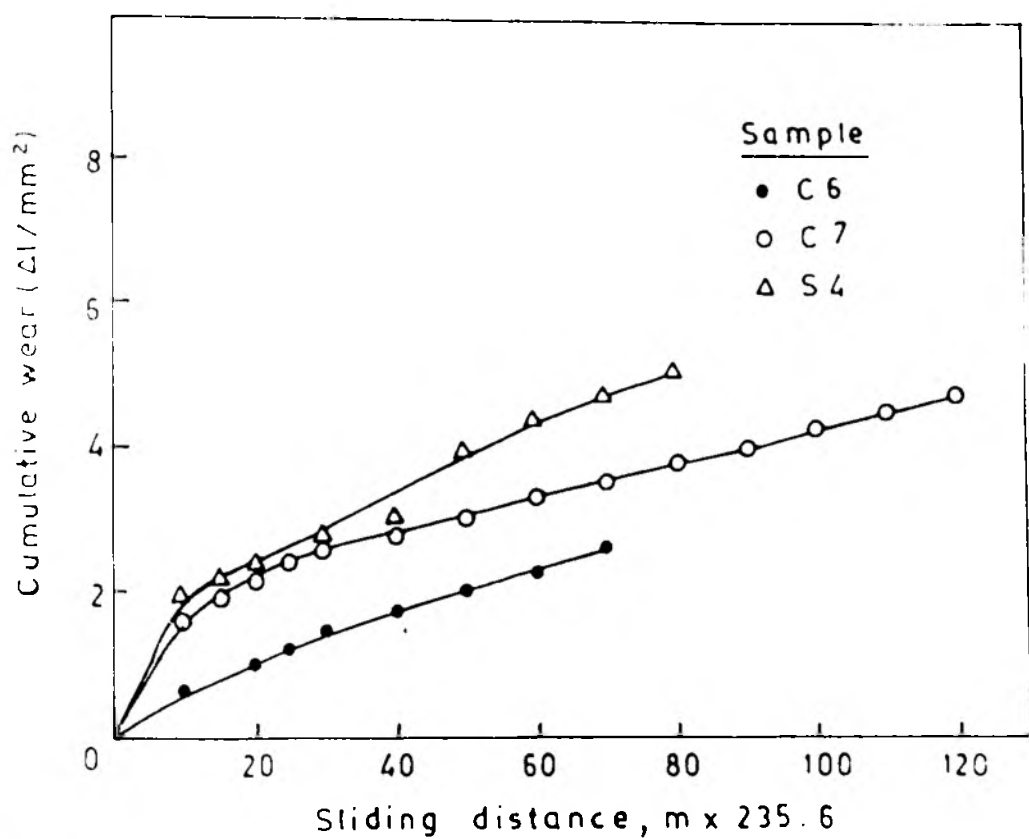
Fig.4.4.44 Cumulative wear Vs Sliding distance (19.6N locd)
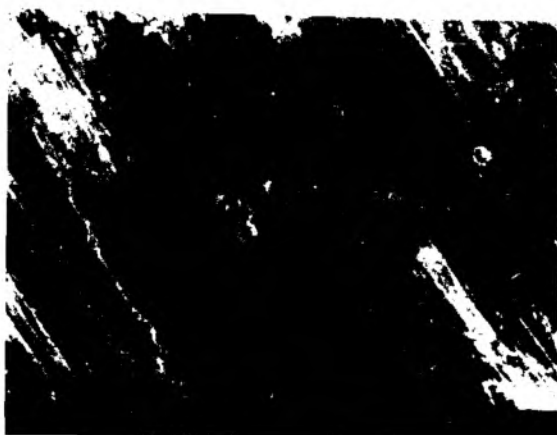
Fig.4.4.45   SEM photograph of the worn out
             surface of steel composite C6
             (adhesive wear, 19.6 N load)

Fig.4.4.46 SEM photograph of the worn surface
           of steel composite C7 (adhesive
           wear, 19.6 N load)

Fig.4.4.47 SEM photograph of the worn surface
of low alloy steel S4 (adhesive
wear, 19.6 N load)
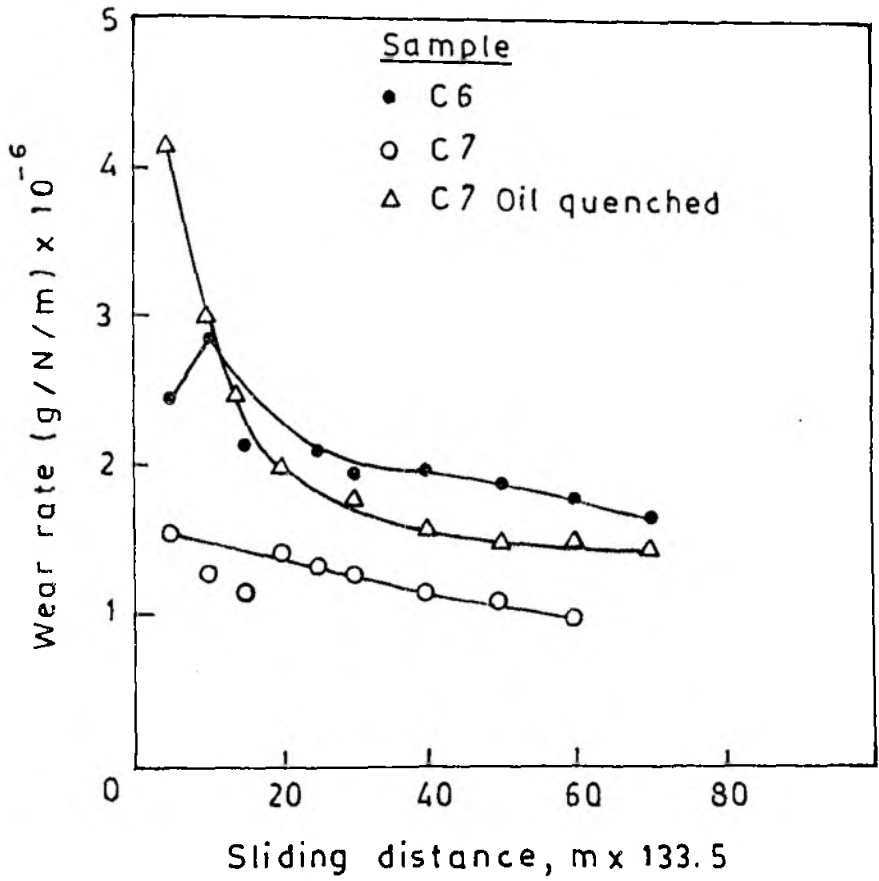
Fig.4.4.48 Wear rate Vs sliding distance (14.7 N load)

quenched and tempered condition). A similar trend is observed in the cumulative wear vs sliding distance plots (Fig. 4.4.49). Wear rates vs sliding distance plots for composite C7 (normalised) under loads of 4.9, 9.8 and 14.7 N, respectively are presented in Fig. 4.4.50. The plots show that there is a decrease in wear rate as the sliding distance increases under all the three loads. The wear rate is lower for the higher load and higher for medium load. A similar trend is observed when cumulative wear vs sliding distance is plotted in Fig. 4.4.51.
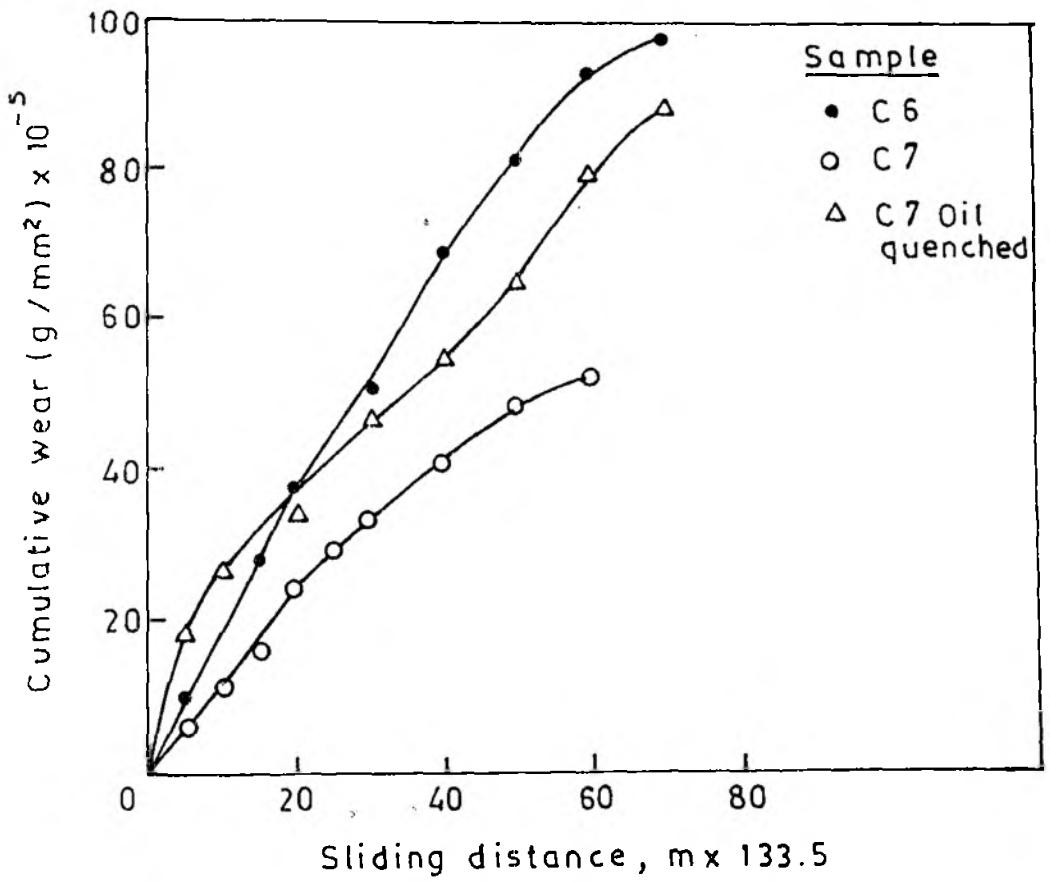
Fig.4.4.49 Cumulative wear Vs sliding distance (14.7N load)
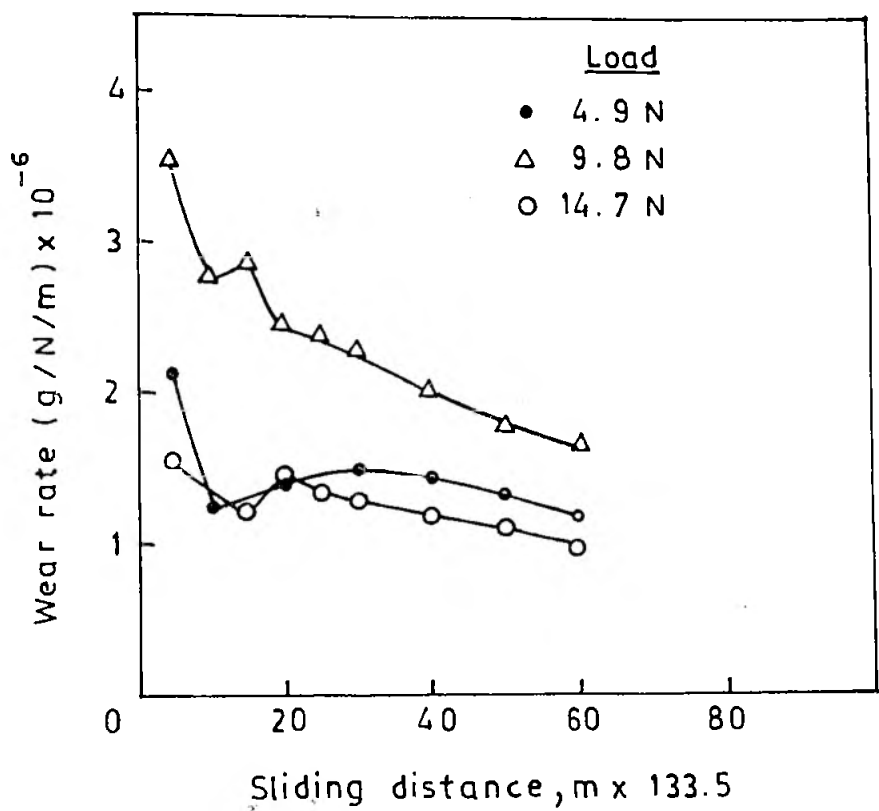
Fig.4.4.50   Wear rate Vs sliding distance (Sample C7)
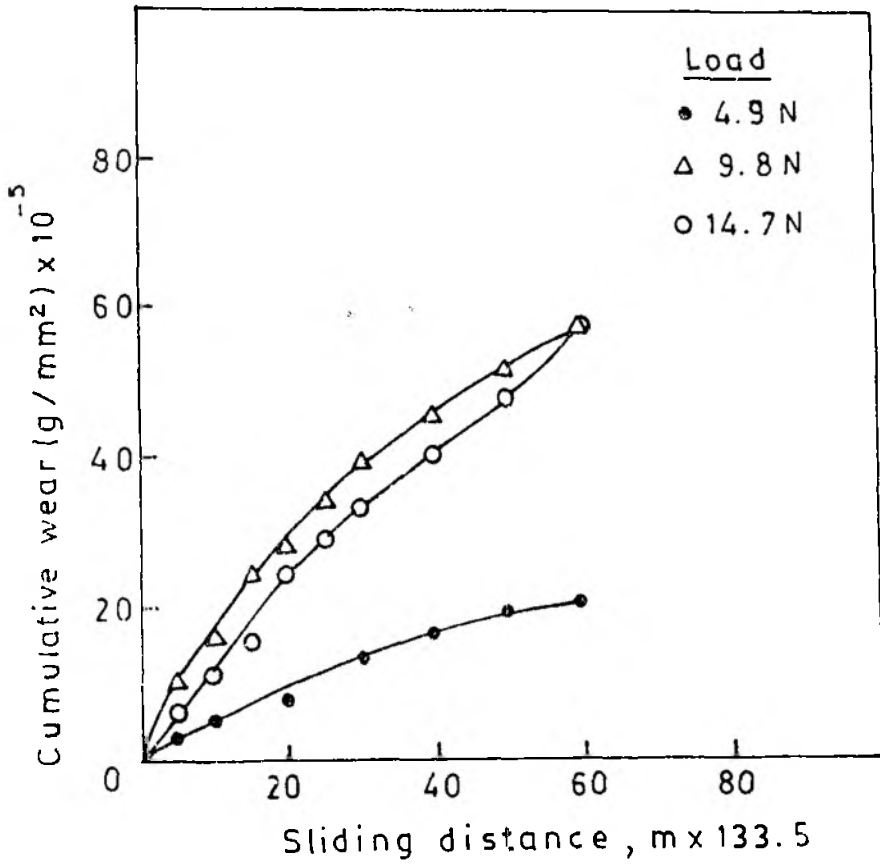
Fig.4.4.51 Cumulative wear Vs sliding distance (Sample C7)

4.4.2 Discussion

Abrasive and adhesive wear tests have been carried out on both TiC reinforced cast iron and steel composites. Abrasive wear occurs when there is a friction between a material under stress and a harder body. Abrasive wear may be due to various mechanisms which cause surface destruction such as cutting, scratching and plastic deformation. Adhesive wear occurs when two solid bodies are in contact and at least one of them is moving. The stress on the body and surface contact results in mating of surface asperities. The mating asperities are known to flow plastically and form strong work hardened junctions. As these break under an imposed tangential traction, material loss from solid may occur. This type of wear is known to occur in braking or clutch mechanisms.

Abrasive and adhesive wear tests have been carried out on both TiC reinforced cast iron and steel composites by pin-on-disc method. In the case of abrasive wear tests, loss in weight of the specimen was determined by interrupting the tests at regular intervals of time to assess the wear and subsequently cumulative wear as well as wear rates were computed. The decrease in specimen length and tangential force were noted with the help of electronic sensors attached to the adhesive wear test unit. The cumulative wear, wear rates and co-efficient of friction were computed. The abraded surfaces of a few representative composite specimens

were examined in scanning electron microscope to assess the
nature of wear. The titanium carbide particle size distribu-
tion of composites are presented in the form of histograms.
The volume percent of graphite present in cast iron compos-
ites have been determined.

The results mentioned on wear characteristics of
both TiC reinforced cast iron and steel composites are the
trends. The absolute values may vary due to intrinsic inho-
mogeniety of the cast composite. The experimental results on
wear tests are discussed.

**Abrasive wear characteristics of TiC reinforced cast iron
composites.**

The plots of abrasive wear rate vs sliding dis-
tance for TiC reinforced cast iron composites in as cast
condition for various applied loads are presented in Fig.
4.4.13 to Fig. 4.4.15 and show that at higher applied loads
namely, 9.8 and 14.7 N, the wear rates are low for composite
B5, whereas it is high for composite B1. A clear picture
emerges when the wear rates of the composites are observed
at different sliding distances and applied loads (Table
4.4.4). It may be seen from the Table that at any given
sliding distance, composite B5 shows a decrease in wear rate
as the applied load is increased. On the other hand compos-
ites B1 and B10 show higher wear rates at 9.8 N applied load
where as low wear rates are observed for the composites at
4.9 and 14.7 N applied load. The composite B10 shows lower

Table 4.4.4

Abrasive wear rate for TiC reinforced cast iron
composites at different sliding distance.

			Wear rate (g/N/m) x 10^{-7}		
Sliding distance -->			20 x 133.5m	40 x 133.5m	60 x 133.5m
Composite No.	Wt Pct Ti	C			
			4.9 N load		
B1	1.48	2.78	4.6	4.6	5.2
B5	3.11	3.12	29.0	21.7	16.8
B10	5.62	4.78	4.6	3.0	2.8
			9.8 N load		
B1			23.6	20.5	16.8
B5			5.1	3.2	3.5
B10			14.5	10.1	7.9
			14.7 N load		
B1			14.2	9.7	NA
B5			4.3	3.2	2.8
B10			4.6	5.4	4.9

wear rates at 4.9 N applied load. There is a sharp increase in wear rates of composite B1 as the applied load is increased from 4.9 N to 9.8 N. In general, there is a decrease in wear rates for all the composites as the sliding distance is increased.

The initial increase in wear rates of the composites may be due to wearing of the softer matrix. As the sliding distance increases, the exposed TiC particles partially support the applied load. The carbide volume percent increased as the titanium content in the composite is increased. It may be seen from Table 4.2.1 and Table 4.2.2 that composites B1, B5 and B10 contain 1.48, 3.11 and 5.82 wt pct Ti respectively, indicating composite B10 is having higher volume percent of TiC compared to composite B1 and B5. The abrasive wear resistance increases with an increase in carbide volume percent [107]. This however, is not true for all types of abrasive wear. Some times, abrasive wear conditions have been classified as `low stress ' and `high stress' abrasion. The term `high stress' abrasion refers to a case where the reinforcement fragments under the applied normal load and increase the wear rate. At `low stress' abrasive conditions there is no fragmentation of reinforced particles. The improvement in wear resistance property of composite B10 for an applied load of 4.9 N is likely to correspond to the low stress abrasive condition. The increase in wear rates for composite B10 at an applied load of 9.8 N may correspond to a change of low stress abrasive

condition to that of high stress one. The carbide particle size is also equally important in addition to carbide volume percent present in composites as it influences the wear resistance property [108]. The histogram (Fig. 4.4.3) for composite B10 show that carbide particles over 45.25 μm size constitute around 55 percent of the total particle volume. The coarser particles are likely to fragment more easily than finer carbide particles under high stress abrasive condition. The decrease in wear rates of composite B10 at an applied load of 14.7 N may be due to transformation of phase as well as heavy plastic deformation of the matrix. Table 4.4.2 shows the hardness values of composites in the as cast condition as well as at the end of abrasive wear test. Both samples of composites B1 and B10 registered an increase in hardness which indicates work hardening.

The composite B1 having 1.48 wt pct Ti has a low volume percent of TiC particles. The histogram (Fig. 4.4.1) for composite B1 shows the presence of a large number of TiC particles below 16 μm. The volume percent of carbide particles being low, the wear rates are high at 9.8 and 14.7 N applied loads. Such a behaviour of a composite is expected. The decrease in the wear rate of composite B1 under 14.7 N load compared to that under 9.8 N load may be due to phase transformation. The microstructure of the abraded surface of composite B1 after test under 14.7 N load show the presence of tempered martensite (Fig. 4.4.52, approximately 495 VPN). Such phase transformations have been observed by other
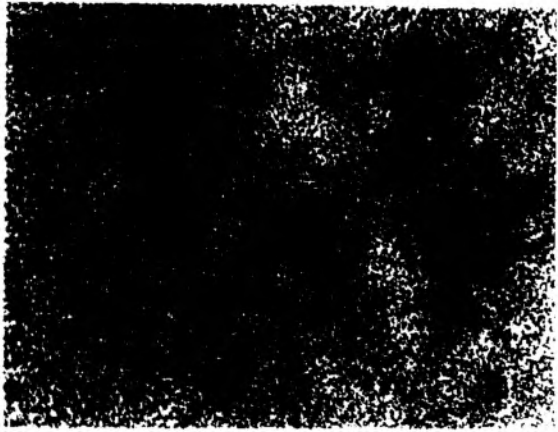
Fig.4.4.52   Abraded surface of cast iron
             composite B1 showing tempered
             martensite (495 VPN), 500X

investigators while examining steels [109] after abrasive tests. The composite has shown higher wear resistance properties at 4.9 N applied load.

The composite B5, containing 3.11 wt pct Ti exhibited higher wear resistance than composites B1 and B10 under 9.8 and 14.7 N applied load. In this sample TiC particles below 16 μm size constitute nearly 90 percent of the total particle volume (Fig. 4.4.2). The under size particle count below 8 μm is also large (Fig. 4.4.2). No perceptible change in the hardness of the wear surface was noted, which means that workhardening or transformation hardening phenomena did not make any appreciable contribution towards the wear resistance of composite B5. Therefore the superior abrasive wear resistance of composite B5 under 9.8 N and 14.7 N loads appears to be due to uniform distribution of a larger volume of finer size carbide particles in this composite. Smaller size particles ensure higher bond strength between the particle and the matrix and provide a larger area for sharing the applied load. However, the particles should not be so small in size that they are removed when scratches are made during abrasive wear [108]. The sharp increase in wear rates of composite B5 under low load of 4.9 N may correspond to a low stress abrasive wear condition. Hosking et al., [85] while studying the effect of particle size of alumina in Al-Al$_2$O$_3$ composite for abrasive wear test have shown that a composite containing ~ 142 μm Al$_2$O$_3$ showed better wear resistance properties over a composite containing 16 μm

Al_2O_3. This indicates that at low stress abrasive conditions carbide particles do not fragment and improve wear resistance properties. In composite B5 wear resistance did improve at low stress abrasive condition because most of the TiC particles were in the finer range.

The comparison of wear data of TiC reinforced cast iron composites with those of standard chromium cast iron specimens (S1 and S2) show that composites have better wear resistance properties. The wear resistance properties of composite B10 at an applied load of 4.9 N and composite B5 at an applied load of 9.8 N and 14.7 N are superior to those of plain and nitrogenated chromium cast irons at least by one order of magnitude. This may be due to higher hardness values of TiC reinforced particles in cast iron composites over those of chromium carbide and nitride particles in chromium cast irons [110, 111]. Khrushov [112], has shown that higher is the hardness of reinforcing material, higher is the wear resistance property.

Adhesive wear characteristics of TiC reinforced cast iron composites

Adhesive wear tests on TiC reinforced composites B2, B3, B4, B6, B7 and B12 were carried out along with a standard spheroidal graphitic cast iron S3 to compare the data. The plots of wear rate vs sliding distance for composites have been presented in Fig. 4.4.26 to Fig. 4.4.28 for 58.8, 78.4 and 98 N applied load. Table 4.4.5 shows wear

Table 4.4.5

Adhesive wear rate for TiC reinforced cast iron
composites at different sliding distances.

Sliding distance -->			Wear rate ($\Delta l/N/m$) x 10^{-10}		
			20 x 330m	60 x 330m	100 x 330m
Composite No.	Wt Pct Ti	C	Vol Pct Graphite		
			58.8 N load		
B2	1.48	4.90	1.61	12.6	13.7	14.5
B3	1.98	3.52	1.75	14.7	14.8	14.8
B4	2.27	3.65	1.33	4.8	7.6	8.0
B6	3.61	3.43	2.97	13.5	15.2	15.5
B7	4.17	3.86	1.88	43.5	41.0	40.4
B12	10.86	5.72	12.42	42.0	14.5	9.5
			78.4 N load		
B2				13.3	14.6	15.2
B3				14.3	15.4	15.8
B4				8.2	7.6	8.0
B6				15.8	16.7	17.0
B7				24.4	30.9	33.6
B12				9.0	4.6	4.6
			98 N load		
B2				12.8	13.5	13.8
B3				12.4	13.8	15.2
B4				9.0	7.8	7.1
B6				14.8	17.5	17.7
B7				29.5	27.2	NA
B12				3.8	1.8	1.7

rates of composites at different sliding distances for different applied loads. It may be seen from the Table that composite B4 for 58.8 N and composite B12 for 78.4 N and 98 N applied loads have shown low wear rates. There is a decrease in wear rates as sliding distance and applied load increases in the case of composite B12. The composite B12 contains 10.86 wt pct Ti, 5.72 wt pct C and 12.42 volume percent graphite, which means the TiC content is high compared to other composites as they contain lower amounts of Ti (Table 4.2.1 and Table 4.2.2). It is often reported that as the volume percent of reinforced particles increases there is a decrease in wear rates [85]. Further, the composite B12 contains 12.42 volume percent graphite. Many investigators have shown an improvement in wear resistance properties in graphite dispersed alloys [88, 113, 114], as graphite is a solid lubricant. Thus composite B12 show better wear resistance properties due to the presence of high volume percent carbide and graphite particles. The initial high rates of wear in composite may be due to removal of graphite under an applied load. Once the graphite is removed the TiC particles stand in relief and carry partially the applied load. The histogram for composite B12 (Fig. 4.4.12) shows an uniform increase in particle size count (volume percent) as the particle size range increases. It is known from earlier investigator on TiC reinforced steel matrix composite [91] that the wear rates decrease

with increasing volume fraction of carbide, decreasing carbide particle size and their spacing.

The composite B4 has shown lower wear rates for 58.8 N applied load and there is an increase in wear rates as the sliding distance increases. The difference in wear rates at 100 x 330 m sliding distance for composites B4 and B12 is very marginal. The composite B4 contains 2.27 wt pct Ti, 3.65 wt pct C and 1.32 volume percent graphite. The TiC particle size distribution of composite B4 (Fig. 4.4.9) show an uniform increase in particle count as size range increases. As the TiC content is lower the wear rate increases for 78.4 and 98 N applied load.

The composites B2, B3 and B6 have shown more or less same wear rates [Table 4.4.5]. The wear rates increase slightly as the sliding distance increases at all the three applied loads. Over 80 percent of the total TiC particles is below 22.62 μm size in composites B2, B3 and B6 (Fig. 4.4.7, Fig. 4.4.8 and Fig. 4.4.10, respectively). Thus, the finer distribution of the particles in composites may be responsible for uniform wear rates at all applied loads and sliding distance. The wear rates of these composites are intermediate between the low wear rates of composites B4 and B12, and the high wear rates of composite B7.

The composite B7 suffered wear at very high rates at all the three applied loads [Table 4.4.5]. Its wear rate decreased to some extent with increase in the sliding

distance at 58.8 N and 98 N applied loads. Under a higher load of 78.4 N its wear rate continue to increase with the sliding distance. The composite contains 4.17 wt pct Ti, 3.86 wt pct C and 1.88 volume percent graphite. The histogram (Fig. 4.4.11) show over 90 percent of total particle volume have TiC particles above 22.62 μm size. The under size count of particles is also low. Though, the TiC volume percent is moderately high, the presence of coarse particles in large number resulted in high wear rates.

The wear rates of a standard spheroidal graphitic iron S3 is shown in Fig. 4.4.29 as a function of sliding distance for various applied loads. The wear rates increase as the sliding distance and applied load increases. The wear rates are at least one order more when compared with those of TiC reinforced cast iron composites. The SEM photograph of the worn out surface of a sample of S3 (Fig. 4.4.40) show widely spaced wear tracks and a few micro cracks. The predominant nature of wear appears to be rubbing.

The plots of co-efficient of friction vs sliding distance for composites are shown in Fig. 4.4.33 to Fig. 4.4.35 for 58.8, 78.4 and 98 N applied loads. A similar plot for standard S3 is shown in Fig. 4.4.36 for all the three applied loads. A lot of fluctuations in the values of co-efficient of friction may be noted. A possible explanation for such fluctuations in the co-efficient of friction values has been suggested on the basis of a stick - slip mechanism

[115]. As the asperities adhere during the wear, the moving parts stick leading to a high value of friction. As the junction ruptures under applied load the friction tends to be zero. Thus the adhesion of asperities followed by rupture of the interface leads to a process of `stick-slip'.

It is important to note that `wear resistance' is not a materials property [116]. The rates of wear when two bodies are sliding against each other depend not only on the properties of the materials involved but also on the geometry of contact both on gross scale and fine scale, on the velocity of sliding, the ambient temperature and environment, presence of lubricants, applied load etc. Thus, it is difficult to attribute a single mechanism operating for wear of a component.

The TiC reinforced cast iron composites which contain graphite can be grouped under self lubricating metal base materials [117]. The adhesive wear resistance of composites improve when they contain TiC particles of various size fractions with an emphasis on the presence of finer particles (composites B12 and B4) along with graphite. Presence of very fine TiC particles alone does not seem to improve the wear resistance properties (composites B2, B3 and B6) significantly. On the other hand, the composite B7 which contains very coarse TiC particles had undergone wear at high rates at all the three applied loads. SEM-EDAX analysis of wear debris (Fig. 4.4.42) has shown presence of both Ti and Fe. This indicates that, there is chipping of

TiC particles and ploughing of iron matrix during the wear. SEM photographs of abraded surface (Fig. 4.4.37 to Fig. 4.4.40) have shown presence of pits which may be due to chipping of TiC particles. The initial hardness values of composites when compared with those at the end of wear tests show in general an increase (Table 4.4.3) indicating the process of plastic deformation and extent of work hardening. Examination of the abraded surfaces of a few representative samples have shown the formation of tempered martensite. Thus the net wear resistance of the composites is derived from the combined effect of the presence of hard TiC wear resistant particles, the lubricating effect of the graphite phase and the process of work hardening and phase transformation at a given applied load.

The magnitude of the co-efficient of friction is said to be an indicator of the wear resistance properties. Generally, wear resistant materials show low values of co-efficient of friction [91]. The composite B12 which had shown better wear resistance properties, had a co-efficient of friction varying from 0.425 to 0.5 only as the applied load was increased from 58.8 N to 98 N. This is contrary to the results of many investigators on self lubricating materials tested under dry sliding [109, 114, 118]. Some exceptions to this do exist and such a behaviour is explained as follows.

During adhesive wear the stress on body and surface contact results in mating of surface asperities. The breaking of each junction will result in a resistance component to sliding and may not detach from the metal surface giving a wear debris. It may simply mean that as the junction breaks, it remains attached to the metal surface as microscopically rough area or if plastic, may be just smeared over the metal surface [119] and this increases the co-efficient of friction. The SEM photographs of the abraded surfaces of composites show some oxide patches (Fig. 4.4.37 to Fig. 4.4.39) which probably formed by localised oxidation of such smeared layers. In the case of spheroidal graphite iron, S3 the co-efficient of friction has shown a decrease as the applied load is increased from 58.8 N to 98 N. On the other hand wear rate has also increased as the applied load is increased from 58.8 N to 98 N. Thus, a decrease in co-efficient of friction does not necessarily mean high wear resistant properties.

Adhesive wear characteristics of TiC reinforced steel composites

The adhesive wear tests of TiC reinforced steel composites C6, C7 and a standard low alloy steel S4 have been carried out at 19.6 N applied load. The plot of wear rate vs sliding distance for the composite samples as well as the standard sample are presented in Fig. 4.4.43. Table 4.4.6 shows wear rates at different sliding distances. It may be noted from Table 4.4.6 that wear rate decreases as

Table 4.4.6

Adhesive wear rate for TiC reinforced steel
composites at different sliding distance.

	Wear rate ($\Delta 1/N/m$) 10^{-10}		
Sliding distance -->	20 x 330m	40 x 330m	60 x 330m
Composite No.			
C6	5.8	4.8	4.2
C7	11.8	8.4	5.0
S4	12.7	9.2	7.8

the sliding distance increases. The composite C6 has shown lower wear rates. The composite C6 contains a higher volume percent of TiC (0.71 wt pct Ti) compared to that in composite C7 (0.14 wt pct Ti). Skolianic et al., [91] have shown that as the volume percent of carbide increases the wear resistance property improves. The wear resistance properties of composite C6 is nearly twice that of low alloy steel S4. The reinforcing component in steel composite, namely TiC, is harder than chromium carbide present in the low alloy steel S4. The SEM photographs of the abraded surfaces of the composite C6 and C7 show pits, microcracks and oxide layer formation (Fig. 4.4.45 and Fig. 4.4.46). It appears that heavy plastic deformation caused cracking and cracks propagated upto the surface. When the cracks propagate, TiC particles are loosened and then are pulled out. The pits observed in SEM photographs (Fig. 4.4.45 and Fig. 4.4.46) also suggest such a possibility. The presence of cracks and oxide layers in the abraded surface of standard S4 (Fig. 4.4.47) indicate that the basic wear mechanism in this steel is similar to that in TiC steel composites. The values of coefficient of friction for steel composites and standard Ni-Cr-Mo low alloy steel are comparable.

Abrasive wear characteristics of TiC reinforced steel composites

Abrasive wear test was carried out on TiC reinforced steel composites C6 and C7. The composite C6 was

tested in normalised condition and composite C7 was tested in both normalised as well as oil quenched and tempered condition. The plot of wear rate vs sliding distance for the composites is presented in Fig. 4.4.48. Table 4.4.7 shows the wear rates at different sliding distances. It may be seen from the Table that wear rate decreases as the sliding distance increases. The normalised sample of composite C7 recorded a lower wear rate compared to those of composite C6 (normalised) and composite C7 (quenched and tempered). The abraded surface of the normalised sample of composite C7 had undergone hardening while the microhardness of the normalised sample (C7) surface increased from 300 VPN to 367 VPN after wear test, that of the oil quenched and tempered sample (C7) increased from 467 VPN to 722 VPN. Such a large increase in hardness of composite C7 (oil quenched and tempered) is most probably the consequence of stress induced transformation of the retained austenite to martensite. But such transformation in a thin volume of material is also likely to produce microcracks due to expansion. TiC particles are loosened and detached by propagation of these microcracks. Hence, the material showed poorer wear resistance.

Fig. 4.4.50 shows wear rate vs sliding distance for composite C7 (normalised) under applied loads of 4.9, 9.8 and 14.7 N. The composite C7 shows better wear resistance at 14.7 N applied load a condition probably that of high stress abrasive wear. As explained in the preceding

Table 4.4.7

Abrasive wear rate for TiC reinforced steel
composites at different sliding distance

	Wear rate (g/N/m) x 10^{-6}		
Sliding distance--->	20 x 133.5m	40 x 133.5m	60 x 133.5m
Composites			
C6	2.25	1.95	1.75
C7	1.35	1.15	0.95
C7 Oil quenched	1.95	1.55	1.45

paragraph composite C7 had shown better wear resistant properties due to work hardening and phase transformation.

4.4.3 Conclusions

The following conclusions may be drawn from the study on abrasive and adhesive wear characteristics of TiC reinforced cast iron and steel composites.

1. Titanium content and TiC particle size distribution in cast iron composites influence the abrasive wear resistance property appreciably.

2. Under low stress abrasive wear condition, a cast iron composite containing high titanium (5.82 wt pct) and coarse TiC particles possess better wear resistance than 12 wt pct Cr cast irons. On the contrary, composites containing medium amount of Ti (3.11 wt pct) with fine TiC particle size distribution perform better under high stress abrasive wear condition.

3. Adhesive wear of TiC reinforced cast iron composites depend both on the amount of titanium present and the volume percent of graphite. The particle size distribution of TiC in cast iron composites play an important role.

4. Composite containing a high amount of titanium (10.86 wt pct) and a high volume percent (12.42 percent) of graphite possess better adhesive wear resistance than

composites containing a low amount of titanium and a low volume percent of graphite.

5.   The pattern of variation of the co-efficient of friction of cast iron composites suggest that a `stick and slip' mechanism operates during the adhesive wear of cast iron composites. The co-efficient of friction values for cast iron composites are more than those of a standard spheroidal graphitic iron.

6.   Debris of cast iron composites show the presence of titanium indicates the fragmentation and loosening of TiC particles.

7.   The wear rates of spheroidal graphitic iron are more than those of cast iron composites under identical loads.

8.   A TiC reinforced plain carbon steel composite has shown better adhesive wear resistance to TiC reinforced alloy steel composite and low alloy steel specimen.

9.   The abrasive wear resistance of a TiC reinforced alloy steel composite in the normalised condition is superior to that of same steel composite in the oil quenched and tempered condition as well as to that of a plain carbon TiC reinforced steel composite in the normalised condition.

CHAPTER - FIVE

GENERAL DISCUSSION AND CONCLUSIONS

5.1 GENERAL DISCUSSION

The present investigation was designed to produce TiC-reinforced cast iron and steel composites through a novel route. Scientific interpretation of the metallurgical characteristics of the TiC reinforced cast iron and steel composites have been provided in the earlier Chapters. In this Chapter, an attempt is being made to analyse and discuss the technological aspects of preparation and application of TiC reinforced ferrous composites. The results of the investigation suggest that TiC-reinforced composites can, in fact, be produced by plasma smelting of ilmenite ore. This process would offer several advantages over the conventional powder metallurgy route of TiC-reinforced ferrous composite preparation. The most important advantages are the following:-

1. This is a single stage process starting from the ore.
2. The melting and casting route offers the prospect of preparing shaped castings.

However, the exercise also exposed the limitations of the smelting-casting route. It has been repeatedly observed during the present investigation that the fluidity of the composite melt depends very much on the Ti and C contents. TiC is a refractory compound and it has very little solubility in liquid iron. It may therefore, be usually assumed that most of the TiC particles remain in suspension

in liquid iron. The fluidity of the melt therefore depends very much on the overall Ti and C percentage or in other words, on the volume percent of TiC particles. For optimum fluidity, the maximum Ti and C contents may be respectively 8-10 wt pct Ti and 3-4 wt pct C only. Therefore, castings containing TiC particles produced through this route is likely to be suitable for the manufacture of wear resistant components. When the melt is impregnated with a high volume fraction of TiC, it loses its fluidity and casting becomes difficult. Moreover, the TiC particles also become coarse. Therefore, the smelting and casting route is suitable only for the preparation of TiC reinforced ferrous composites with a relatively low volume fraction of TiC.

The tribological properties of the composites have been found to be quite attractive. The results indicate that the cast iron composites may be judiciously used for both adhesive and abrasive wear resistant applications. For applications involving adhesive wear, annealed or normalised samples having sufficient amount of free graphite along with finely dispersed TiC particles appear to be the most suit-able. On the other hand, a chilled matrix in which TiC particles are also dispersed offers better resistance to abrasive wear. Thus the same cast iron many be utilised for both adhesive and abrasive wear applications by simply selecting the appropriate microstructure and heat treatment.

The present study has also highlighted the importance of TiC particle size distribution and volume fraction. It may be interesting to note that minor pick up of magnesium or zirconium into the melt from the crucible lining also had its own effect in the TiC particle size distribution and graphitisation kinetics. Although this aspect has been noted, the mechanisms involved has not been completely elucidated in the present study. Further work needs to be carried out to develop a complete understanding of the phenomena involved.

Carbothermic reduction of ilmenite in a graphite crucible, however, does not permit the preparation of TiC reinforced steel composites by a single stage smelting operation, due to the inevitable pickup of carbon. TiC reinforced steel composites were, therefore, prepared by adding a master alloy containing TiC to liquid steel. Although composites were successfully produced by this technique, the difficulties involved need to be analysed. From the data on Ti recovery, it is apparent that the major part of TiC is lost presumably by oxidation before incorporation into the melt. Secondly, there is carbon pick up from the master alloy and hence the matrix carbon content also raises. There is, therefore, scope for further improvement in the process technology in the future work. However, in spite of such limitations in the production technique, the author believes that the wear resistant properties of TiC

reinforced steel composites have been adequately focussed through the present study. The forged TiC reinforced steel composites performed better than a quenched and tempered low alloy steel even in abrasive wear situations.

The following major conclusions may therefore be drawn from this work :

5.2 MAJOR CONCLUSIONS

1. TiC reinforced cast iron composites may be conveniently produced by the carbothermic reduction of ilmenite ore in a bed of steel scrap in a plasma reactor. However, the Ti and carbon contents in such composites needs to be restricted to 8-10 wt pct Ti and 3-4 wt pct C, respectively, to ensure flowability of the melt from the furnace. Composites with higher Ti and carbon contents can not be cast.

2. TiC reinforced cast iron composites possess attractive wear resistance property. The extent of wear resistance depends on both TiC particles size and volume fraction and the matrix structure, which are influenced by the pick up of Mg and Zr from the furnace lining, the cooling rate and by heat treatment.

3. Steel based composites may also be prepared by impregnating liquid steel melt with TiC rich Fe-TiC master alloy. Although the recovery of TiC in this process is low, the steel based composites possess attractive wear resistance and mechanical properties.

REFERENCES

1. S. Ray, J. Mater. Sci., 28, (1993), 5397-5413

2. Technical literature from 'Chromalloy' Metal Tectonics Company Bulletin 54, Sinter Cast Division, Western Highway, West Nyack, New York 10994

3. B.V. Chalmers, T.Z. Kattamis, J.A. Cornie and M.C. Flemings in J. Beech and H. Jones (eds) 'Proc. Conf. on Solidification Process' 1987, Institute of Metals, London (1987), PP 435-438

4. K.H. Miska, Mater. Eng., 11, (1975), 67-70

5. S.E. Tarkan and M.K. Mai, Met. Prog., 105, (1974), 99-102

6. B.S. Terry and O.S. Chinyamakobvu, J. Mater. Sci. Lett., 10, (1991), 628-629

7. H. Lehuy, G. Cliche and S. Dallaire, Mater. Sci. and Eng., A125, (1990), L11 - L14

8. B.S. Terry and O.S. Chinyamakobvu, Mater. Sci. and Tech., 7, (1991), 842-848

9. O. Kubaschewski and E. LL. Evans, `Metallurgical Thermochemistry', Pargamon press, London, (1965), 336-343

10. D.R. Mac Rae, Plasma Chemistry and Plasma Processing 9, (1989) (Supplement), 85 S.

11. K. Upadhya, J.J. Moore and K.J. Reid, J. of Metals, 36, (1984), 46

12. C.A. Pickles, A. Mc Lean and C.B. Alcock, Can. Met. Quart., 24, (1985), 319

13. R.T. Jones, N.A. Barcza and T.R. Curr, Preprint Second International Plasma Symposium; World progress in plasma applications, 9-11 Feb. 1993, Pulo Alto, California, USA

14. N.A. Barcza, T.R. Curr and R.T. Jones, Preprint 9th International Symposium on Plasma Chemistry, ISPC-9, 3-8 Feb. 1989, Bari, Italy.

15. J.C. Hall, Mintek Review 6, (1987), 47

16. G.K. Bhat, J. Vac. Sci. Technol., 18(3), (1981), 1293

17. `McGraw Hill Encyclopedia of Science and Technology' 10, (1982), 508.

18. K. Upadhya, Trans. I.I.M., 38, (1985), 472

19. V. Ibberson, New Scientist, 26 July, 1984, 19

20. E. Pfender, Chapter 5, `Gaseous Electronics' Eds. M.H. Hirshand H.J. Oskam Vol.1, Academic Press, New York NY, (1978), 351

21. G.K. Bhat, Pure Appl. Chem., 56, (1984), 209-214.

22. J.E. Gomersall, Minket Review 6, (1987), 28

23. W.J. Maddever and R.S. Segsworth, Can. Met. Quart., 15, (1976), 49-52

24. R.S. Segsworth, W.J. Maddever and R.M. Nikolic, Electric furance conference proc., ISS-AIME, 33, (1977), 223-224

25. R.S. Segsworth and C.B. Alcock, US. Patent 4,006,284, Feb. (1977)

26. C.A. Pickles, A. Mc Lean, C.B. Alcock and R.S. Segeworth, `Advances in Extractive Metallurgy', The Institute of Mining and Metallurgy, London, (1977), 69

27. W.J. Maddever, R.M. Nikolic, A. Mc Lean, and R.S. Segsworth, Proc. AIME Electric Furance Conf., 34, (1976), 257-265

28. D.R. Mac Rae, `Plasma Technology in Metallurical Processing' Ed. J. Feinmann, Iron and Steel Society Inc., 410 Commonwealth Drive Warrendale, PA 15086, (1987), 149-162

29. D.R. Mac Rae, Proceedings of the 6th International Ferroalloys Congress Cape Town, Johannesburg 1, (1992), 21.

30. R.K. Galgali, U. Syamaprasad, S.K. Mishra and B.C. Mohanty, Trans. I.I.M., 41, (1988), 489-491

31. M. Hansen, `Constitution of binary alloys', Mc Graw Hill Book Co. Inc., New York, (1958), pp 723-727.

32. F. Laves and H.J. Wallbaum, Naturwissenschaften, 27, (1939), 674-675.

33. P. Dawez and J.L. Taylor, Trans. AIME., 188, (1950), 1173-1176

34. H.W. Worner, J. Inst. Metals, 79, (1951), 173-188

35. W. Rostoker, Trans. AIME, 194, (1952), 209-210

36. T.B. Massalski (ed.)`Binary alloy phase diagrams', ASM Materials Information Soc. USA, 1, (1990), 888-891

37. Y. Murakami, H. Kimura and Y. Nishimura, Trans. Natl. Res. Inst. Met., 1, (1959), 7.

38. M. Morozova, M. Khripun and S. Ariya, Zh. Obshch Khim., 32, (1962), 2072.

39. C.E. Lowell and W.S. Williams, Rev. Sci. Instrum., 32, (1961), 1120

40. W.A. Chupka, J. Berkowitz, C. Giese and M. Inghram J. Phys. Chem., 62, (1958), 611.

41. G.L. Humphery, J. Am. Ceram. Soc., 34, (1951), 2261

42. K.K. Kelley and E.G. King, U.S. Bur. Mines. Bull, 592, (1961)

43. F.D. Richardson, J. Iron & Steel Inst., London, 175, (1953), 33

44. S. Fujishino and N.A. Gokeen, J. Phys. Chem., 65, (1961), 161

45. D.T. Gawne and G.M.H. Lewis, Mater. Sci and Tech., 1, (1985), 183-191

46. C. Webnscuan, Proc. of the Intnat. Conf. on HSLA Steels, Beijing, (1985), ASM, P 199-206

47. K.J. Irvine and F.B. Pickering, J. Iron & Steel Inst., 201, (1963), 944-959

48. K.A. El-Fawakhry, M.L. Mishreky and M.M. Erssa, Scand. J. Metall., 19, (1990) 33-38

49. K.A. El-Fawakhry, M.F. Mekkawy, M.L. Mishreky and M.M. Eissa, Iron and Steel Inst. Japan. Internat., 31 (1991), 1020-1025

50. M.F. Mekkawy, K.A. El-Fawakhry, M.L. Mishreky and M.M. Eissa, Scand. J. Metall., 19, (1990), 82-84

51. I.M. Robertson, Mater. Sci and Tech., 9, (1993), 1031-1036

52. K.J. Irvine, F.B. Pickering and T. Gladman, J. Iron & Steel Inst., 205, (1967), 161-182

53. K. Balasubramanian, A. Kroupa and J.S. Kirkaldy, Metall. Trans., 23A, (1992), 709-727

54. R.G. Coltters, Mater. Sci. and Eng., 76, (1985), 1-50

55. G.V. Samsonov, I.I. Timofeeva and L.A. Klochkov, Sov. Powder Metall. Met. Ceram., 83, (1969), 918

56. W.S. Williams, Mater. Sci. and Eng., A 105/106, (1988), 1-10

57. I.E. Campbell and E.M. Sherwood (eds.), 'High Temperature Materials and Technology', John Wiley and Sons Inc USA, (1967), pp 324

58. W.S. Williams, J. Appl. Phys., 35, (1964), 1329-1338

59. W.S. Williams, in 'Proprietes Thermodynamiques Physiques et Structurales des Derives Semimetalliques' Eds du Centre National de la Recherche Scientifique, Paris, (1967), pp 181-189

60. T.S. Srinivasan and E.J. Lavernia, J. Mater. Sci., 27, (1992), 5965-5981

61. P.J. Lloyd, Inter. Natl. Met. Rev., 39, (1994), 1-23

62. J.L. Ellis, Tools Eng., April, (1957), 103-105

63. F.A. Badia and P.K. Rohatgi, Trans. AFS, 79, (1969), 346

64. S. Ray, M.Tech. dissertation, Indian Institute of Technology, Kanpur, (1969)

65. P.K. Rohatgi, R. Asthana and S. Das, Inter. . . Met. Rev., 31 (1986), 115-139

66. A.M. Patton, J. Inst. Met., 100 (1972), 197-201

67. A. Banerjee, P.K. Rohatgi and W. Reif, Metall., 38 (7), (1984), 656

68. L.E. Kindliman and G.S. Anseli, Met. Trans., 1, (1970), 507

69. F.A. Badia and P.K. Rohatgi, Trans. AFS, 77, (1969), 402

70. Deonath, R.T. Bhat and P.K. Rohatgi, J. Mater. Sci., 15, (1980), 1241

71. B.C. Pai and P.K. Rohatgi , J. Mater. Sci., 13, (1979), 329

72. P.K. Rohatgi, B.C. Pai and S.C. Panda, J. Mater. Sci., 14, (1979), 227.

73. D.M. Karpinos, P.M. Askarov and O.V. Abramov, Sov. Powder. Metall. Met. Ceram., 21, (1992), 213

74. J. Sugishita, S. Fujiyoshi and T. Imure, Wear, 81, (1982), 209

75. J.V. Naidich, Prog. Surf. Membr. Sci., 14, (1981), 354, Re ferred by B.S. Terry and O.S. Chinyamakobvu, Mater. Sci. and Tech., 8, (1992), 399-405

76. B.S. Terry and O.S. Chinyamakobvu, Mater. Sci. & Tech., 8, (1992), 399-405

77. P.R. Beeley, A.J. Baker, P.A. Blackmore and A. Segal, Met. Techn., 8, (1981), 268.

78. M. Xiaojun, A.J. Baker and P.R. Beeley, Foundryman, 84, (1991), 66-70

79. T.Z. Kattamis and T. Suganuma, Mater. Sci and Eng., A 128, (1990), 241-252

80. W.I. Silence, J. Lubr. Technol., 100, (1978), 428

81. B. De Celis, Wear, 116, (1987), 287-298.

82. H.J. Heine, Foundry Mange. Technol., 85, (1987), 25-29

83. I.M. Hutching, Mater. Sci and Tech., 10, (1994), 513-517

84. I.M. Hutchings, 'Tribology: friction and Wear of Engineering Materials' (1992), London, Edward Arnold.

85. F.M. Hasking, F. Folgan Portillo, R. Wunderlin and R. Mehra bian, J. Mater. Sci., 17, (1982), 477-498

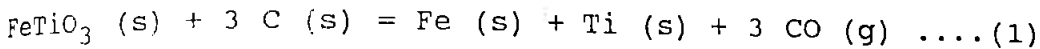86. K. Anand and Kishore, Wear, 85, (1983), 163-169

87. S. Wilson and A. Ball, in 'Tribology of Composite Materials' (ed P.K. Rohatgi et al.,), (1990), 103-112, Metals Park OH. ASM

88. B.C. Pai and P.K. Rohatgi, Trans. Indian Inst. Met., 27, (1974), 97

89. N. Saka and D.P. Karalekas, in 'Wear of Materials 1985' (ed. K.C. Ludema), New York, ASME, (1985), 784-793

90. P.J. Mutton, B.A. Hugaas and W. Sinclair, Mater. Foram, 16, (1992), 87-90

91. S. Skolianos, T.Z. Kattamis, M. Chen and B.V. Chambers, Mater. Sci. and Eng., A183, (1994), 195-204

92. N.S. Poonawala, PhD Thesis, Dept. of Metallurgy, IIT, Khargapur, (1991)

93. M. Riss, Y. Khodorovsky, `Production of ferro-alloys', (Translated by I.V. Savin), Mir Publishers, Moscow, (1967), 218-230

94. C.W. Chang and J. Szekely, J. Metals, 34(2), (1982), 57

95. P. Fauchais, M. Boulos and E. Pfender, 'Plasma Technology in Metallurgical Processing' (Ed. J. Feinman), Iron and Steel Society, Inc., 410 Commonwealth Drive Warrendale PA 15086, 11

96. L. Darken and R. Gurry, `Physical chemistry of metals', Mc Graw Hill Book Co. Inc., Tokyo, (1953), 304-305

97. Brick, Gordon and Phillips, `Structure and Properties of Metals and Alloys', Tata-McGraw Hill Publications.

98. K. Strauss (Ed.) `Applied science in the casting of metals', Pergamon press, (1970), 179-185

99. J.S. Gittus, Iron and Steel, 34, (1961), 124

100. S. Banerjee, Iron and Steel, 42, (1969), 55

101. G.M. Hammond, E.J. Walls, W.B. Pierce and R.A. Flinn, Trans. AFS, 62, (1954), 385

102. C. Bodsworth, `Physical chemistry of iron and steel manufacture', ELBS, (1963), 406-410

103. T. Shiraiwa, N. Fujino and J. Murayama, Trans. Iron and Steel Inst., Japan, 10, (1970), 406-412

104. I.A Ibrahim, F.A. Mohamed and E.J. Lavernia, J. Mater. Sci., 26, (1991), 1137-1156

105. H. Stuart, J. Metals, 43, (1991), 35-40

106. J.R. Paules, J. Metals, 43, (1991), 41-44

107. A.E Miller, J. Metals, 35 (10), (1983), 56-62

108. K.J. Bhansali and R. Mehrabian, J. Metals, 34 (9), (1982), 30-34

109. A.W.J. de Gee, Internat. Met. Rev., (Review No. 239), No. 2, (1979), 57-67

110. J. Vatavuk and J.R. Mariano, J. Metals, 44, (1992), 13-14

111. Kirk-Othmer (ed.), `Encyclopedia of chemical techonology', John Wiley & Sons, New York, 15, (1981), 874

112. M.M. Khruschov, Wear, 28, (1974), 69-88

113. M. Suwa, K. Komuro and K. Soeno, J. Japn. Inst. Met., 41, (1977), 511

114. F.A. Badia and P.K. Rohatgi, SAE Trans., 78(2), (1969), 1200

115. F.P. Bowden and L. Leben, Proc. Roy. Soc., A169, (1939), 371

116. I.M. Hutching, Mater. Sci. and Eng., A184, (1994), 185-195

117. J. Sugishita and S. Fujiyoshi, Wear, 77, (1982), 181-193

118. P.K. Rohatgi, S. Ray and Y. Liu, Int. Mater. Rev., 37, (1992), 129

119. A.D. Sarkar, `Wear of metals', Internat. Series on Mater. Sci. and Tech., Pergamon press (UK), 18, (1976), 55
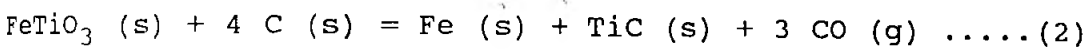
APPENDIX - I

Thermodynamic calculations for reduction of ilmenite are presented in this Appendix.

$FeTiO_3$ (s) + 3 C (s) = Fe (s) + Ti (s) + 3 CO (g) ....(1)

G^O_T = 202,968.3 - 117.56 T Cal

Hence, G^O_T = 0 at T = 1726.5 K

G^O_{2000} = - 32.15 k Cal

$FeTiO_3$ (s) + 4 C (s) = Fe (s) + TiC (s) + 3 CO (g) .....(2)

G^O_T = 158,368.3 - 114.4 T Cal

Hence, G^O_T = 0 at T = 1384.3 K

G^O_{2000} = - 70.4 k Cal

$3FeTiO_3$ (s) + TiC (s) = 3 Fe (s) + 4 TiO_2 (s) + CO (g) .(3)
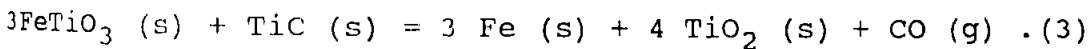
G^O_T = - 6728.31 - 21.12 T Cal

Hence, G^O_T = 0 well below room temperature

It may be seen from reactions represented by Eq. [1] and Eq. [2] that the formation of carbide is favoured over ele-mental metallisation. The carbide - oxide reaction represented by Eq. [3] shows that reaction product is titanium dioxide. Thus, the thermodynamic calculations on reduction of ilmenite by carbon as a reductant have shown similar trend to those of titanium dioxide reduction described in section 4.1.2